



# Earth Observation for the Assessment of Long-Term Snow Dynamics in European Mountains

Analysing 35-Year Snowline Dynamics in Europe Based on High  
Resolution Earth Observation Data between 1984 and 2018

Dissertation zur Erlangung der Doktorwürde der  
naturwissenschaftlichen Fakultät der  
Julius-Maximilians-Universität Würzburg

Vorgelegt von

**Zhongyang Hu**

August 2019



致我亲爱的白睿智和我的外婆钱月妹。

To my dearest Ruizhi Bai, and my grandma Yuemei Qian.

Cover Photo: Landsat image in false colour composite illustrating the snow and ice (in blue) in the Alps.

---

Eingereicht am: 13.08.2019

**Von:** Zhongyang Hu (M.Sc.)

**Ort:** Lehrstuhl für Fernerkundung der Julius-Maximilians-Universität Würzburg,  
in Kooperation mit dem Deutschen Fernerkundungsdatenzentrum (DFD) des  
Deutschen Zentrums für Luft- und Raumfahrt (DLR)

**1. Gutachterin:** Prof. Dr. Claudia Künzer

**2. Gutachter:** Prof. Dr. Stefan Dech

**1. Prüferin:** Prof. Dr. Claudia Künzer

**2. Prüfer:** Prof. Dr. Jürgen Rauh

Tag der mündlichen Prüfung: 12.02.2020

---

This dissertation was prepared in the department "Land Surface Dynamics" at the German Remote Sensing Data Center (DFD), Earth Observation Center (EOC) of the German Aerospace Center (DLR), Oberpfaffenhofen, Germany.

---

子曰：

“可与言而不与之言，失人；

不可与言而与之言，失言。

知者不失人，

亦不失言。”

—— 《论语·卫灵公》

---

“Not everything that can be counted counts,  
and not everything that counts can be counted.”

—— William Bruce Cameron



# Table of Contents

<b>Table of Contents .....</b>	<b>VII</b>
<b>Acknowledgements .....</b>	<b>XI</b>
<b>Abstract.....</b>	<b>XIII</b>
<b>Kurzfassung (German Abstract) .....</b>	<b>XV</b>
<b>摘要 (Chinese Abstract) .....</b>	<b>XVII</b>
<b>List of Figures.....</b>	<b>XIX</b>
<b>List of Tables .....</b>	<b>XXV</b>
<b>Abbreviations and Acronyms .....</b>	<b>XXVII</b>
<b>1 Introduction.....</b>	<b>1</b>
1.1 Introduction to Cold Regions .....	3
1.1.1 Geographical Extent of Cold Regions .....	3
1.1.2 Cold Regions in the Context of Climate Change .....	5
1.1.3 Snow as a Crucial Cold Region Component in the European Mountains.....	7
1.1.4 The Need for Earth Observation (EO)-based Snow Dynamic Monitoring in Europe .....	8
1.2 Research Foci and Objectives of the Thesis .....	9
1.3 Structure and Context of the Thesis .....	13
<b>2 State-of-the-Art: Results of the Literature Review of Remote Sensing on Cold Regions .....</b>	<b>17</b>
2.1 Earth Observation Studies Contributing to Cold Region Monitoring in Europe .....	17
2.1.1 Overview of the Reviewed Studies.....	18
2.1.2 Cold Region Extent Delineation .....	21
2.1.3 Snow Dynamics Monitoring.....	24
2.1.4 Glacier Dynamics Monitoring.....	30
2.2 Identified Challenges of Earth Observation on Cold Regions.....	39
2.2.1 Challenges with Regards to Spatiotemporal Scale and Study Area Settings.....	39
2.2.2 Challenges with Regards to Data Availability, Cost and Suitability of Different EO Sensor Types.....	41

2.2.3 Challenges with Respect to Method Applicability.....	42
2.3 The Need and Potential of the Landsat Archive for Long-Term Snow Monitoring in Mountainous Areas.....	46
<b>3 Study Areas.....</b>	<b>49</b>
3.1 Location and Topography .....	49
3.2 Climatology .....	53
3.3 Hydrology .....	55
3.4 Land Cover.....	57
3.5 Snow Phenology .....	59
3.6 Socioeconomic Situation .....	61
<b>4 Data .....</b>	<b>65</b>
4.1 Satellite Imagery.....	65
4.1.1 Landsat Data.....	67
4.1.2 Sentinel-2 Data.....	70
4.1.3 ASTER Data.....	71
4.2 Digital Elevation Model (DEM) .....	73
4.3 Climate Reanalysis Data.....	74
4.4 In-Situ Data .....	76
4.5 Auxiliary Data .....	77
<b>5 Developed Framework of Snowline Retrieval and Assessment .....</b>	<b>81</b>
5.1 Optical Imagery Pre-Processing .....	81
5.2 Snow Classification and Validation .....	83
5.3 Regional Snowline Elevation (RSE) Retrieval and Accuracy Assessment .....	85
5.4 Time Series Densification Using Random Forest Regression (RFR) .....	87
5.5 Regional Snowline Retreat Curve (RSRC) Derivation and Validation .....	89
<b>6 Results of Snowline Dynamics in Europe.....</b>	<b>93</b>
6.1 Analysis of Landsat Collection 1 Availability over Europe .....	93
6.1.1 Suitability of Different Landsat Processing Levels and Tiers .....	94
6.1.2 Spatiotemporal Distribution of the Landsat Collection 1 TM/ETM+/OLI/TIRS L1TP Products in Europe.....	96
6.1.3 Cloud Obstruction of the Landsat Collection 1 TM/ETM+/OLI/TIRS L1TP Products in Europe.....	99



6.2	Snow Cover Maps and Regional Snowline Elevation (RSE) .....	102
6.2.1	Snow Classifications and Accuracy Assessment.....	102
6.2.2	Regional Snowline Elevations (RSEs) and Accuracy Assessment .....	104
6.2.3	Modelled Regional Snowline Elevations (RSEs) and Accuracy Assessment .....	107
6.3	Long-term Snowline Dynamics in European Mountains .....	111
6.3.1	Intra-annual Variations of Regional Snowlines during the Ablation Seasons 1984–2018 .....	111
6.3.2	Inter-Annual Variability of Regional Snowlines during the Ablation Seasons 1984–2018 .....	112
6.3.3	Accuracy Assessment of Regional Snowline Retreat Curves (RSRCs) .....	117
6.4	Potential Climate Drivers and Consequences of the Detected Long-Term Snowline Dynamics in the European Mountains .....	119
6.4.1	Snowline Dynamics and Air Temperature Anomalies.....	119
6.4.2	Snowline and Discharge Dynamics during the Ablation Seasons 2000–2016.....	121
<b>7</b>	<b>Discussion.....</b>	<b>123</b>
7.1	Gaps in the Long-Term Landsat Collection 1 Archive .....	123
7.1.1	Significant TM Data Gaps in the 1990s and Southwestern Europe.....	123
7.1.2	Influence of Cloud Cover and Haze on Data Availability .....	125
7.1.3	Influence of Cloud Cover on Snowline Elevation Statistics.....	127
7.2	Challenges Regarding Accurate Snow Cover Mapping and Regional Snowline Elevation (RSE) Retrieval.....	128
7.2.1	Challenges for Accurate Snow Cover Mapping .....	128
7.2.2	Challenges for Accurate Regional Snowline Elevation (RSE) Retrieval.....	129
7.2.3	Challenges for Accurate Regional Snowline Elevation (RSE) Modelling.....	130
7.2.4	Challenges for Validating Snow Cover Maps and Regional Snowline Elevation (RSE) Results.....	131
7.3	Characterizing Regional Snowline Elevation (RSE) Dynamics .....	133
7.3.1	Challenges of Accurately Deriving Regional Snowline Retreat Curves (RSRCs).....	133

7.3.2 Observed Regional Snowline Dynamics in European Mountains.....	134
7.4 Potential Applications of Regional Snowline Dynamics.....	135
<b>8 Conclusion and Outlook .....</b>	<b>139</b>
8.1 Summary and Conclusive Findings .....	139
8.1.1 The State-of-the-Art of Earth Observation in Cold Region Monitoring.....	140
8.1.2 Availability and Suitability of the Long-Term Landsat Archive for Snow Monitoring in European Mountains.....	142
8.1.3 Spatiotemporally Transferable Framework for Snowline Derivation in Mountainous Areas.....	144
8.1.4 Characteristics, Potential Climate Drivers, and Consequences of the Detected Long-Term Snowline Dynamics in European Mountains .....	145
8.2 Outlook and Future Opportunities .....	146
<b>References .....</b>	<b>149</b>
<b>Eidesstattliche Erklärung.....</b>	<b>173</b>
<b>Curriculum Vitae - Zhongyang Hu .....</b>	<b>175</b>

## Acknowledgements

It would not be possible to make my doctoral study through without the help of a large number of people. In particular, I would like to express my special thanks to the following persons:

Firstly, I would like to express my sincere gratitude to my supervisor at the German Remote Sensing Data Center (DFD) at the German Aerospace Center (DLR), Prof. Dr. Claudia Kuenzer, for guiding me from the initial to the final level of my doctoral study. Her logical thinking as well as extensive knowledge is a great treasure.

Secondly, my sincere thanks go to Prof. Dr. Stefan Dech for taking on the second evaluation, and for showing a scientific interest in this work, as well as to Prof. Dr. Christopher Conrad for helpful comments towards the start of my doctoral study.

Thirdly, I acknowledge the contribution of Dr. Andreas Dietz, for his support in a helpful and cheerful way, and his willingness to always discuss new and up-to-date insights of the snow topics in remote sensing community.

I am also grateful to the following colleagues from DLR-DFD at the department "Land Surface Dynamics": Soner Üreyen, Mariel Dirscherl, and Celia Baumhoer, who helped me with proofreading, and gave me constructive suggestions. I would like to express my appreciation to Dr. Emmanuel Da Ponte, Dr. Kersten Clauss, and Dr. Marco Ottinger, with whom I went through all the ups and downs that such a big work comes with.

Lastly, I would like to thank Ruizhi Bai for the endless support, motivation, and a comprehensive proofreading. I am indebted to Ruizhi Bai for reminding me what is truly important in my life and for making me stronger than I could have ever imagined. Whenever I was nervous, frustrated, and lost, Ruizhi Bai always cheered me up. Besides, this work is dedicated to my dear parents (Zhi'ang Hu and Xiangying Wu) and grandparents (Yuemei Qian, Zurong Wu, Xinmo Hu, and Sugui Chen), for their love, financial support, and encouragement during the past years. Without their support, I will never be able to come to Germany and receive this valuable education in Germany.

Oberpfaffenhofen, 22.07.2019

Zhongyang Hu



## Abstract

Worldwide, cold regions are undergoing significant alterations due to climate change. Snow, the most widely distributed cold region component, is highly sensitive to climate change. At the same time, snow itself profoundly impacts the Earth's energy budget, biodiversity, and natural hazards, as well as hydropower management, freshwater management, and winter tourism/sports. Large parts of the cold regions in Europe are mountain areas, which are densely populated because of the various ecosystem services and socioeconomic well-being in mountains. At present, severe consequences caused by climate change have been observed in European mountains and their surrounding areas. Yet, large knowledge gaps hinder the development of effective regional and local adaptation strategies. Long-term and evidence-based regional studies are urgently needed to enhance the comprehension of regional responses to climate change.

Earth Observation (EO) provides long-term consistent records of the Earth's surface. It is a great alternative and/or supplement to conventional in-situ measurements which are usually time-consuming, cost-intensive and logistically demanding, particularly for the poor accessibility of cold regions. With the assistance of EO, land surface dynamics in cold regions can be observed in an objective, repeated, synoptic and consistent way. Thanks to free and open data policies, long-term archives such as Landsat Archive and Sentinel Archive can be accessed free-of-charge. The high- to medium-resolution remote sensing imagery from these freely accessible archives gives EO-based time series datasets the capability to depict snow dynamics in European mountains from the 1980s to the present. In order to compile such a dataset, it is necessary to investigate the spatiotemporal availability of EO data, and develop a spatiotemporally transferable framework from which one can investigate snow dynamics.

Among the available EO image archives, the Landsat Archive has the longest uninterrupted records of the Earth's land surface. Furthermore, its 30 m spatial resolution fulfils the requirements for snow monitoring in complex terrains. Landsat data can yield a time series of snow dynamics in mountainous areas from 1984 to the present. However, severe Landsat data gaps have occurred across certain regions of Europe. Moreover, the Landsat Level 1 Precision and Terrain (L1TP) data is scarcer (up to 50% less) in high-latitude mountainous areas than in low-latitude mountainous areas. Given the abovementioned facts, the Regional Snowline Elevation (RSE) is selected to characterize the snow dynamics in mountainous areas, as it can handle cloud obstructions in the optical images. In this thesis, I present a five-step framework to derive and densify RSE time series in European mountains, i.e. (1) pre-processing, (2) snow detection, (3) RSE retrieval, (4) time series densification, and (5) Regional Snowline Retreat Curve (RSRC) production.

The results of the intra-annual RSE variations show a uniquely high variation in the beginning of the ablation seasons in the Alpine catchment Tagliamento, mainly toward higher elevation. As for inter-annual variations of RSE, median RSE increases in all selected catchments, with an average speed of around  $4.66 \text{ m} \cdot \text{a}^{-1}$  (median) and  $5.87 \text{ m} \cdot \text{a}^{-1}$  (at the beginning of the ablation season). The fastest significant retreat is observed in the catchment Drac ( $10.66 \text{ m} \cdot \text{a}^{-1}$ , at the beginning of the ablation season), and the slowest significant retreat is observed in the catchment Uzh ( $1.74 \text{ m} \cdot \text{a}^{-1}$ , at the beginning of the ablation season). The increase of RSEs at the beginning of the ablation season is faster than the median RSEs, whose average difference is nearly  $1.21 \text{ m} \cdot \text{a}^{-1}$ , particularly in the catchment Drac ( $3.72 \text{ m} \cdot \text{a}^{-1}$ ). The results of the RSRCs show a significant rise in RSEs at the beginning of the ablation season, except for the Alpine catchment Alpenrhein and Var, and the Pyrenean catchment Ariege. It indicates that 11.8 and 3.97 degrees Celsius less per year are needed for the regional snowlines to reach the middle point of the RSRC in the Tagliamento and Tysa, respectively. The variation of air temperature is regarded as an example of a potential climate driver in this thesis. The retrieved monthly mean RSEs are highly correlated (mean correlation coefficient  $\bar{R} = 0.7$ ) with the monthly temperature anomalies, which are more significant in months with extremely low/high temperature. Another case study that investigates the correlation between river discharges and RSEs is carried out to demonstrate the potential consequences of the derived snowline dynamics. The correlation analysis shows a good correlation between river discharges and RSEs (correlation coefficient,  $R=0.52$ ).

In this thesis, the developed framework signifies a better understanding of the snow dynamics in mountain areas, as well as their potential triggers and consequences. Nonetheless, an urgent need persists for: (1) validation data to assess long-term snow-related observations based on high-resolution EO data; (2) further studies to reveal interactions between snow and its ambient environment; and (3) regional and local adaptation-strategies coping with climate change. Further studies exploring the above-mentioned research gaps are urgently needed in the future.

## Kurzfassung

Weltweit erleben kalte Regionen signifikante Veränderungen durch den Klimawandel. In kalten Regionen ist der Schnee die an der weitesten verbreiteten Komponente, welche sehr sensibel auf Klimaänderungen reagiert. Zugleich beeinflusst der Schnee selbst das Energiebudget der Erde, die Biodiversität, Naturgefahren sowie Wasserenergiegewinnung, Süßwassergewinnung, Wintertourismus und Wintersport. Große Teile der kalten Regionen in Europa sind Gebirgsregionen. Diese sind dicht besiedelt, da Gebirgsregionen verschiedenste Ökosystemservices bereitstellen und sozioökonomisches Wohlbefinden ermöglichen. Heute kann man schwerwiegende Konsequenzen in Europäischen Gebirgen und deren angrenzenden Gebieten wahrnehmen. Dennoch verhindern große Wissenslücken die Entwicklung effektiver und regionaler/lokaler Anpassungsstrategien. Um regionaler Auswirkungen durch den Klimawandel besser verstehen zu können, ist es enorm wichtig Langzeitstudien und beweisorientierte regionale Studien durchzuführen.

Erdbeobachtung (EO) bietet durchgängige Langzeitaufzeichnungen der Erdoberfläche. Dies ist eine großartige Alternative und/oder Ergänzung zu konventionellen in-situ Messungen, welche meist zeitaufwändig, teuer und logistisch herausfordernd sind – vor allem in kalten Regionen, die schwer zugänglich sind. Mit der Hilfe von Erdbeobachtung können Oberflächendynamiken objektiv, wiederholt, synoptisch und kontinuierlich aufgenommen werden. Dank freier und offener Datenpolitik, Langzeitmissionen wie Landsat und Sentinel sind diese Daten inzwischen ohne zusätzliche Kosten zugänglich. Durch die oben genannten Rahmenbedingungen, besteht die Möglichkeit aus hoch bis mittel aufgelöste Satellitenbilder erdbeobachtungs-basierte Zeitreihen zu erstellen, die die Schneedynamiken in Europäischen Gebirgen abbilden. Um dieses Ziel zu erreichen, muss die räumliche und zeitliche Verfügbarkeit von Erdbeobachtungsdaten überprüft werden und ein Rahmenwerk geschaffen werden (übertragbar in Zeit und Raum), um Schneedynamiken aus Erdbeobachtungsdaten großflächig ableiten zu können.

Unter den verfügbaren Erdbeobachtungsarchiven bietet das Landsat Archiv die längsten und kontinuierlichsten Aufzeichnungen der Landoberfläche. Zudem erfüllt die räumliche Auflösung von 30 m die Anforderungen, Schnee in komplexem Terrain zu monitoren. Basierend auf Landsat L1TP Daten (z.B. terrainkorrigiert) ist es möglich, Zeitreihen von Schneedynamiken in Gebirgsregionen zwischen 1984 und 1991/1999 zu erstellen. Des Weiteren ist Landsat L1TP in hohen Breitengraden seltener verfügbar (bis zu 50 % weniger) als in Gebirgsregionen der gemäßigten Breiten. Basierend auf den oben genannten Fakten wurde die Regionale Höhe der Schneefallgrenze (RSE) ausgewählt um Schneedynamiken in Gebirgsregionen zu charakterisieren, da diese Wolken in optischen Szenen bewältigen kann.

In dieser Arbeit wurde ein fünf-Stufen Rahmenwerk geschaffen, um RSE-Zeitserien in Europäischen Gebirgen abzuleiten und zu verdichten. Die Prozessierungskette besteht aus (1) Vorprozessierung, (2) Schneedetektion, (3) RSE-Ableitung, (4) Zeitreihenverdichtung und (5) Erstellung einer regionalen Schneegrenzen-Rückgangsfunktion (RSRC).

Die Ergebnisse der intra-annualen RSE Variationen zeigen eine einzigartige hohe Variation im Beginn der Abschmelzsaison im alpinen Einzugsgebiet Tagliamento, meist in höheren Gebieten. Wie für die inter-annualen Variationen des RSE, steigt auch der Median des RSE in allen ausgewählten Einzugsgebieten mit einer durchschnittlichen Geschwindigkeit von  $4.66 \text{ m} \cdot \text{a}^{-1}$  (median) und  $5.87 \text{ m} \cdot \text{a}^{-1}$  (zum Beginn der Schmelze). Der schnellste signifikante Rückgang kann im Einzugsgebiet Drac ( $10.66 \text{ m} \cdot \text{a}^{-1}$ , Beginn der Schmelze) beobachtet werden, der langsamste Rückgang im Einzugsgebiet Uzh ( $1.74 \text{ m} \cdot \text{a}^{-1}$ , Beginn der Schmelze). Der Anstieg des RSE zu Beginn der Schmelzsaison ist schneller als der Median des RSE, dessen mittlere Differenz  $1.21 \text{ m} \cdot \text{a}^{-1}$  beträgt. Insbesondere für das Drac Einzugsgebiet ( $3.72 \text{ m} \cdot \text{a}^{-1}$ ). Die Ergebnisse des RSRC zeigen signifikante Anstiege des RSE zu Beginn des Schmelzsaison, ausgenommen davon sind die alpinen Einzugsgebiete Alpenrhein und Var und das Einzugsgebiet Ariege in den Pyrenäen. Dies lässt darauf zurückschließen, dass  $11.8 \text{ }^{\circ}\text{C}$  und  $3.97 \text{ }^{\circ}\text{C}$  Grad weniger pro Jahr nötig sind für Tagliamento und Tysa, damit die regionalen Schneegrenzen den Mittelpunkt des RSRC erreicht. Zudem wird die Variation der Lufttemperatur als beispielhafter Treiber des Klimas in dieser Thesis gesehen. Die monatlich abgeleiteten mittleren RSE korrelieren stark (mittlerer korrelations Coefficient  $\bar{r} = 0.7$ ) mit monatlichen Temperaturanomalien. In Monaten mit extrem hohen/tiefen Temperaturen ist die Korrelation am stärksten. Ein anderes Fallbeispiel untersucht die Korrelation zwischen Abfluss in Flüssen und RSE, um die potenziellen Konsequenzen der abgeleiteten Schneefallgrendynamiken zu ermitteln. Die Korrelationsanalyse weist eine gute Korrelation auf ( $R=0.52$ ).

Das in dieser Arbeit entwickelte Rahmenwerk ist nur ein Beginn, um das Wissen über Schneedynamiken in Gebirgsregionen zu verbessern und potentiell auslösende Faktoren und Konsequenzen zu verstehen. Dennoch wird folgendes dringend benötigt: (1) Validierungsdaten für schnee-basierte Langzeitbeobachtungen aus hochaufgelösten Erdbeobachtungsdaten; (2) weitere Studien zu Interaktionen zwischen Schnee und die umgebende Umwelt; und (3) regionale und lokale Anpassungsstrategien, um Auswirkungen des Klimawandels zu meistern. Weitere Studien in den oben genannten Punkten werden in der Zukunft stark frequentiert sein, damit Wissens- und Forschungslücken geschlossen werden können.



## 摘要 (Chinese Abstract)

由于气候变化，全世界的寒冷区正在经历着巨大的变化。冰雪是在寒冷区中分布最广的组分，并且对气候变化高度敏感。与此同时，冰雪本身也在极大地影响着地球的辐射平衡，生物多样性，自然灾害，水电管理，淡水管理以及冰雪旅游和冬季体育项目。大部分的欧洲寒冷区分布在山区。得益于山地丰富的生态系统服务和社会经济福祉，欧洲山区也分布着大量的人口。目前，由气候变化引起的诸多严重后果已经在欧洲山区及其周围地区被观测到。然而，我们现在对寒冷区气候变化的了解还不足以支撑有效的区域性应对战略方案的制定。因此，我们迫切地需要进行长时序的基于观测数据的区域研究，从而更好地应对气候变化。

地球观测能够向我们提供各种时空分辨率的地表数据。考虑到传统的田野调查时常需要耗费巨大的人力物力，并且在可达性较低的寒冷区有巨大的局限性，地球观测是一种对传统实地测量很好的替代与补充。在地球观测的帮助下，我们可以客观并且可重复地获取寒冷区概要和一致的地表面动态数据。得益于数据开放政策，现在 Landsat, ASTER 和 Sentinel 数据已经可以免费使用。在这个背景下，利用开放的中高分辨率的遥感图像构建基于地球观测的时间序列，可以帮助我们揭示从 20 世纪 80 年代到现在的欧洲山区的冰雪动态。为了达成这一目标，我们首先需要调查地球观测数据的时空可用性，并开发一个时空可转移框架来提取冰雪动态。

在现有的地球观测数据中，Landsat 拥有最长且不间断的地表记录数据。同时，Landsat 所能提供的 30 米的空间分辨率也满足了在复杂地形下监测冰雪的要求。利用 Landsat L1TP (标准地形校正) 数据，我们可以构建从 1984 年到现在的山区冰雪动态时序。然而，在欧洲区域有着严重的 Landsat 数据缺失。此外，Landsat L1TP 数据在高纬度山区的数据量也比在低纬度山区更为稀少 (最高可达 50%)。鉴于上述因素，本文选取了区域雪线高程指数来表征山区的冰雪动态，因为区域雪线高程指数可以应对光学影像中的云遮盖。本文开发了一个五步框架来提取欧洲山区的区域雪线高程指数时间序列，包含了 (1) 图像预处理，(2) 冰雪分类，(3) 区域雪线高程指数提取，(4) 时间序列构建，以及 (5) 区域雪线撤退曲线计算。

根据区域雪线高程指数的年内变化，在位于阿尔卑斯山的 Tagliamento 流域内，区域雪线高程指数在融雪季节之初显示出向高的海拔后退的趋势。根据区域雪线高程指数的年际变化，在所有选定流域的区域雪线高程指数的中位数都明显地逐年增加，平均速度约为每年 4.66 米 (中位数) 和每年 5.87 米 (融雪季节初)。最快速的雪线上升发生在 Drac 流域 (融雪季节初: 每年 10.66 米)，最缓慢的则位于 Uzh 流域 (融雪季节初: 每年 1.74 米)。雪线在融雪季节初期的上升速度快于中位数，其平均差异大约是 1.21 米每年，特别是在 Drac 流域这个差异更达到了每年 3.72 米。除了位于阿尔卑斯山的 Alpenrhein 流域和 Var 流域以及位于比利牛斯山的 Ariege 流域之外，区域雪线撤退曲线的结果显示出消融季节开始时，区域雪线高程指数具有显著升高。这表明越来越少的温度 (Tagliamento: 11.8° C, Tysa: 3.97° C) 被需要，让区域雪

线达到区域雪线撤退曲线的中点。此外，在本文中气温的变化作为雪线上升的一个气候驱动因子，月平均域雪线高程指数与月温度异常呈现了高度的相关性（平均相关系数为 0.7），这在极端低/高温出现的月份更为明显。为了研究雪线在融雪季节上升的潜在后果，河流径流和雪线高程指数之间的相关性分析，显示出河流流量与 RSE 之间存在较强的相关性（相关系数为 0.52）。

本文所开发的雪线动态提取框架只是一个开始，为了丰富对山区冰雪地动态的认知，以及潜在诱因和后果，我们仍然迫切得需要以下研究：（1）对高分辨率地球观测数据所提取的冰雪产品精度进行评估的验证数据集；（2）进一步研究冰雪动态与其周围环境之间的相互作用；（3）应对气候变化的区域和地方适应战略的制定。对于探索上述知识和研究空白的进一步研究在未来仍是非常需要的。

## List of Figures

<b>Figure 1-1:</b> The cryospheric components in the Northern and Southern Hemispheres in polar projection. Modified according to Vaughan et al. (2013).....	2
<b>Figure 1-2:</b> Stability of the global cold regions. The darker the blue colour is the more frequent the areas are mapped as cold regions. ....	5
<b>Figure 1-3:</b> The thematic sketch of the cryospheric components and their time scales. Source: Lemke et al. (2007).....	6
<b>Figure 2-1:</b> Thematic diagram of cold region monitoring by space-borne Earth Observation (EO). Modified according to Hu et al. (2017). ....	18
<b>Figure 2-2:</b> Study Objectives of the reviewed EO (Earth Observation)-based cold region studies in Europe.....	19
<b>Figure 2-3:</b> Overview of the applied EO (Earth Observation) sensors employed in the reviewed cold region studies in Europe. Sensors used fewer than four times are shown in the class "others", which includes Advanced Land Observing Satellite (ALOS)-Phased Array type L-band Synthetic Aperture Radar (PALSAR), IKONOS, Japanese Earth Resources Satellite-1 Synthetic Aperture Radar (JERS-1 SAR), Pleiades, Sentinel-1, Sentinel-2, WorldView-1/2, TerraSAR-X, COntellation of small Satellites for the Mediterranean basin Observation (COSMO-SkyMed), Sentientl-1, MEdium Resolution Imaging Spectrometer (MERIS), etc.....	20
<b>Figure 2-4:</b> Geographical distribution of the reviewed EO (Earth Observation) based cold region studies in Europe. ....	21
<b>Figure 2-5:</b> Cold regions in Europe delineated according to integrated stability parameter. Modified according to Hu et al. (2017). ....	22
<b>Figure 2-6:</b> 19-year mean Snow Cover Duration (SCD) between 2000 and 2018 derived from Global Snow Pack (GSP) data based on Dietz et al. (2015) (left), and the scatter plot between mean SCD (2000–2018) and cold region stability (right). The two horizontal anomalous lines are artefacts due to the spatial resolution downscaling occurring in the mountain areas and their surrounding regions. Modified according to Hu et al. (2017).....	23
<b>Figure 2-7:</b> Optical and Synthetic Aperture Radar (SAR) sensors for snow-related applications. Modified according to Kuenzer et al. (2014).....	40
<b>Figure 2-8:</b> Optical, Synthetic Aperture Radar (SAR), and Passive Microwave (PM) sensors for glacier-related applications. Modified according to Kuenzer et al. (2014).....	40
<b>Figure 3-1:</b> Location of the study areas, and their elevation information. Data Source: Tachikawa et al. (2011).....	50
<b>Figure 3-2:</b> Topographic characteristics of each study area. Data Source: Tachikawa et al. (2011).....	51
<b>Figure 3-3:</b> Climate classes of the study areas according to Köppen-Geiger climate classification. Data Source: Rubel and Kottek (2010).....	53

**Figure 3-4:** Long-time mean annual temperature climate charts (1984–2018) for the meteorological stations near/within the investigated catchments: a) Ariege: FRE00106205, b) Serge: SPE00156585, c) Drac: FRM00007591, d) Var: FRM00007690, e) Alpenrhein: GME00128830, f) Adda: ITE00100554; g) Salzach: AU000006306, h) Tagliamento: ITM00016045, i) Uzh: UPM00033631, j) Tysa: UPM00033647. Data Source: Menne et al. (2012). ..... 54

**Figure 3-5:** Observed trends of river flood timing in Europe (left) and observed average timing of river floods in Europe (right) between 1960 and 2010. On the left, the colour scale indicates earlier or later floods in days · a<sup>-1</sup>. The Europe is divided into four regions with distinct drivers: (1) Northeastern Europe (earlier snowmelt); (2) North Sea (later winter storms); (3) Western Europe along the Atlantic coast (earlier soil moisture maximum); and (4) parts of the Mediterranean coast (stronger Atlantic influence in winter). On the right, each arrow represents one hydrometric station. Colour and arrow direction indicate the average timing of floods, and lengths of the arrows indicate the concentration of floods within a year. Modified according to Blöschl et al. (2017)..... 55

**Figure 3-6:** Runoff characteristics during the ablation season (from April to June, 1984–2018) of each investigated study area. Data Source: C3S (2017)..... 56

**Figure 3-7:** Land cover information of each study area. Data Source: Defourny et al. (2016). ..... 58

**Figure 3-8:** Characteristics of the snow phenology (2000–2018) in each study area. Data Source: Dietz et al. (2015). ..... 60

**Figure 3-9:** Freshwater abstraction by source in 2015. The pie chart shows the annual data, for the year 2015, for water abstraction by source at the European level. The quarterly values have been used to show the development of seasonal water abstraction by source. Q1: January to March, Q2: April to June, Q3: July to September, and Q4: October to December, in European Environment Agency (EEA) member countries: Austria, Belgium, Bulgaria, Croatia, Czech Republic, Denmark, Estonia, Finland, Germany, Greece, Hungary, Ireland, Italy, Latvia, Lithuania, Luxembourg, Malta, Netherlands, Norway, Poland, Romania, Slovakia, Slovenia, Spain, Sweden, Switzerland, United Kingdom and Cooperating countries: Albania, Montenegro, Serbia, the Former Yugoslav Republic of Macedonia. Source: EEA (2018)..... 61

**Figure 3-10:** Water use by economic sectors in 2015. For the pie chart, the data series are calculated annually for 2015 of water abstraction by sector at the European level. The quarterly values have been used to show the development of seasonal water use by sectors in Europe. Economic sectors were identified according to the Statistical Classification of Economic Activities in the European (NACE) classes. Q1: January to March, Q2: April to June, Q3: July to September, and Q4: October to December. In European Environment Agency (EEA) member countries: Austria, Belgium, Bulgaria, Croatia, Czech Republic, Denmark, Estonia, Finland, Germany, Greece, Hungary, Ireland, Italy, Latvia, Lithuania, Luxembourg, Malta, Netherlands, Norway, Poland, Romania, Slovakia, Slovenia, Spain, Sweden, Switzerland, United Kingdom and Cooperating countries: Albania, Montenegro, Serbia, the Former Yugoslav Republic of Macedonia. Source: EEA (2018)..... 62

<b>Figure 3-11:</b> Gross value added from all economic sectors and total water abstraction in the European Union (EU)-28 (2000 = index 100). Time series cover the period of 1990–2015. The comparison between water abstraction and gross value added has been made based on gross value added at basic price in euros for the EU-28. Source: EEA (2018). .....	63
<b>Figure 3-12:</b> Population distribution of each study area in 2011. Data Source: GEOSTAT (2011). .....	64
<b>Figure 4-1:</b> Bandpass wavelengths for the employed sensors in this thesis, i.e. Landsat 4–5 Thematic Mapper (TM), Landsat 7 Enhanced Thematic Mapper Plus (ETM+), Landsat 8 Operational Land Imager/Thermal Infrared Sensor (OLI/ TIRS) sensor, Advanced Spaceborne Thermal Emission and Reflection Radiometer (ASTER), and Sentinel-2. Modified according to USGS (2015). .....	66
<b>Figure 4-2:</b> Overview of the elevation information in Europe derived from ASTER GDEM Version 2 (Tachikawa et al., 2011). .....	74
<b>Figure 4-3:</b> 2 m air temperature on April 1, 2018 12:00 (Coordinated Universal Time) over the whole Europe derived from ERA5 (C3S, 2017). .....	75
<b>Figure 4-4:</b> Location of National Oceanic and Atmospheric Administration-Global Historical Climatology Network (NOAA-GHCN) and European Climate Assessment & Dataset (ECA&D) Stations across Europe.....	76
<b>Figure 4-5:</b> Major hydrological basins and their sub-basins. This dataset divides the European continent according to its hydrological characteristics. Data source: Lehner et al. (2008). .....	77
<b>Figure 4-6:</b> Mean Snow Cover Duration (SCD) between 2000 and 2018 derived from the Global Snow Pack (GSP). Data Source: Dietz et al. (2015). .....	78
<b>Figure 4-7:</b> Glacier outlines of Saint Sorlin and Sarenes from the Randolph Glacier Inventory (RGI) (Pfeffer et al., 2014a), near the catchment Drac. ....	78
<b>Figure 4-8:</b> Location of the Global Runoff Data Centre (GRDC) Stations across Europe. ....	79
<b>Figure 5-1:</b> Effects of atmospheric and topographic correction: left: original raw Digital Number (DN) image in false colour composite (RGB: SWIR-NIR-RED); right: ATCOR-corrected image in false colour composite (RGB: SWIR-NIR-RED). .....	81
<b>Figure 5-2:</b> Main processing steps during atmospheric correction. Modified according to Richter and Schläpfer (2011). .....	82
<b>Figure 5-3:</b> Multispectral profiles of main land covers: left: atmospherically and topographically corrected image in false colour composite (RGB: SWIR-NIR-RED), right: multispectral profiles of snow/ice, vegetation and water body. (Data source: Landsat 8 Operational Land Imager/Thermal Infrared Sensor (OLI/TIRS) near the catchment Drac at path/row: 196/029 acquired on 07 June 2017). .....	83

**Figure 5-4:** Estimation of Regional Snowline Elevation (RSE) from the combined cumulative histograms of the snow covered pixels (in blue) and land pixels (in orange). In the x-axis,  $P_1$  indicates that there are  $P_1$  land pixels above the RSE;  $P_2 - P_1$  there are  $P_2 - P_1$  snow pixels below the RSE,  $P_2$  alone means the sum of land pixels above the RSE and snow pixels below the RSE, and  $T_P$  stands for the total number of pixels. Modified according to Hu et al. (2019b)..... 86

**Figure 5-5:** Theoretical Regional Snowline Retreat Curve (RSRC) based on the Accumulated Temperature (AT) and Regional Snowline Elevation (RSE).  $AT_{EA}$  are the AT at the end of the ablation season, whose RSEs is the  $RSE_{max}$ .  $AT_{min}$  and  $AT_{max}$  are the minimum/maximum AT observed within the ablation season. Accumulated Temperature of the Mid-Ablation season ( $AT_{MA}$ ) is the mid-point of the RSRC, which is the AT value of the mid-ablation season. The solid line represents the standard situation, and the dash lines are the RSRC with different regression coefficients. The dash lines and dot-dash lines represents the behaviour of the RSRCs in different slope and intercept values. Modified according to Hu et al. (2019b)..... 90

**Figure 6-1:** Quality indicators of the Landsat scenes archived in Collection 1 dataset (1982–2017) over Europe..... 95

**Figure 6-2:** Temporal pattern of monthly Landsat 4–5 Thematic Mapper (TM), Landsat 7 Enhanced Thematic Mapper Plus (ETM+), and Landsat 8 Operational Land Imager/Thermal Infrared Sensor (OLI/TIRS) Level 1 Precision and Terrain (L1TP) acquisition amounts over Europe archived in Collection 1 dataset. Modified according to Hu et al. (2019a). ..... 97

**Figure 6-3:** Spatial distribution of Landsat 4–5 Thematic Mapper (TM), Landsat 7 Enhanced Thematic Mapper Plus (ETM+), and Landsat 8 Operational Land Imager/Thermal Infrared Sensor (OLI/TIRS) Level 1 Precision and Terrain (L1TP) scenes over Europe archived in Collection 1 dataset between 1984 and 2017. .... 98

**Figure 6-4:** The frequency of cloud occurrence of Landsat 4–5 Thematic Mapper (TM), Landsat 7 Enhanced Thematic Mapper Plus (ETM+), and Landsat 8 Operational Land Imager/Thermal Infrared Sensor (OLI/TIRS) Level 1 Precision and Terrain (L1TP) scenes in Collection 1 archive based on  $F_{mask}$ ..... 100

**Figure 6-5:** Boxplots of seasonal cloud cover per scene in the main European mountain areas: (a) Scandinavian Mountains, (b) Scotland, (c) Iceland, (d) Pyrenees, (e) Alps, and (f) Carpathian Mountains. Modified according to Hu et al. (2019a)..... 101

**Figure 6-6:** Snow Classification based on (a) Landsat 8 Operational Land Imager/Thermal Infrared Sensor (OLI/TIRS) and (b) Moderate Resolution Imaging Spectroradiometer (MODIS) imagery in the Catchment Drac on 07 June 2017, and the atmospherically and topographically corrected image in false colour composite (RGB: SWIR-NIR-RED) (c), as well as two zoom-ins (d–e)..... 103

<b>Figure 6-7:</b> Snowlines based on Regional Snowline Elevations (RSEs) during the ablation season (from April to June) 2018 within the investigated catchments: a) Adda, b) Alpenrhein, c) Ariege, d) Drac, e) Salzach, f) Serge, g) Tagliamento, h) Tysa, i) Uzh, and j) Var. Modified according to Hu et al. (2019b). .....	105
<b>Figure 6-8:</b> Accuracy assessment of the retrieved Regional Snowline Elevation (RSE) of each catchment, based on the Representativeness Index (RI), Error Index (EI), Precision, Recall, and F-score in each investigated catchment: a) Adda, b) Alpenrhein, c) Ariege, d) Drac, e) Salzach, f) Serge, g) Tagliamento, h) Tysa, i) Uzh, and j) Var.....	106
<b>Figure 6-9:</b> Time series of the modelled Regional Snowline Elevations (RSEs) displayed in solid blue line, and snow coverage derived from the Global Snow Pack (GSP) during the ablation seasons 1984–2018. ....	108
<b>Figure 6-10:</b> Frequency of the Regional Snowline Elevations (RSE) above a certain elevation during the ablation seasons between 1984 and 2018 within the investigated catchments: a) Adda, b) Alpenrhein, c) Ariege, d) Drac, e) Salzach, f) Serge, g) Tagliamento, h) Tysa, i) Uzh, and j) Var. The blue solid line indicates the 35-year median RSE at each day-of-year during an ablation season.....	112
<b>Figure 6-11:</b> Steepness of the Regional Snowline Retreat Curves (RSRCs) of the investigated catchments between 1984 and 2018. Modified according to Hu et al. (2019b). .....	114
<b>Figure 6-12:</b> Box-whisker plots presenting max, min, median as well as 25 <sup>th</sup> and 75 <sup>th</sup> percentiles of the Accumulated Temperatures (ATs) between April and June of the investigated catchments (1984–2018). Modified according to Hu et al. (2019b). .....	115
<b>Figure 6-13:</b> Accumulated Temperature of the Mid-Ablation season (AT <sub>MA</sub> ) of the Regional Snowline Retreat Curves (RSRCs) of the investigated catchments between 1984 and 2018. Modified according to Hu et al. (2019b). .....	116
<b>Figure 6-14:</b> Box-whisker plots presenting max, min, median as well as 25 <sup>th</sup> and 75 <sup>th</sup> percentiles of the Corrected R <sup>2</sup> of the Regional Snowline Retreat Curves (RSRCs). .....	118
<b>Figure 6-15:</b> Box-whisker plots presenting max, min, median as well as 25 <sup>th</sup> and 75 <sup>th</sup> percentiles of the Mean Absolute Error (MAE) of the Regional Snowline Retreat Curves (RSRCs). .....	118
<b>Figure 6-16:</b> Box-whisker plots presenting max, min, median as well as 25 <sup>th</sup> and 75 <sup>th</sup> percentiles of the Root Mean Squared Error (RMSE) of the Regional Snowline Retreat Curves (RSRCs). .....	118
<b>Figure 6-17:</b> Temporal variation of the Regional Snowline Elevations (RSEs) during the ablation seasons 1984–2018 in each investigated catchment. The blue dash lines represent smoothed RSEs using Savitzky–Golay filter with 2 <sup>nd</sup> order polynomial in 3-day window.....	120
<b>Figure 6-18:</b> Landsat-based Regional Snowline Elevations (RSEs), MODIS-based snow coverage, and river discharges measured at ground station during the ablation season 2000–2016 in the Alpine catchment Alpenrhein. ....	121

**Figure 6-19:** Landsat-based Regional Snowline Elevations (RSEs), MODIS-based snow coverage, and river discharges measured at ground station during the ablation season 2000–2016 in the Alpine catchment Salzach. ....122

**Figure 7-1:** The influence of cloud/haze on snow cover classification. (a) Landsat surface reflectance true colour combination; (b) Snow cover classification; (c) CFmask cloud cover classification; (d) Snow beneath haze according to snow and cloud classification. ....126

**Figure 7-2:** Details of the spatial uncertainty assessment of the Median Snowline Elevations (MSEs) during the end of the ablation seasons between 1984 and 2017 for the selected mountain areas: a) the Pyrenees (PN, Path/Row: 198/030) during June, b) the Alps (AP, Path/Row: 195/029) during May and c) the Carpathian Mountains (CP, Path/Row: 183/028) during April. Red colour indicates overestimated areas (snow-free areas above median SLE) and blue colour indicates underestimated areas (snow-covered areas below the median SLE). The base-map is a hill-shade derived from the Digital Elevation Model (DEM). Modified according to Hu et al. (2019a). ....127



## List of Tables

<b>Table 2-1:</b> Empirical equations for Snow Water Equivalent (SWE) and Snow Depth (SD) calculation. Modified according to Hu et al. (2017). .....	28
<b>Table 2-2:</b> References for existing glacier inventories derived from satellite imagery for European glaciers (excluding Greenland). Modified according to Hu et al. (2017).....	38
<b>Table 2-3:</b> Benefits and limitations of optical imagery for cold region monitoring. Modified according to Hu et al. (2017).....	44
<b>Table 2-4:</b> Benefits and limitations of Synthetic Aperture Radar (SAR) imagery for cold region monitoring. Modified according to Hu et al. (2017).....	45
<b>Table 3-1:</b> Overview of the investigated catchments. ....	52
<b>Table 4-1:</b> Bands characteristics of the selected Earth Observation (EO) sensors in this study: Landsat Thematic Mapper (TM), Enhanced Thematic Mapper Plus (ETM+), Operational Land Imager/Thermal Infrared Sensor (OLI/TIRS), Advanced Spaceborne Thermal Emission and Reflection Radiometer (ASTER), and Sentinel-2 (S2). CW stands for central wavelength in $\mu\text{m}$ , and SR stands for spatial resolution in meter. ....	66
<b>Table 4-2:</b> Bands characteristics of Landsat Thematic Mapper (TM), Enhanced Thematic Mapper Plus (ETM+), Operational Land Imager/Thermal Infrared Sensor (OLI/TIRS). CW stands for central wavelength in $\mu\text{m}$ , and SR stands for spatial resolution in meter. ....	69
<b>Table 4-3:</b> Bands characteristics of Sentinel-2. ....	71
<b>Table 4-4:</b> Bands characteristics of ASTER, in which SR stands for spatial resolution. ....	73
<b>Table 4-5:</b> Summary of input variables for Random Forest Regression (RFR) derived from ERA5 dataset. ....	75
<b>Table 5-1:</b> Demonstrative confusion matrix relating satellite-derived snow classifications with ground snow-depth observations. ....	85
<b>Table 5-2:</b> Performance measures for assessing the Regional Snowline Elevation (RSE) outcomes.....	87
<b>Table 6-1:</b> Confusion matrix relating satellite-derived snow classifications and ground snow-depth observations. Modified according to Hu et al. (2019b). ....	104
<b>Table 6-2:</b> Percentage of the variance ( $R^2$ ) explained by the Random Forest Regression (RFR), and root mean squared error (RMSE).....	107
<b>Table 6-3:</b> Permutation importance of each input variable in the investigated catchments. ....	109
<b>Table 6-4:</b> Summary of the Trend analysis with regards to median RSEs and the RSEs at the beginning of the ablation seasons between 1984 and 2018. ....	117
<b>Table 6-5:</b> Summary of the correlation analysis between Regional Snowline Elevations (RSEs) and monthly air temperature anomalies in each month during the ablation seasons 1984–2018.....	119



## Abbreviations and Acronyms

a	Annum
AAR	Accumulation Area Ratio
AATSR	Advanced Along Track Scanning Radiometer
ACCA	Automatic Cloud Cover Assessment
AFWA	Air Force Weather Agency
ALOS	Advanced Land Observing Satellite
ANN	Artificial Neural Network
ANSA	AFWA NASA Snow Algorithm
ASTER	Advanced Spaceborne Thermal Emission and Reflection Radiometer
AT	Accumulated Temperature
AT <sub>0</sub>	Accumulated Temperature from the previous month
ATLAS	Advanced Topographic Laser Altimeter System
AT <sub>MA</sub>	Accumulated Temperature of the Mid-Ablation season
ATSR-2	Along-Track Scanning Radiometer-2
AVHRR	Advanced Very High Resolution Radiometer
AWS	Automatic Weather Station
BRDF	Bidirectional Reflectance Distribution Function
BT	Brightness Temperature
C3S-CDS	Copernicus Climate Change Service-Climate Data Store
CCI	Climate Change Initiative
CDS	Climate Data Store
CLSU	Constrained Least Squares Unmixing
cm	Centimeter

## Abbreviations and Acronyms

---

Corrected R <sup>2</sup>	Corrected Coefficient of Determination
COSMO-SkyMed	COntellation of small Satellites for the Mediterranean basin Observation
CRREL	Cold Regions Research and Engineering Laboratory
DBAR	Digital Belt and Road Initiative
DDV	Dense Dark Vegetation
DEM	Digital Elevation Model
DFD	German Remote Sensing Data Center
DGPS	Differential Global Positioning System
D-InSAR	Differential Interferometric Synthetic Aperture Radar
DLR	German Aerospace Center
DN	Digital Number
EA	Expected Agreement
EC	European Commission
ECA&D	European Climate Assessment & Dataset
ECMWF	European Centre for Medium-Range Weather Forecasts
ECV	Essential Climate Variable
EEA	European Environment Agency
EI	Error Index
EIS	Endmember Induction Algorithm
ELA	Equilibrium Line Altitude
EM	End-Member
EUMETNET	European Meteorological Services Network
Envisat-ASAR	Envisat-Advanced Synthetic Aperture Radar
EO	Earth Observation
EOC	EOS Operations Center
EORC	Earth Observation Research Center

EOS	Earth Observing System
EOSAT	Earth Observation Satellite Company
ERA	ECMWF ReAnalysis
EROS	Earth Resources Observation and Science
ERS	European Remote Sensing
ERTS	Earth Resources Technology Satellite
ESA	European Space Agency
ESA-CCI-LC	European Space Agency-Climate Change Initiative-Land Cover
ETM+	Enhanced Thematic Mapper Plus
EU	European Union
FAO	Food and Agriculture Organization
FMI	Finnish Meteorological Institute
FT-ESDR	Global Record of Daily Landscape Freeze/Thaw Status
GBFM	Global Boreal Forest Mapping
GCOS	Global Climate Observing System
GDEM	Global Digital Elevation Model
GDS	Ground Data System
GEE	Google Earth Engine
GEOCRI	Group on Earth Observations Cold Regions Initiative
GLAS	Geoscience Laser Altimeter System
GLMS	Global Land Ice Measurements from Space
GLS2000 GCP	Global Land Survey 2000 Ground Control Point
GMES	Global Monitoring for Environment and Security
GRDC	Global Runoff Data Centre
GSFC	Goddard Spaceflight Center
GSP	Global Snow Pack
HiMAC	High Mountain and Cold Regions Using big Earth Data

## Abbreviations and Acronyms

---

hm <sup>3</sup>	Cubic Hectometer
HUT	Helsinki University of Technology
IC	International Cooperator
ICESat	Ice, Cloud and Land Elevation Satellite
IMS	Interactive Multisensor Snow and Ice Mapping System
InSAR	Interferometric Synthetic Aperture Radar
IPCC	Intergovernmental Panel on Climate Change
IPCC AR5	Fifth Assessment Report of the Intergovernmental Panel on Climate Change
JAXA	Japan Aerospace Exploration Agency
JERS-1	Japanese Earth Resources Satellite-1
J-space Systems	Japan Space Systems
K	Kelvin
km	Kilometer
km <sup>2</sup>	Square Kilometer
L1GS	Systematic Correction
L1GT	Systematic Terrain Correction
L1TP	Level 1 Precision and Terrain
LaSRC	Landsat 8 Surface Reflectance Code
LEDAPS	Landsat Ecosystem Disturbance Adaptive Processing System
LGAC	Landsat Global Archive Consolidation
LiDAR	Light Detection and Ranging
LSMA	Linear Spectral Mixture Analysis
LUT	Look Up Table
m	Meter
m <sup>3</sup>	Cubic Meter
MAE	Mean Absolute Error

XXX

MEaSURES	Making Earth System Data Records for Use in Research Environments
MEMSCAG	Multiple End Member Snow Covered Area and Grain size
MERIS	Medium Resolution Imaging Spectrometer
MESMA	Multiple Endmember Spectral Mixture Analysis
METI	Ministry of Economy, Trade and Industry
Mfmask	Mountainous Fmask
mio	Million
mm	Millimeter
MODIS	Moderate Resolution Imaging Spectroradiometer
MSI	Multispectral Instrument
MSS	MultiSpectral Scanner
NACE	Statistical Classification of Economic Activities in the European Community
NASA	National Oceanic and Atmospheric Administration
NDSI	Normalized Difference Snow Index
NDSI-FRA	FRAction of snow-covered area algorithm
NDVI	Normalized Difference Vegetation Index
NDWI	Normalized Difference Water Index
NESDIS	National Environmental Satellite, Data, and Information Service
NIR	Near Infra-Red
NLR	Norwegian Linear Reflectance-to-Snow-Cover Algorithm
NOAA-GHCN	National Oceanic and Atmospheric Administration - Global Historical Climatology Network
NRT	Near Real Time
NSIDC	National Snow and Ice Data Center
NSIDC	National Snow & Ice Data Center
NT	Total number of Negative False pixels

## Abbreviations and Acronyms

---

OA	Overall Accuracy
OBIA	Object-Based Image Analysis
OLI	Operational Land Imager
OLS	Ordinary Least Squares
PA	Producer's Accuracy
PALSAR	Phased Array type L-band Synthetic Aperture Radar
PCD	Payload Correction Data
PF	Total number of Positive False pixels
PM	Passive Microwave
QA4EO	Quality Assurance framework for Earth Observation
QuickScat	Quick Scatterometer
$\overline{R}$	Mean Correlation Coefficient
$R^2$	Coefficient of Determination
RFR	Random Forest Regression
RGB	Red Green Blue
RGI	Randolph Glacier Inventory
RI	Representativeness Index
RMSE	Root Mean Square Error
RSE	Regional Snowline Elevation
RSRC	Regional Snowline Retreat Curve
RT	Real-Time
s	Second
SAO	Snow Accumulation Onset
SAR	Synthetic Aperture Radar
SCA	Snow Cover Area
SCD	Snow Cover Duration



SCF	Snow Cover Fraction
SCI	Science Citation Index
SCM	Snow Cover Melt
SCS	Snow Cover Start
SD	Snow Depth
SDC	Snow Depletion Curves
SDI	Snow Darkening Index
SGS	Snow Grain Size
SI	Snow Impurity
SLC	Scan Line Corrector
SMA	Spectral Mixture Analysis
SME	SnowMelt End
SnowPEX	Satellite Snow Product Intercomparison and Evaluation Exercise
SPD	Spectral Polarization Difference
SPIRIT	SPOT 5 stereoscopic survey of Polar Ice: Reference Images and Topographies
SPOT	Satellite Probatoire de l'Observation de la Terre
SR15	Special Report on Global Warming of 1.5 °C
SRM	Snowmelt Runoff Model
SRTM	Shuttle Radar Topography Mission
SSM/I	Special Sensor Microwave/Imager
SWE	Snow Water Equivalent
SWIR	Short Wave Infra-Red
SYKE	Finnish Environment Institute
T <sub>0</sub>	Base Temperature
TDRSS	Tracking and Data Relay Satellite System
TIRS	Thermal Infrared Sensor

## Abbreviations and Acronyms

---

TKK-SCA	Helsinki University of Technology-Snow Cover Area method
TM	Thematic Mapper
Tmask	multiTemporal mask
TP	Total number of Pixels
UA	User's Accuracy
UAV	Unmanned Aerial Vehicle
USGS	United States Geological Survey
UTC	Coordinated Universal Time
VISNIR	VISible-Near-Infra-Red
WRS	Worldwide Reference System
WVM	Water Vapour Map
°C	Celsius
%	Percentage
‰	Permyriad
κ	Kappa Coefficient
ρ	Reflectance
μm	Micrometer

# CHAPTER 1

## 1 Introduction

Worldwide, climate is undergoing significant changes. The recent Intergovernmental Panel on Climate Change (IPCC) Special Report on “global warming of 1.5 °C” (SR15) pointed out that “warming greater than the global average has already been experienced in many regions and seasons, with higher average warming over land than over the ocean (high confidence)” (Allen et al., 2018). Cold regions are sensitive to climate change, especially regions that belong to the cryosphere (i.e. snow, ice, and frozen ground illustrated in Figure 1-1). Observations have suggested various trends in the response of cold regions to the warming climate, including glacier retreat, early snowmelt onset, sea ice shrinking, and permafrost thawing (Kaser et al., 2010; Lemke et al., 2007; Radić et al., 2014; Vaughan et al., 2013). In this context, observing cold region dynamics can elucidate the regional response to ongoing climate change. Ultimately, deriving cold region dynamics in a continuous, timely and reliable manner will facilitate adaptation-strategies for coping with climate change.

IPCC (2014) emphasized the necessity of long-term observations on environmental and social indicators in the European cold regions. Conventional in-situ measurements are not well-suited for such a purpose due to their intensive labour and material requirements, the poor accessibility of cold regions, and, in particular, their spatiotemporally discontinuity (i.e. not a real-time, sparsely distributed, and/or limited observation time span) (Greuell et al., 2007; Rabatel et al., 2005). In these regards, satellite-based Earth Observation (EO) represents a promising alternative to in-situ measurements. So far, EO sensors have acquired a tremendous amount of data at different spatial and temporal resolutions. Thanks to the free and open EO data policies, large volumes of long-term EO data; such as the Landsat program begun in 1972, the Advanced Very High Resolution Radiometer (AVHRR) begun in 1978, the Moderate Resolution Imaging Spectroradiometer (MODIS) and

the Advanced Spaceborne Thermal Emission and Reflection Radiometer (ASTER) begun in 1999, and the novel European Sentinel fleet begun in 2014; are now free-of-charge (Woodcock et al., 2008; Wulder et al., 2012). Thus, EO ensures objective, repeated, synoptic, consistent and large-scale monitoring of land surface dynamics in cold regions. Due to the accessibility of these datasets, many EO research initiatives have been established to better observe and understand cold region dynamics, for example the Group on Earth Observations Cold Regions Initiative (GEOCRI).

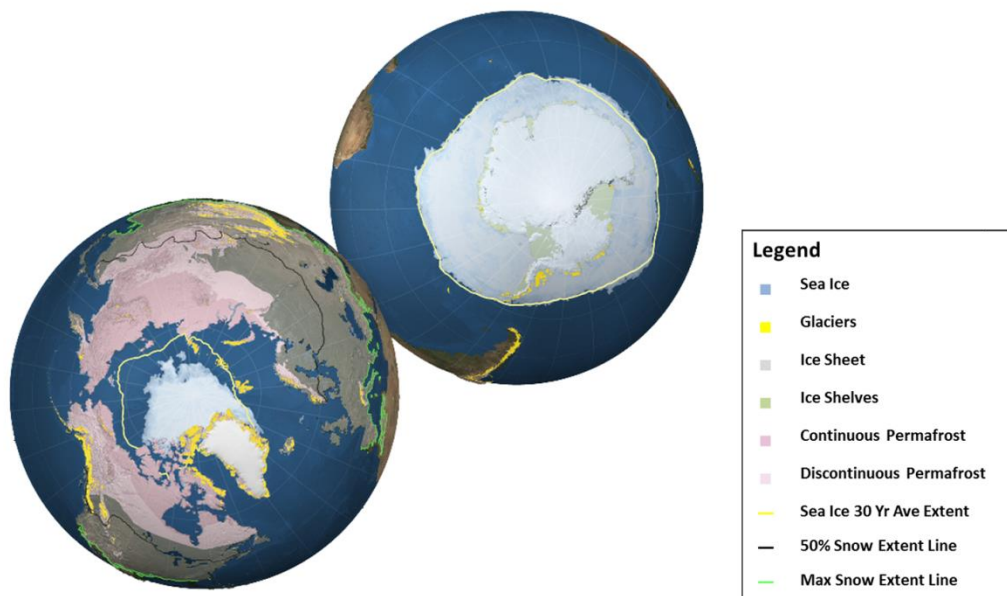


**Figure 1-1:** The cryospheric components in the Northern and Southern Hemispheres in polar projection. Modified according to Vaughan et al. (2013).

To date, numerous EO-based projects/initiatives have produced geospatial information relevant to cold regions worldwide. These projects/initiatives include the Interactive Multisensor Snow and Ice Mapping System (IMS) provided by the National Oceanic and Atmospheric Administration/National Environmental Satellite, Data, and Information Service (NOAA/NESDIS) (Helfrich et al., 2007; Ramsay, 1998), the MODIS snow cover products (Hall et al., 2002), the Global Land Ice Measurements from Space (GLIMS) project (Raup et al., 2007b, 2007a), the global inventory of glacier outlines from the Randolph Glacier Inventory (RGI) (Pfeffer et al., 2014a), the European Space Agency’s (ESA) GlobSnow product coordinated by the Finnish Meteorological Institute (FMI) (Metsämäki et al., 2015; Solberg et al., 2010), the GlobPermafrost initiative (2016–2019) launched by ESA (Bartsch et al., 2016), the Global Record of Daily Landscape Freeze/Thaw

Status (FT-ESDR) from the NASA's Making Earth System Data Records for Use in Research Environments (MEaSUREs) program (Kim et al., 2012), the German Aerospace Center-German Remote Sensing Data Center's (DLR-DFD) Global Snow Pack (GSP) dataset (Dietz et al., 2015), the Global Boreal Forest Mapping (GBFM) project led by the Earth Observation Research Center (EORC) of the Japan Aerospace Exploration Agency (JAXA) (Rosenqvist et al., 2004), the High Mountain and Cold Regions Using big Earth Data (HiMAC) service of the Digital Belt and Road Initiative (DBAR) (Qiu et al., 2017), and the IPCC "Special Report on Climate Change and Oceans and the Cryosphere", planned to be finalized in September 2019. To date, given the continuously improving computational capacity and exponentially increasing EO data volume, there is an urgent need to develop a framework to assess cold region dynamics with the EO data legacy as well as the new EO data using improved features, such as the enhanced radiometric and spatiotemporal resolution in ESA's Sentinel-2 constellation.

## **1.1 Introduction to Cold Regions**

In 1884, the term "cold region" was first used by the German scientist Wladimir Köppen (1846–1940), who spoke of a "Kalter Gürtel" (a German word which means "cold belt") to characterize global climate zones (Köppen, 1884). Presently, the term "cold region" is still frequently used by engineers, environmental scientists, physicists, and other scientists.

### **1.1.1 Geographical Extent of Cold Regions**

The term "cold region" can be defined by either geographical extent or geographical characteristics (e.g., climate). To date, the most accepted geographical-extent-based definition of "cold region" is given by the GEOCRI. Its definition (Qiu et al., 2016) identifies the cold regions as polar region and high-mountain areas, whose geographical extent includes the Arctic, the Antarctic, high-latitude oceans, the Himalaya Third Pole, and mountainous cold areas. At a regional scale, there are also many descriptive definitions of cold regions. In Europe, Heal (1998) defined the Arctic and the Alpine areas as the European cold regions. In China, the cold regions were defined by Li and Liu (2011) as the

northern area of the Qinling Mountains and the Huaihe River. Air temperature is the most commonly used parameter to delineate cold regions quantitatively. Its use dates back to the 19th century, when Köppen (1884) identified the cold region as the region with 1–4 moderate months (i.e. mean temperature of 10–20 °C) and 8–11 cold months (i.e., mean temperature <10 °C). Similarly, Chen et al. (2006) located the cold regions in China according to: (1) mean temperature of the coldest month <3 °C, (2) less than 5 months with mean temperature >10 °C, and (3) mean annual temperature <5 °C. Apart from air temperature, a 30 cm frost penetration depth once in 10 years (Andersland and Ladanyi, 2013) is also a frequently applied criterion used by engineers. Yang et al. (2000) mapped the cold regions in China in a more comprehensive manner via the thresholding of 10 different climate factors. Apart from the aforementioned definitions, the most acknowledged definition of “cold region” is proposed by the Cold Regions Research and Engineering Laboratory (CRREL) (Bates and Bilello, 1966). CRREL takes four parameters into consideration when determining the cold region extent, including: (1) air temperature (0 °C and –18 °C isotherms), (2) snow depth (30 and 61 cm isolines), (3) ice cover (100 and 180 annual mean unnavigable days), and (4) frozen ground extent (permafrost and 30 cm frost penetration).

Based on the CRREL’s definition and the ECMWF ReAnalysis (ERA)-Interim reanalysis data from the European Centre for Medium-Range Weather Forecasts (ECMWF), Hu et al. (2017) calculated the cold region stability map according to the following criteria: (1) the frequency of negative air temperature occurrence is no less than 50% of time in the coldest month of the year; (2) the maximum snow depth on the ground is more than 30 cm; and (3) temperatures < 0 °C occurs on at least 100 days. Subsequently, a stability index is calculated indicating the frequency of the areas identified as cold regions. The method has been further applied globally in this thesis (Figure 1-2). The result shows the cold regions are mostly distributed in the Northern Hemisphere and Antarctica. In the Northern Hemisphere, the geographical extent of cold regions includes the northern parts of North America, Greenland, Scandinavia, Russia, the Hindu-Kush Himalaya Third Pole, and the European high mountains (e.g., the Alps and the Carpathian Mountains).

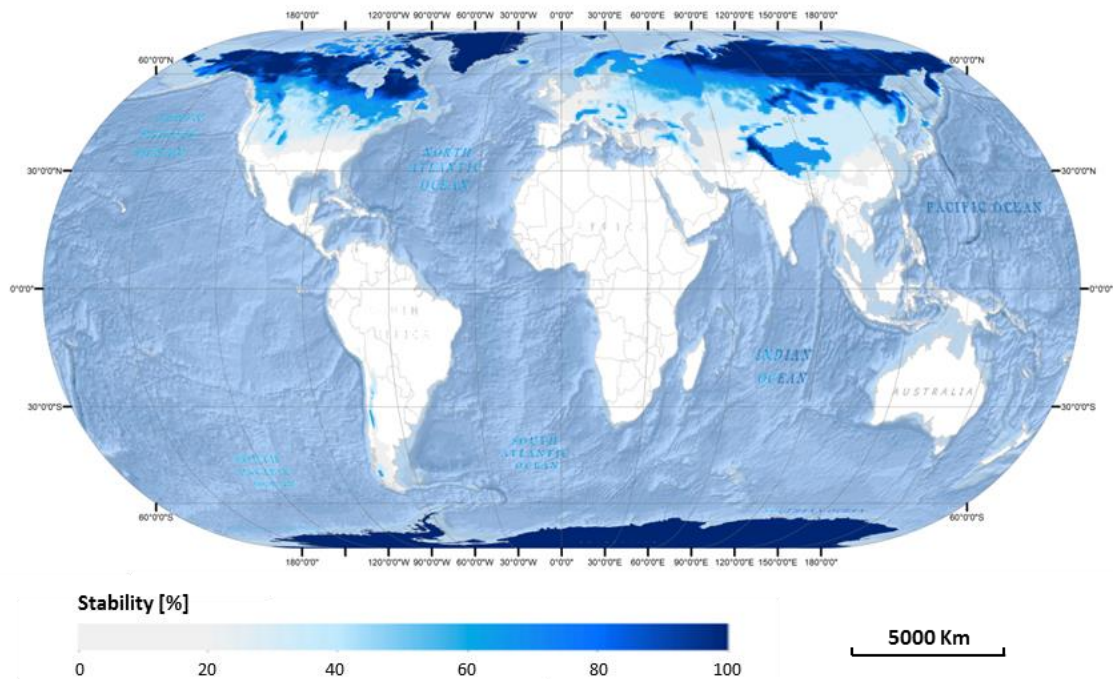


**Figure 1-2:** Stability of the global cold regions. The darker the blue colour is the more frequent the areas are mapped as cold regions.

### 1.1.2 Cold Regions in the Context of Climate Change

Cold regions consist of a variety of land covers, including cryospheric components (i.e. snow, glacier, and frozen ground), boreal forest, tundra, and the living organisms therein. The key characteristic of a cold region is the existence of frozen water in its various forms, e.g., snow, glaciers and ice caps, ice shelves and ice sheets, sea ice, lake and river ice, frozen ground and permafrost (Figure 1-3). These components play an important role in regards to the global surface energy budget, the hydrological cycle, primary productivity, surface gas exchange and sea level (Vaughan et al., 2013). These components not only passively reflect climate change, but also actively and enduringly impact the physical, biological and social systems of Earth's surface (Vaughan et al., 2013).

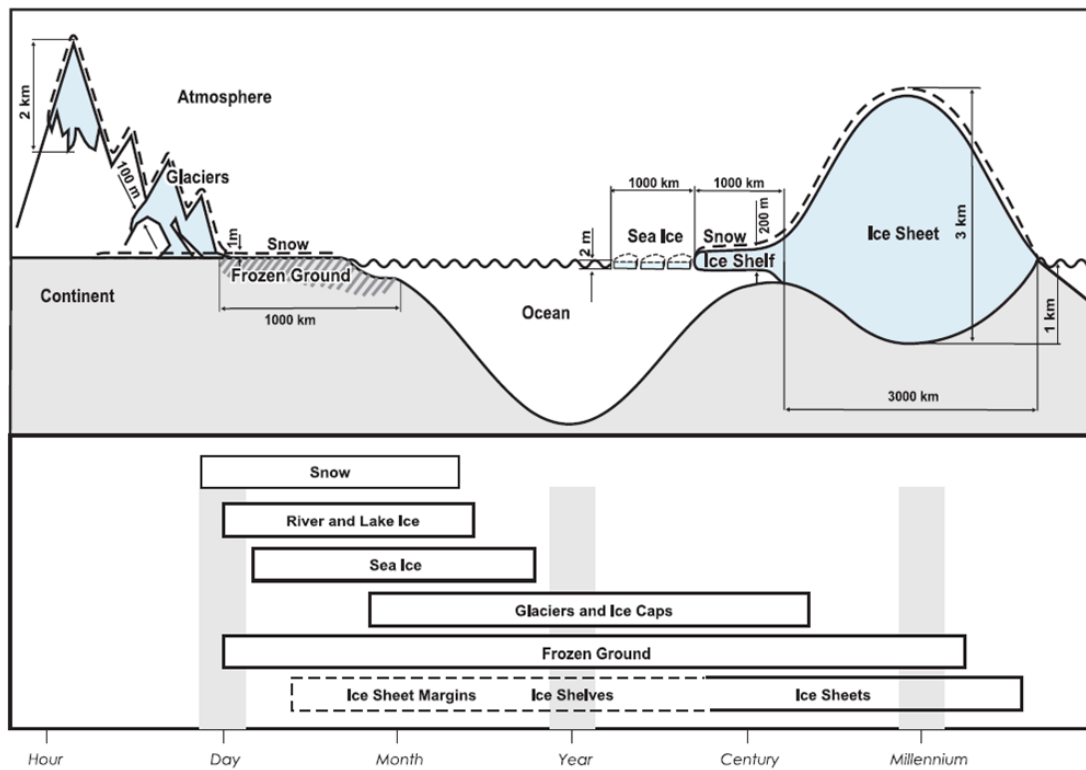


**Figure 1-3:** The thematic sketch of the cryospheric components and their time scales. Source: Lemke et al. (2007).

Covering up to 45.2 million km<sup>2</sup> of the land surface during the winter (Lemke et al., 2007), snow is the most widely distributed cold region component in the Northern Hemisphere. Snow cover influences the Earth’s energy budget, biodiversity, and hydropower potential, as well as possible natural hazards and winter tourism (Barnett et al., 2005; Chen et al., 2015; Ciscar et al., 2011). The second most widespread cryospheric component in cold regions is frozen ground. Permafrost thaw has resulted in significant carbon/methane emission (Anisimov, 2007; Schuur et al., 2009), which accelerates the warming of the climate. Also, the periodic melting of its active layer has a great impact on civil infrastructure (Andersland and Ladanyi, 2013), due to the consequential alteration in hydrological and geomorphological regimes. Ice sheets, ice caps and glaciers are the primary contributors to sea level rising, and are critical freshwater reservoirs (Kaser et al., 2010; Lemke et al., 2007; Radić et al., 2014). Apart from the cryospheric components, biospheric components are also essential in cold regions, among which the boreal forest is the most widespread terrestrial biome (Nasholm et al., 1998). Boreal forests, as well as tundra, play an important role in atmospheric pollution uptake (Obrist et al., 2017; Shotyk, 2017), biodiversity (Sala et al., 2000), organic nitrogen mineralization (Nasholm et al.,



1998), as well as the stability of regional and global climate patterns (Bonan et al., 1992). Furthermore, boreal forests and tundra are important habitats for diverse flora and fauna, and their economic value (Bogdanski and others, 2008; Östlund et al., 1997; Pisarenko and Strakhov, 1996) is significantly pronounced in Northern countries such as Russia, Canada, and Sweden.

### **1.1.3 Snow as a Crucial Cold Region Component in the European Mountains**

Snow covers up to 8.5 million km<sup>2</sup> of the land surface in Europe during the winter (Henderson and Leathers, 2010), and persists in the high latitude and high altitude areas. The Global Climate Observing System (GCOS) identified snow as an Essential Climate Variable (ECV) (Mason et al., 2003), which is a suitable measure of climate change. In response, observing snow dynamics has been included in the ESA's Climate Change Initiative (CCI) program to better support the comprehension of long-term snow dynamics. To date, observations reported a continuously decreasing trend of snow coverage over the past 90 years, in particular during the ablation seasons (EEA, 2009; Stocker et al., 2013). In Europe, mountains cover around 2 million km<sup>2</sup> with a population of more than 94 million (Schuler et al., 2004). These European mountains are one of the most climate sensitive regions (EC, 2009), due to fragile ecosystems providing various ecosystem services and socioeconomic wellbeing (Beniston et al., 1997; Diaz et al., 2003). Studies show that climate change has profoundly altered the Alpine hydrological system during the 20<sup>th</sup> century, with an observed speed of change more rapid than the global average (EC, 2009). Given that the majority of the annual runoff in European mountain areas is snowmelt-dominated (Barnett et al., 2005), it is important to investigate the long-term snow dynamics in European mountains. However, there are large gaps in our knowledge regarding local responses of snow cover to climate change in snow-fed basins (EEA, 2017a; IPCC, 2014), and limited scientific knowledge and high uncertainty set the barriers for developing effective climate strategies. In this context, retrieving and analysing long-term snowline elevation dynamics can provide valuable information to better understand the local impacts of climate change. It can therefore contribute to regional and local adaptation-strategies.

### **1.1.4 The Need for Earth Observation (EO)-based Snow Dynamic Monitoring in Europe**

It has been recognized by studies that the impacts of climate change differ significantly among regions (IPCC, 2014). Over the past decades, "Europe as a whole has experienced great climate variability and extremes (Christensen et al., 2007; Christensen and Christensen, 2003; Luterbacher et al., 2004), such as continuously increasing average temperatures particularly in northern Europe (IPCC, 2014, 2013), more frequent high-temperature extremes and less frequent low-temperature extremes (Füssel et al., 2012; Seneviratne et al., 2012; Stocker et al., 2013), increasing annual precipitation in northern Europe and decreasing precipitation in some areas of southern Europe (Füssel et al., 2012), and increasing mean sea level, excluding the northern Baltic Sea (Albrecht et al., 2011; Füssel et al., 2012; Haigh et al., 2010; Menéndez and Woodworth, 2010). As a result, significant changes in land, freshwater, and marine ecosystems have occurred in Europe (Parry et al., 2007). For example, advancement in the mean onset dates of spring events (e.g., bud burst, breaking hibernation, flowering, migration, snowmelt) has affected much of Europe's flora and fauna (Cleland et al., 2007; Dietz et al., 2012; Menzel et al., 2006; Penuelas et al., 2013). Annual maximum water discharge from melting has increased in parts of northwestern Europe (Giuntoli et al., 2012; Petrow and Merz, 2009), and the water quality of the River Meuse (western Europe) has increasingly deteriorated due to more frequent and intense droughts induced by climate change (Van Vliet and Zwolsman, 2008)." (Hu et al., 2017) These factors urge the development of regional and evidence-based adaptation strategies for mitigating ongoing climate change. For this purpose, observations should not only focus on a mesoscale assessment, but also the identification of local vulnerability.

Snow and glaciers are the most frequently monitored cold region components in Europe because of their high sensitivity to climate change. To further carry out long-term and sustainable cold region monitoring, data accessibility, compatibility, and consistency are desired (IPCC, 2014). In these regards, satellite-based EO data is preferred to conventional in-situ measurements. With satellite remote sensing we can continuously observe and monitor the Earth's surface and ensure objective, repeated, synoptic and

consistent information in cold region land surface dynamics. EO has long been employed for environmental assessment by means of time-series analyses (Hostert et al., 2015; Lambin and Strahlers, 1994). Time series analysis has increased in importance because of its use in addressing questions across different research domains that examine detailed local information over a large spatial scale (Hostert et al., 2015).

Hu et al. (2017) found that studies focusing on local responses to climate change are mainly glacier-related studies using high resolution EO data, while mesoscale assessment of glaciers is scarce. In Europe, an overall retreat of glaciers has been reported. Conversely, in snow-related studies, the snow dynamics vary region by region, and less is known about the local dynamics. Currently, there are mutual and large-scale snow studies based primarily on MODIS data. While these studies provide timely and large scale information on snow dynamics, there are two obvious limitations, i.e. relatively short time span and coarse spatial resolution. Such problems are particularly pronounced when investigating local snow dynamics, consequently there are few long-term (> 30 years) and quantitative studies on local snow dynamics. As a result, there are large gaps in our knowledge regarding local responses of snow cover to climate change, especially in the European mountains.

## **1.2 Research Foci and Objectives of the Thesis**

As explained in the previous sections, observing snow dynamics is essential for understanding and coping with climate change. IPCC (2013) projected with a high confidence that snow coverage in the Northern Hemisphere is continuously shrinking during the ablation seasons, particularly in mid-latitude mountains (IPCC, 2014, 2013). In this context, the observation of long-term snow dynamics in mid-latitude European mountain areas is particularly important. Studies also show that responses to the warming climate are highly significant, and these mountains are climate-sensitive and vulnerable. To date, snow as an ECV has been intensively studied. On the other hand, the currently available observations mostly focus on deriving 2D-snow-cover information at a continental/hemispherical scale with a limited time-span (i.e. mostly during the period 2000–2018). Large knowledge gaps regarding local responses to climate change,

especially in the elevational direction, hinder adaptation-strategy making. Hence, evidence-based adaptation strategies for coping with climate change lends itself to using the quantitative assessment of long-term snow dynamics in mountainous areas, and employing snowline elevation as a proxy. Doing so can better provide pertinent information regarding freshwater management, snow-related hazard forecasts, and winter sport/tourism management.

*The primary objective of this dissertation is to develop a framework to retrieve and characterize snowline dynamics in Europe, based on optical satellite imagery.*

Spaceborne EO imagery is the main data source for snow monitoring in large areas, since it can provide long-term consistent records of the Earth's surface. There are heretofore hundreds of EO satellites in orbit, which have collected several Petabytes of data (Kuenzer et al., 2015). Initiated in 1972, the Landsat program; which uses a sensors MultiSpectral Scanner (MSS), Thematic Mapper (TM), Enhanced Thematic Mapper Plus (ETM+), Operational Land Imager/Thermal Infrared Sensor (OLI/TIRS); provides the longest continuous record of satellite remote sensing data (Chander et al., 2009; Kuenzer et al., 2015). Another long-term archive is the AVHRR series, which launched its first sensor in 1978. In addition, readily accessible global time series data such as AATSR (Advanced Along Track Scanning Radiometer), MODIS, and MERIS (Medium Resolution Imaging Spectrometer) have been available since 1991, 1999, and 2002, respectively (Bachmann et al., 2015; Kuenzer et al., 2015). More recently, the European Union (EU) has initiated the Copernicus program, previously known as Global Monitoring for Environment and Security (GMES) (Donlon et al., 2012; Drusch et al., 2012). The various Sentinel missions (Donlon et al., 2012; Drusch et al., 2012; Ingmann et al., 2012; Torres et al., 2012) also represent essential components of EO imagery collection efforts.

These open data policies promote the utility of the large volume of EO data. Therefore, EO archives hold a great potential to discover long-term snowline elevation dynamics in Europe. Among these EO archives, the recent reorganized United States Geological Survey's (USGS) Landsat Collection 1 archive is the world's longest uninterrupted EO dataset. The more than three-decade records of Earth surface at 30 m resolution recorded by its TM, ETM+, and OLI/TIRS sensors between 1984 and 2018, make

the Landsat Collection 1 archive a unique data source for long-term snow dynamic studies. The European Copernicus program conducted by the ESA also is providing the EO images acquired by its Sentinel satellites with no charge to users. Thanks to these large-volume and freely accessible satellite imagery, as well as with increasingly newly acquired EO data from the satellite constellations in orbit, EO has entered a new era (Chi et al., 2016; Gorelick et al., 2016). Meanwhile, the great advancement in computational power further improves the capacity of handling a large volume of data. Developments in both EO data acquisition and in processing enable the retrieval and analysis of long-term snowline dynamics.

*In this dissertation, the intention is to exploit the potential of the large-volume and freely accessible high-resolution Landsat, ASTER, and Sentinel-2 data, and to develop a spatiotemporally transferable framework for data processing to retrieve and analyse long-term snowline dynamic.*

To achieve these objectives, the first task of this dissertation is to carry out a comprehensive literature review regarding the cold region land surface dynamics in Europe. The objective of the review is to clarify the state-of-the-art approaches to analysing cold region dynamics with regards to snow and glaciers in Europe, as they are strongly associated in the European mountains. Subsequently, leading methods in deriving different perspectives of the snow and glacier dynamics are highlighted and compared. Most importantly, the current research gaps within the field are identified.

#### **Research Questions: Group 1**

1. How can Earth Observation support the delineation of a cold region boundary in Europe?
2. What are the most frequently applied EO satellites/sensors for the analysis of cold region dynamics in Europe?
3. What are the advantages and disadvantages of the existing different sensor types and methods?
4. What studies dealing with cold region dynamics in Europe have been undertaken so far?
5. What are the research and knowledge gaps with respect to cold region dynamics?

The second objective is to provide a comprehensive overview of data availability and its suitability for remote-sensing-based assessment of snow dynamics in the European mountains. The aim is to elucidate the potentials and opportunities of the long-term Landsat Archive for applications in snowline dynamic retrieval.

**Research Questions: Group 2**

1. What is the spatiotemporal availability of the Landsat Collection 1 archive during the period of 1984-2018?
2. What are the most suitable processing levels and tiers of Landsat Collection 1 data for snowline dynamics retrieval?
3. What are the advantages and disadvantages influencing the retrieval of snowline dynamics using Landsat imagery?

The third objective of this thesis is to develop a spatiotemporally transferable framework for snowline derivation in mountainous areas based on long-term, free-of-charge optical datasets. Additionally, based on the resulting long-term snowline time-series, metrics characterizing the snowline retreat during the ablation seasons require development.

**Research Questions: Group 3**

1. How can snowlines in mountainous areas be retrieved using the long-term Landsat Archive and Sentinel-2 dataset?
2. How can the gaps in snowline time series be filled when there are no satellite observations available?
3. How can snow cover dynamics during ablation seasons in mountainous areas be characterized?

The final objective of this dissertation is to investigate three geographical questions: the long-term snowline dynamics in mid-latitude European mountains, their potential climate drivers and their consequences. The answers to these three geographical questions have the potential to contribute to strategizing responses to ongoing climate change.

**Research Questions: Group 4**

1. What are the patterns of intra- and inter-annual snowline variations in mid-latitude European mountains?
2. What are the potential climate drivers of the detected long-term snowline dynamics in European mountains?
3. What are the potential consequences of the detected long-term snowline dynamics in European mountains?

In brief, specific objectives addressed in this dissertation are as follows:

- 1) Provide a comprehensive literature review of EO-based methods and observations of cold region dynamics in Europe.
- 2) Investigate the spatiotemporal availability and suitability of the Landsat Collection 1 archive for snow monitoring in European mountains.
- 3) Develop a spatiotemporally transferable framework for deriving and characterizing long-term snowline dynamics during the ablation seasons in Europe.
- 4) Explore the potential climate drivers and consequences of the derived long-term snowline dynamics during the ablation seasons in Europe.

### 1.3 Structure and Context of the Thesis

The dissertation consists of eight chapters that are outlined as follows:

**Chapter 1 (Introduction)** starts with a brief introduction to the significance of cold regions, particularly with respect to climate change. Subsequently, the chapter emphasizes the need for spatial information on cold region dynamics for decision-makers. The chapter also highlights the need for EO-based local snow dynamic monitoring in Europe. The motivation, research objectives and research questions, as well as the overall structure of this dissertation are provided at the end of this chapter.

**Chapter 2 (State-of-the-Art: Results of the Literature Review of Remote Sensing on Cold Regions)** presents a comprehensive literature review summarizing the status and spatial distribution of EO-based studies regarding cold region monitoring in Europe. An overview of EO-based observations of snow and glaciers is also provided. Subsequently, challenges of EO for cold region observation is discussed with regards to (1) spatiotemporal scale and study area settings, (2) data availability, costs and suitability of different EO sensor types, and (3) method applicability. Lastly, based on the literature review, this chapter explores the potential of Landsat derived time-series in assessing snow cover dynamics in mountainous areas within Europe – the prime objective of this thesis.

**Chapter 3 (Study Areas)** focuses on the geographical settings of the selected study areas, outlining physical, geographical and socioeconomic characteristics.

**Chapter 4 (Data)** presents the multiple data sources employed for the assessment of snow dynamics in European mountains. The major data sources are satellite imagery, Digital Elevation Model (DEM), climate reanalyses data, and in-situ measurements. The details are provided in the following sections, together with the description of the employed auxiliary datasets.

**Chapter 5 (Developed Framework of Snowline Retrieval and Assessment)** introduces the novel methodological framework for the assessment of long-term snowline dynamics in European mountains. The developed framework includes (1) pre-processing, (2) snow detection, (3) regional snowline elevation retrieval, (4) time-series densification, and (5) regional snowline retreat curve production. The details of each step are described in the following subsections.

**Chapter 6 (Results of Snowline Dynamics in Europe)** presents the results of snowline dynamics in Europe in five sections: (1) data availability, (2) snow classifications, RSEs, and validation, (3) 35-year intra-annual and inter-annual snowline variability in European mountains, (4) the analysis between snowline dynamics and the potential climate driver(s), and (5) the possible consequence of the observed snowline dynamics. The first part answers the research question regarding the long-term Landsat availability, including quality control of data selection (e.g. ascending/descending scenes, tiers, and processing levels). Afterwards, the snow classifications, RSEs, and modelled RSE time-series are



provided, together with accuracy assessments. Based on the retrieved 35-year RSE time-series, the intra-annual and inter-annual snowline variability during the ablation seasons are analysed for each study area. Ultimately, two case studies are presented. The first case study links a climate driver (temperature anomalies and extremes) to the obtained snowline dynamics, aiming to investigate the possible triggers causing the observed snowline dynamics. The other study links the snowline dynamics to run-off observations, attempting to analyse the potential consequences (e.g. flood risk increase) of the observed snowline dynamics

**Chapter 7 (Discussion)** discusses the obtained results from the previous section. It includes the four sections: (1) gaps in Long-term Landsat Collection 1 archive, (2) challenges regarding snowline elevation derivation and validation, (3) different aspects of the observed snowline elevation dynamics, and (4) the potential triggers and consequences in relation to the detected snowline dynamics. The first part investigated Landsat data gaps specifically regarding missing observations and cloud observation, in the context of snowline dynamics retrieval. Afterwards, the challenges within snowline dynamics derivation and validation are discussed. Then the observed snowline dynamics are discussed in relation to their peripheral geographical settings and to results in pre-existing studies. In the last part, potential applications of the derived RSE dynamics are discussed. Also, results from the two case studies, both of which investigate associations between the potential climate drivers and consequences of the detected snowline elevation dynamics, are discussed.

**Chapter 8 (Conclusion and Outlook)** summarizes conclusive findings in relation to the objectives and research questions described in the introduction (section 1.2) of this thesis. Additionally, outlook and future opportunities of EO for long-term and large-scale snow dynamics observations are discussed, as well as the potential statistical techniques for further geoscientific analysis. Ultimately, several messages regarding the observed snow dynamics in mid-latitude European mountains are provided for decision-makers, stakeholders, and snow/hydrological/winter tourism managers.



## CHAPTER 2

## 2 State-of-the-Art: Results of the Literature Review of Remote Sensing on Cold Regions

This chapter summarizes the up-to-date current status and spatial distribution of EO-based studies with regard to cold region monitoring in Europe. Also, an overview of EO-based cold region dynamics observation is provided with regards to snow and glaciers. Subsequently, challenges of EO on cold region observation is discussed with regards to (1) spatiotemporal scale and study area settings, (2) data availability, costs and suitability of different EO sensor types, and (3) method applicability. Lastly, bases on the literal review, the prime objective of this thesis has come into being, which is to explore the potential of Landsat derived time series in assessing snow cover dynamics in mountain areas within Europe.

### 2.1 Earth Observation Studies Contributing to Cold Region Monitoring in Europe

The observation of the cold regions in Europe has a long history. It can trace back to 1894 at the 6<sup>th</sup> International Geological Congress, when the International Glacier Commission was established in Zurich (Switzerland) to systematically monitor large-scale glaciers. To date, plentiful resources of cold regions observation exist for Europe, including satellite imagery, photography, paintings and other graphics. Among these methods, conventional field measurements are often time-consuming, cost intensive, logistically demanding, and challenging, particularly in cold regions with low accessibility (Berthier et al., 2004). Hence, such data are usually spatiotemporally discontinuous, i.e., not up-to-date, sparsely distributed, and only cover a limited time span (Greuell et al., 2007; Rabatel

et al., 2005). A promising alternative to field measurements is EO. For more than four-decade, EO has acquired an enormous amount of images at different spatiotemporal resolutions. Because of the free and open data policies of some EO archives (Woodcock et al., 2008; Wulder et al., 2012), a tremendous amount of EO data are now free-accessible, for instance, AVHRR, MODIS, Landsat, ASTER, and ESA’s Copernicus data. Thanks to these EO satellite constellations, the cold regions can be monitored continuously. Meanwhile EO also ensures the collection of objective, repeated, synoptic, consistent and large-scale information for land surface dynamics in cold regions (Figure 2-1).

Prior to the formulation of the specific research topic of this thesis, a comprehensive literature research was performed, which aims to summarize the state-of-the-art with regards EO-based cold region monitoring, and thereafter identify the existing research gaps. Such literature review along with its results is summarized in this section, and the complete study has been published in detail by Hu et al. (2017).

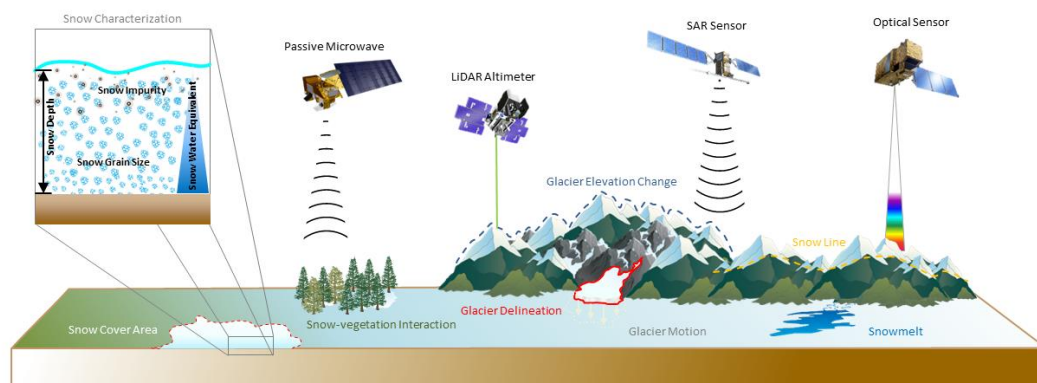


**Figure 2-1:** Thematic diagram of cold region monitoring by space-borne Earth Observation (EO). Modified according to Hu et al. (2017).

### 2.1.1 Overview of the Reviewed Studies

Given the challenge summarizing all the cold-region-related studies within a thesis, only the SCI (Science Citation Index) articles focusing on snow and glacier dynamics in Europe are investigated. The following section presents an overview of the reviewed EO-based snow and glacier studies, categorized by (a) study objectives, (b) applied sensors, and (c) study areas (i.e. geographical distribution). It should be noted that one study may have multiple objectives, study areas and/or EO data. Thus, inherently “multi-counted” is not avoidable in the presented statistics.

In total, 211 EO-based snow/glacier publications were reviewed. These reviewed articles were published in the time frame from 1980 to 2018. Therein, a total of 21 publications were found that used EO data to observe snow and glacier in Europe. Information on study objectives regarding EO-based glacier and snow studies are summarized in Figure 2-2. The most investigated topic is snow cover area mapping, which takes up 21% of the investigated publications. Among glaciologists and geoscientists, glacier motion has aroused the greatest interest, being covered in approximately 17% of the reviewed publications. Only few (12) publications concerning glacier elevation/volumetric change researches were found. Glacier inventories have the smallest number of related publications, since the glacier inventories are usually updated at a 5–10-year interval.

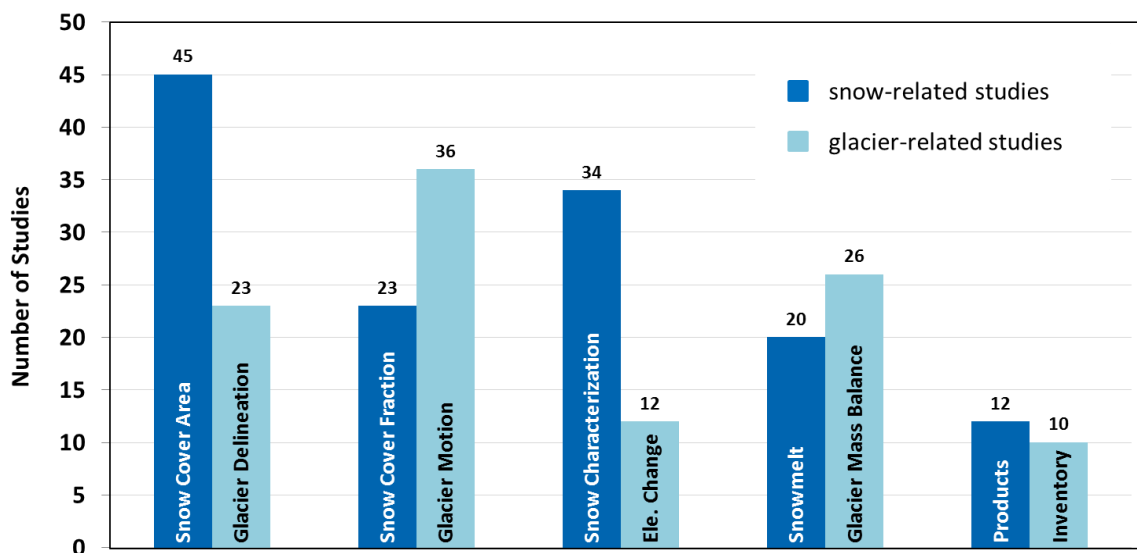


**Figure 2-2:** Study Objectives of the reviewed EO (Earth Observation)-based cold region studies in Europe.

The most prevalently employed satellite data is Landsat imagery (Figure 2-3) in both snow (68) and glacier (42) studies. In terms of the snow-related researches MODIS are also commonly (29) applied. Only a quarter of the snow studies used Synthetic Aperture Radar (SAR) and Passive Microwave (PM) data. Yet for glacier-related studies, SAR imagery are frequently utilized, particularly the European Remote Sensing-1/2 (ERS) data during the “Ice Phase”. Moreover, the value of the Light Detection and Ranging (LiDAR) should not be neglected with regards to glacier Digital Elevation Model (DEM) calibration and verification.

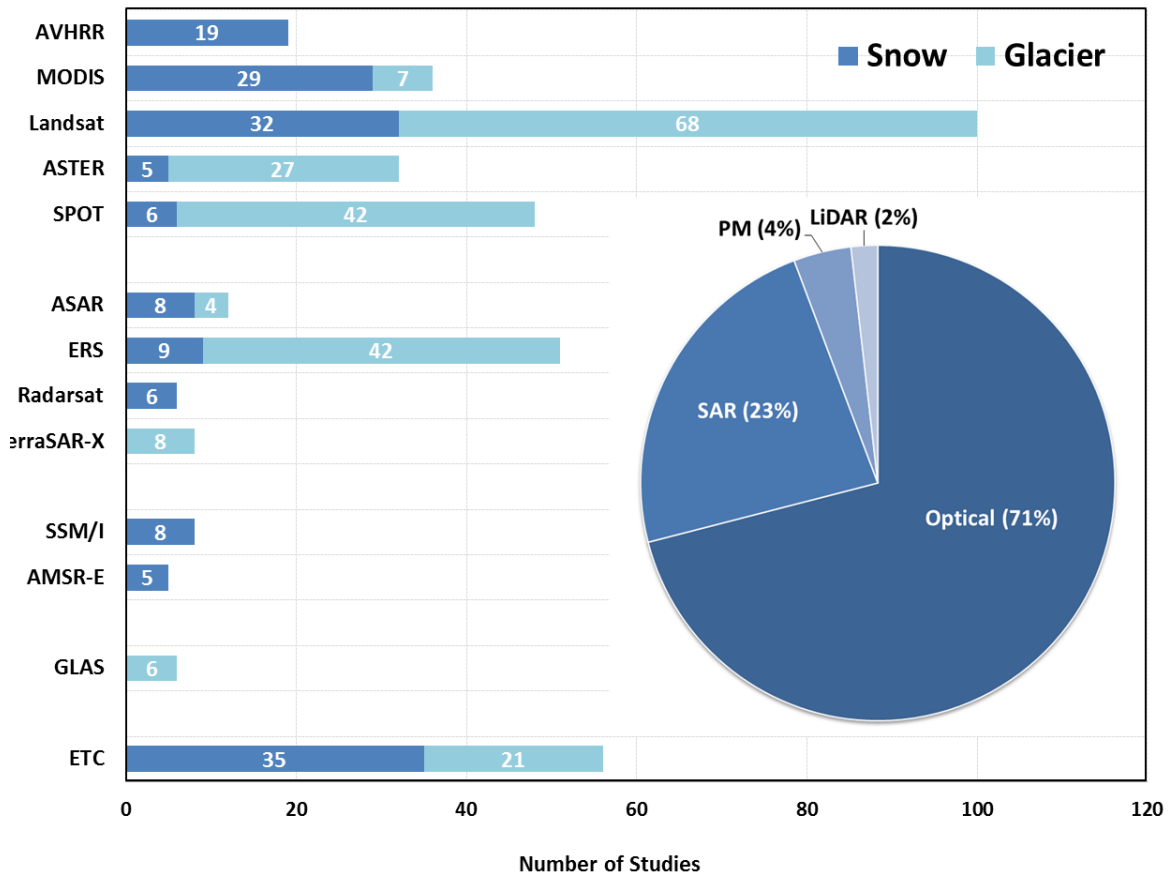


**Figure 2-3:** Overview of the applied EO (Earth Observation) sensors employed in the reviewed cold region studies in Europe. Sensors used fewer than four times are shown in the class “others”, which includes Advanced Land Observing Satellite (ALOS)-Phased Array type L-band Synthetic Aperture Radar (PALSAR), IKONOS, Japanese Earth Resources Satellite-1 Synthetic Aperture Radar (JERS-1 SAR), Pleiades, Sentinel-1, Sentinel-2, WorldView-1/2, TerraSAR-X, Constellation of small Satellites for the Mediterranean basin Observation (COSMO-SkyMed), Sentinel-1, MEdium Resolution Imaging Spectrometer (MERIS), etc.

In terms of the geographical distribution of the study areas, Figure 2-4 illustrates that Norway (including Svalbard) and the European Alps are the hotspots. Almost half of the reviewed snow-related publications focused on the European Alps. In the different parts of the Alps, the Italian Alps received the most attention, which is almost twice as much as the second most investigated Alpine area (i.e. the Swiss Alps). Regarding the reviewed glacier-related articles, more than 50% of these publications focus on Norwegian areas (including Svalbard). It follows by the European Alps (30%), and therein the French Alps and the Swiss Alps are the most frequently studied regions.

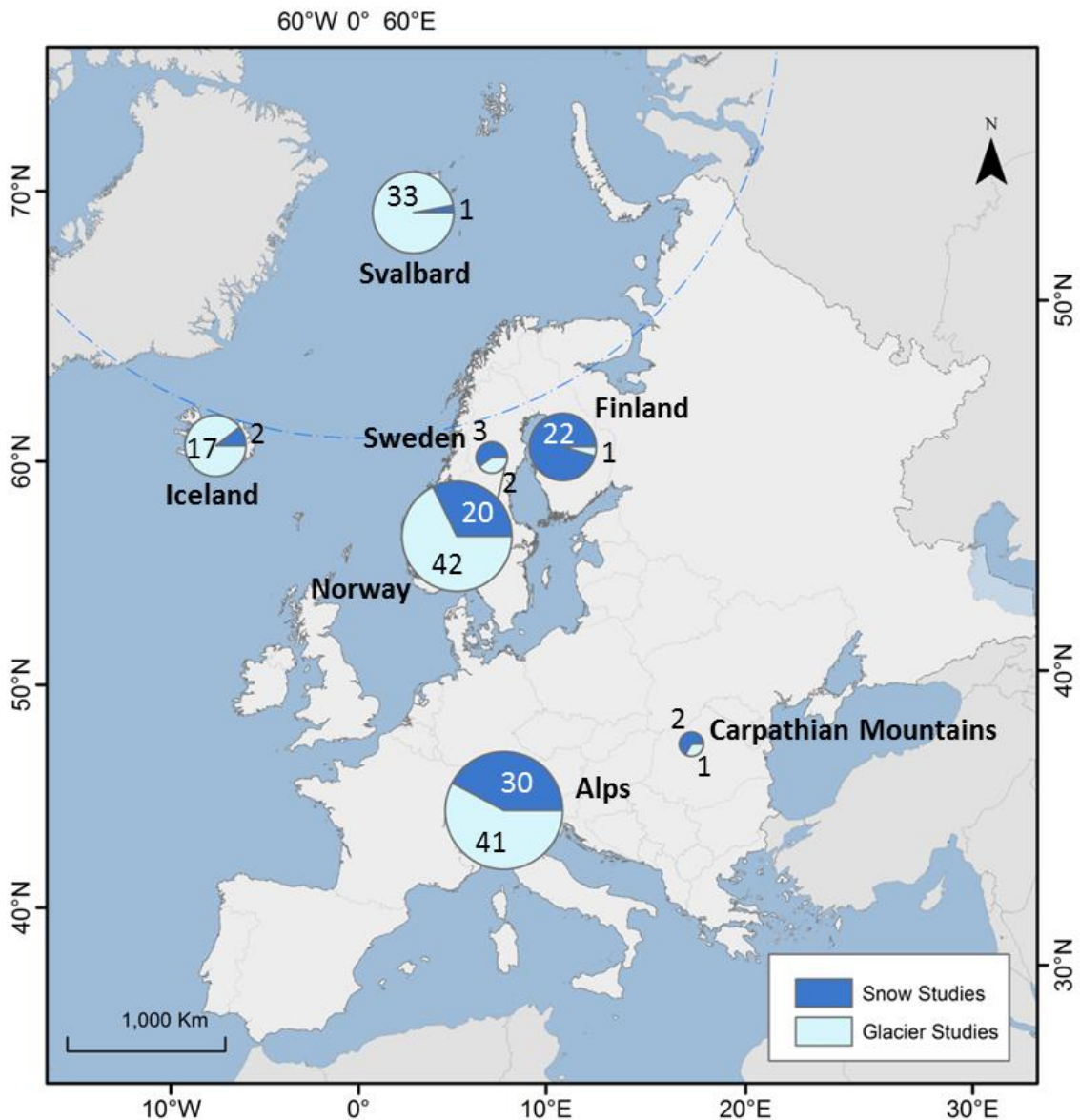


**Figure 2-4:** Geographical distribution of the reviewed EO (Earth Observation) based cold region studies in Europe.

### 2.1.2 Cold Region Extent Delineation

To assess cold region dynamics, firstly the cold region extent needs to be delineated. So far, mapping cold region is often realized by quantitatively analyzing temperature. For instance, "Köppen (1884) characterized cold regions as areas with 1–4 moderate months (i.e., mean temperature between 10 °C and 20 °C) and 11–8 cold months (i.e., mean temperature less than 10 °C). Chen et al. (2006) mapped cold regions in China based on the mean temperature of the coldest month (below 3 °C), fewer than 5 months with mean

temperature above 10 °C, and mean annual temperature below 5 °C. In addition to air temperature, Yang et al. (2000) located the cold regions in China via thresholding 10 different climate factors.” (Hu et al., 2017) Also, frost penetration can be used to determine cold region extent. “To identify the southern boundary of cold regions, a 30-cm frost penetration depth occurring once in 10 years is a generally accepted criterion (Andersland and Ladanyi, 2013). To date, the most comprehensive and widely-acknowledged definition was provided by CRREL (Bates and Bilello, 1966), which located the cold regions in the Northern Hemisphere according to temperature (0 °C and –18 °C isotherms), snow depth (30 and 61 cm isolines), ice cover (100 and 180 annual mean unnavigable days), and frozen ground extent (permafrost and 30 cm frost penetration).” (Hu et al., 2017) Based on the CRREL’s definition, Hu et al. (2017) produced the cold region stability map (Figure 2-5), together with the ERA-Interim Archive from ECMWF (Berrisford et al., 2011). This map has been utilized as the “reference map” for cold region mapping using EO data. The map indicates the geographical extent of the cold regions in Europe, which includes the Carpathian Mountains, the European Alps, Finland, Sweden, Iceland, and Norway (including the Svalbard Archipelago).

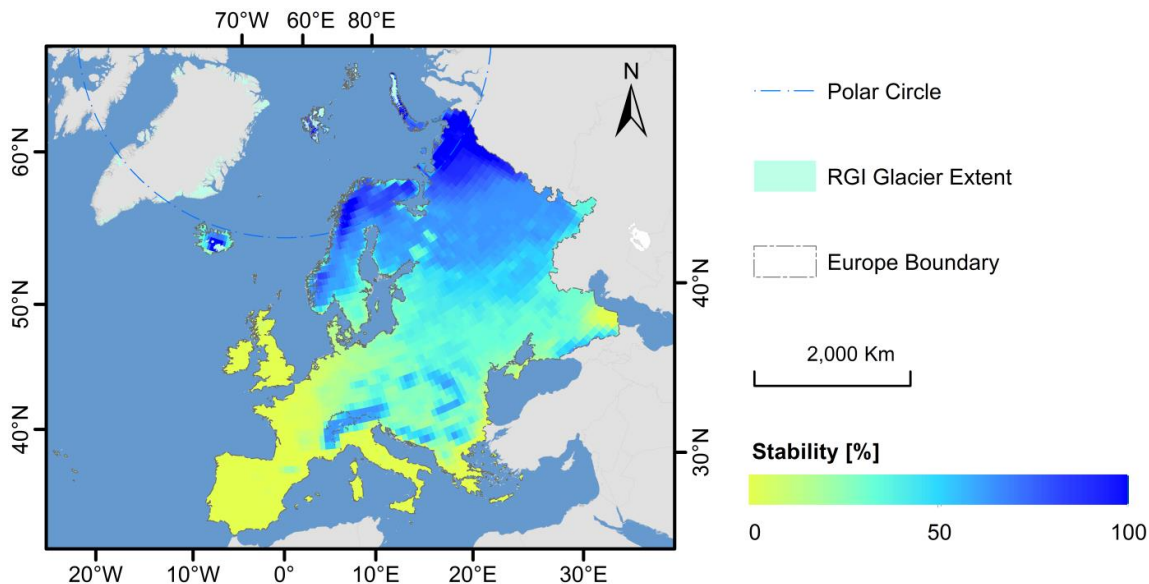


**Figure 2-5:** Cold regions in Europe delineated according to integrated stability parameter. Modified according to Hu et al. (2017).

Even though cold region could be delineated roughly using the climate reanalysis data, the resultant map is often of coarse resolution. For regional-to-local scale studies, higher



resolution maps are required. Given the difficulty of deriving air temperature and snow depth solely depending on EO data, alternative indicators are required. Since snow is an ECV, temporal metrics of snow cover derived from EO data have a great potential for delineating a cold region boundary. Meanwhile, “an EO-derived cold region boundary would improve the spatial resolution (e.g., 500 m using MODIS data) resulted from the reanalysis data (i.e., 80 km from ERA-Interim). Among the temporal snow cover parameters, the suitability of 19-year mean SCD derived from GSP data set (Dietz et al., 2015) from DLR-DFD is explored (Figure 2-6). The DLR-DFD GSP is a cloud-free time series of daily snow cover processed from the operational 500 m MODIS daily snow cover products MOD10A1 and MYD10A1 (Hall et al., 2002), and has been validated using the European Climate Assessment & Dataset (ECA&D) station data in Europe (details see Dietz et al. (2015)) To ensure the consistency of spatial resolution, the spatial resolution of mean SCD data is downscaled from 500 m to 80 km (the spatial resolution of the ERA-Interim data set and the cold region stability result). A correlation analysis between mean SCD (2000–2018) and cold region stability is performed. The results indicate high correlation ( $R^2 = 0.734$  with a  $p$ -value  $< 0.001$ ).” (Hu et al., 2017) The extent of the stable cold region is of a mean SCD larger than 180 days.

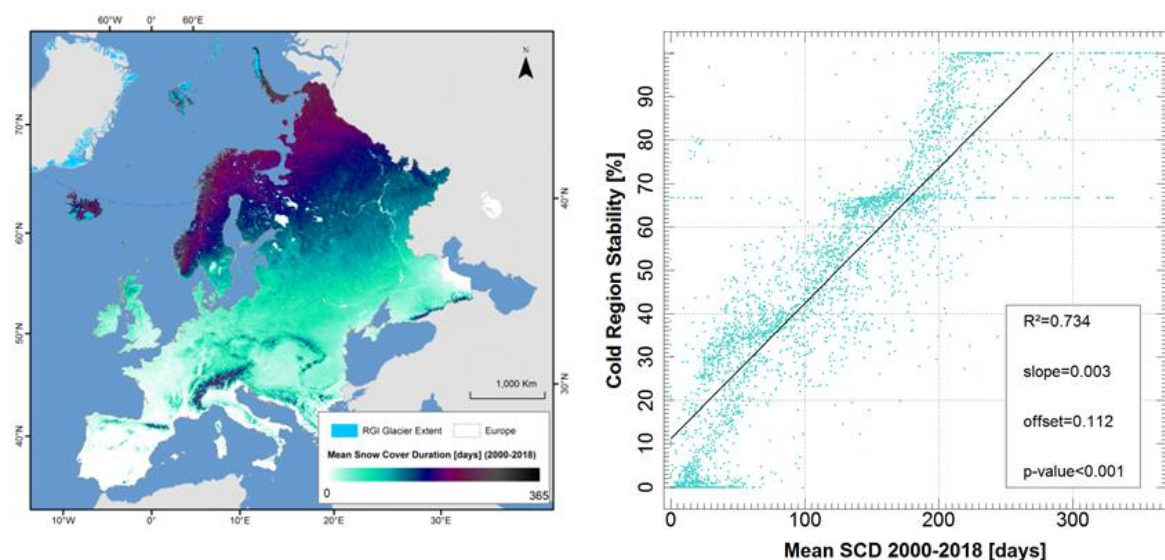


**Figure 2-6:** 19-year mean Snow Cover Duration (SCD) between 2000 and 2018 derived from Global Snow Pack (GSP) data based on Dietz et al. (2015) (left), and the scatter plot between mean SCD (2000–2018) and cold region stability (right). The two horizontal anomalous lines are artefacts due to the spatial resolution downscaling occurring in the mountain areas and their surrounding regions. Modified according to Hu et al. (2017).

### 2.1.3 Snow Dynamics Monitoring

**Snow Cover Area (SCA):** Thresholding band-ratio(s) is the most frequently used method in SCA mapping. “Among the existing threshold-based algorithms, SNOMAP (Hall et al., 1995; Riggs et al., 1994) is the most quintessential example. The originally proposed Normalized Difference Snow Index (NDSI)  $\geq 0.4$  (Hall et al., 1995; Riggs et al., 1994) has been universally applied to identify snow covered area.” (Hu et al., 2017)

$$\text{NDSI} = \frac{\text{GREEN-SWIR}}{\text{GREEN+SWIR}} \quad (2.1)$$

Whereas, single thresholding based on NDSI may provide erroneous results over very dark targets, i.e., black spruce forest, water bodies. “To avoid such misclassification, further threshold(s) were introduced in addition to NDSI  $\geq 0.4$ . For example, Winther and Hall (1999) included  $\rho_{b4}$  (reflectance at band 4)  $\geq 0.11$  for Landsat TM imagery, Xiao et al. (2004) used  $\rho_{b3} \geq 0.11$  for SPOT-VEGETATION images, Foster et al. (2011) additionally restricted  $\rho_{b2} \geq 0.1$  and  $\rho_{b4} \geq 0.1$  to MODIS data, etc.” (Hu et al., 2017) Another well-known issue regarding snow classification is snow-in-forest. “Usually, this problem is addressed by supplementarily computing the Normalized Difference Vegetation Index (NDVI).

$$\text{NDVI} = \frac{\text{NIR-RED}}{\text{NIR+RED}} \quad (2.2)$$

Afterwards, a NDSI—NDVI threshold field can be employed to identify snow in forest pixels according to Klein et al. (1998).” (Hu et al., 2017) Besides, if thermal bands are available, a thermal mask (e.g., 283 K proposed by Romanov et al. (2000)) should be considered to further eliminate contaminated snow pixels (e.g., cloud, coastal sand, aerosol-influenced pixels). In addition to the above-mentioned methods, maximum likelihood (Turpin et al., 1999), crisp and fuzzy soft classifiers (Pepe et al., 2010), linear-interpolation-based method (Metsämäki et al., 2002) were also developed and applied in Europe. “Due to the inherent challenges of SAR sensors—dry snow penetration and single-frequency configuration—mapping SCA using SAR data independently is difficult. Yet PM sensors with multi-frequency channels hold potential for mapping snow cover utilizing the inverse correlation between surface emission and radar frequency” (Hu et al., 2017), e.g., Grody, 1991; Grody

and Basist, 1996; Kongoli et al., 2007. Meanwhile, the limitation of PM-based methods should be also noted, including the restriction to dry snow, difficulty in determining thin snow (<5 cm) (Foster et al., 2011), very coarse resolution (e.g., SSM/I with 25 km resolution), and attenuation of forest (Kurvonen and Hallikainen, 1997). “Contemporaneously, an optical-PM-scatterometer blended algorithm (i.e., AFWA NASA Snow Algorithm, ANSA) was developed by the US Air Force Weather Agency (AFWA) and NASA jointly (Foster et al., 2009, 2007, 2011).” (Hu et al., 2017) Apart from the mono-temporal spatial extent of SCA, multi-temporal SCA information is also crucial for snow cover dynamics assessment. Snow Cover Duration (SCD), Snow Cover Start (SCS), and Snow Cover Melt (SCM) (Wang and Xie, 2009) are the most prevalently used metrics. In Europe, Dietz et al. (2012) studied the temporal snow cover characteristics in Europe between 2000 and 2011 based MODIS-Terra/Aqua daily snow cover products.

**Snow Cover Fraction (SCF):** Given the well-known inherent issue of satellite images, pixel mixture, FSC results may be more superior informative than binary classifications. So far, there are two popular algorithms for FSC derivation, i.e., the Norwegian Linear Reflectance-to-Snow-Cover Algorithm (NLR) developed by Andersen (1982), and the MODIS-based NDSI-FRA (FRAction of snow-covered area) algorithm introduced by Andersen (1982) and Salomonson and Appel (2004). “The NLR method was established assuming a linear relationship between the pixel signal and FSC (Andersen, 1982). Initially, the algorithm was developed for estimating FSC in Norway, based on NOAA-AVHRR data. In fact, it can be regarded as a 2-EM (End-Member) SMA (Spectral Mixture Analysis) model (Solberg et al., 2010). Later, Zhu and Woodcock (2014a) modified the NLR algorithm to build the snow detection module of Tmask (multiTemporal mask, an automated cloud, cloud shadow, and snow detection method) for Landsat data. Using NDSI values, the NDSI-FRA algorithm has been applied to generate MOD10A1 (Terra) and MYD10A1 (Aqua) FSC products (Rittger et al., 2013). It was originally developed to estimate FSC using MODIS-Terra imagery (Salomonson and Appel, 2004). Subsequently, Salomonson and Appel (2006) expanded the algorithm to data available from the Aqua platform as well.” (Hu et al., 2017) Also, the classical spectral unmixing technique has been utilized for SCF estimation since the 1990s, e.g., Nolin et al., 1993; Rosenthal and Dozier, 1996; Painter et al., 2003, 1998. “Foppa et al. (2004) rendered a Linear Spectral Mixture Analysis (LSMA) to NOAA-AVHRR data for the whole European Alps. The authors suggested

that the presented processing chain is appropriate for operational and the Near Real Time (NRT) applications since it is simple, fast, objective, and reproducible. Later, Foppa et al. (2007) validated the results quantitatively over the European Alps based on higher resolution satellite imagery (ASTER). In the European Alps, Veganzones et al. (2014) applied a much advanced unmixing technique to MODIS data. The algorithm includes two parts: a (partially) Constrained Least Squares Unmixing (CLSU) and an Endmember Induction Algorithm (EIS).” (Hu et al., 2017) Moreover, spectral unmixing is also an alternative for detecting snow-in-forest, e.g., Vikhamar and Solberg, 2003a, 2003b; Metsämäki et al., 2012. Last but not least, optical reflectance model-based methods are also widely used, for example, SCAMod developed by the Finnish Environment Institute (SYKE) (Metsämäki et al., 2004, 2005; Salminen et al., 2009; Vepsäläinen et al., 2001).

**Snow Characterization:** Snow Depth (SD), Snow Grain Size (SGS), Snow Water Equivalent (SWE), and Snow Impurity (SI) are the most often studied metrics with regards to snow pack characterization. In the optical data domain, SGS and SI are often derived because of the reflectance dependence in the visible (for SI) and NIR (for SGS) range (Warren, 1982; Warren and Wiscombe, 1980). “(Fily et al., 1997) discovered an empirical linear relationship between Landsat TM reflectance and SGS. The authors suggested the use of a band at 1.2  $\mu\text{m}$  because of the highly pronounced SGS effect and low influence due to atmosphere and SI at this wavelength. Painter et al. (2003) developed a Multiple Endmember SMA (MESMA) based model, MEMSCAG (Multiple End Member Snow Covered Area and Grain size), to model FSC and SGS using hyperspectral data. In order to map light-absorbing snow impurities (e.g., black carbon, mineral dust, and volcanic ash), Di Mauro et al. (2015) introduced a Snow Darkening Index (SDI).” (Hu et al., 2017) When it comes to the SWE estimation, PM data is the backbone because of the high correlation between the Brightness Temperature (BT) functions and SWE (Hallikainen and Jolma, 1992, 1986). “(Hallikainen and Jolma, 1992) performed a correlation analysis for 17 BT metrics and SWE map-derived values in Finland. Their conclusion suggested that  $BT_{10V} - BT_{37V}$  and  $BT_{18V} - BT_{37V}$  are the most suitable (i.e., have the highest correlation coefficients) for estimating SWE in small areas.” (Hu et al., 2017) Table 2-1 summarizes empirical methods for SD and SWE calculation. Alternatively, Artificial Neural Network (ANN) (Santi et al., 2014, 2012) and the Helsinki University of Technology (HUT) snow microwave emission model (Pulliainen et al., 1999) are also employed to derive SWE and

SD retrieval using PM data. "Tedesco et al. (2004) compared the performance of an ANN-based technique, an empirical algorithm (Spectral Polarization Difference method, SPD (Aschbacher, 1989)) and the iterative inversion of the HUT snow emission model in retrieving SWE and SD. The authors found that the best results were obtained from the ANN method trained with experimental data. Satisfactory results were also received using the other two methods when SWE is less than 17 cm or excluding springtime measurements." (Hu et al., 2017) Furthermore, (Hallikainen et al., 2003) explored the usability of active microwave data to derive SWE in Finland. By integrating the Special Sensor Microwave/Imager (SSM/I) and the Quick Scatterometer (QuickScat) data, the authors concluded that the PM-scatterometer-combined SWE retrieval method is superior to the methods solely based on PM data.

**Table 2-1:** Empirical equations for Snow Water Equivalent (SWE) and Snow Depth (SD) calculation. Modified according to Hu et al. (2017).

Equation	Annotation	Reference
$SD = \frac{GT - 0.085}{0.036}$	$GT = \frac{BT_{37H} - BT_{18H}}{37 - 18}$	Hallikainen and Jolma, 1992
$SWE = 0.27 \cdot SD$		Hallikainen and Jolma, 1992
$\Delta T = F(SWE) - F(SWE = 0)$	$F = BT_{18H} - BT_{37H}$	Hallikainen, 1984
$SD = 1.59 \cdot (BT_{18H} - BT_{37H})$		Chang et al., 1987
$SWE = a_0 + a_1 \cdot [(BT_{19V} - BT_{37V}) + (BT_{19V} - BT_{19H})]$	$a_0$ and $a_1$ are empirical coefficients	Aschbacher, 1989
$SWE = c \cdot (BT_{18H} - BT_{37H})$	$c$ is the slope of linear fit $4.8 \text{ mm} \cdot \text{K}^{-1}$	Armstrong and Brodzik, 2001
$SD = 1.59 \cdot (BT_{19H} - 6) - (BT_{37H} - 1)$		Armstrong and Brodzik, 2001
$SWE_{\text{non-forested}} = a_0 - a_1 \cdot (BT_{36.5V} - BT_{18.7V})$	$a_0$ and $a_1$ are empirical coefficients	Lemmetyinen et al., 2006
$SWE_{\text{forested}} = a_0 - a_1 \cdot [(BT_{36.5V} - BT_{18.7V}) - BT_{18.7V} - BT_{18.7H}]$		Lemmetyinen et al., 2006
$SWE = a_0 + a_1 \cdot (BT_{23V} - BT_{89V})$	$a_0, a_1, a_2, a_3$ are empirical coefficients	Kongoli et al., 2007
$SWE = a_2 + a_3 \cdot (BT_{23V} - BT_{31V})$		Kongoli et al., 2007

**Snowmelt:** To monitor snowmelt processes, spatiotemporal snowmelt information is needed. The conventional snowmelt area maps can be generated based on multi-temporal SAR images, utilizing the seasonal backscattering variability caused by variations of snow liquid water content and surface roughness of the snow pack. So far, the leading method is the change detection algorithm developed by Nagler and Rott (2000), which is based on a ratio between the backscattering coefficient of wet snow and a reference image, pixel by pixel. Thereafter, a  $-3$  dB threshold is suggested to separate wet snow from peripheral land-covers. Similarly, Koskinen et al. (1997) and Pulliainen et al. (2001) developed the Helsinki University of Technology SCA method (TKK-SCA) to detect wet snow cover area based on the observed backscattering, as well as those of reference surface and wet snow. "To determine the date of snowmelt onset, the temporal variations in backscattering and/or brightness temperature can be employed. For instance, Rawlins et al. (2005) derived the timing of snowmelt in the pan-Arctic during the spring of 2000 using daily QuikSCAT-SeaWinds backscattering time series. For multi-temporal snowmelt retrieval, Rotschky et al. (2011) analyzed the spatiotemporal pattern of snowmelt-refreeze cycles in Svalbard using 9-year (from 2000 to 2008) QuikSCAT time series." (Hu et al., 2017) Furthermore, Wang et al. (2011) combined active (QuikSCAT) and passive (SMM/I) microwave satellite data to determine snowmelt onset between 2000 and 2009. For the purpose of snowmelt runoff estimation, Snowmelt Runoff Model (SRM (Martinec et al., 1998)) is the most frequently employed model. "Martinec (1975) initially developed the SRM for small European river basins, and it has subsequently been successfully applied worldwide (Martinec et al., 1998). Swamy and Brivio (1996) explored the potential of optical EO data (Landsat dataset) together with ground meteorological and hydrological information to improve snowmelt runoff modelling for the Italian Alps. Nagler et al. (2008) presented a practical data assimilation scheme for short-term runoff forecasts in Alpine basins exemplified by the Ötztal drainage basin (Austrian Alps)." (Hu et al., 2017) The authors emphasized that meteorological-forecast-induced errors are more influential than satellite-derived snow cover information with regards to resultant runoff simulations.

**Operational Snow Products:** The history of operational snow product development can reach back to 1960s, when "weekly binary snow cover charts of the Northern Hemisphere have been provided by NOAA/NESDIS based on manual inspection by trained meteorologists using optical satellite imagery (Armstrong and Brodzik, 2001; Matson and

Wiesnet, 1981; Robinson et al., 1993). After the successful development of IMS in 1997, snow extent maps can be generated at daily intervals in a more efficient and accurate manner (Helfrich et al., 2007; Ramsay, 1998). Such products are usually only suitable for studies at a global scale due to their medium resolution (1 km introduced in 2014). In December 1999, MODIS-Terra was launched. One year later, the MODIS-Terra 500 m daily snow cover product (MOD10A1) became available through the National Snow and Ice Data Center (NSIDC). The product is generated using the SNOMAP algorithm (Hall et al., 1995; Riggs et al., 1994). During the Globsnow-1/2 project (Metsämäki et al., 2015), ESA also developed its SCA and SWE products based on ERS-2/ATSR-2 (Along-Track Scanning Radiometer-2) (1995–2003) and Envisat-AATSR (2002–2012) data. For more snow product information and data access, it is suggested that readers explore what is offered by the NSIDC. Given the existence of various snow-related products, intercomparison and validation are essential. Toward this end, ESA launched the SnowPEX (Satellite Snow Product Intercomparison and Evaluation Exercise) project within the Quality Assurance framework for Earth Observation (QA4EO) to intercompare and validate the major satellite snow products for the Northern Hemisphere and the globe. It is expected that the results will be published in the near future.” (Hu et al., 2017) In central Europe (42°~51°N, 5°~30°E), Notarnicola et al. (2013) implemented the EURAC algorithm to produce a near-real-time snow extent product at 250 m resolution based on the MODIS data.

#### **2.1.4 Glacier Dynamics Monitoring**

**Glacier Extent Delineation:** Glacier extent is the basic parameter for glacier dynamics monitoring. GLIMS (Raup and Khalsa, 2010) proposed a guideline for glacier extent delineation, i.e. circumscribing both the glacier ice and snow body and all adjacent debris at the end of the ablation season. At present, optical imagery is the most used dataset for glacier extent delineation. So far, manual digitization is the most straightforward way to delineate glacier outlines using a background image displayed as a false colour composite (e.g., ASTER bands 4-3-2 (Błaszczuk et al., 2009), TM 5-4-3 or TM 4-3-2 (Baumann et al., 2009; Paul et al., 2015, 2007), ETM+ 7-4-2 (Follestad and Fredin, 2007)). Also, “several (semi-) automated techniques have been developed to extract glacier bodies of snow and ice from EO data. Among them, taking advantage of the



significant spectral contrast between the Short Wave Infra-Red (SWIR) and the visible band, the band ratio method (thresholding ratio image, e.g., Bayr et al., 1994; Hall et al., 1987; Paul, 2002; Paul et al., 2002) is the most widely acknowledged and utilized algorithm. Lastly, manual correction and median filtering are recommended to improve the results (Paul et al., 2002). Further information with regard to the threshold sensitivity, different band combinations and spatial resolutions can be found in (Paul et al., 2016). By far, this algorithm has become the backbone for delineating glacier outlines in many glacier inventories (e.g., Carturan et al., 2013; Paul et al., 2011a, 2011b, 2004b; Paul and Andreassen, 2009; Pfeffer et al., 2014b; Winsvold et al., 2014). Other classification algorithms have also been applied, but scarcely for glacier delineation: Serandrei-Barbero et al. (1999) applied fuzzy contextual classification to map the glaciers in the Italian Alps; Robson et al. (2016) implemented the Object-Based Image Analysis (OBIA) to classify more than 100 glaciers in the Austrian Alps for three time steps semi-automatically." (Hu et al., 2017) Moreover, studies comparing the mainstream delineation techniques have been carried out by Paul (2000), Paul et al. (2016, 2015, 2013, 2002), Paul and Käab (2005). "The key conclusions from these studies are:

- 1) Generally, the Digital Number (DN) based simple ratio methods had the best results (fast, robust and strict to the pixel boundary). Digitization and the band-ratio method are consistent in clean glaciers;
- 2) Simple ratios are relatively insensitive to threshold selection. Yet the additional TM1 threshold is of higher threshold sensitivity;
- 3) Atmospheric correction for TM2 is important when NDSI is used;
- 4) Manual correction is recommended to correct misclassifications caused by debris cover, proglacial lakes, shadowed areas, and clouds.
- 5) Using thresholds of the panchromatic band (e.g., OLI 8) divided by SWIR could improve the spatial resolution, but this increases the workload in manual correction.

Since mapping shadowcast glaciated areas is the most critical point by far (Paul and Käab, 2005), TM3/TM5 with TM1 correction or NDSI is therefore often preferred. However, the local environmental settings concerning vegetation and/or water conditions must always be considered to select the most proper ratio (Paul et al., 2015)." (Hu et al., 2017) At present, "automated identification of debris cover remains a well-recognized challenge

particularly for optical data (Paul et al., 2013, 2011b; Racoviteanu et al., 2009), mainly due to its spectral similarity to the surrounding terrain. To tackle the problem, some EO-based techniques have been developed mainly based on the thermal band(s). A pioneer study was undertaken by Lougeay (1974), who explored the potential of thermal remote sensing to identify different moraine types and glacier ice based on thermal contrast. Also, several empirical methods using the relationship between debris thickness and temperature have been developed (e.g., Mihalcea et al., 2008; Ranzi et al., 2004). An obvious drawback of these methods is the lack of spatiotemporal transferability, since field measurement and recalibration are imperative. As alternatives, Paul et al. (2004a) developed a semi-automatic multisource (i.e., multispectral data and DEM) method to map the supraglacial debris, and compared it to multispectral-data-based ANN classification." (Hu et al., 2017) Nevertheless, an Interferometric Synthetic Aperture Radar (InSAR) coherence image derived from SAR images holds a potential to determine debris cover, which takes low coherence as an indication of glacier existence (Atwood et al., 2010; Robson et al., 2016).

**Glacier Motion:** Glacier motion is one of the most important perspectives of glacier dynamics monitoring. Conventionally, the retreat/advance of glaciers is retrieved from bi/multi-temporal glacier outlines (e.g., Holobâcă, 2016). Yet, "to extract the velocity field and the displacement within the glaciated area(s), more advanced techniques are needed. So far, there are two leading methods for velocity field extraction, image offset-tracking and D-InSAR (Differential InSAR). Image offset-tracking can be applied to both optical and SAR data. A 2D velocity field can be derived by determining the movement of identifiable supraglacial objects (e.g., crevasses, moraines) or speckles, using a window (also known as a search chip/patch) moving with an n-pixel step to find the peak cross-correlation. In the optical field, this is usually termed "image matching", for instance, (Berthier et al., 2005; Heid and Kääb, 2012a; Kääb et al., 2016, 2005; Schubert et al., 2013). A detailed comparison of different image matching techniques can be found in (Heid and Kääb, 2012b; Paul et al., 2015). Also, to measure glacier motion in Europe, speckle/feature and coherence tracking are widely applied to TerraSAR-X (X-band) data for the Swiss Alps (Schubert et al., 2013) and Svalbard (Schellenberger et al., 2017), ERS-1/2 SAR (C-band) in Svalbard (Strozzi et al., 2002), Radarsat-2 (C-band) in Svalbard (Schellenberger et al., 2016), and the Japanese Earth Resources Satellite-1 (JERS-1; L-band) in Svalbard (Strozzi et al., 2006) using amplitude/phase patterns and coherence. D-InSAR is an alternative to

offset-tracking. It includes: a two-scene technique (DEM elimination technique), a three-scene technique (three-pass technique) and a four-scene technique (four-pass technique) (Adam and Jonsson, 1997). D-InSAR is amongst the most accurate techniques (Schubert et al., 2013; Strozzi et al., 2002). Whereas, it is restricted to a short temporal baseline in order to avoid the loss of coherence. A significant drawback of D-InSAR is that it only depicts motion in the slant-range direction. Only in a special case, when dual-azimuth image pairs (ascending and descending passes) are available and coherence is retained, might D-InSAR conquer this problem. Otherwise, an azimuth displacement component derived from coherence tracking is often combined with the D-InSAR result to build the motion both in slant-range and in the azimuth direction.” (Hu et al., 2017) To further retrieve a 3D velocity field, the flow direction is required. An often applied assumption is that the glacier ice bodies flow parallel to the surface (Joughin et al., 1998). It is noteworthy that such assumption is actually is error-prone, given the fact that flow tends to be upward in the ablation zone and downward in the accumulation zone (Paterson, 2016).

**Glacier Elevation and Volumetric Change:** To assess the responses of glaciers to climate change, glacier volumetric change is superior to glacier areal change due to the time delay of glacier extent shrink (Oerlemans, 2001). “The volumetric change can be calculated by multiplying the average glaciated area by the glacier elevation change within a certain time span (Hannisdóttir et al., 2015). DEM subtraction is the most straightforward way to calculate glacier elevation change. The DEM(s) can be derived from photogrammetry using aerial photography, airborne SAR interferometry, airborne LiDAR, and topographic maps. Regarding the EO data, optical sensors of stereo geometry, e.g., ASTER, the Satellite Probatoire de l'Observation de la Terre 5 (SPOT5), IKONOS, Quickbird, WorldView, Pléiades, have enduring popularity. Of these optical sensors, ASTER is of particular interest thanks to its free accessibility (unlimited public access since 1 April 2016), extraction software based on automated algorithms (e.g., SilcAst, PCI Geomatics), comparably short revisit time interval, long-term operation (16-day revisit time from 2000 to present), and relatively high resolution at near-global coverage (15 m nadir and backward for band 3). Before the subtraction, reprojection, co-registration and resampling are imperative for heterogeneous DEMs. Paul et al. (2015) suggested downscaling the finer resolution image using algorithms more complicated than nearest neighbour to avoid

artefacts and horizontal disalignment within a sub-pixel. Moreover, when the pixel size difference is at least two times, a block average filter is recommended. Similarly, users can also use InSAR to generate interferometric DEMs. However, radar penetration of the snow and ice makes interferometric DEM subtraction more complicated for glacial studies (Frey and Paul, 2012; Gardelle et al., 2012; Nuth and Kääb, 2011). Nevertheless, SAR still provides valuable elevation change information, especially when the glacier surface experienced ice-water phase change (e.g., precipitation and melting). Magnússon et al. (2011) explored the potential of InSAR for detecting regional glacier uplift and subsidence. Even though the Ice, Cloud and Land Elevation Satellite-Geoscience Laser Altimeter System (ICESat-GLAS) has the best vertical accuracy (0.15 m (Zwally et al., 2002)) and the best consistency (Nuth and Kääb, 2011) of these elevation products, it has two major drawbacks for glacier elevation change measurement: approximately 70 m diameter footprint with 170 m ground spacing along track, and shift of the footprint centers (Kääb, 2008). To tackle the problem, two leading methods exist for glacier elevation change estimation based on altimetry data: the repeat-track method and the cross-over method (Kääb et al., 2012; Moholdt et al., 2010; Pritchard et al., 2009). In Europe, Moholdt et al. (2010) tested two ICESat repeat-track methods for deriving glacier elevation changes in Svalbard and validated the results against cross-over points and the SPOT 5 stereoscopic survey of Polar Ice: Reference Images and Topographies (SPIRIT) DEM. The results confirmed the validity of repeat-track methods for mapping short-term Arctic glacier elevation changes.” (Hu et al., 2017) The comparison studies among ICESat Altimeter, DEMs and topographic maps were carried out by Nuth et al. (2010) and Kääb (2008). The authors emphasized the value of ICESat data in deriving glacier elevation/volumetric change at a regional scale.

**Glacier Mass Balance:** Glacier mass balance is defined as the change of the mass of (part of) the glacier over a certain time frame (Cogley et al., 2011). For glacier mass balance studies at a decadal scale, solely glacier area or length change is not representative enough (Rabatel et al., 2016). Traditionally, “glacier mass balance is directly measured via snowpits and stakes. However, such glaciological measurement has an obvious drawback, i.e. the laboriousness of long-term and large-scale monitoring. EO-based mass balance retrieval has thus gained increasing attention in recent years. The most widely-applied EO-based method is the “geodetic method” (Finsterwalder, 1954).

Hannesdóttir et al. (2015) employed this method to reconstruct the mass balance of glaciers in the southeast part of the Vatnajökull ice cap for a seven-year span from ~1890 to 2010 based on multiple sources including glacial geomorphological features, historical photographs, maps, aerial images, the Differential Global Positioning System (DGPS) measurements, a LiDAR survey and several optical satellite images (i.e., SPOT5, MODIS, Landsat). The glacier-wide geodetic mass balance,  $B_G$ , can be expressed as:

$$B_G = \bar{\rho} \times \frac{\Delta H}{\Delta t} \quad (2.3)$$

where  $\bar{\rho}$  denotes glacier-wide average density, which is either obtained from field measurement or oftentimes assumed to be  $900 \text{ m}\cdot\text{kg}^{-3}$  (Cogley, 2009; Huss, 2013). The areal-mean thickness/elevation change  $\Delta H$  is averaged through a certain time-span  $\Delta t$  (Cogley, 2009). The uncertainties of this method have been well-documented (Cogley, 2009; Nuth et al., 2012; Sapiano et al., 1998). Apart from bias in  $\Delta H$ , when converting elevation changes into water equivalent volume changes, the simplified assumption of ice density  $\bar{\rho}$  is error-prone especially in compressible firnpack (Huss, 2013; Nuth et al., 2012; Sapiano et al., 1998). In addition, the time-span  $\Delta t$  is significantly uncertain with regard to the acquisition dates of the EO data (Cogley, 2009). To construct mass balance time series, the geodetic method is usually hampered by the scarcity of long-term consistent annual elevation data, so alternatives are desired. The Equilibrium Line Altitude (ELA) is an appropriate indicator for glacier mass balance (Braithwaite, 1984). ELA refers to the mean altitude of the equilibrium line which divides the accumulation zone and the ablation zone and therefore has zero climatic mass balance (Cogley et al., 2011). Based on ELA variability, Rabatel et al. (2016) reconstructed glacier-wide mass balance time series for 30 glaciers in the French Alps from 1983 to 2014. As an alternative to ELA, albedo from satellite measurements is useful for depicting glacier mass balance in a time series manner. Dumont et al. (2012) explored the relationship between measured annual mass balance and MODIS-derived glacier albedo. They observed strong correlation ( $R^2 > 0.9$ ) between the albedo and mass balance and argued that albedo is more informative than ELA with regard to glacier surface. The "satellite albedo method" was developed and applied for Vatnajökull (Iceland) using NOAA-AVHRR imagery (Calluy et al., 2005) and Svalbard using MODIS data (Greuell et al., 2007). In addition to the aforementioned algorithm for glacier mass balance calculation, other methods also exist, such as the Accumulation Area Ratio

(AAR) method (Kulkarni, 1992) and the “flux gate” method (Nuth et al., 2012) (only for tidewater glaciers).” (Hu et al., 2017) In Europe, AAR method is often applied to assess mass balance for glaciers in Svalbard.

**Glacier Inventory:** In principle, a glacier inventory usually summarizes two aspects of the glacier information, i.e. glacier extent and glacier-related parameters (e.g., identification code, coordinates, total surface area, length, elevation, mean aspect and slope). “For the purpose of glacier delineation in regional glacier inventories, orthophotographs and historic maps are valuable resources because they contain information gathered before the availability of EO data. The primarily EO-based glacier inventories for Europe (excluding Greenland) are summarized in Table 1. The Landsat fleet is by far the most often used backbone of glacier inventory generation. The Landsat fleet has several merits compared to ASTER or SPOT, which are also popular sensors in glaciological studies (see Figure 2-3): large swath width, free accessibility, long-term records, georeferencing and orthorectification (Winsvold et al., 2014). The methods were summarized in the previous sections. As seen in Table 2-2, ratio image thresholding and manual digitization are the most frequently applied delineation methods. Regarding the updating interval, 5 to 10 years is suggested (Paul et al., 2007) in order to reveal highly variable changes as well as the spatial patterns of changes (Paul and Andreassen, 2009). Topographical information is the most often extracted glacier parameter, and can be automatically calculated from the existing freely available DEMs. The suitability of national and global DEMs with regard to glacier-specific topographic parameter extraction was investigated by Frey and Paul (2012) for a sample of 1786 Swiss glaciers. The study concluded that the first choice is local, high quality DEMs. When such DEMs are not available, the Shuttle Radar Topography Mission (SRTM) DEMs are preferred to ASTER GDEMs. Notwithstanding better results obtained from SRTM DEMs, both DEMs are useful for calculating topographic parameters in glacier inventories. In terms of the calculation, Paul et al. (2009) recommended the standardized calculation of relevant glacier parameters (9 basic and 7 auxiliary parameters). Apart from topographical attributes, mass balance information is one of the most essential variables for glacier studies. Mass balance information is seldom included. Recently, some inventories have started to include or update mass balance information. For example, Hannesdóttir et al. (2015) included the average geodetic mass balance for the outlet glaciers of southeast Vatnajökull. ” (Hu et al.,

2017) So far, the Randolph Glacier Inventory (RGI) is the only global glacier inventory (excluding Greenland and the Antarctic), whose first version was released on 22 February 2012. The latest RGI Version 5.0 (released 20 July 2015) has ingested some of the mass balance data from the WGMS mass balance database (Arendt et al., 2015).

**CHAPTER 2 State-of-the-Art: Results of the Literature Review of Remote Sensing on Cold Regions**

**Table 2-2:** References for existing glacier inventories derived from satellite imagery for European glaciers (excluding Greenland). Modified according to Hu et al. (2017).

Location	Year	Sensor	DEM	Method <sup>1</sup>	References
<b>Globe (RGI)</b>	1999 or later	Landsat fleet, etc.	SRTM, SPOT DEM, ASTER GDEM2	T + D	Arendt et al., 2015; Pfeffer et al., 2014a
<b>European Alps</b>	2003	Landsat fleet	STRM	T	Paul et al., 2011b
<b>Austrian Alps</b>	1985, 1992	Landsat fleet	—	T	Paul, 2002
	1985, 2003, 2013	Landsat fleet, ALOS PALSAR	SRTM, Local DEM	S	Robson et al., 2016
<b>French Alps</b>	1967/71, 1985/86, 2003, 2006/09	Landsat fleet	Local DEM	S	Gardent et al., 2014
<b>Italian Alps</b>	1987, 2009	Landsat fleet	Local DEM	T	Carturan et al., 2013
<b>Swiss Alps</b>	1985	Landsat fleet, SPOT	Local DEM	S/U/T/M	Kääb et al., 2002; Paul et al., 2002
	1985, 1992, 1998/99	Landsat fleet	Local DEM	T	Paul et al., 2004b
<b>Iceland</b>	1890–2010	Landsat fleet, MODIS, SPOT	Local DEM	D	Hannesdóttir et al., 2015
<b>Norway</b>	LIA–2003	Landsat fleet	—	D	Baumann et al., 2009
	1999	Landsat fleet	Local DEM	T	Paul and Andreassen, 2009
	1966, 1997, 2003, 2006	Landsat fleet	Local DEM	T	Paul et al., 2011a
	1947/85, 1988/97, 1999–2006	Landsat fleet	Local DEM	T	Winsvold et al., 2014
<b>Svalbard</b>	1930s–2010	ASTER, Landsat fleet, SPOT	SPOT DEM, ASTER GDEM2	D	Nuth et al., 2013
	2000–2006	ASTER, Landsat fleet,	ASTER generated	T+D	Błaszczek et al., 2009

<sup>1</sup> Delineation method for EO data: T = Thresholded Ratio Image; S = Supervised Classification; U = Unsupervised Classification; D = Digitization. LIA: Little Ice Age.



## **2.2 Identified Challenges of Earth Observation on Cold Regions**

The previous section summarizes the EO-based studies on cold regions with respects to snow and glacier dynamics in Europe. Thereof, enormous challenges still exist, when deriving the land surface dynamics of cold regions in Europe. Meanwhile, these challenges also shed light on the pathway for future studies, based on identified methodological and geoscientific research gaps.

### **2.2.1 Challenges with Regards to Spatiotemporal Scale and Study Area Settings**

The reviewed studies are carried out at very different scales. Snow is highly temporal-dynamic. Given that most of the snow dynamic studies focus on a regional-to-hemispherical scale, high spatial resolution is not so critical comparing to the high temporal resolution, when analysing large scale snow cover characteristics. Often, snow dynamic studies are dependent on high temporal EO data (Figure 2-7). In contract, "glacier studies are mostly presented at an individual glacier scale, and only a limited number of studies focus on regional scales (e.g., the European Alps, the Svalbard Archipelago). The time interval of EO-based glacier studies varies from monthly to decadal (Figure 2-8), while most of the studies are multi-temporal observations at an annual interval." (Hu et al., 2017) In this regard, high spatial resolution is more desired for glacier dynamic studies.

In terms of the study area settings, a large part of the cold regions in Europe are situated mostly in high-latitude regions and/or in mountain areas. "Typical problems regarding high latitude areas are the occurrence of polar darkness and frequent cloud cover, which has a great influence on optical data availability. On the other hand, the total number of acquired observations increases owing to the increased overlap of individual paths of polar orbiting satellites at high attitudes. Also, some areas in high latitudes are simply not covered by EO data. In mountainous areas, the complex and steep terrain is

problematic for SAR image processing.” (Hu et al., 2017) Therefore, combining optical and SAR data to study cold region dynamics is urgently desired.

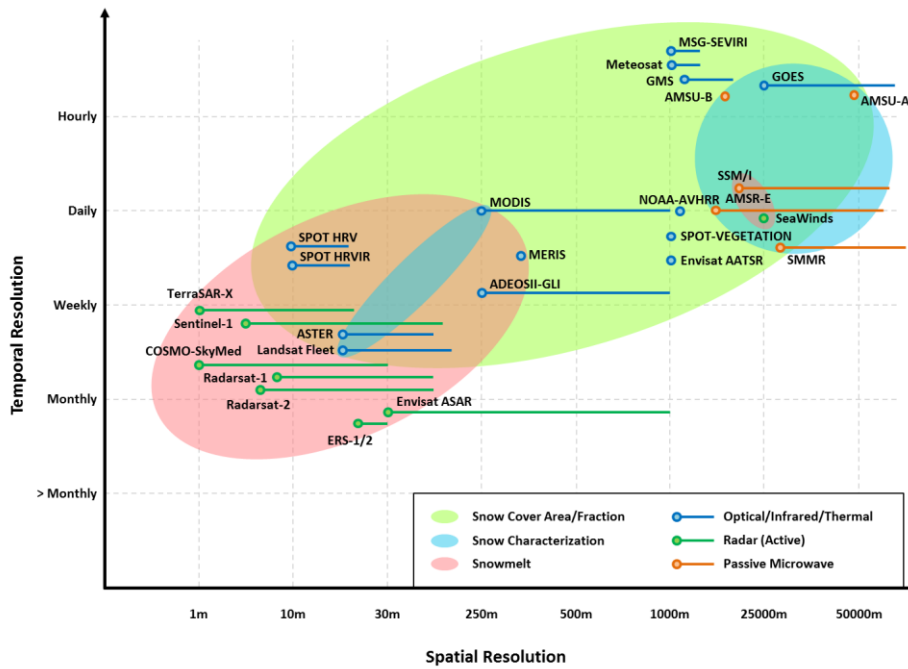


Figure 2-7: Optical and Synthetic Aperture Radar (SAR) sensors for snow-related applications. Modified according to Kuenzer et al. (2014).

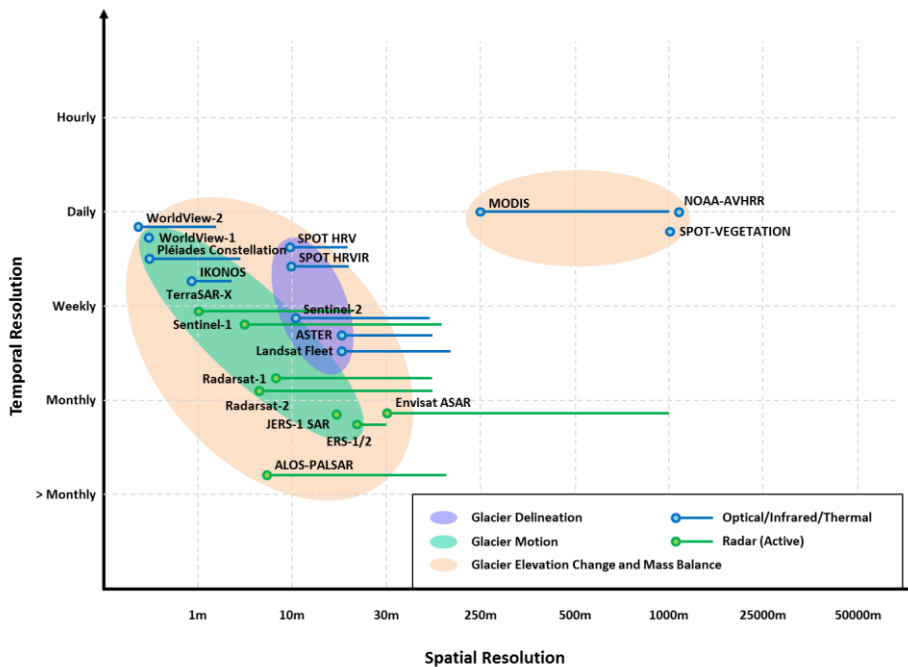


Figure 2-8: Optical, Synthetic Aperture Radar (SAR), and Passive Microwave (PM) sensors for glacier-related applications. Modified according to Kuenzer et al. (2014).

### **2.2.2 Challenges with Regards to Data Availability, Cost and Suitability of Different EO Sensor Types**

The selection criteria of EO data depend on various factors: (1) study area extent, (2) focused time span, (3) required accuracy, (4) data suitability and availability, as well as (5) data accessibility and cost. "Very high-resolution optical and SAR data are generally quite expensive. Optical imagery of medium to coarse resolution (e.g., Landsat, ASTER, MODIS, AVHRR) is available for free and has been frequently used in cold region dynamic analyses. Among these sensors, geostationary sensor provides the highest temporal resolution, which could provide NRT information with regards to the general cold region land surface dynamics. In terms of SAR and LiDAR data, their availability is limited and data gaps often exist (e.g., between the termination of the Envisat-Advanced Synthetic Aperture Radar (Envisat-ASAR) and the launch of Sentinel-1). At a first glance, the day-night all weather operation of SAR sensors makes them particularly intriguing for studying cold regions in Europe. However, ice/snow penetration, the complex topography and related geometric distortion effects in SAR data (layover, foreshortening, SAR shadows etc.) make this data not very suitable for the analyses in complex terrains. Generally, optical data have strong capabilities for retrieving almost all glacier- and snow-related parameters for cold region monitoring. Especially now with the Sentinel fleet in orbit (combination of Landsat with Sentinel-2A/B) the very high revisit time makes these data suitable for monitoring highly dynamic snow cover changes.

The benefits and limitations of optical and SAR data are further summarized in Table 2-3 and Table 2-4 for optical and SAR sensors, respectively. The only spaceborne LiDAR sensor, ICESat-GLAS, provided data during 2003–2009. It has a relatively large footprint (70 m) and ground spacing (170 m) along track, which is problematic for monitoring small glaciers. Nevertheless, the value of ICESat-GLAS observations as a calibration and validation data set should be emphasized. In general, PM data are less influenced by the atmosphere (apart from precipitation clouds); they offer high temporal resolution at global coverage. However, the spatial resolution of PM data is coarse, which makes this data type less suitable for regional studies. In terms of snow monitoring, it remains the major data set used in retrieving SWE. There are difficulties in using PM data to detect: (1) wet snow

cover, and (2) thin snow cover (<5 cm snow) in heavily forested areas. In addition, PM data is strongly influenced by different snow pack physical properties. Underutilization of the recently available sensors is recognized. For example, there are only a few studies using Sentinel-2 for snow monitoring in Europe. For monitoring glaciers in Europe, researchers so far rarely used Sentinel-1, Sentinel-2 and TerraSAR-X data." (Hu et al., 2017) Thanks to ESA's free-accessible Copernicus Program, the EO data availability has been significantly promoted. Yet researches with regards to methodological transferability are still highly desirable, particularly for long-term studies.

### **2.2.3 Challenges with Respect to Method Applicability**

Presently, various methods have been developed and applied to retrieve land surface dynamics in cold regions of Europe at different spatiotemporal scales. "For each topic, some methods have been widely applied, e.g., ratio-image thresholding for glacier delineation and snow cover area mapping, InSAR and offset-tracking for glacier motion monitoring, DEM subtraction for estimating glacier elevation/volumetric change, the "geodetic method" for glacier mass balance estimation, spectral unmixing and modelling for snow cover fraction derivation, empirical relationship for snow water equivalent retrieval, and snow runoff models for snowmelt prediction. Apart from the empirical algorithms developed for snow characterization (limited by dependency on field data), the other algorithms have been widely applied and validated in different regions at different scales. However, the aforementioned methods are usually based on a specific satellite sensor only. Their application may suffer from some sensor-inherent drawbacks. Currently, fully transferable multi-sensor-based methods, which combine the advantages of several sensors, or which have proven their easy transferability in space and time, are still relatively rare.

Because the existing semi-automatic algorithms for glacier delineation are mainly based on optical data, there are significant drawbacks in mapping glacier debris cover, as automatic algorithms cannot distinguish between this debris and the surrounding terrain. The required post manual correction obstructs algorithm automation. Combining novel InSAR coherence based algorithms with such optical-based algorithms thus hold a great potential for a fully automatized glacier delineation procedure. In terms of snow cover area

monitoring, the most well recognized problem is snow cover detection in forested areas, which has a significant influence on the accuracy of snow cover product. Furthermore, the lack of a large-scale reference/validation data set complicates the accuracy assessment for snow cover products.” (Hu et al., 2017) Besides, in addition to areal snow cover information, deriving SWE and SD in a high spatial resolution with high accuracy is urgently required to comprehensively characterize the snow pack.

**Table 2-3:** Benefits and limitations of optical imagery for cold region monitoring. Modified according to Hu et al. (2017).

Aspect	Benefits	Limitation
<b>General</b>	Good data availability and accessibility	No usable data under cloud cover and polar darkness
	Good global spatiotemporal coverage	Relatively few spectral bands to distinguish snow/ice Atmospheric absorption and scattering
<b>Glacier delineation</b>	Fast, robust, semi-automated algorithm	Problematic identification in cases of debris cover
<b>Glacier elevation change</b>	Automated algorithm	High optical contrast is needed
	No snow/ice penetration	Limited number and accessibility of stereo-geometric sensors
<b>Glacier mass balance</b>	Usefulness for building time series	SLA does not always represent ELA
		Albedo only provides relative mass balance
<b>Glacier motion</b>	Long-term historic record	Error in image orthorectification processing and whisk-broom acquisition
<b>Snow Cover Area</b>	Fast, robust, semi-automated algorithm	Confusion between snow and dark targets (e.g., black spruce forest, water bodies)
<b>Snow Cover Fraction</b>	Fast, robust, straightforward algorithm	Proper endmember selection is required
		Limited number of bands in multispectral data
<b>Snow Grain Size &amp; Impurity</b>	High sensitivity	Only for the upper layer of the snow pack
<b>Snow Water Equivalent &amp; Depth</b>	N/A	N/A
<b>Snowmelt</b>	High temporal resolution	Cannot distinguish between wet snow and dry snow

**Table 2-4:** Benefits and limitations of Synthetic Aperture Radar (SAR) imagery for cold region monitoring. Modified according to Hu et al. (2017).

<b>Aspect</b>	<b>Benefits</b>	<b>Limitation</b>
<b>General</b>	Day-night all-weather operation	Snow/ice penetration Complex format and big data size. Propagation effects in ionosphere
<b>Glacier delineation</b>	Debris cover is less problematic	Unable to detect glaciers based on single frequency amplitude/phase image
<b>Glacier elevation change</b>	Very accurate	Coherence requirement (InSAR & D-InSAR) Penetration correction is necessary
<b>Glacier mass balance</b>	N/A	N/A
<b>Glacier motion</b>	Most accurate (D-InSAR) and very accurate for offset-tracking	Need for retained coherence (Coherence tracking and D-InSAR) Only slant-range motion (D-InSAR) Requires large image patches for incoherent intensity tracking
<b>Snow Cover Area</b>	N/A	Only able to detect wet snow
<b>Snow Cover Fraction</b>	N/A	N/A
<b>Snow Grain Size &amp; Impurity</b>	N/A	N/A
<b>Snow Water Equivalent &amp; Depth</b>	Physical model based method	Mostly single frequency sensors
<b>Snowmelt</b>	Can detect wet snow	N/A

## **2.3 The Need and Potential of the Landsat Archive for Long-Term Snow Monitoring in Mountainous Areas**

Previous sections illustrate the long history of EO-based snow observation, including mapping SCA, characterizing snow pack, and monitoring snowmelt processes. Therein, SCA is the most frequently utilized parameter for characterizing long-term snow dynamics using medium-to-coarse spatial resolution EO data. Whereas, precisely deriving long-term snow dynamics under the complex terrain (e.g., mountain areas) based on medium to coarse spatial resolution data is challenging (Severskiy and Zichu, 2000), due to mixed pixels, variable land covers, regional precipitation and temperature patterns, as well as shadowing effects. Thus, EO data providing higher spatial resolution would be intriguing.

Since the launch of Landsat 1 (initially named as the Earth Resources Technology Satellite, ERTS) on July 23, 1972, the Landsat series has been providing optical EO data over four decades. So far, it is the longest uninterrupted operating EO program that is also free-accessible since 2008 (Wulder et al., 2012). The Landsat Archive is, therefore, an invaluable EO dataset for land surface studies. Landsat-based snow topics are still focused by the current (2018–2023) Landsat Science Team. Thanks to the improved geometric and radiometric accuracy, the monitoring of snow has been significantly benefited from the newest Landsat generation (Landsat 8 OLI/TIRS) (Roy et al., 2014). Furthermore, USGS unprecedentedly reorganized the global Landsat 1–5 MSS, Landsat 7 ETM+, Landsat 8 OLI/TIRS, and the majority of Landsat 4–5 TM scenes into the USGS Collection 1 archive in May 2018, which promotes the time series analysis by providing consistently geometrically and radiometrically calibrated and tiered products (USGS/EROS, 2017). Yet Landsat-based snow studies were rarely carried out to a time series level of more than 30-years (Hu et al., 2017). In Europe, only a limit number of Landsat-based snow studies exist, which assess snow cover dynamics in European mountains for more than 30 years. Even though Landsat continuously orbits the Earth since the 1970s, observations are not available for the whole time series due to mission constraints, ground infrastructure and operation efficiency (Arvidson et al., 2006). The data gaps caused by technical and management problems, the near two-week revisit time interval, and cloud cover pose challenges when it comes to the



analysis of the highly variable snow cover dynamics from Landsat, which might ultimately explain the lack of existing long-term time series studies.

Despite the aforementioned challenges and limitations, one of the major objectives of this study is hence to investigate the potential of Landsat-derived time series in assessing snow cover dynamics in mountain areas within Europe. The following aspects have been analysed for this purpose: (1) the spatiotemporal pattern of Landsat Collection 1 Level 1 Precision and Terrain (L1TP) corrected products across Europe, in particular the mountain areas; (2) the frequency of cloud cover of the Landsat Collection 1 L1TP dataset in Europe. Due to the signal saturation of Landsat MSS data over snow and ice (Altena and Kääb, 2017), the absence of the thermal band and the incompleteness of the Landsat MSS Collection 1 reprocessing, Landsat 1–5 MSS data have been excluded from this thesis. Afterwards, based on the Landsat availability, a framework will be developed for analysing long-term snow dynamics in mountain areas using 35-year Landsat time series.



## CHAPTER 3

### 3 Study Areas

#### 3.1 Location and Topography

In this thesis, the major European mountains are first analysed with regards to the Landsat data availability. The selected catchments are located between  $41.45^{\circ}$  –  $49.16^{\circ}$  N and  $0.10^{\circ}$  –  $24.92^{\circ}$  E at the mid-latitude range of Europe, spanning 11 countries (Andorra, Austria, Switzerland, Germany, Spain, France, Hungary, Italy, Romania, Slovakia and Ukraine). In total, these cover a territory of 74425.18 km<sup>2</sup>. Among the selected catchments, the largest catchment is Ariege in the Pyrenees covering a territory of approximately 13681.63 km<sup>2</sup>. The smallest catchment is Uzh in the Carpathian Mountains, which cover a territory of approximately 2202.73 km<sup>2</sup>. The major rivers in each catchment are: the Danube (Salzach, Tysa, and Uzh), the Ebro (Serge), the Gironde (Ariege), the Po (Adda), the Rhine (Alphenrhein), the Rhône (Drac), the Tagliamento (Tagliamento), and the Var (Var). The majority of the study areas are snow-fed basins. Figure 3-1 and Figure 3-2 show the geographical extent of each study area and their topographic information. The elevation of the investigated catchments ranges from –5 m to 3889 m. Except for the investigated Carpathian catchments and Alpine catchment Tagliamento, the maximum elevation ranges of the other investigated catchments are above 2900 m. The catchment of lowest maximum elevation is the Carpathian catchment Uzh, which is below 1500 m. Figure 3-2 illustrates the detailed elevation information indicating the proportion of different elevation ranges. Among the study areas, catchments Ariege, Tagliamento, Uzh and Tysa cover the least high elevation zones. For each investigated catchment, the slope information is summarized in Table 3-1. The mean slopes of the study areas range from  $7.51^{\circ}$  to  $22.36^{\circ}$ . In general, the slopes of the Carpathian catchments are lower than the rest of the catchments.

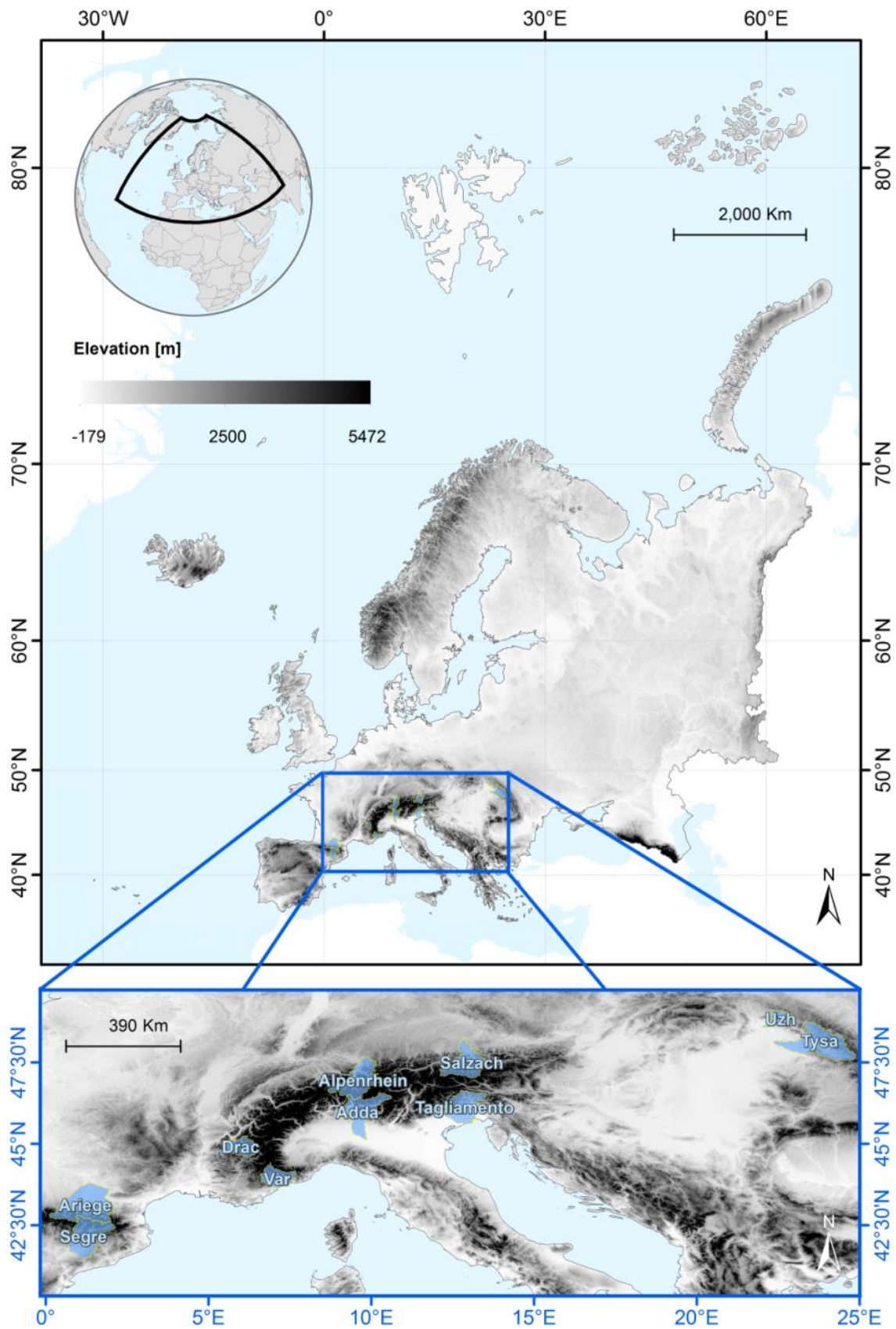


**Figure 3-1:** Location of the study areas, and their elevation information. Data Source: Tachikawa et al. (2011).

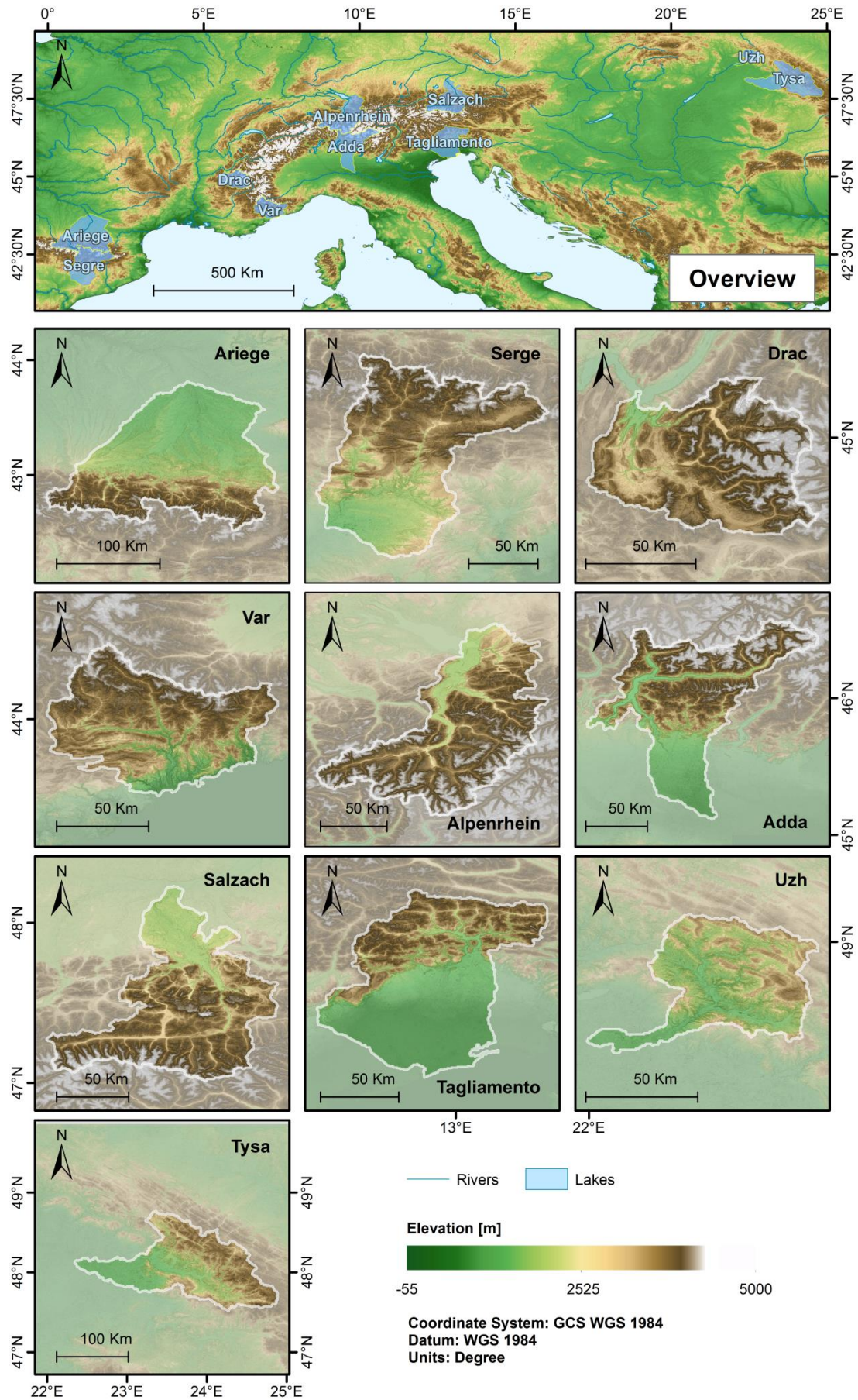


Figure 3-2: Topographic characteristics of each study area. Data Source: Tachikawa et al. (2011).

**Table 3-1:** Overview of the investigated catchments.

Study area	Country <sup>1</sup>	River	Area [km <sup>2</sup> ]	Elevation [m]			Slope [degree]		
				min	mean	max	min	mean	max
<b>Adda</b>	CH, IT	Po	7855.44	-5.00	1150.66	3844.00	0.00	18.94	88.01
<b>Alpenrhein</b>	DE, AT, CH	Rhine	7785.03	242.00	1602.23	3289.00	0.00	20.19	80.87
<b>Ariege</b>	AD,FR, ES	Gironde	13681.63	43.00	715.17	3213.00	0.00	12.64	73.13
<b>Drac</b>	FR	Rhône	3570.83	192.00	1613.51	3889.00	0.00	22.36	85.57
<b>Salzach</b>	DE, AT	Danube	6770.63	336.00	1251.68	3540.00	0.00	18.50	86.42
<b>Serge</b>	AD,FR, ES	Ebro	9148.34	25.00	1125.57	3103.00	0.00	15.04	72.99
<b>Tagliamento</b>	IT	Tagliamento	7051.67	2.00	529.06	2529.00	0.00	12.84	85.68
<b>Tysa</b>	UA,RO, HU	Danube	12066.92	39.00	667.17	2272.00	0.00	13.30	66.62
<b>Uzh</b>	SK, UA	Danube	2202.73	58.00	250.91	1487.00	0.00	7.51	55.62
<b>Var</b>	FR	Var	4291.96	1.00	1181.12	2966.00	0.00	21.67	77.71

<sup>1</sup> Country Abbreviations: AD: Andorra, AT: Austria, CH: Switzerland, DE: Germany, ES: Spain, FR: France, HU: Hungary, IT: Italy, RO: Romania, SK: Slovakia, UA: Ukraine.

## 3.2 Climatology

Köppen-Geiger climate classification is the most frequently used climate classification map, which is provided by Kottek et al. (2006), Rubel et al. (2017), and Rubel and Kottek (2010) with a spatial resolution of 0.5 degree (30 arc minutes) representative for the 50-year period 1951–2000. Figure 3-3 shows the Köppen-Geiger climate classification map for the investigated catchments, which mainly include Bsk (arid, steppe, and cold), Cfa (warm temperature, no dry season, hot summer, and cold winter), Cfb (warm temperature, no dry season, warm summer, and cold winter), Cfc (warm temperature, no dry season, cool summer, and cold winter), Csa (warm temperature, dry summer, hot summer, and cold winter), Csb (warm temperature, dry summer, warm summer, and cold winter), and Dfc (boreal, no dry season, cool summer, and cold winter) in the Pyrenean catchments, Cfa, Cfb, Cfc, Dfc, Dfb (boreal, no dry season, warm summer, and cold winter), and ET (Alpine Tundra) in the Alpine catchments, and Cfb, Dfb and Dfc in the Carpathian catchments. To characterize the detailed feature of temperature and precipitation in the investigated catchments, 10 stations data from NOAA-GHCN are displayed in Figure 3-4.

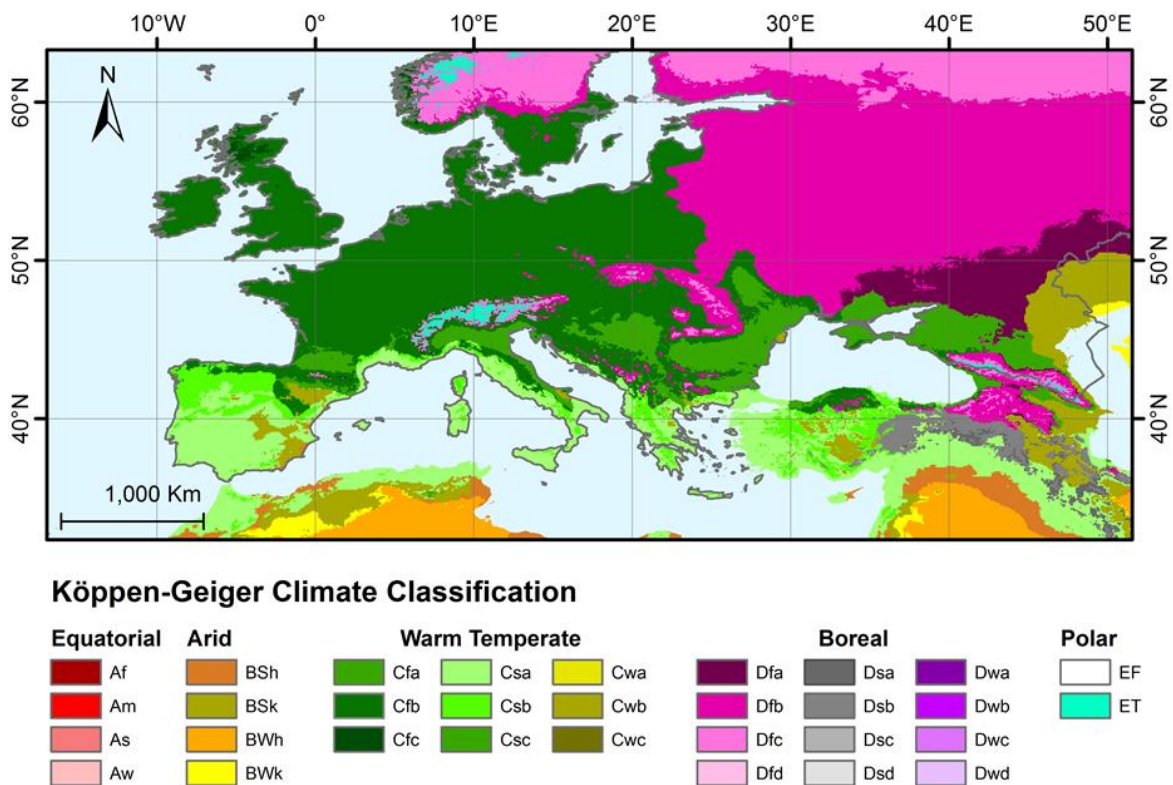


**Figure 3-3:** Climate classes of the study areas according to Köppen-Geiger climate classification. Data Source: Rubel and Kottek (2010).

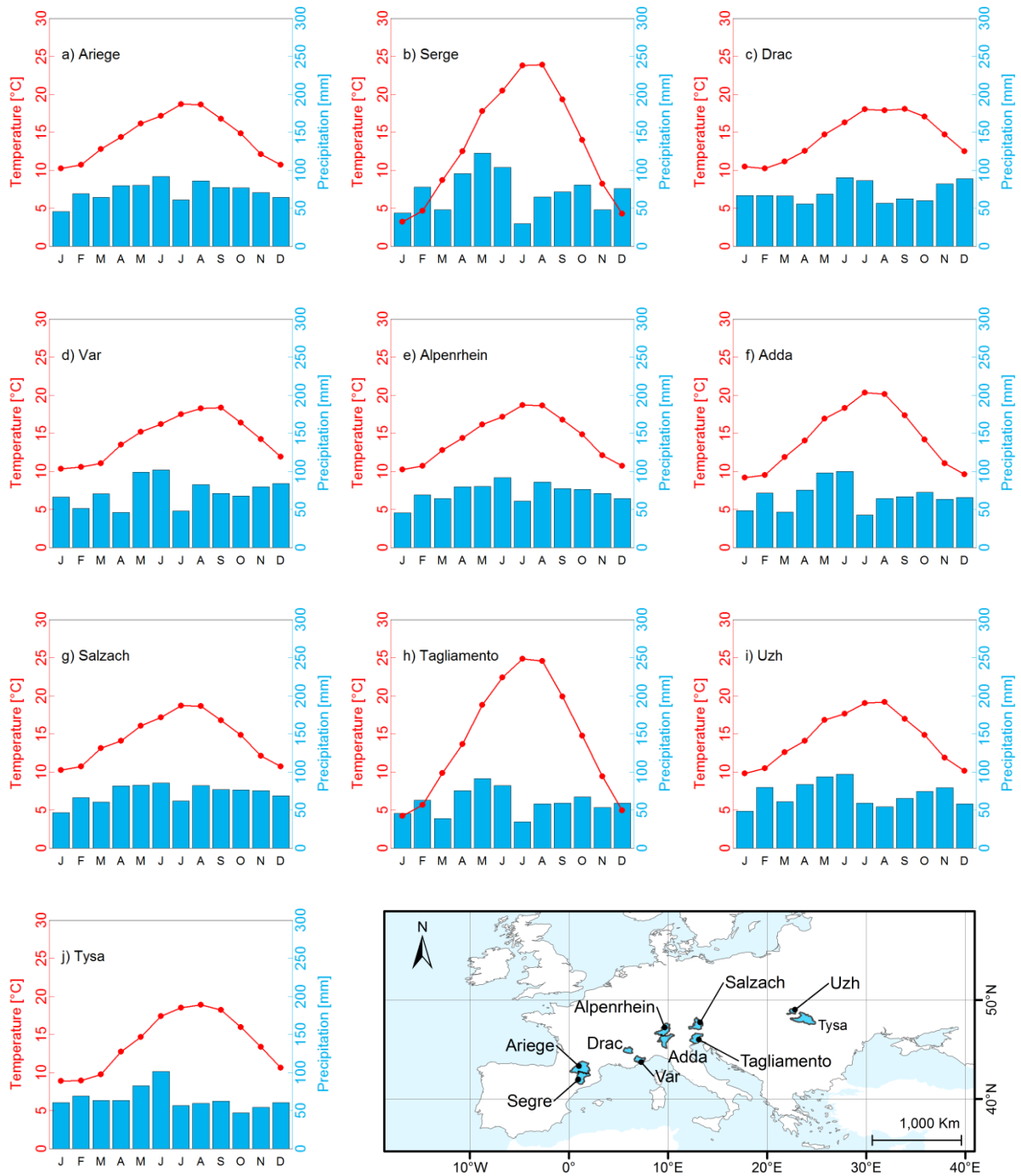


**Figure 3-4:** Long-time mean annual temperature climate charts (1984–2018) for the meteorological stations near/within the investigated catchments: a) Ariège: FRE00106205, b) Serge: SPE00156585, c) Drac: FRM00007591, d) Var: FRM00007690, e) Alpenrhein: GME00128830, f) Adda: ITE00100554; g) Salzach: AU000006306, h) Tagliamento: ITM00016045, i) Uzh: UPM00033631, j) Tysa: UPM00033647. Data Source: Menne et al. (2012).



### 3.3 Hydrology

Annual runoff in the selected catchments is mainly snowmelt-dominated (Barnett et al., 2005). However, in the context of warming climate, (Blöschl et al., 2017) found that the magnitude and timing of river floods are shifting (Figure 3-5). However, such shift is not consistent in large-scale. It is noteworthy that in the three selected mountain areas (the Pyrenees, the Alps, and the Carpathian Mountains), the floods mainly occur during the end of ablation seasons with a trend towards early dates. Furthermore, for each catchment, daily mean and peak runoff from 1984 to 2018 have been calculated and demonstrated in Figure 3-6. It has been shown that in the Alpine catchments Drac, Alpenrhein, and Salzach, high average daily runoff has been observed in March and April. Also, regarding the daily peak runoff, the pattern is similar as the daily mean runoff, while the high daily peak runoff values are more obvious in the Carpathian catchment than the daily mean runoff.

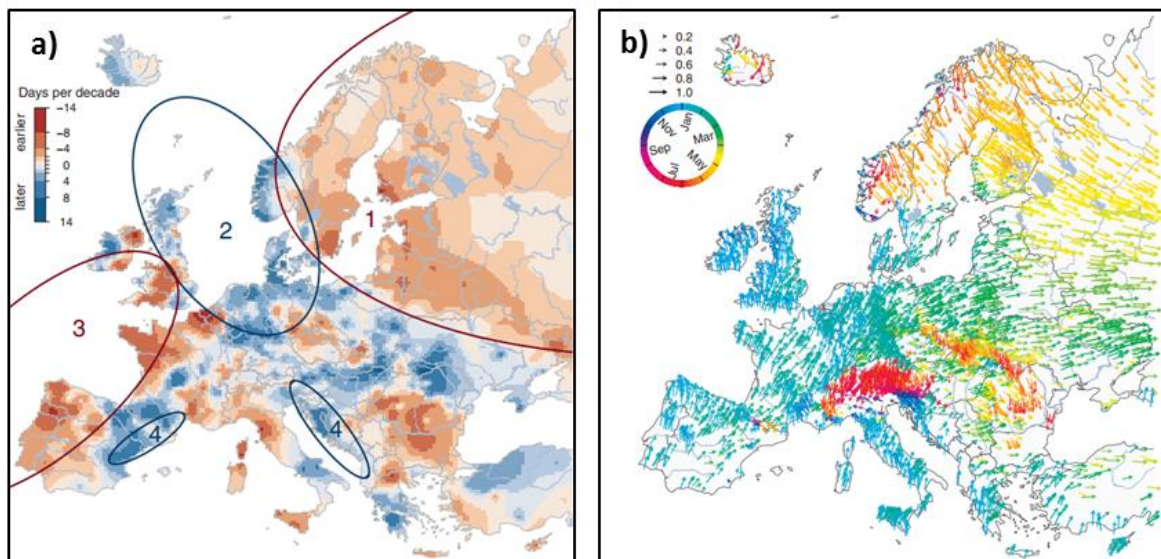


**Figure 3-5:** Observed trends of river flood timing in Europe (left) and observed average timing of river floods in Europe (right) between 1960 and 2010. On the left, the colour scale indicates earlier or later floods in days  $\cdot$  a<sup>-1</sup>. The Europe is divided into four regions with distinct drivers: (1) Northeastern Europe (earlier snowmelt); (2) North Sea (later winter storms); (3) Western Europe along the Atlantic coast (earlier soil moisture maximum); and (4) parts of the Mediterranean coast (stronger Atlantic influence in winter). On the right, each arrow represents one hydrometric station. Colour and arrow direction indicate the average timing of floods, and lengths of the arrows indicate the concentration of floods within a year. Modified according to Blöschl et al. (2017).

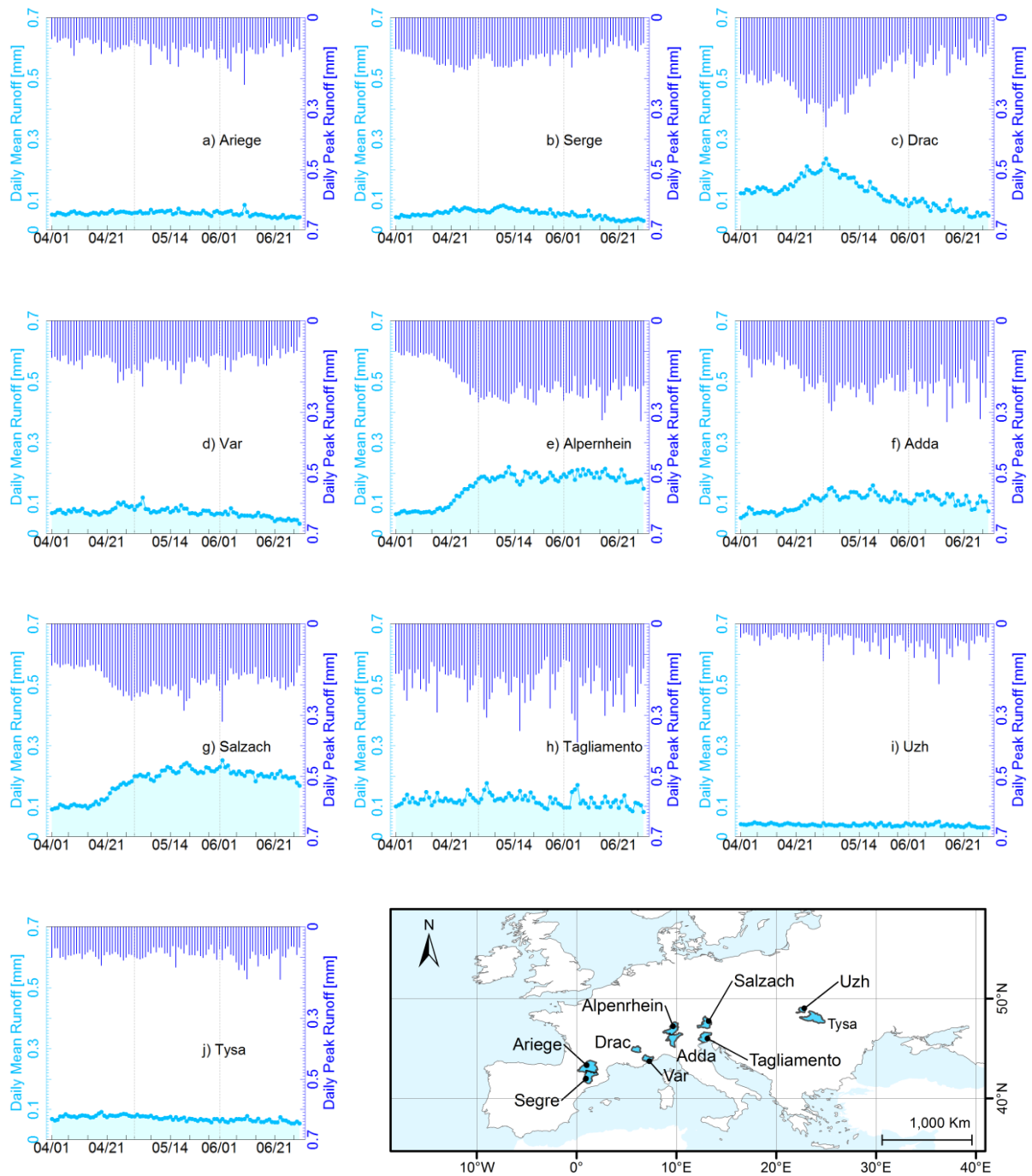


**Figure 3-6:** Runoff characteristics during the ablation season (from April to June, 1984–2018) of each investigated study area. Data Source: C3S (2017).

### 3.4 Land Cover

To derive the land cover information in the selected catchments, the European Space Agency-Climate Change Initiative-Land Cover (ESA-CCI-LC) product version 1.4 is used. ESA-CCI-LC is produced by combining EO-based surface reflectance and ground-truth observations at 300 m spatial resolution (Defourny et al., 2016). The validation against the GlobCover 2009 (Arino et al., 2012) shows that the ESA-CCI-LS product has an overall accuracy of 73.2% (Defourny et al., 2016). The ESA-CCI-LS 2015 product (Figure 3-7) shows the major land cover (> 10%) types in:

- **Ariege** (the Pyrenees) are *Herbaceous cover* (35.29%), *Tree cover, broadleaved, deciduous, closed to open (>15%)* (21.53%), and *Grassland* (12.70%);
- **Serge** (the Pyrenees) are *Tree cover, needleleaved, evergreen, closed to open (>15%)* (38.82%), and *Herbaceous cover* (18.40%);
- **Drac** (the Alps) are *Grassland* (25.78%), and *Tree cover, needleleaved, evergreen, closed to open (>15%)* (20.77%);
- **Var** (the Alps) are *Tree cover, needleleaved, evergreen, closed to open (>15%)* (45.44%), and *Grassland* (19.86%);
- **Alpenrhein** (the Alps) are *Grassland* (39.01%), and *Tree cover, needleleaved, evergreen, closed to open (>15%)* (23.59%);
- **Adda** (the Alps) are *Tree cover, needleleaved, evergreen, closed to open (>15%)* (16.45%), *Grassland* (15.50%), *Herbaceous cover* (13.63%), and *Tree cover, broadleaved, deciduous, closed to open (>15%)* (12.40%);
- **Salzach** (the Alps) are *Tree cover, needleleaved, evergreen, closed to open (>15%)* (31.28%), *Grassland* (30.27%), and *Tree cover, mixed leaf type (broadleaved and needleleaved)* (11.79%);
- **Tagliamento** (the Alps) are *Herbaceous cover* (36.46%), *Tree cover, broadleaved, deciduous, closed to open (>15%)* (14.54%), and *Tree cover, mixed leaf type (broadleaved and needleleaved)* (10.68);
- **Uzh** (the Carpathian Mountains) is *Tree cover, broadleaved, deciduous, closed to open (>15%)* (75.08%);
- **Tysa** (the Carpathian Mountains) are *Tree cover, broadleaved, deciduous, closed to open (>15%)* (34.63%), *Cropland, rainfed* (16.76%), and *Tree cover, needleleaved, evergreen, closed to open (>15%)* (12.78%).

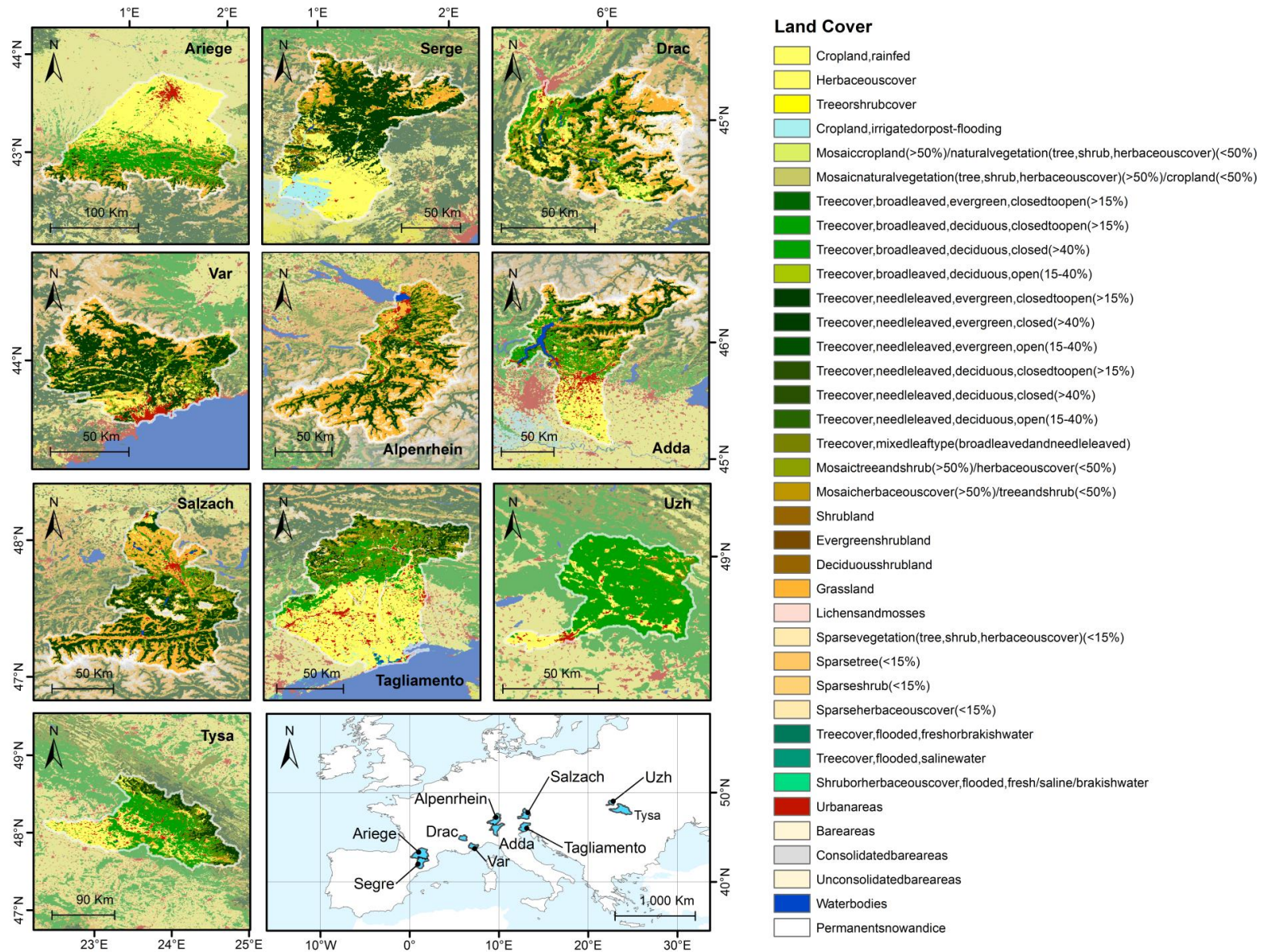
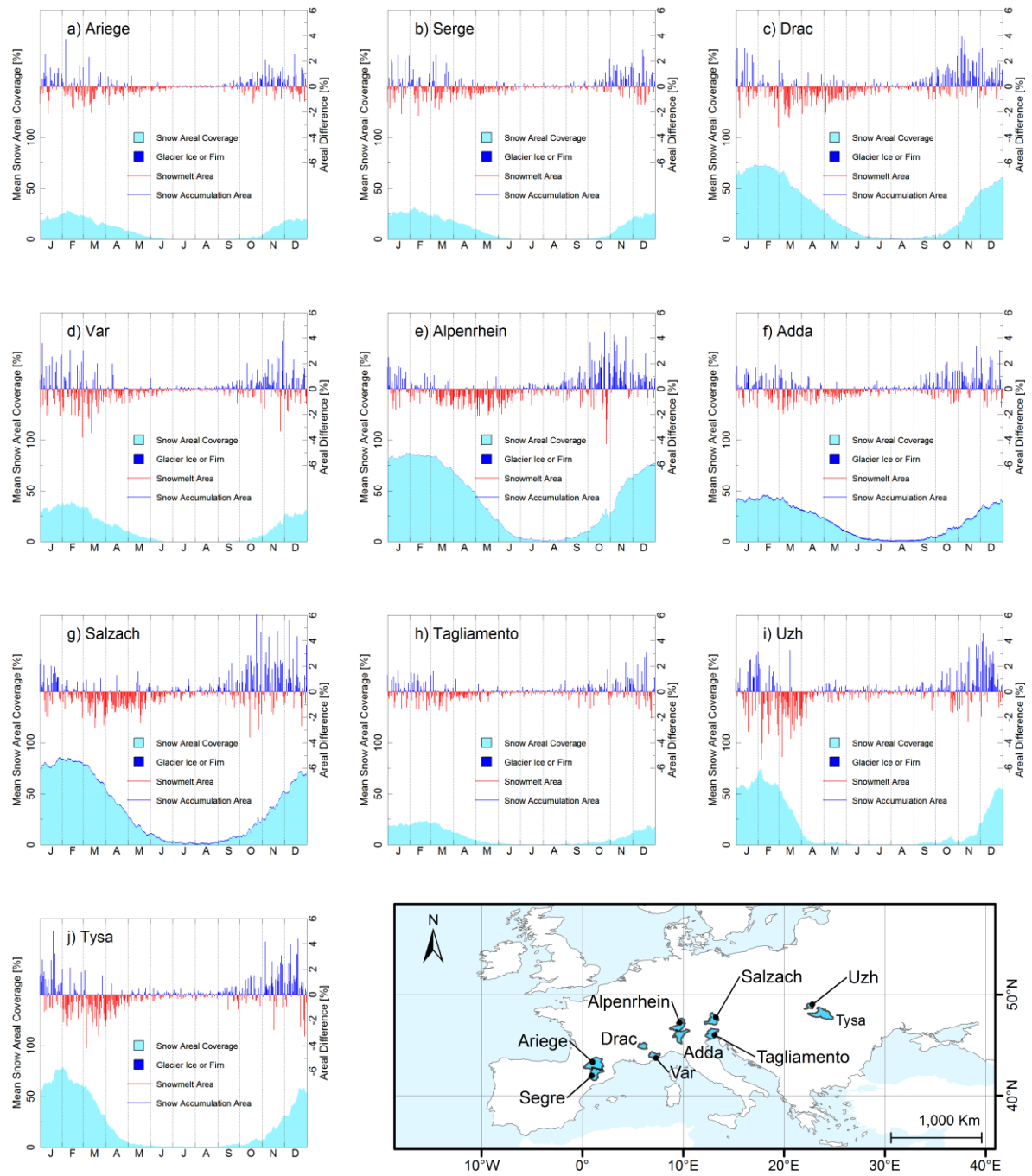


Figure 3-7: Land cover information of each study area. Data Source: Defourny et al. (2016).

### 3.5 Snow Phenology

The Global Snow Pack (GSP) (Dietz et al., 2015) is based on the daily MODIS snow cover product MOD10A1 and consists of daily, cloud-free information about the global snow cover extent at 500 m resolution. Taking the advantage of dense and gapless snow coverage information GSP, Snow Depletion Curves (SDCs) can be calculated accordingly. The SDCs illustrate the variation of mean snow cover area (in percentage) through a whole year during the period 2000–2018. On the top of each SDC plot Figure 3-8, the red/blue bars illustrate the average SCA differences compared to the previous day. A red bar (negative value) shows that the snow coverage is shrinking. Vice versa, a blue bar (positive value) shows that the snow coverage is increasing i.e. there is a snowfall event. Given that GSP is a daily SCA product, it is possible to estimate the glaciated and firn-covered areas by detecting the pixels covered by snow/ice for more than 90% of the days from 2000 to 2018. The dark blue areas in the SDCs illustrate firn and/or glacier ice coverage.

Given the possible intermediate snowfall events within the near-two-week Landsat revisit time, it is difficult to retrieve snow distribution dynamics throughout the whole year using the Landsat Archive (Hall, 2012). In this regard, it is necessary to determine the end of the ablation season, as it provides a good balance among the occurrence of intermediate snowfall events, persistence of observable snow, exposure of glacier ice and/or firn, and availability of cloudless scenes. Seen from the Figure 3-8, the selection of April to June, fulfils the aforementioned requirements. However, in the Carpathian catchments Uzh and Tysa, it is more beneficial to include the snowline elevation information in March, as the most of the snow depletion are occurred in March. However, the frequent occurrence of snowfall events during March to June should be taken into consideration when interpreting the snowline elevation results.



**Figure 3-8:** Characteristics of the snow phenology (2000–2018) in each study area. Data Source: Dietz et al. (2015).

### 3.6 Socioeconomic Situation

In the investigated catchments, the majority of them are snow-fed. In this regard, the snowmelt is strongly associated with the water abstraction and consumption. Water resources are important in Europe. EEA (2018) reported that near 30 % of the total European habitants was exposed to water scarcity conditions, which is 10% more than that in 2014. Geographically, these populations are mainly distributed in the densely populated European urban areas, agriculture-dominated areas of southern Europe and Mediterranean islands. Water scarcity is mainly caused by climate change and water demand (EEA, 2018). Figure 3-9 summarizes the main freshwater abstraction in European Environment Agency (EEA) member and cooperating countries in 2015. It shows the rivers are the dominant sources of freshwater abstraction (65%) in these countries. The water used by economic sectors of those countries in 2015 is further demonstrated in Figure 3-9. Therein, agriculture, forestry and fishing are the main water economic sectors, which take up to 40.4% of the water use from January to September.

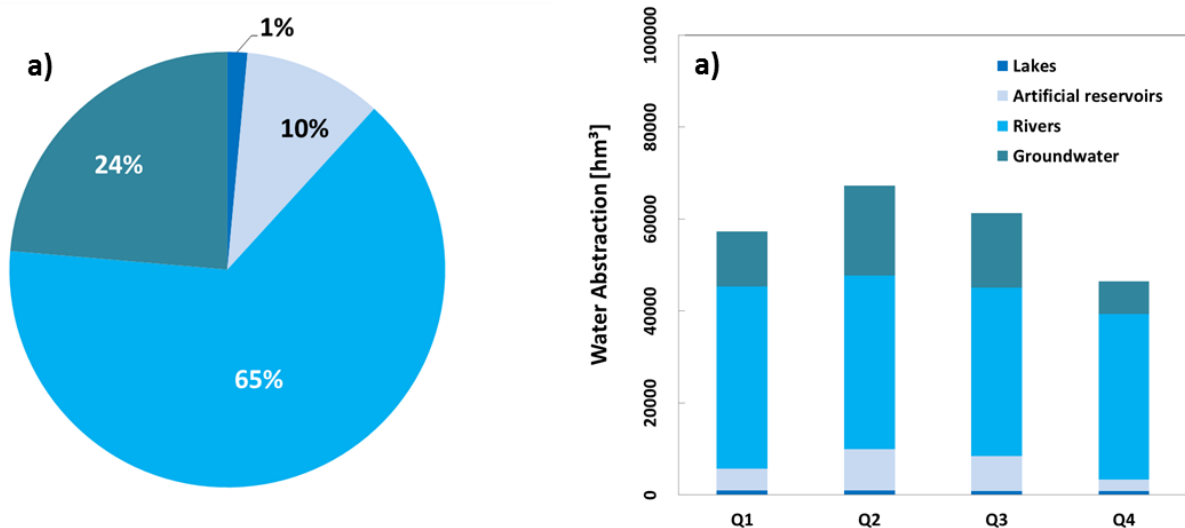


**Figure 3-9:** Freshwater abstraction by source in 2015. The pie chart shows the annual data, for the year 2015, for water abstraction by source at the European level. The quarterly values have been used to show the development of seasonal water abstraction by source. Q1: January to March, Q2: April to June, Q3: July to September, and Q4: October to December, in European Environment Agency (EEA) member countries: Austria, Belgium, Bulgaria, Croatia, Czech Republic, Denmark, Estonia, Finland, Germany, Greece, Hungary, Ireland, Italy, Latvia, Lithuania, Luxembourg, Malta, Netherlands, Norway, Poland, Romania, Slovakia, Slovenia, Spain, Sweden, Switzerland, United Kingdom and Cooperating countries: Albania, Montenegro, Serbia, the Former Yugoslav Republic of Macedonia. Source: EEA (2018).

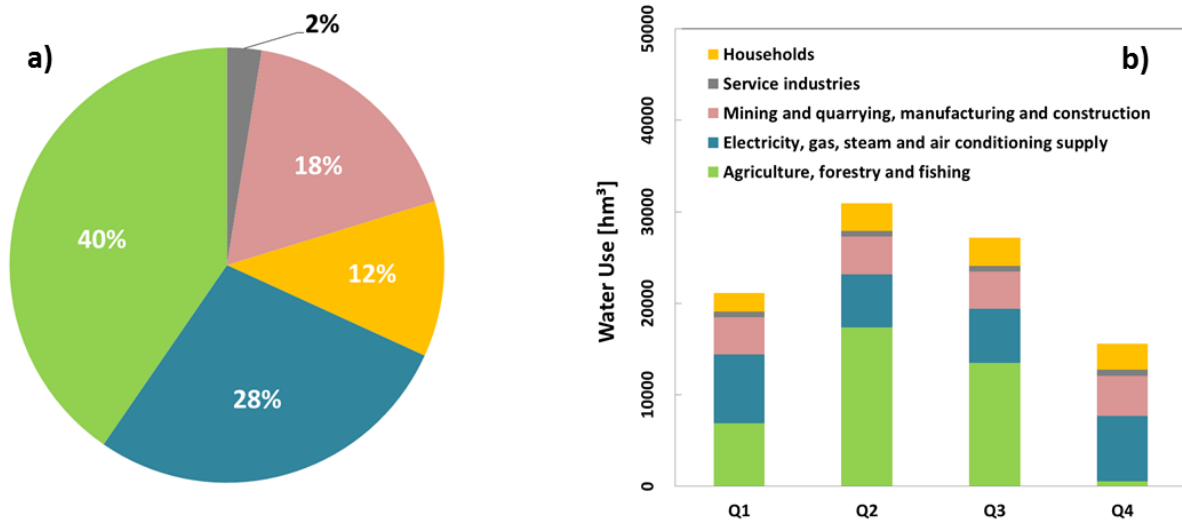


**Figure 3-10:** Water use by economic sectors in 2015. For the pie chart, the data series are calculated annually for 2015 of water abstraction by sector at the European level. The quarterly values have been used to show the development of seasonal water use by sectors in Europe. Economic sectors were identified according to the Statistical Classification of Economic Activities in the European (NACE) classes. Q1: January to March, Q2: April to June, Q3: July to September, and Q4: October to December. In European Environment Agency (EEA) member countries: Austria, Belgium, Bulgaria, Croatia, Czech Republic, Denmark, Estonia, Finland, Germany, Greece, Hungary, Ireland, Italy, Latvia, Lithuania, Luxembourg, Malta, Netherlands, Norway, Poland, Romania, Slovakia, Slovenia, Spain, Sweden, Switzerland, United Kingdom and Cooperating countries: Albania, Montenegro, Serbia, the Former Yugoslav Republic of Macedonia. Source: EEA (2018).

Since 1990s, efforts in development in water conveyancing, efficiency gains in water use and socioeconomic transformations have resulted in over 9% reduction in total water abstraction in Europe (Figure 3-10). Meanwhile, in western and southern Europe, water abstraction for cooling in electricity generation, as well as for households in southern Europe has been observed slightly increased (EEA, 2018). Due to the abandonment of old industrial installations and agricultural areas, approximately 50% water abstraction reduction has been observed in eastern Europe until 2010s (Alcantara et al, 2013; Hartvigsen, 2013). Also, Figure 3-10 demonstrates around 52% increase in the gross value added from all economic sectors from 2000 to 2015. EEA (2018) pointed out the absolute decoupling in the EU economy. The observed absolute decoupling between water abstraction and gross value added generated from all economic sectors at basic price would also explain the decrease in water abstraction (EEA, 2018).



Regarding the population density, Figure 3-11 shows that densely populated cities are located within and/or near to the investigated catchments. For instance, Toulouse is located in the Pyrenean catchment Ariège, Barcelona is located near the Pyrenean catchment Serre, and Milano is near to the Alpine catchment Adda. As water demand is a key factor with regards to water scarcity, which is largely influenced by population and related economic activities, the study of snowmelt and runoff during the ablation seasons therein can provide valuable information to better understand the local impacts of climate change. It can therefore contribute to regional and local adaptation-strategies making in relation to water resource management.

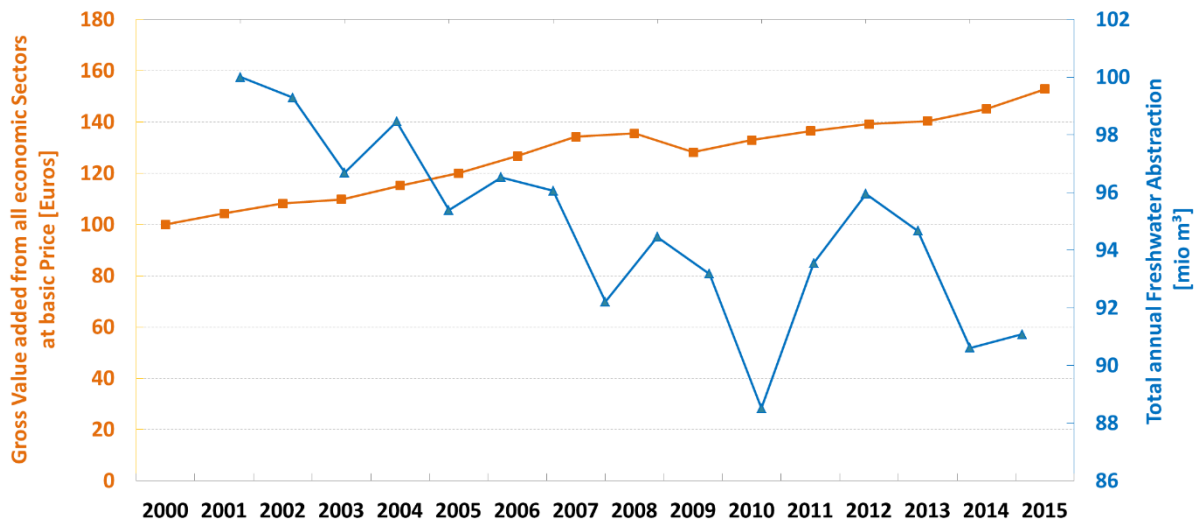


**Figure 3-11:** Gross value added from all economic sectors and total water abstraction in the European Union (EU)-28 (2000 = index 100). Time series cover the period of 1990–2015. The comparison between water abstraction and gross value added has been made based on gross value added at basic price in euros for the EU-28. Source: EEA (2018).

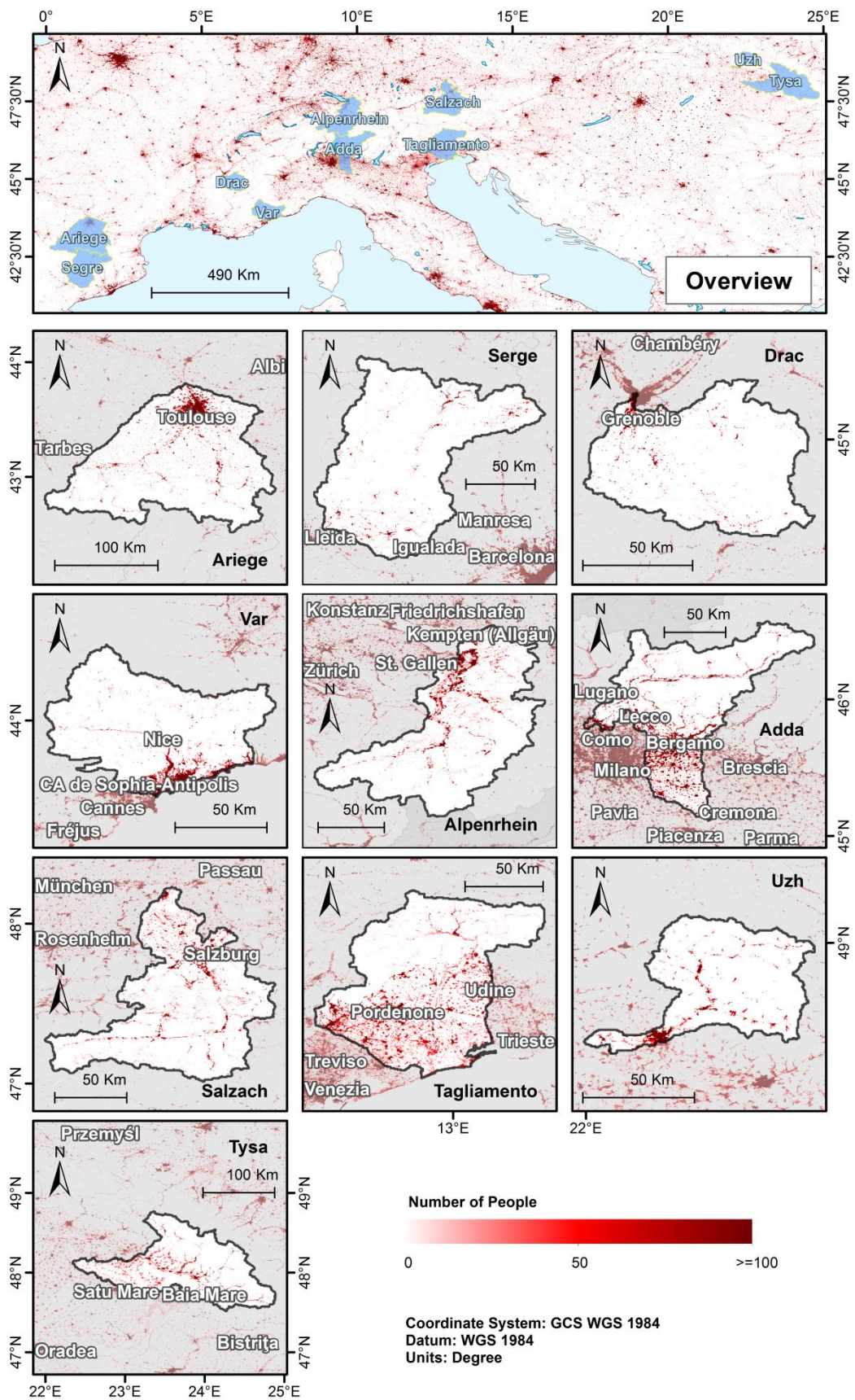


**Figure 3-12:** Population distribution of each study area in 2011. Data Source: GEOSTAT (2011).

## CHAPTER 4

### 4 Data

This chapter outlines the multiple data sources employed for the snow dynamic assessment in European mountains. The major data sources include satellite imagery, Digital Elevation Model (DEM), climate reanalyses data, and in-situ measurements. The details are provided in the following sections, together with the description of the employed auxiliary datasets.

#### 4.1 Satellite Imagery

In this thesis, three (semi-) high resolution and free-of-charge optical datasets are utilized, including (1) Landsat Thematic Mapper (TM), Enhanced Thematic Mapper Plus (ETM+), Operational Land Imager/ Thermal Infrared Sensor (OLI/TIRS) between 1984 and 2018; (2) Advanced Spaceborne Thermal Emission and Reflection Radiometer (ASTER) between 2000 and 2007, and (3) Sentinel-2A/2B Multispectral Instrument (MSI) between 2015 and 2018. The comparison of the wavelength among the applied EO sensors is shown in Figure 4-1. As the ASTER/SWIR sensor defected in late April, 2008, and SWIR information is important for detecting snow, the ASTER acquisitions after April 2008 are not adapted. To guarantee the image quality, only radiometrically calibrated and orthorectified Landsat, ASTER, and Sentinel-2 products are utilized, which include Landsat L1TP, AST\_L1T, and Sentinel-2 L1C. In the context of snow detection, green, red, NIR, and SWIR bands are the most frequently utilized bands. Also, the thermal bands provide useful information in distinguishing snow from other bright but warm surfaces. Thus, thermal bands are also employed in this thesis, once they are available. The band configurations regarding the employed bands of the selected EO sensors are displayed in Table 4-1.

**Table 4-1:** Bands characteristics of the selected Earth Observation (EO) sensors in this study: Landsat Thematic Mapper (TM), Enhanced Thematic Mapper Plus (ETM+), Operational Land Imager/Thermal Infrared Sensor (OLI/TIRS), Advanced Spaceborne Thermal Emission and Reflection Radiometer (ASTER), and Sentinel-2 (S2). CW stands for central wavelength in  $\mu\text{m}$ , and SR stands for spatial resolution in meter.

Sensor	Landsat			Sentinel-2			ASTER					
	TM/ETM+	CW	SR	OLI/TIRS	CW	SR	S2	CW	SR	ASTER	CW	SR
Green	2	0.56	30	3	0.56	30	3	0.56	10	1	0.56	15
Red	3	0.66	30	4	0.66	30	4	0.67	10	2	0.66	15
NIR	4	0.83	30	5	0.87	30	8a	0.83	20	3N	0.82	15
SWIR	5	1.65	30	6	1.61	3	11	1.61	20	4	1.65	30
TIRS	6	11.4	60/120*	10	10.9	100*				13	10.6	90**

\* TM Band 6, ETM+ Band 6, and TIRS Band 10/11 are acquired at 120, 60, and 100 meters resolution, respectively, but products are resampled to 30 meters pixels.

\*\* ASTER thermal band 13 is acquired at 90 meters resolution. The image is resampled to 30 meters pixels to guarantee data consistency.

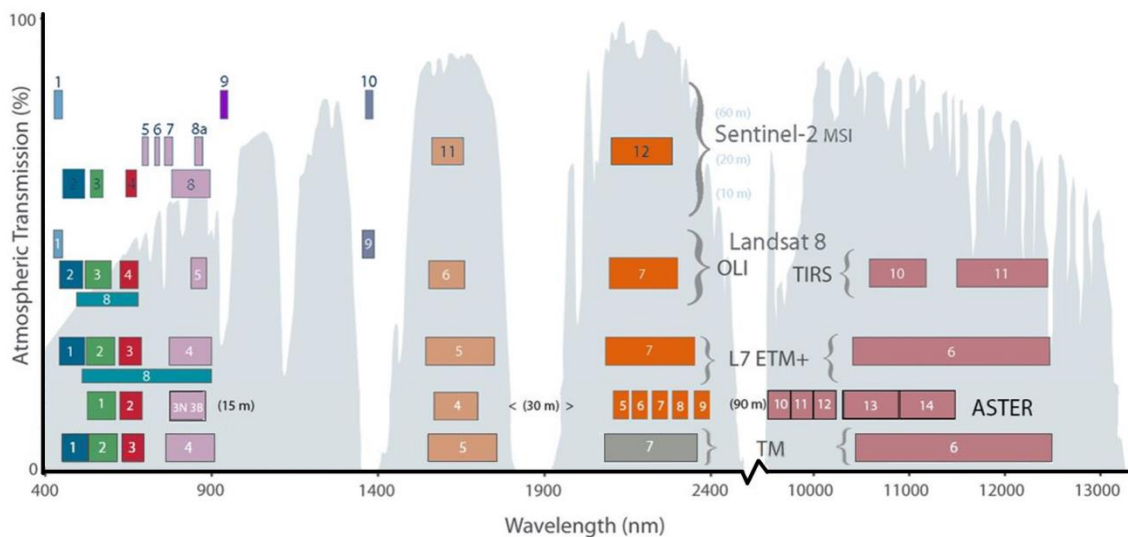


**Figure 4-1:** Bandpass wavelengths for the employed sensors in this thesis, i.e. Landsat 4–5 Thematic Mapper (TM), Landsat 7 Enhanced Thematic Mapper Plus (ETM+), Landsat 8 Operational Land Imager/Thermal Infrared Sensor (OLI/ TIRS) sensor, Advanced Spaceborne Thermal Emission and Reflection Radiometer (ASTER), and Sentinel-2. Modified according to USGS (2015).

### 4.1.1 Landsat Data

For more than four-decade, the Landsat series of satellites have the longest uninterrupted operation history, providing temporal record of the land surface and its modification. As of January 1st 2015, Wulder et al. (2016) reported that the volume of Landsat data already exceeds 5.5 million archived at USGS. All these images are categorized using a spatial referencing system (i.e., Worldwide Reference System, WRS), which partitions Landsat images into approximately  $185 \times 185$  km<sup>2</sup> squares (known as scenes). Presently, approximately 1200 scenes are being acquired by Landsat 7 and Landsat 8 in orbit (Wulder et al., 2016). In order to support the long-term data analyses, the USGS reorganized the global Landsat 1–5 MSS, the majority of Landsat 4–5 TM, Landsat 7 ETM+, and Landsat 8 OLI/TIRS into Collection 1 structure. The significant change in management of the USGS Landsat Archive not only varies metadata and file names, but also ensures the quality consistency through time and across different Landsat instruments. Landsat Collection 1 constitutes of Landsat 1–8 Level-1 products. These Landsat Level-1 products are of three processing levels, i.e., Level 1 Precision and Terrain (L1TP), Systematic Terrain Correction (L1GT), and Systematic Correction (L1GS):

- **L1TP scenes** are of the highest quality, and thus suitable for pixel-based time series analyses. L1TP images are radiometrically calibrated and orthorectified using Global Land Survey 2000 Ground Control Points (GLS2000 GCPs) and a Digital Elevation Model (DEM) to correct elevation displacement;
- **L1GT scenes** are radiometrically calibrated. Geometric corrections are applied only based on on-board spacecraft data, and elevation displacement is corrected using DEM data;
- **L1GS scenes** are radiometrically calibrated. However, geometric corrections are only applied systematically using on-board spacecraft ephemeris data.

Together with data quality control, Level-1 data of different processing levels are assessed and categorized into three tiers, i.e. Tier 1, Tier 2 and Real-Time (RT):

- **Tier 1 scenes** consist of the L1TP products, whose geo-registration is consistent and within prescribed image-to-image tolerances of no larger than 12-meter radial Root Mean Square Error (RMSE).

- **Tier 2 scenes** include all L1GT and L1GS data, and the L1TP data that do not meet the geo-registration constraint.
- **Real-Time scenes** are newly-acquired Landsat 7 ETM+ and Landsat 8 OLI/TIRS data, which are later transitioned to either Tier 1 or Tier 2 after 14–16 days (Landsat 8) or about 26 days (Landsat 7).

Among the three tiers above, Tier 1 is of the highest available data quality, and hence the Tier 1 data are regarded most suitable for time series analyses. For the detailed information about Collection 1 Level 1 products, readers should refer to USGS/EROS (2017).

The detailed information in relation to the spectral configuration of each Landsat sensor is summarized in Table 4-2. In this thesis, due to the signal saturation of Landsat 1–5 MSS data over snow and ice (Altena and Kääh, 2017) and the absence of the thermal band, Landsat 1–5 MSS data have been excluded from this study. The Landsat Archive is the main dataset for this thesis. Therefore, the spatiotemporal distribution of Landsat TM, ETM+, and OLI/TIRS Collection 1 data archived at USGS (USGS/EROS, 2017) are firstly analysed to maintain an overview of the Landsat data availability across the whole Europe. Once the density of time series is analysed, images are atmospherically and topographically corrected, and then used for snow classification within the selection study areas.

**Table 4-2:** Bands characteristics of Landsat Thematic Mapper (TM), Enhanced Thematic Mapper Plus (ETM+), Operational Land Imager/Thermal Infrared Sensor (OLI/TIRS). CW stands for central wavelength in  $\mu\text{m}$ , and SR stands for spatial resolution in meter.

Bands	Sensors	MSS				MSS			ETM+			OLI/TIRS		
		Landsat 1-3	Landsat 4-5	WL	SR	Landsat 4-5	WL	SR	Landsat 7	WL	SR.	Landsat 8	WL	SR.
Ultra-Blue (coastal/aerosol)												Band 1	0.435-0.451	30
Blue					Band 1	0.45-0.52	30	Band 1	0.45-0.52	30	Band 2	0.452-0.512	30	
Green		Band 4	Band 1	0.5-0.6	60**	Band 2	0.52-0.60	30	Band 2	0.52-0.60	30	Band 3	0.533-0.590	30
Red		Band 5	Band 2	0.6-0.7	60**	Band 3	0.63-0.69	30	Band 3	0.63-0.69	30	Band 4	0.636-0.673	30
Near Infrared (NIR) 1		Band 6	Band 3	0.7-0.8	60**	Band 4	0.76-0.90	30	Band 4	0.77-0.90	30	band 5	0.851-0.879	30
Near Infrared (NIR) 2		Band 7	Band 4	0.8-1.1	60**									
Shortwave Infrared (SWIR) 1					band 5	1.55-1.75	30	band 5	1.55-1.75	30	Band 6	1.566-1.651	30	
Shortwave Infrared (SWIR) 2					Band 7	2.08-2.35	30	Band 7	2.09-2.35	30	Band 7	2.107-2.294	30	
Panchromatic								Band 8	0.52-0.90	15	Band 8	0.503-0.676	15	
Cirrus											Band 9	1.363-1.384	30	
Thermal Infrared (TIRS) 1					band 6	10.40-12.5	120/30*	band 6	10.40-12.50	60/30*	Band 10	10.60-11.19	100/30*	
Thermal Infrared (TIRS) 2											Band 11	11.50-12.51	100/30*	

\* TM Band 6, ETM+ Band 6, and TIRS Band 10/11 were acquired at 120, 60, and 100 meters resolution, respectively, but products are resampled to 30 meters pixels.

\*\* Original MSS pixel size was 79 x 57 meters; production systems now resample the data to 60 meters

### 4.1.2 Sentinel-2 Data

The Sentinel-2 mission is a part of ESA's Copernicus program, consisting of two polar-orbiting satellites (i.e. Sentinel-2A and 2B) placed in the same sun-synchronous orbit (at 786 km altitude with a 10:30 a.m. descending node), phased at 180° to each other. It supports GMES by offering multi-spectral high-resolution optical imagery over global terrestrial surfaces. "GMES is an EU-led initiative designed to establish a European capacity for the provision and use of operational monitoring information for environment and security applications. This capacity is seen to be composed of three modules, which together constitute the functional GMES 'system':

- The production and dissemination of information in support of EU policies for Environment and Security;
- The mechanisms needed to ensure a permanent dialogue between all stakeholders and in particular between providers and users;
- The legal, financial, organisational and institutional frame to ensure the functioning of the system and its evolution.

Many elements of the modules already exist but have been conceived, designed and managed in isolation, thus limiting interoperability and production of relevant information. The coherence, efficiency and sustainability of a shared information system for Europe will be the added value of GMES. Developing compatibility between the existing elements, establishing cooperation between the organisations and filling the gaps where necessary will achieve this goal." (Drusch et al., 2012) At present, Sentinel-2A and 2B are providing EO data since January 2015 and March 2017, respectively. In 2016, two more satellite, Sentinel-2C and 2D, were ordered to be launched from 2021 onwards to join the constellation.

The Sentinel-2 constellation is initially designed to provide continuous SPOT-and-Landsat-type EO data, contributing to ongoing multispectral EO. Sentinel-2 constellation is monitoring Earth's surface dynamics between latitudes 56° S and 84° N. Sentinel-2 acquisitions are of wide swath width (approximately 290 km), and high revisit time (10 days at the equator with one satellite, and 5-days with 2 satellites under cloud-free conditions which results in 2–3 days at mid-latitudes), including islands larger 100 km<sup>2</sup>, EU islands, all other islands less than 20 km from the coastline, the whole Mediterranean Sea, all inland water bodies and all closed seas.



At the moment, MSI payloads acquire, store and then download up to 1.6 TB of data per orbit. The MSI has 13 spectral bands spanning from the VISible-Near-Infra-Red (VISNIR) to SWIR at 10 to 60 m spatial resolution (see Table 4-3).

**Table 4-3:** Bands characteristics of Sentinel-2.

Bands		Wavelength [ $\mu\text{m}$ ]	Spatial Resolution [m]
Ultra-blue (coastal/aerosol)	Band 1	0.433–0.453	60
Blue	Band 2	0.458–0.523	10
Green	Band 3	0.543–0.578	10
Red	Band 4	0.650–0.680	10
Red Edge (RE) 1	Band 5	0.698–0.713	20
Red Edge (RE) 2	Band 6	0.733–0.748	20
Red Edge (RE) 3	Band 7	0.773–0.793	20
Near Infrared (NIR)	Band 8	0.785–0.900	10
Near Infrared narrow (NIRa)	Band 8a	0.855–0.875	20
Water vapour	Band 9	0.935–0.955	60
Cirrus	Band 10	1.360–1.390	60
Shortwave Infrared (SWIR) 1	Band 11	1.565–1.655	20
Shortwave Infrared (SWIR) 2	Band 12	2.100–2.280	20

### 4.1.3 ASTER Data

ASTER (Advanced Spaceborne Thermal Emission and Reflection Radiometer) is a multispectral imager on board NASA's Terra spacecraft, which is the first one of a series of multi-instrument spacecraft forming NASA's Earth Observing System (EOS) launched in December 1999. ASTER is an international cooperative program among NASA, Japan's Ministry of Economy, Trade and Industry (METI), and Japan Space Systems (J-space systems), to achieve the goal: to develop a scientific comprehension of the Earth as an integrated system, its response to change, and to better predict variation and trends in climate, weather, and natural hazards. To date, ASTER has successfully provided enormous land surface dynamic records, including reflectance, surface temperature, and elevation.

ASTER is the solely high-resolution sensor on Terra, operating in a sun-synchronous orbit, 30 minutes behind Landsat ETM+. There are three ASTER telescopes, i.e. VNIR, SWIR, and TIR, which together cover a wide spectral region with 14 bands (Table 4-4). Therein, an additional backward-looking near-infrared band (Band 3B) provides stereo coverage, which helps the generation of stereographical DEM. The spatial resolutions of the three telescopes are 15 m in VNIR, 30 m in SWIR, and 90 m in TIR, respectively. A footprint of a single ASTER scene covers an area of 60 x 60 km. It should be pointed out that ASTER SWIR band failed in April 2008, which causes the data discontinuity thereafter.

Every day, approximately 650 scenes are acquired by ASTER. However, unlike Landsat, ASTER images the earth following the ASTER Scheduler situated in Japan at ASTER Ground Data System (GDS) with inputs from both US and Japan. Subsequently, the images are sent to the EOS Operations Center (EOC) at the Goddard Spaceflight Center (GSFC). The scheduler is designed to maximize the science return over a time period of each day, which priorities the acquisition based on the rank of alternative observing modes (and non-observing instrument modes) for each time-step. ASTER is a good supplement to the Landsat Archive, especially after 2003 when Landsat 7 ETM+ SLC-off issue occurred. However, the value of ASTER Archive differs among regions due to its heterogeneous data availability.

**Table 4-4:** Bands characteristics of ASTER, in which SR stands for spatial resolution.

Bands		Wavelength [ $\mu\text{m}$ ]	SR [m]	Radiometric Res.
Green	Band 1	0.52–0.60	15	8-bit
Red	Band 2	0.63–0.69	15	8-bit
Near Infrared (NIR) 1	Band 3N	0.78–0.86	15	8-bit
Near Infrared (NIR) 2	Band 3B	0.78–0.86	15	8-bit
Shortwave Infrared (SWIR) 1	Band 4	1.60–1.70	30	8-bit
Shortwave Infrared (SWIR) 2	Band 5	2.145–2.185	30	8-bit
Shortwave Infrared (SWIR) 3	Band 6	2.185–2.225	30	8-bit
Shortwave Infrared (SWIR) 4	Band 7	2.235–2.285	30	8-bit
Shortwave Infrared (SWIR) 5	Band 8	2.295–2.365	30	8-bit
Shortwave Infrared (SWIR) 6	Band 9	2.360–2.430	30	8-bit
Thermal Infrared (TIR) 1	Band 10	8.125–8.475	90	12-bit
Thermal Infrared (TIR) 2	Band 11	8.475–8.825	90	12-bit
Thermal Infrared (TIR) 3	Band 12	8.925–9.275	90	12-bit
Thermal Infrared (TIR) 4	Band 13	10.25–10.95	90	12-bit
Thermal Infrared (TIR) 5	Band 14	10.95–11.65	90	12-bit

## 4.2 Digital Elevation Model (DEM)

Elevation information is indispensable for snow dynamic assessment in mountain areas. So far, there are multiple commercial and freely open global DEMs (EEA, 2017b), e.g., SRTM, ASTER GDEM (Global Digital Elevation Model), WorldDEM, PlanetDEM. Among these DEMs, SRTM and ASTER GDEM are the most frequently employed ones. Yet SRTM only covers the area between 56°S and 60°N. Given that large proportion of land surface in Europe is of high latitude, ASTER GDEM is selected for elevation information retrieval in this thesis.

The initial ASTER GDEM was released to public in June 2009. It is a joint work between METI and NASA. The current version (i.e. ASTER GDEM Version 2), released in October 2011, is generated by applying the refined production algorithm and including additional 0.26 million stereo-pairs. It results in significant improvements over the first version in spatial resolution,

horizontal and vertical accuracy, and water body detection. The subset of ASTER GDEM v2 is displayed in Figure 4-2. Its spatial resolution is 30 m, covering the land surface between 83° N and 83° S.

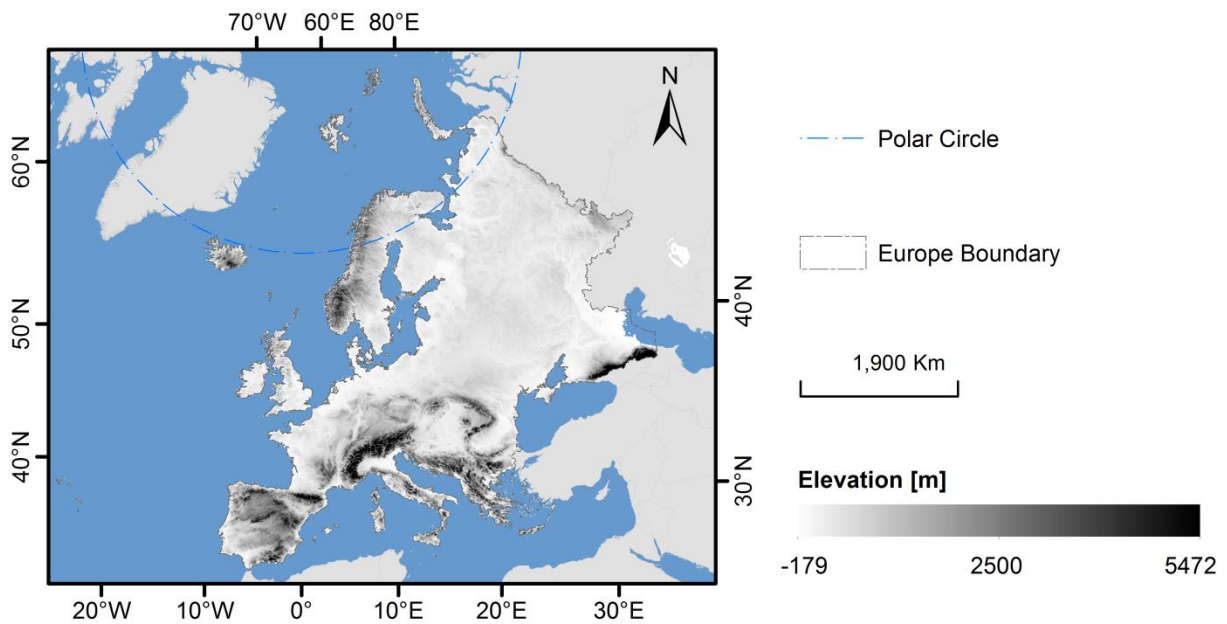


**Figure 4-2:** Overview of the elevation information in Europe derived from ASTER GDEM Version 2 (Tachikawa et al., 2011).

### 4.3 Climate Reanalysis Data

ERA5 is the latest climate reanalysis data produced by ECMWF, integrating modelled data with observations across the world into a global and consistent dataset using the laws of physics. ERA5 offers a large quantity of atmospheric, land and oceanic climate variables worldwide at one hour interval. The first segment of the ERA5 dataset was released in June 2018 for public use (from 1979 to within 3 months of real time). Eventually, the entirely ERA5 dataset spanning from 1950 to present is expected to be released for use in late 2019. Figure 4-3 illustrates the 2 m air temperature on 12:00 over the whole Europe.

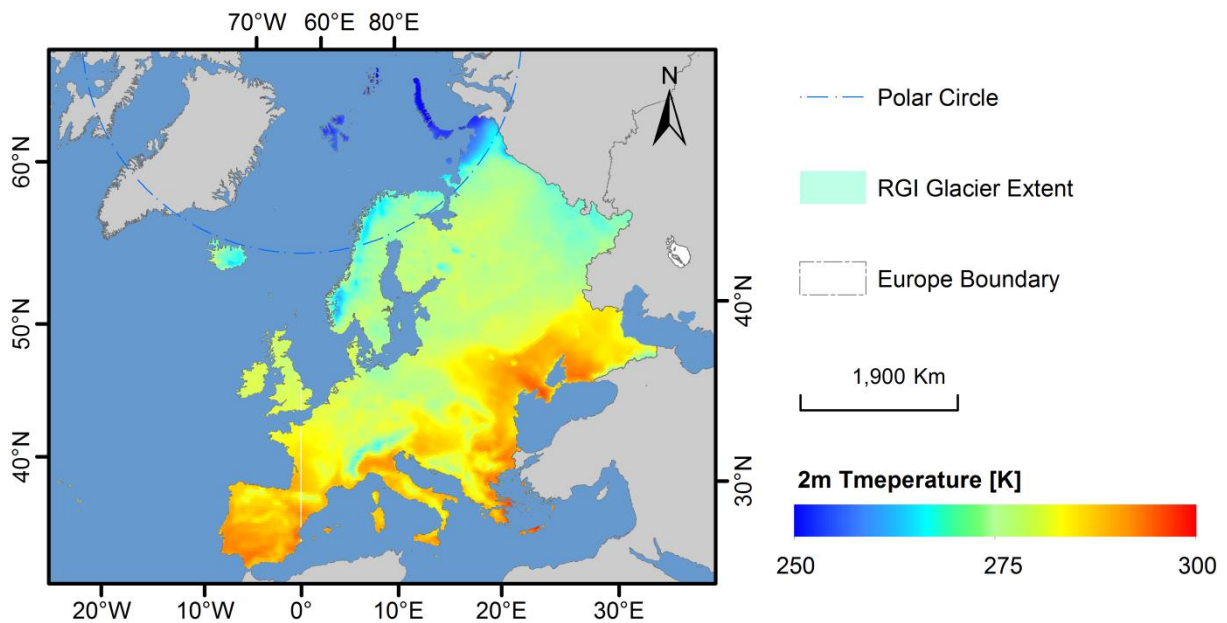


**Figure 4-3:** 2 m air temperature on April 1, 2018 12:00 (Coordinated Universal Time) over the whole Europe derived from ERA5 (C3S, 2017).

km) and one hour, respectively. ERA5 covers the complete globe. The ERA5 data are stored in the Copernicus Climate Change Service-Climate Data Store (C3S-CDS) in the GRIB format. In this thesis, five parameters (listed in Table 4-5) are pre-selected to analyse the interaction between their variations and snowline dynamics during the ablation seasons 1984–2018. Since the temporal resolution of the ERA5 data is one hourly, with each selected catchment, six statistical measures are calculated, i.e. maximum, minimum, mean, 25<sup>th</sup>, 50<sup>th</sup>, and 75<sup>th</sup> percentiles. In addition, the cumulative sums of the 2 m air temperature, of the total precipitation, and of the runoff are computed to further include the effects over the time-span.

**Table 4-5:** Summary of input variables for Random Forest Regression (RFR) derived from ERA5 dataset.

Parameter Name	Units	Short Name	Parameter ID
<b>2 m air temperature</b>	K	2t	167
<b>Runoff</b>	m	ro	205
<b>Skin temperature</b>	K	skt	235
<b>Snow depth</b>	m of water equivalent	sd	141
<b>Total precipitation</b>	m	tp	228

## 4.4 In-Situ Data

To date, there two leading methods of validating the snow cover products, i.e. using (very-high) resolution satellite images and in-situ observations. As higher resolution satellite imagery is often not open and freely accessible, the obtained snow classifications are compared with the snow depth observations from the National Oceanic and Atmospheric Administration-Global Historical Climatology Network (NOAA- GHCN) (Menne et al., 2012) and ECA&D. GHCN-Daily is an integrated dataset of in-situ meteorological measures from land surface stations worldwide. It constitutes of numerous daily climate observations from more than 100,000 stations in 180 countries and territories, which integrates a common suite of quality assurance reviews. In Europe, there are 1910 stations with snow depth records between 1984 and 2018 consecutively or intermittently. The second in-situ dataset is ECA&D, which was initiated in 1998 supported by the European Meteorological Services Network (EUMETNET) and the European Commission (EC). Nowadays, ECA&D is integrating observations from 15563 meteorological stations in 63 European countries. The spatial distributions of NOAA-GHCN and ECA&D stations across Europe are shown in Figure 4-4. In this thesis, daily snow depth records from GHCN-Daily and ECA&D between 1984 and 2018 are originated from 65 meteorological stations within the selected study areas.

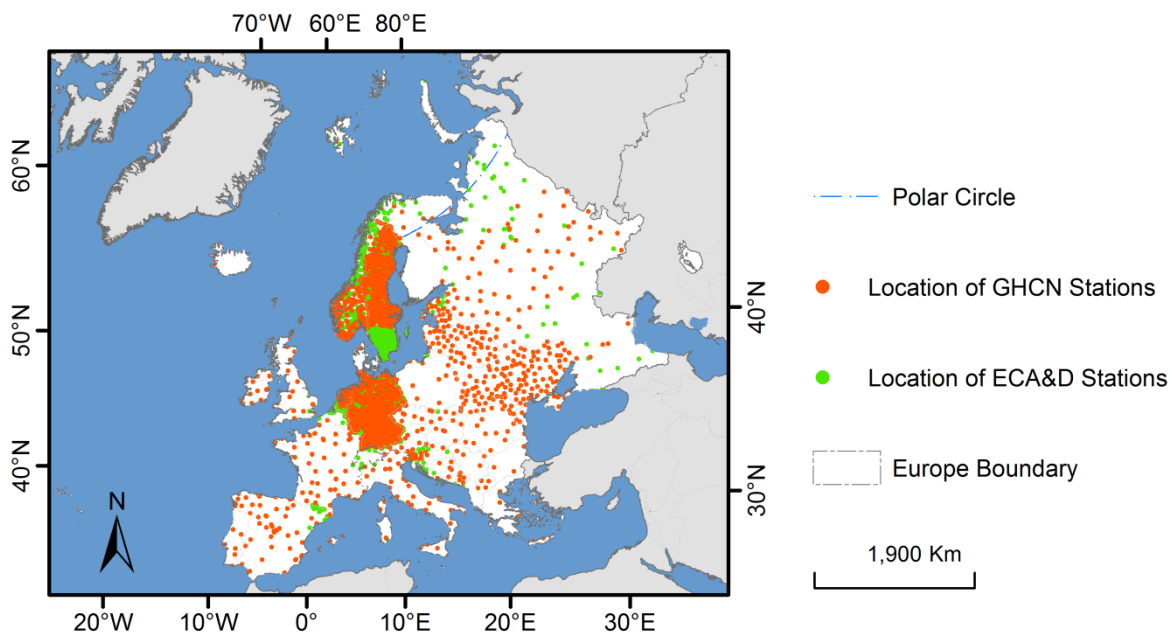


**Figure 4-4:** Location of National Oceanic and Atmospheric Administration-Global Historical Climatology Network (NOAA-GHCN) and European Climate Assessment & Dataset (ECA&D) Stations across Europe.

## 4.5 Auxiliary Data

There are four auxiliary datasets utilized in thesis, providing the supplementary information in relation to catchment extent, snow coverage, glacier extent, and river discharge. Catchment extent is important for clipping/merging satellite images of different footprints to a unified geographical extent. The (sub-) catchment extent applied is the Hydrological basin shapefiles in Europe provided by the Food and Agriculture Organization (FAO) displayed in Figure 4-5.

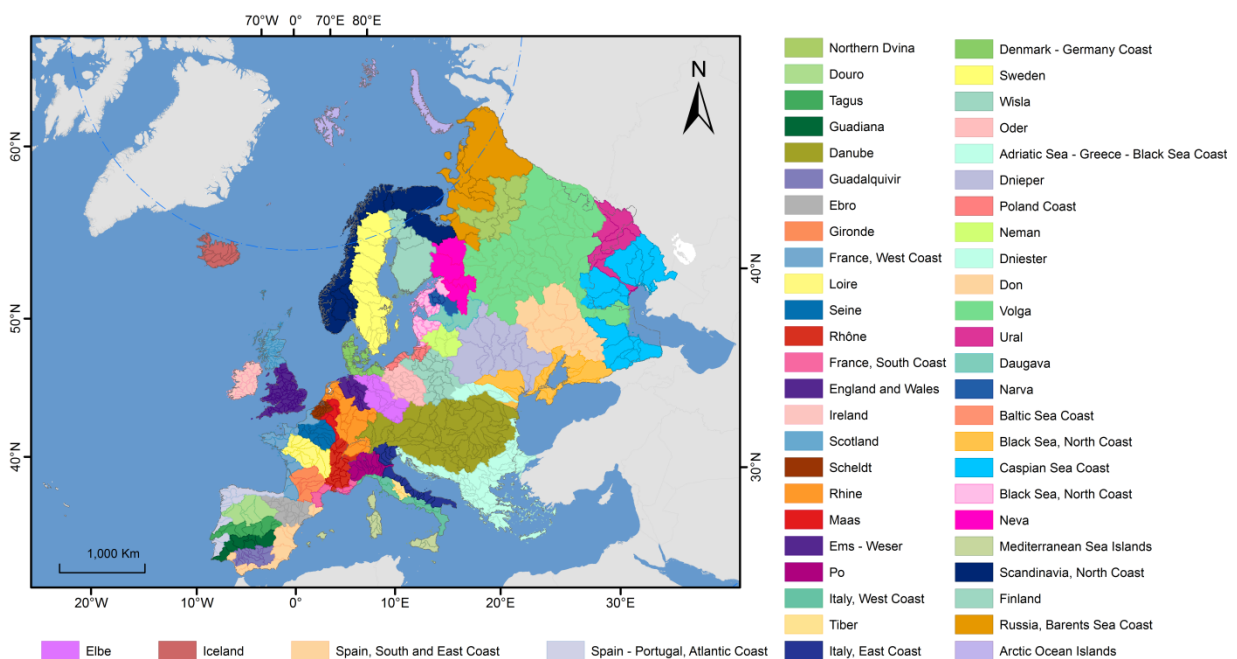


**Figure 4-5:** Major hydrological basins and their sub-basins. This dataset divides the European continent according to its hydrological characteristics. Data source: Lehner et al. (2008).

Snow cover information is important with regards to the snow coverage evaluation, intermediate snowfall event detection, and ablation period determination for a specific catchment. In these regards, GSP dataset (Dietz et al., 2015) from DLR-DFD is included. The DLR-DFD GSP provides a cloud-free time series of daily snow cover processed from the operational 500 m MODIS daily snow cover products MOD10A1 and MYD10A1 (Hall et al., 2002), and has been validated using ECA&D station data in Europe (details see Dietz et al., 2015). The mean snow cover duration between 2000 and 2018 derived from GSP within Europe is shown in Figure 4-6.

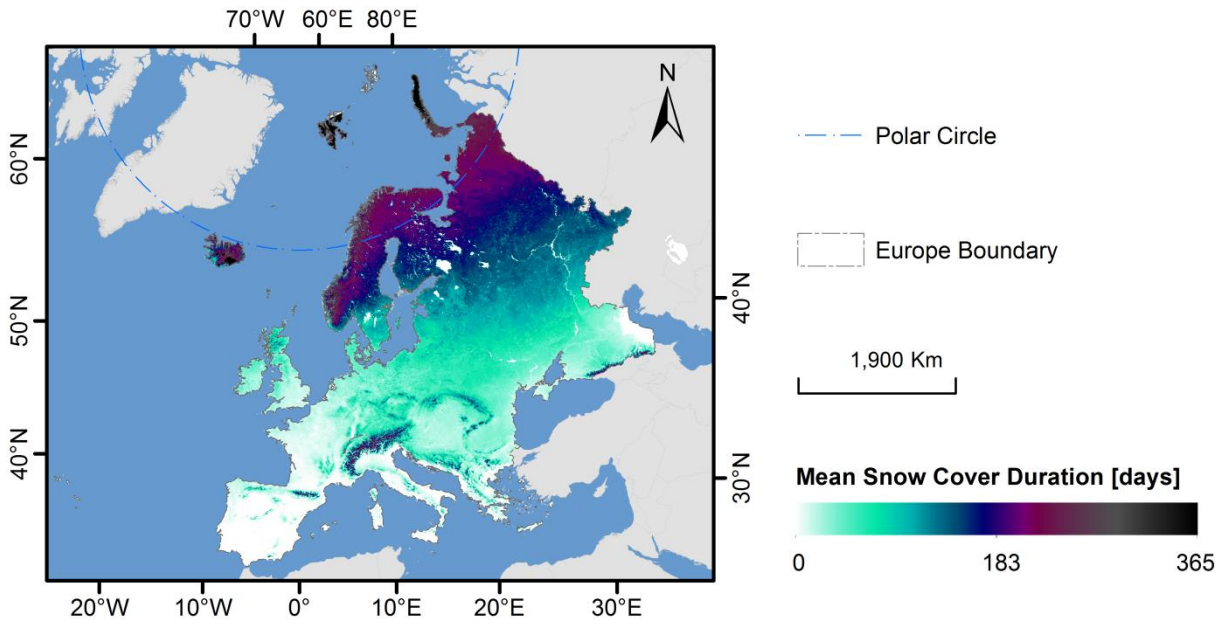


**Figure 4-6:** Mean Snow Cover Duration (SCD) between 2000 and 2018 derived from the Global Snow Pack (GSP). Data Source: Dietz et al. (2015).

Because glaciers influence snowline dynamics at a regional scale, it is required to calibrate the snowline dynamics in glaciated regions with the elevation information of the glacier(s). This elevation information is derived from RGI and the ASTER GDEM v2. The RGI is the first complete global glacier inventory (excluding Greenland and the Antarctic) released on 22 February 2012. It is based on EO data, including Landsat fleet, ASTER, SPOT5 HRS, SRTM DEM, ASTER GDEM, etc. Figure 4-7 illustrates an example of the glacier outlines of Saint Sorlin and Sarenes from the RGI, near the catchment Drac.

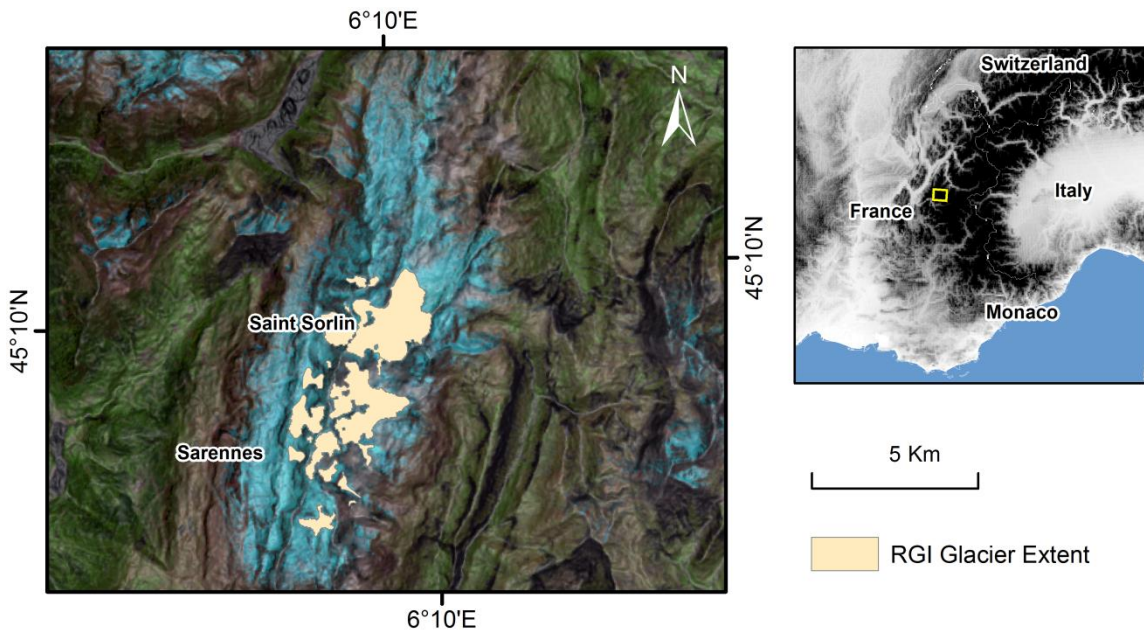


**Figure 4-7:** Glacier outlines of Saint Sorlin and Sarenes from the Randolph Glacier Inventory (RGI) (Pfeffer et al., 2014a), near the catchment Drac.



To investigate the patterns of river discharge, records from the Global Runoff Data Centre (GRDC) are employed. GRDC archive has collected international data up to two centuries, and has been widely used in regional and global long-term hydrological studies. Supported by WMO, the GRDC archive is now holding river discharge data of more than 9500 stations from 161 countries (Figure 4-8). For researchers, universities and other organisations, data are available for research programmes and projects via research proposals.

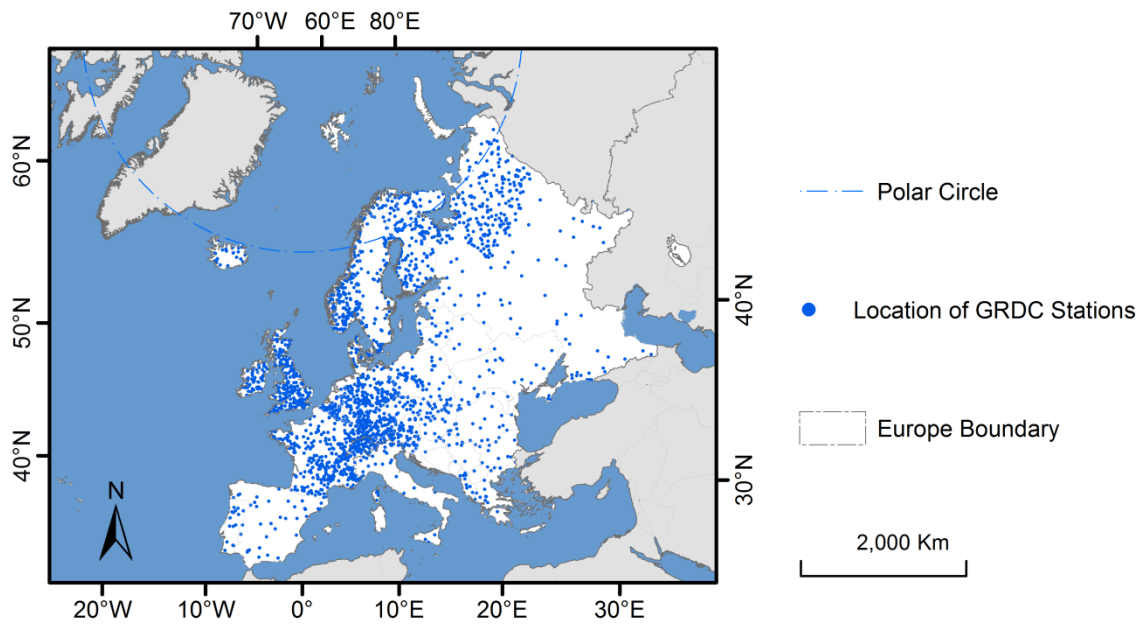


**Figure 4-8:** Location of the Global Runoff Data Centre (GRDC) Stations across Europe.



## CHAPTER 5

### 5 Developed Framework of Snowline Retrieval and Assessment

This chapter presents a fast, novel, and transferable framework for the assessment of long-term snowline dynamics in European mountains, including (1) pre-processing, (2) snow detection, (3) regional snowline elevation retrieval, (4) time series densification, and (5) regional snowline retreat curve production.

#### 5.1 Optical Imagery Pre-Processing

To obtain physically comparable surface reflectance, atmospheric and topographic corrections are performed using ATCOR-3 (Richter and Schläpfer, 2011) for each Landsat, ASTER, and Sentinel-2 image (Figure 5-1). Therein, ASTER GDEM Version 2 (Tachikawa et al., 2011) is employed for slope and elevation information derivation.

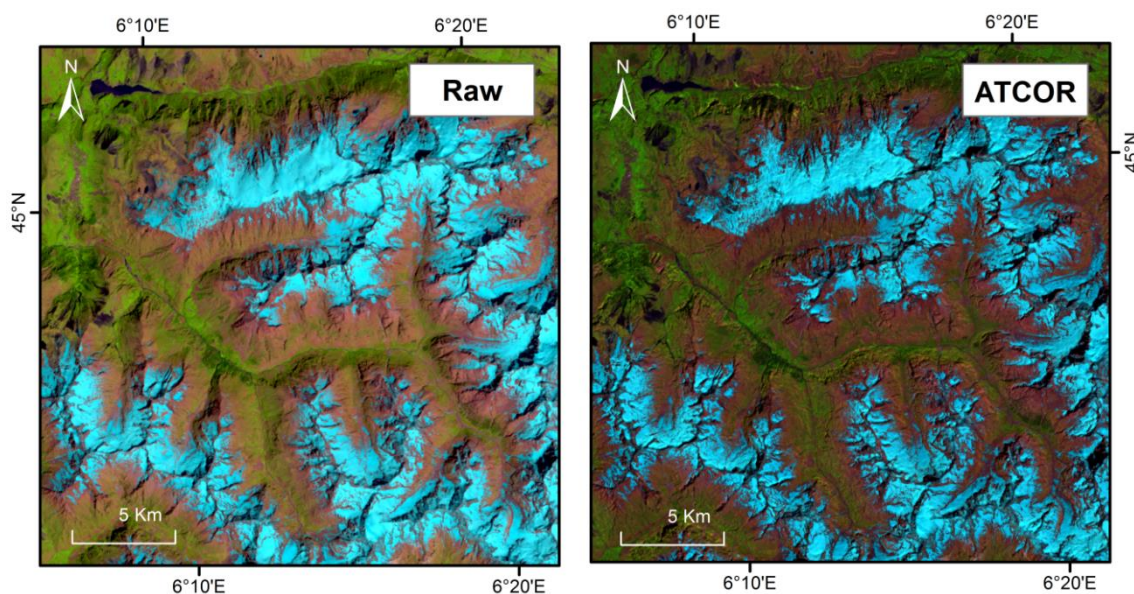


**Figure 5-1:** Effects of atmospheric and topographic correction: left: original raw Digital Number (DN) image in false colour composite (RGB: SWIR-NIR-RED); right: ATCOR-corrected image in false colour composite (RGB: SWIR-NIR-RED).

The major processing steps regarding the atmospheric correction are demonstrated in Figure 5-2. It contains 10 sub-processors, including (1) the sensor-specific Look Up Tables (LUTs) reading, (2) pre-classification and land covers (i.e. land, water, haze, cloud, and shadow) masking, (3) an optional haze or cirrus removal, (4) optional shadow removal, (5) visibility or aerosol optical thickness map calculation based on the Dense Dark Vegetation (DDV) method, (6) aerosol model (path radiance behaviour in the blue to red bands) updating (only if a blue band exists and the update option is enabled), (7) Water Vapour Map (WVM) computation, (8) iterative surface reflectance retrieval, (9) spectral polishing (for hyperspectral instruments), and (10) BRDF (Bidirectional Reflectance Distribution Function) correction. For detailed information, the reader should refer to the ATCOR manual (Richter and Schläpfer, 2011) or Asrar and Asra, 1989; Schowengerdt, 2006; Slater, 1980.

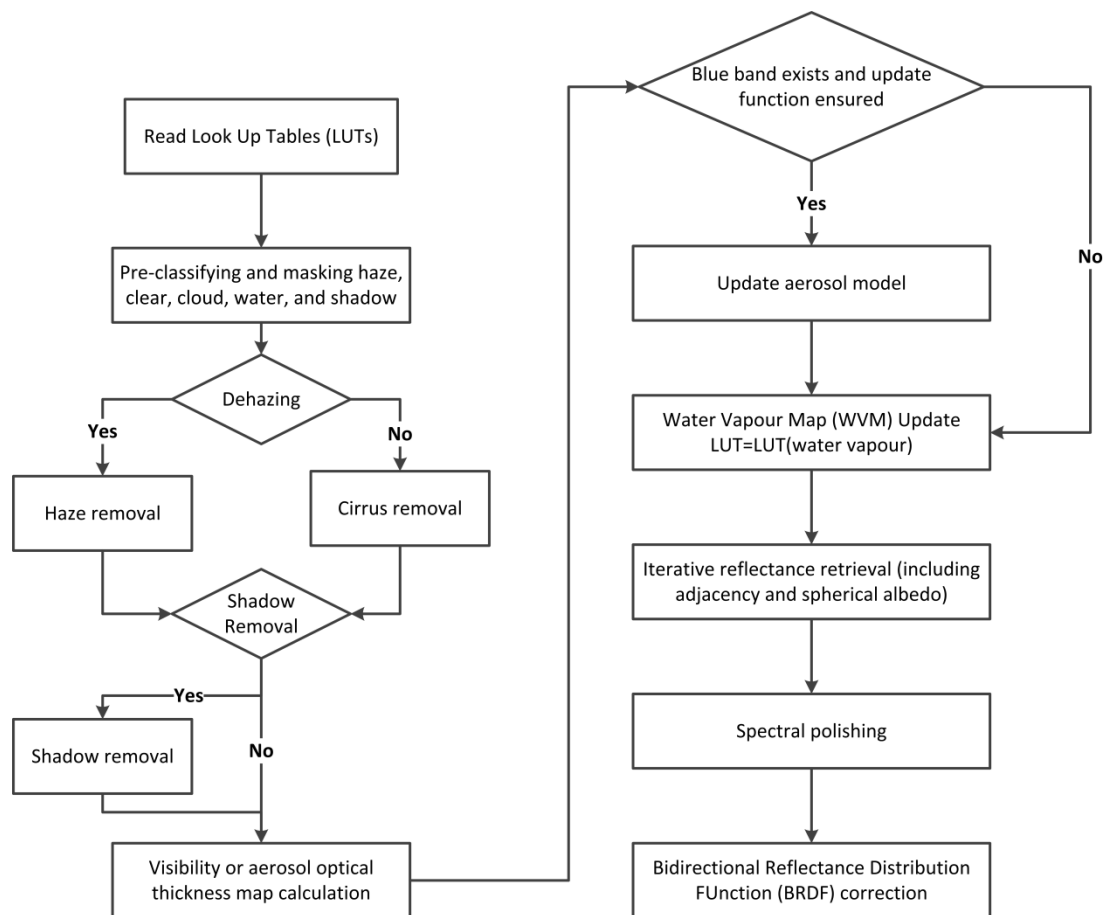


**Figure 5-2:** Main processing steps during atmospheric correction. Modified according to Richter and Schläpfer (2011).

## 5.2 Snow Classification and Validation

To classify snow cover in optical images, there are two major processing steps, i.e. snow detection based on a decision tree of multiple thresholds, and non-snow land cover masking using cloud mask, water mask, shadow mask and/or thermal mask:

- **Snow Detection** is realized by applying the algorithms developed by Klein et al. (1998) and Poon and Valeo (2006) in this thesis. The algorithm separates snow cover from ambient surroundings based on the significant signal contrast between the green and the SWIR band (Figure 5-3). "The algorithm is based on a decision tree with multiple thresholds on NDSI, the green band, and the Near Infra-Red (NIR) band. To detect snow in forested areas, the NDSI-NDVI field is utilized to calibrate the snow cover classification results therein.

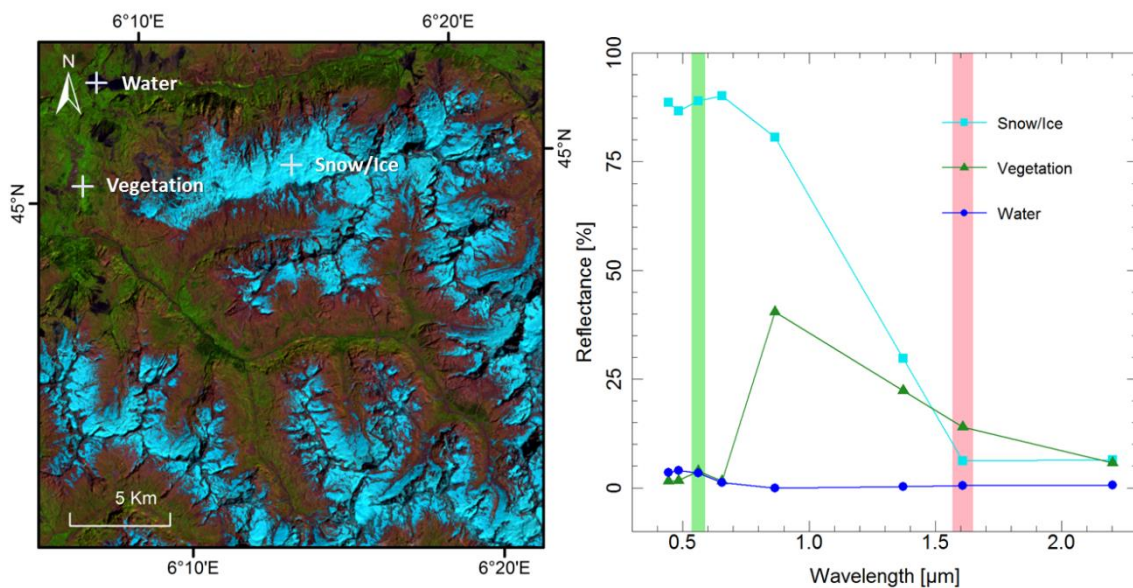


**Figure 5-3:** Multispectral profiles of main land covers: left: atmospherically and topographically corrected image in false colour composite (RGB: SWIR-NIR-RED), right: multispectral profiles of snow/ice, vegetation and water body. (Data source: Landsat 8 Operational Land Imager/Thermal Infrared Sensor (OLI/TIRS) near the catchment Drac at path/row: 196/029 acquired on 07 June 2017).

- **Cloud Mask:** Three different types of cloud masks are applied due to different designations of Landsat, ASTER and Sentinel-2. Firstly, to mask out the clouds in Landsat scenes, the Mountainous Fmask (MFmask) is applied (Foga et al., 2017; Frantz et al., 2018; Zhu et al., 2015; Zhu and Woodcock, 2012). Secondly, for Sentinel-2 images, clouds are masked out by employing "s2cloudless", an automated single-scene pixel-based cloud detector developed by

the Sentinel Hub's research team. Thirdly, to identify the clouds in ASTER scenes, the Automatic Cloud Cover Assessment (ACCA) (Irish, 2000; Irish et al., 2006) is applied.

- **Water Mask:** High NDSI values usually indicate the presence of the snow in optical EO imagery. However, high NDSI values could also be observed in clear water bodies. Therefore, the water bodies must be masked out to avoid misclassification. Because the water bodies commonly show positive Normalized Difference Water Index (NDWI) values" (Hu et al., 2019b) based on Gao (1996):

$$NDWI = \frac{NIR - SWIR}{NIR + SWIR} \quad (5.1)$$

and "the reflectance of water bodies in the green band is relatively low, the water mask is generated based on thresholding these two values.

- **Shadow Mask:** Shadow-cast areas are normally treated as non-valid pixels. In this study, the shadow pixels are identified following the methods from the SnowPEX Team (Ripper et al., 2015). Thereafter, the shadow-cast pixels are masked out in the snow cover results.

- **Thermal Mask:** Both Landsat and ASTER have thermal band(s). To filter out bright and warm surfaces such as warm rocks in the classification results, a thermal threshold (< 288 K) introduced by Metsämäki et al. (2015) is applied to Landsat- and ASTER- based snow classifications. Sentinel-2 does not have any thermal band, which could potentially commit more commission errors over bright and warm targets. " (Hu et al., 2019b) In this thesis, the snow classifier and masks are applied in sequence to obtain snow classification results.

In order to assess the accuracy of the obtained binary snow classification results, the validation is performed using the contemporary snow depth measurements from NOAA-GHCN and ECA&D dataset. As the reference dataset, the snow depth is converted into snow/snow-free information according to the 1-cm-threshold proposed by Parajka et al. (2010b). Once the observed snow depth is >1 cm, the corresponding pixel is regarded as a snow pixel, and vice versa. Based on the validation results, a confusion matrix can be generated (Table 5-1). Afterwards, Producer's Accuracy (PA), User's Accuracy (UA), Overall Accuracy (OA), and Kappa Coefficient ( $\kappa$ ) (Equation 5.2–5.6) are calculated according to the confusion matrix.

$$\text{Producer's Accuracy (PA)}_{\text{snow}} = \frac{A}{A+C} \quad (5.2)$$

$$\text{User's Accuracy (UA)}_{\text{snow}} = \frac{A}{A+B} \quad (5.3)$$

$$\text{Overall Accuracy (OA)} = \frac{A+D}{A+B+C+D} \quad (5.4)$$

$$\text{Expected Agreement (EA)} = \frac{(A+B) \times (A+C) + (C+D) \times (B+D)}{(A+B+C+D)^2} \quad (5.5)$$

$$\text{Kappa Coefficient (}\kappa\text{)} = \frac{OA-EA}{1-EA} \quad (5.6)$$

Where A (the number of pixels which are identified as snow in both classification results and snow depth measurements), B (the number of pixels which are identified as snow in classification results, but as snow-free according to the snow depth measurements), C (the number of pixels which are identified as snow-free in classification results, but as snow according to the snow depth measurements), and D (the number of pixels which are identified as snow-free in both classification results and snow depth measurements) are illustrated in the demonstrative confusion matrix in Table 5-1.

**Table 5-1:** Demonstrative confusion matrix relating satellite-derived snow classifications with ground snow-depth observations.

Classification \ Observation	Snow depth > 1cm	Snow depth ≤ 1cm
Snow	A	B
Snow-free	C	D

### 5.3 Regional Snowline Elevation (RSE) Retrieval and Accuracy Assessment

To date, there are various definitions of snowline, according to the objectives of the studies, e.g., geographical studies, meteorological studies, hydrological studies. Krajčí et al. (2014) reviewed the existing snowline definitions, thereafter, a new term Regional Snowline Elevation (RSE) was proposed for remote-sensing-based applications. "The RSE is defined as

the elevation where there are as few as possible snow pixels below it, and as few as possible land pixels above it. Methodologically, the RSE can be determined as the elevation where the minimum value of the sum of two cumulative histograms (i.e. cumulative histogram of snow pixel elevations and land pixel elevations) is reached (Figure 5-4).” (Hu et al., 2019b)The index itself was originally validated by Krajčič et al. (2014) against the snow depth measurements from climate stations and field campaigns, and the accuracy was reported as 86%. The most influential factors with regards to RSE accuracy are vegetated areas and shadows adjacent to the snowline.

To assess the accuracy of the retrieved RSEs, five quality indices are developed therefor (Table 5-2). The first quality index is Representativeness Index (RI) measuring the percentage of valid pixels (i.e. labelled as snow or land) within the spatial extent of a catchment. The second quality index, Error Index (EI), is a measure of the percentage of erroneous pixels (i.e. snow pixels below the RSE, PF, and snow free pixels above the RSE, NT) according to the corresponding RSE. By definition, the obtained RSE should result in as few erroneous pixels as possible. Thereby, EI is introduced as the ratio between the number of erroneous pixels and the total number of pixels (TP). The concepts of the rest three indices were originally introduced by Dong and Peters-Lidard (2010), Painter et al. (2009), and Rittger et al. (2013) for accuracy assessment.

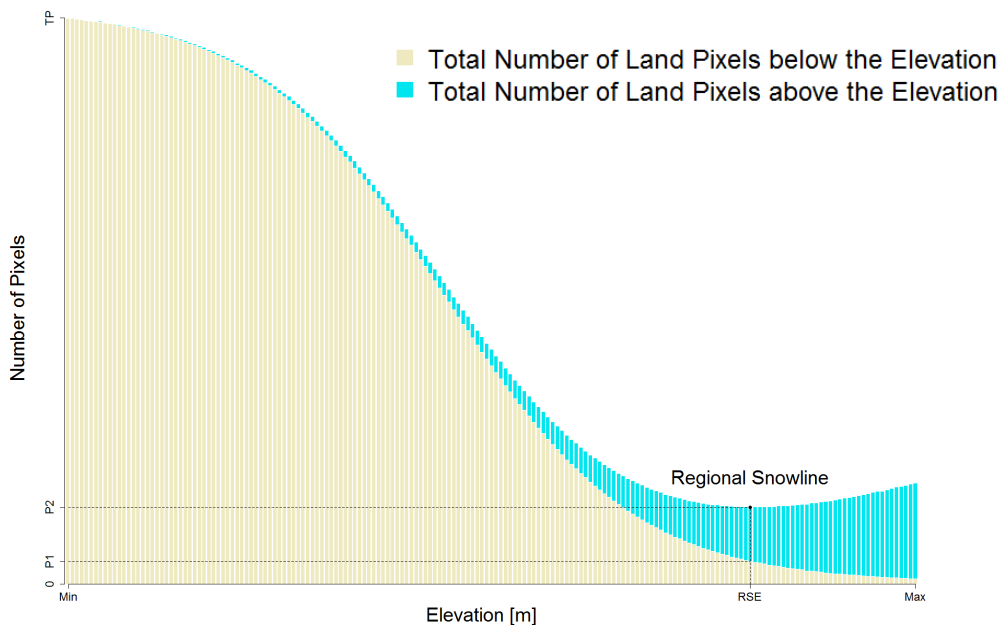


**Figure 5-4:** Estimation of Regional Snowline Elevation (RSE) from the combined cumulative histograms of the snow covered pixels (in blue) and land pixels (in orange). In the x-axis,  $P_1$  indicates that there are  $P_1$  land pixels above the RSE;  $P_2 - P_1$  there are  $P_2 - P_1$  snow pixels below the RSE,  $P_2$  alone means the sum of land pixels above the RSE and snow pixels below the RSE, and  $T_p$  stands for the total number of pixels. Modified according to Hu et al. (2019b).



**Table 5-2:** Performance measures for assessing the Regional Snowline Elevation (RSE) outcomes.

Performance Measure	Definition
Representativeness Index (RI)	$\frac{PT+NT+PF+NF}{TP}$
Error Index (EI)	$\frac{NT+PF}{PT+NT+PF+NF}$
Precision	$\frac{PT}{PT+NF}$
Recall	$\frac{PT+NT}{PT+NF}$
F-score	$\frac{2PT}{2PT+PF+NF}$

TP: total number of pixels with the corresponding catchment extent.

PT: total number of positive true pixels (snow in snow classification, pixel above RSE).

NT: total number of negative true pixels (land in snow classification, pixel above RSE).

PF: total number of positive false pixels (snow in snow classification, pixel below RSE).

NF: total number of negative false pixels (land in snow classification, pixel below RSE).

## 5.4 Time Series Densification Using Random Forest

### Regression (RFR)

Landsat constellation, ASTER, and Sentinel-2 constellation have an inherent trade-off between the spatial resolution and temporal resolution. In this regards, although high spatial resolution is achieved, the near-two-week temporal resolution of the Landsat satellite constellation poses a challenge in monitoring highly dynamic snowline. To densify the time series, a classic machine learning technique, Random Forest Regression (RFR) is applied, together with the daily climate reanalysis data to fill the gaps when no satellite images are available. The random forest technique was developed by Breiman (2001), who introduced the random forest as a classifier/regressor constituting a collection of tree-structured classifiers (i.e. trees) that are independent and identically distributed random vectors, and each tree casts a unit vote for the most popular class. RFR is a non-linear statistical ensemble method, for a regression purpose. It has the following major advantages (Breiman, 2001; Liaw et al., 2002), which makes it ideal for the densification of the RSE time series:

- Straightforward inclusion or exclusion of explanatory variables according to data availability and user requirements;
- Ability of handling unbalanced dataset and high dimensional dataset;
- Robustness to outliers and non-linear data;
- Ability of dealing with multicollinearity in explanatory variables;
- Capability of coping with both numeric and categorical explanatory variables;
- Relatively small number of user-specified model parameters;
- Low risk of overfitting;
- Calculation of explanatory variable importance;
- Parallelizability and fast prediction and training speed.

Before the implementation of the RFR, the extracted RSEs need to be “cleaned”. To ensure the high quality of the input RSEs, a threshold of RI > 20% has been set to filter out RSE results which are not representative due to the lack of valid observations (e.g., too much cloud obstruction, large cast-shadow area). In this thesis, the RFR is implemented using the R package “RandomForest” (Liaw et al., 2002). The parameterization of the user-defined variables is: the number of regression trees to grow ( $n_{tree} = 500$ ), the number of predictors sampled for splitting at each node ( $m_{try} = p/3$ , where  $p$  is the number of the variables), and the minimum size of terminal nodes ( $n_{odesize} = 5$ ). The input explanatory variables are 2 m air temperature, total precipitation, skin temperature, snow depth, and runoff from the ERA5 dataset. For each variable, the maximum, minimum, mean, 25<sup>th</sup>, 50<sup>th</sup>, 75<sup>th</sup> percentiles, and cumulated sum are calculated. Given that 2 m air temperature may be counteracted due to negative values, its cumulated sum has been hence calibrated by adding the observations from the previous month (March). To assess the model performance, the coefficient of determination ( $R^2$ ), RMSE, and Mean Absolute Error (MAE) for each model are calculated. To assess the importance of each input variable, the permutation importance (percentage increase in mean squared error) for each implemented Random Forest model is computed.

## 5.5 Regional Snowline Retreat Curve (RSRC) Derivation and Validation

Subsequent to the RSEs derivation and time series densification, Regional Snowline Retreat Curves (RSRCs) can be generated to characterize the retreat of the regional snowline during an ablation season. Given the fact that snowmelt is highly temporal dynamic, and RSE variation is usually not monotonous during an ablation season because of the occurrence of intermediate snowfall events (Hu et al., 2019a). In fact, it is more likely that the relationship between AT and RSE dynamic metrics during an ablation season is monotonous. To reduce the impact of the non-monotonicity, Accumulated Temperature (AT), instead of date, is linked to RSEs time series to generate RSRCs. However, the influence of the intermediate snowfall events cannot be totally eliminated. Since the conventional Ordinary Least Squares (OLS) regression technique is of very low break point, it cannot handle the contaminated RSE results influenced by the intermediate snowfall events. Therefore, the robust M-estimator (Hampel et al., 2011) is applied. Normally an RSRC is of sigmoid shape. Thus, a logistic link function is firstly applied to the RSE time series (Equation 5.7) for a better model fitting. The robust regression is then implemented using the R package "MASS". The form of RSRC can be expressed by Equation 5.7 and Equation 5.9:

$$RSE_i = \frac{RSE_{max}}{1 + e^{k \cdot AT_i + b}} \quad (5.7)$$

$$AT_{MA} = \frac{b}{-k} \quad (5.8)$$

$$AT_i = \int_0^i (\bar{T}_i - T_0) \cdot di + AT_0 \approx \sum_1^i \sum_{j=1}^{24} (\bar{T}_{ij} - T_0) + AT_0 \quad (5.9)$$

where the  $RSE_{max}$  is the highest RSE, which equals to the highest elevations from the DEM. In case of the glaciated areas  $RSE_{max}$  is approximated by 95 percentile of the elevations in delineated glacier outlines from the RGI. The slope ( $k$ ) is always a negative value, whose absolute value represents the steepness of an RSRC. The ratio between the intercept ( $b$ ) and  $-k$  (Equation 5.8) is a coefficient indicating the Accumulated Temperature of the Mid-Ablation season ( $AT_{MA}$ , the mid-point of the RSRC). The generalized behaviour of RSRC in relation to

the coefficients is illustrated in Figure 5-5.  $AT_i$  represents the AT at the  $i^{\text{th}}$  day within the ablation season, which is the integral of the daily air temperature above the base temperature ( $T_0$ ) added by the AT from the previous month ( $AT_0$ ). By adding the  $AT_0$  to the  $AT_i$ , it calibrates the shift of consecutive air temperatures below  $0\text{ }^{\circ}\text{C}$  at the beginning of an ablation season.” (Hu et al., 2019b) In this thesis,  $AT_i$  is approximated by calculating the daily average of hourly 2 m air temperature measures from the ERA5 dataset, and the base temperature is set as the melting point ( $0\text{ }^{\circ}\text{C}$ ) for snow/ice (Equation 5.9). Besides, three statistics from the summary of each RSRC are extracted to perform the accuracy assessment, including the corrected coefficient of determination (corrected  $R^2$ ) adapted for robust regression (Willett and Singer, 1988), MAE, and RMSE.

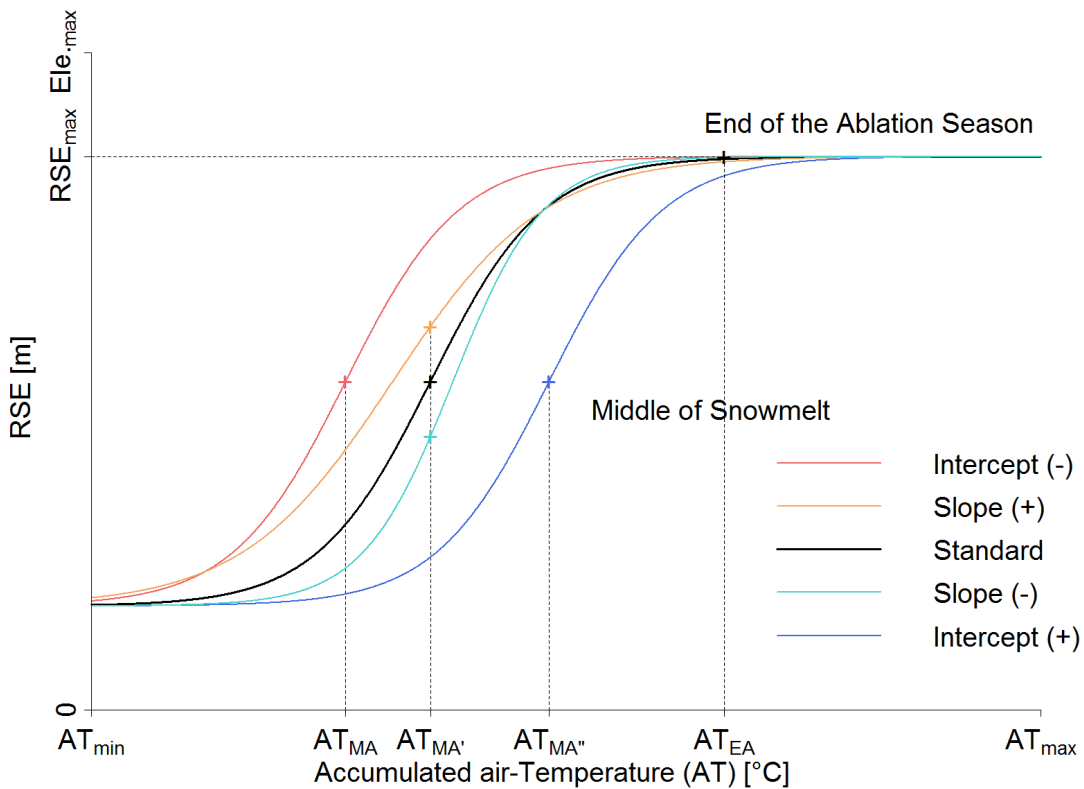
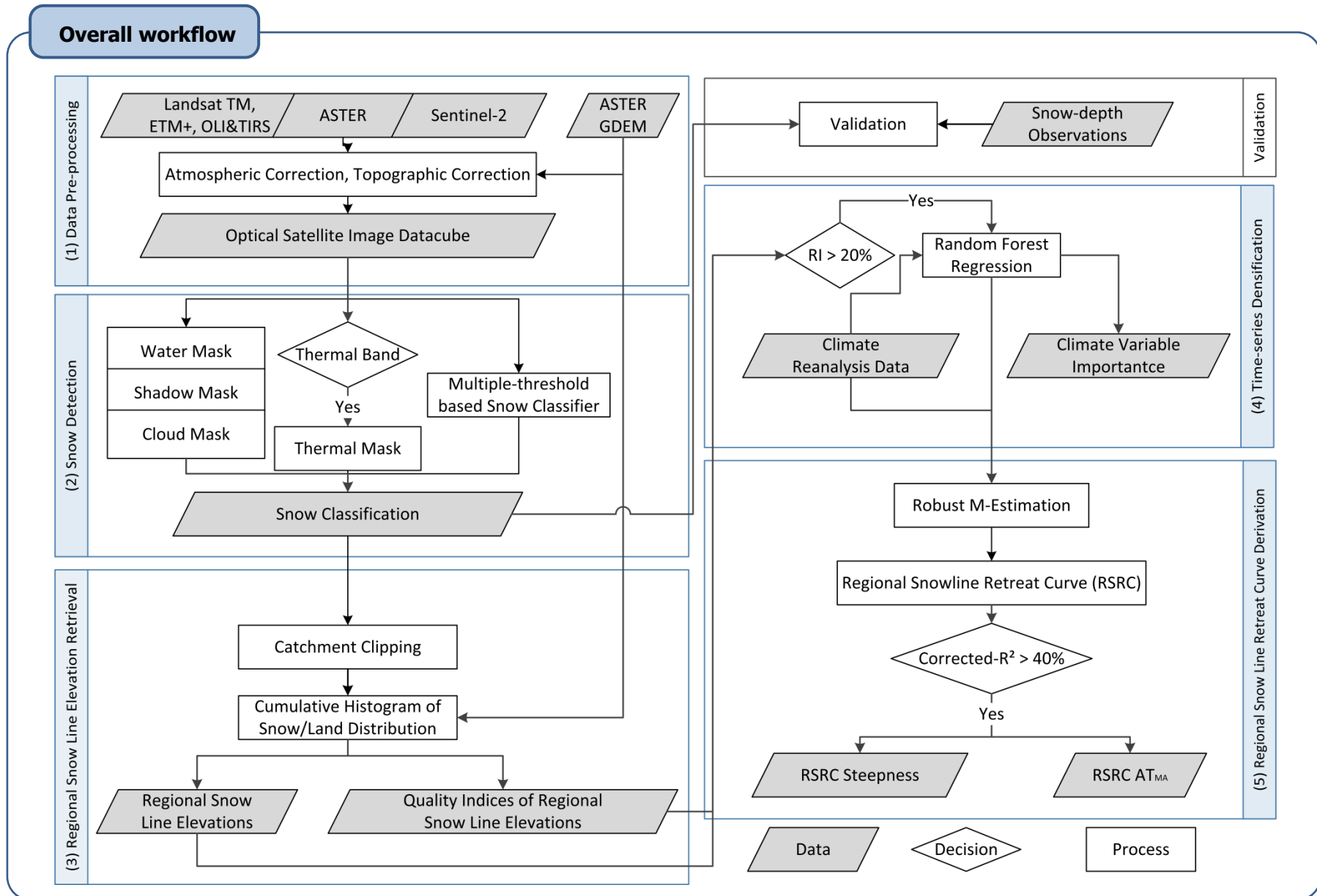


**Figure 5-5:** Theoretical Regional Snowline Retreat Curve (RSRC) based on the Accumulated Temperature (AT) and Regional Snowline Elevation (RSE).  $AT_{EA}$  are the AT at the end of the ablation season, whose RSEs is the  $RSE_{max}$ .  $AT_{min}$  and  $AT_{max}$  are the minimum/maximum AT observed within the ablation season. Accumulated Temperature of the Mid-Ablation season ( $AT_{MA}$ ) is the mid-point of the RSRC, which is the AT value of the mid-ablation season. The solid line represents the standard situation, and the dash lines are the RSRC with different regression coefficients. The dash lines and dot-dash lines represents the behaviour of the RSRCs in different slope and intercept values. Modified according to Hu et al. (2019b).





## CHAPTER 6

### 6 Results of Snowline Dynamics in Europe

This chapter presents the results of snowline dynamics in Europe, with regards to five perspectives: (1) data availability, (2) snow classifications, Regional Snowline Elevations (RSEs), and validation, (3) 35-year intra-annual and inter-annual snowline variability in European mountains, (4) the analysis between snowline dynamics and the potential climate driver(s), as well as (5) the possible consequence of the observed snowline dynamics. The first part answers the research question regarding the long-term Landsat availability, including quality control of data pre-selection (e.g. ascending/descending scenes, tiers, and processing levels). Afterwards, the snow classifications, RSEs, and densified RSE time series are provided, together with the accuracy assessment. Based on the retrieved 35-year RSE time series, the intra-annual and inter-annual snowline variabilities during the ablation seasons are analysed for each study area. Ultimately, two case studies are presented. The first case study links a climate driver (air temperature anomalies) to the obtained snowline dynamics, aiming to investigate the possible triggers causing the observed snowline dynamics. The other one linked the snowline dynamics to river discharge observations, exploring the potential consequences (e.g. flood risk increase) of the observed snowline dynamics.

#### 6.1 Analysis of Landsat Collection 1 Availability over Europe

In this section, the availability of Landsat Collection 1 archive over Europe is analysed, providing an overview of long-term Landsat viability for time series analysis of snow dynamics in Europe. Firstly, the data volume Landsat 4–8 TM/ETM+/OLI/TIRS data in Collection-1 are presented, according to ascending/descending orbits, tiers and processing levels. Then the spatial distribution of the archived Landsat Collection 1 TM/ETM+/OLI/TIRS data over Europe is presented, together with the monthly Landsat Collection 1 TM/ETM+/OLI/TIRS data volume. Accordingly, locations and periods of existing Landsat data gaps during 1982–2017 in Europe

are identified. Given the great impact of cloud obstruction on optical satellite image availability, the cloud cover information derived from the MFmask is analysed to delineate the locations as well as the severity of cloud cover in the Landsat Collection 1 time series.

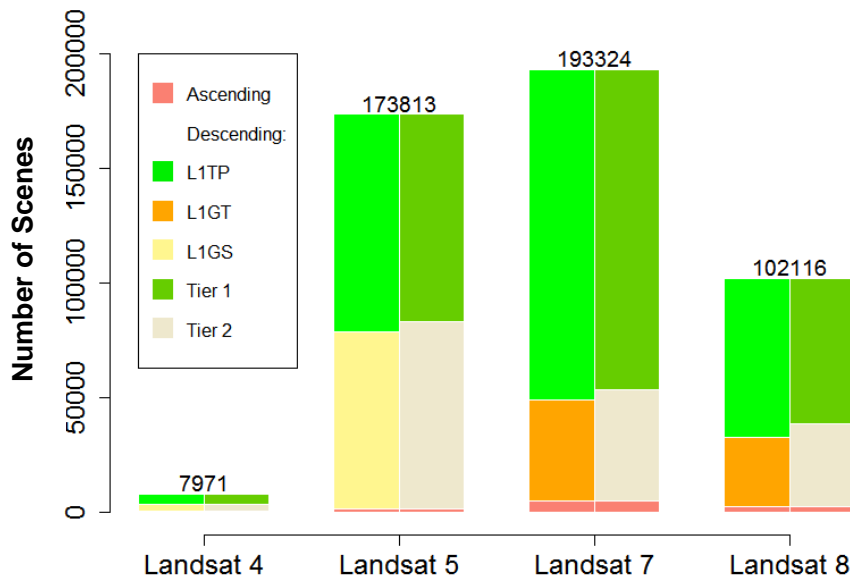
### 6.1.1 Suitability of Different Landsat Processing Levels and Tiers

In May 2018, the USGS unprecedentedly reorganized the global Landsat 1–5 MSS, Landsat 7 ETM+, Landsat 8 OLI/TIRS, and the majority of Landsat 4–5 TM scenes into the USGS Collection 1 archive. The reorganized Landsat scenes were categorized into three tiers, i.e. Tier 1, Tier 2, and RT which consist of daily updated metadata available online. Among these three tiers, Tier 1 (“stackable” data for time series analysis) is the strictest quality indicator for time series analysis (for details please refer to section 4.1.1). It is characterized by the highest quality in terms of radiometric and geometric calibration. Figure 6-1.a shows that only 59 % of the Landsat 4 and 52% of the Landsat 5 TM data meet the Tier 1 criterion. On the other hand, the Tier 1 criterion is met by 72% of the Landsat ETM+ and 62% of the Landsat OLI/TIRS scenes. For long-term time series in cloud-prone areas, for example snow covered mountain regions (Martinuzzi et al., 2007; USGS/EROS, 2017), USGS suggests to lower the selection criterion from Tier 1 to L1TP processing level in order to filter out unsuitable time series input scenes (USGS/EROS, 2017). For the presented study, the Landsat Collection 1 archive available between 1982 and 2017 has been analysed across the entire Europe based on the available metadata information as of January 16, 2018 and again has been rechecked on March 22, 2018. Therein, approximately 100,000 scenes have been acquired by Landsat 7 ETM+ after May 31, 2003, when the SLC permanently failed. It has been estimated that nearly 22% of the pixels are unusable in SLC-off Landsat 7 ETM+ acquisition (Markham et al., 2004).

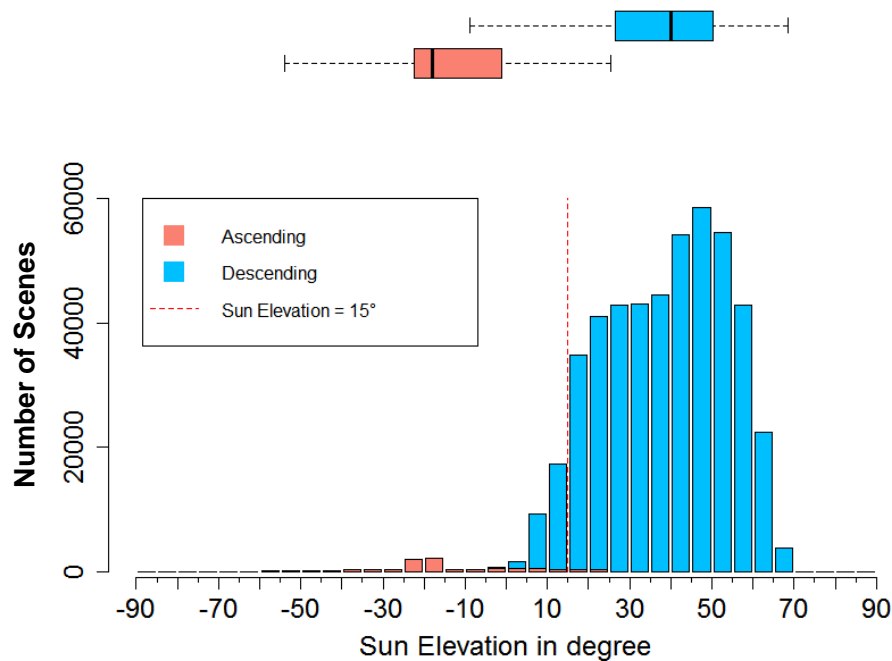
Given that some ascending scenes (i.e. “night-time” acquisitions) may provide additional usable images during the polar day in Northern Europe, the metadata of the ascending scenes was checked as well. However, Figure 6-1.b shows that more than 93% of the ascending scenes contain sun elevation below 15°, which are therefore not appropriate for accurate atmospheric correction and post-processing. In this view, only the descending scenes (a total of 1189 path/row footprints) which were processed to the L1TP level were eventually used for the availability and snow condition analysis in this study. In total, the metadata of 477,224 Landsat acquisitions over Europe in the USGS Landsat Collection 1 dataset were incorporated.



In this thesis, Landsat acquisitions archived by other International Cooperators (ICs) are not considered, as the scenes held by ICs are often not free-accessible, and only pre-processed according to the ICs' individual norms.



(a) The total number of archived Landsat 4–5 TM, Landsat 7 ETM+ and Landsat 8 OLI/TIRS scenes at different processing levels and tiers



(b) Sun elevation of the archived Landsat Collection 1 ascending (i.e. "night-time" acquisition) and descending (i.e. "day-time" acquisition) scenes

**Figure 6-1:** Quality indicators of the Landsat scenes archived in Collection 1 dataset (1982–2017) over Europe.

To systematically detect snow cover and cloud cover, the USGS Landsat Surface Reflectance Level-2 Science Products were utilized, including the Landsat Ecosystem Disturbance Adaptive Processing System (LEDAPS) products for Landsat TM and ETM+ scenes and the Landsat 8 Surface Reflectance Code (LaSRC) products for Landsat 8 OLI/TIRS scenes. In accordance with the availability analysis, all Level-2 Tier 1 surface reflectance products, as well as the L1TP scenes categorized in Level-2 Tier 2 surface reflectance products provided by the Google Earth Engine (GEE), have been selected and used for snow and cloud detection.

### **6.1.2 Spatiotemporal Distribution of the Landsat Collection 1 TM/ETM+/OLI/TIRS L1TP Products in Europe**

The spatiotemporal distribution of data availability is directly linked to the density of the snow cover time series and the occurrence of missing values therein. The USGS Landsat Collection 1 archive currently (as of January 16, 2018) holds around 315,000 TM/ETM+/OLI/TIRS L1TP images acquired over Europe between 1982 and 2017 (Figure 6-3). The effect of footprint overlapping is well-pronounced (shown as the checkerboard pattern) in Europe. The maximum number of acquisitions is located over Southern Europe, particularly the Alps, and parts of the Scandinavian Mountains. Northernmost Europe such as Svalbard has fewer L1TP scenes than the rest of Europe due to the low winter sun elevation angles and severe cloud cover. Albeit a large number of acquisitions are acquired in these regions due to extremely overlapped footprints, these images can rarely be pre-processed at the L1TP level. In mountain areas, approximately 500 acquisitions per footprint are archived in Collection 1 over the Alps, and a similar number of images are also acquired over the Carpathian Mountains and the Pyrenees. The number of available scenes can reach more than 1,000 (e.g., in the Northern Alps and Central Carpathians), where footprints are overlapped. The mountains in Northern Europe have deficient acquisitions, especially those located on islands (e.g., Iceland, Scotland, and Svalbard). Although the footprint overlapping is more significant within these areas, for the majority of Iceland and Scotland no more than 280 scenes per footprint have been acquired for any of these locations.

The temporal distribution of monthly availability of the archived Landsat Collection 1 data at the L1TP processing level is illustrated in Figure 6-2. Generally, the intra-annual data volume shows a seasonality pattern with the maximum appearing in the summertime and the minimum occurring in midwinter. The overall inter-annual pattern also has obvious periodical

disparities, which are almost inconsistent with the timeline of different Landsat missions. Before the launch of Landsat 7 ETM+ (1982–1999, epoch 1), the data availability reaches its minimum. The availability is elevated during the Landsat 5 TM and Landsat 7 ETM+ cooperation time (1999–2013, epoch 2). Later, the availability reaches its maximum after the launch of Landsat 8 OLI/TIRS (2013 to present, epoch 3), which is annually almost twice as much as the amount during epoch 1. In epoch 1, most of the acquisitions in Europe were contributed by the Landsat 5 TM, while Landsat 4 TM acquired only a few L1TP scenes between 1987 and 1992 over Europe. Since Landsat 7 ETM+ became operational, the majority of the archived scenes in Europe have been acquired by Landsat 7 ETM+ during the epoch 2. Later, in epoch 3, Landsat 8 OLI/TIR became the backbone. In the meantime, Landsat 7 ETM+ consecutively provided L1TP scenes to the Landsat Archive. Two periods (1982–1984 and 1991–1999) of sparse acquisitions can be identified in Figure 6-2. For the first period (1982–1984), even though Landsat 4 TM was launched in 1982, the data actually became available only after the year 1984. Accordingly, the length of the whole time series is, in fact, shorter. Another significant data scarcity is observed between 1992 and 2000, except for 1995 and 1998. During this period, only a limited number of Landsat 5 TM scenes were acquired mainly over Western Europe.

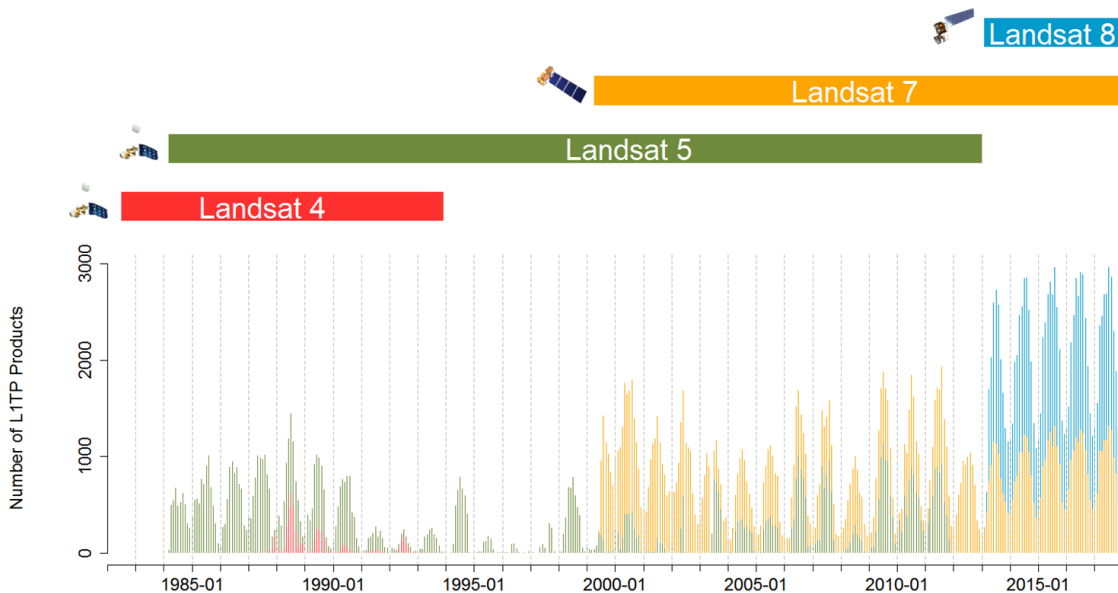


**Figure 6-2:** Temporal pattern of monthly Landsat 4–5 Thematic Mapper (TM), Landsat 7 Enhanced Thematic Mapper Plus (ETM+), and Landsat 8 Operational Land Imager/Thermal Infrared Sensor (OLI/TIRS) Level 1 Precision and Terrain (L1TP) acquisition amounts over Europe archived in Collection 1 dataset. Modified according to Hu et al. (2019a).

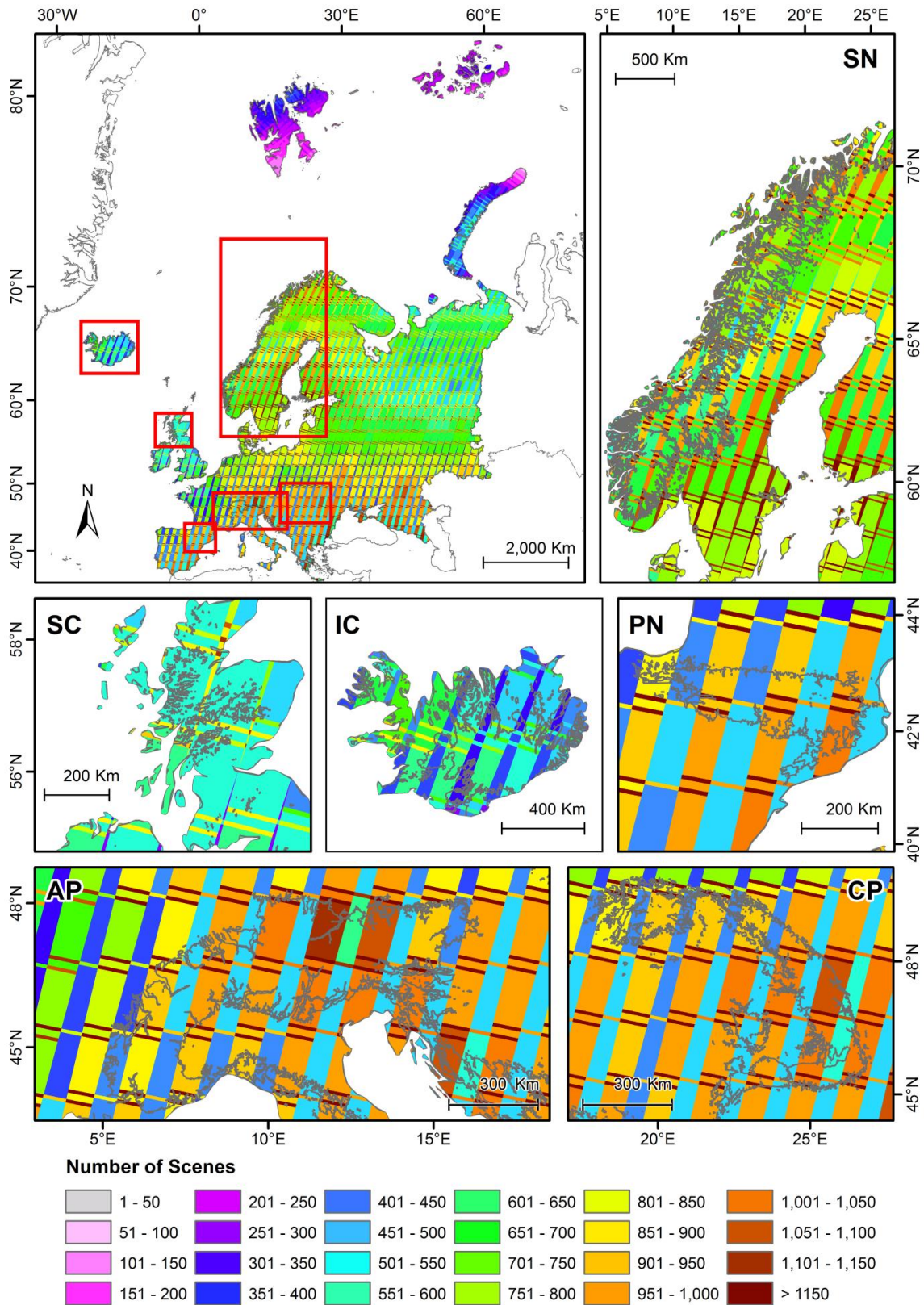


**Figure 6-3:** Spatial distribution of Landsat 4–5 Thematic Mapper (TM), Landsat 7 Enhanced Thematic Mapper Plus (ETM+), and Landsat 8 Operational Land Imager/Thermal Infrared Sensor (OLI/TIRS) Level 1 Precision and Terrain (L1PT) scenes over Europe archived in Collection 1 dataset between 1984 and 2017.

### 6.1.3 Cloud Obstruction of the Landsat Collection 1 TM/ETM+ /OLI/TIRS L1TP Products in Europe

For optical snow monitoring, clouds do not only obstruct optical EO observation but also cause challenges in separating snow and clouds. The frequency of each pixel in Europe covered by clouds during the period 1982–2017 is presented in Figure 6-4, based on the “Level-2 Pixel Quality Assurance Bit Flag” in the USGS Landsat Collection 1 Level-2 Surface Reflectance Tier 1 and 2 L1TP products. Geographically, the occurrence of clouds tends to be more frequent in mountainous areas (> 70%) and high latitude regions (> 50%), yet lower in low latitude plains (< 50%) and the Mediterranean (< 30%). This is highly consistent with the local geographical settings, e.g., topography and climatology. Among the selected study areas, Scotland has the densest cloud cover. More than 80% of Landsat L1TP scenes within the regions around Ben Nevis are cloud covered. Severe cloud cover (> 60%) is also observed in the ice-cap peripheral areas in Iceland, the northwest face of the Scandinavian Mountains as well as the north face of the Pyrenees. Cloud cover is less severe in the Carpathian Mountains and the Alps, with exception of the high peaks. No more than 55% of these acquisitions are cloud covered.

The seasonal cloud cover patterns from the selected six mountain areas have been illustrated in Figure 6-5. They are calculated based on the cloud flags in the Landsat metadata file. Again, the Scandinavian Mountains (Figure 6-5.a), Scotland (Figure 6-5.b) and Iceland (Figure 6-5.c) are the most cloud-prone regions among all months, where the median cloud coverage stays around 40% throughout the whole year. The upper quantile of the cloud cover in these regions persists at approximately 70% in each month. In addition, the cloud cover is much more long-lasting in Scotland and Iceland, whose lower quantile of cloud cover are mostly above 30% and 20% respectively. An anomaly is the cloud cover of Iceland in December (Figure 6-5.c), which is obviously lower than in other months. The intra-annual cloud cover variation of mountains in Southern Europe (the Alps, Carpathian Mountains, and the Pyrenees) presents a cosine-curve shape. Most of the Landsat summer acquisitions have no more than 50% cloud coverage. The lower quantile is approximately 5% in July and August.

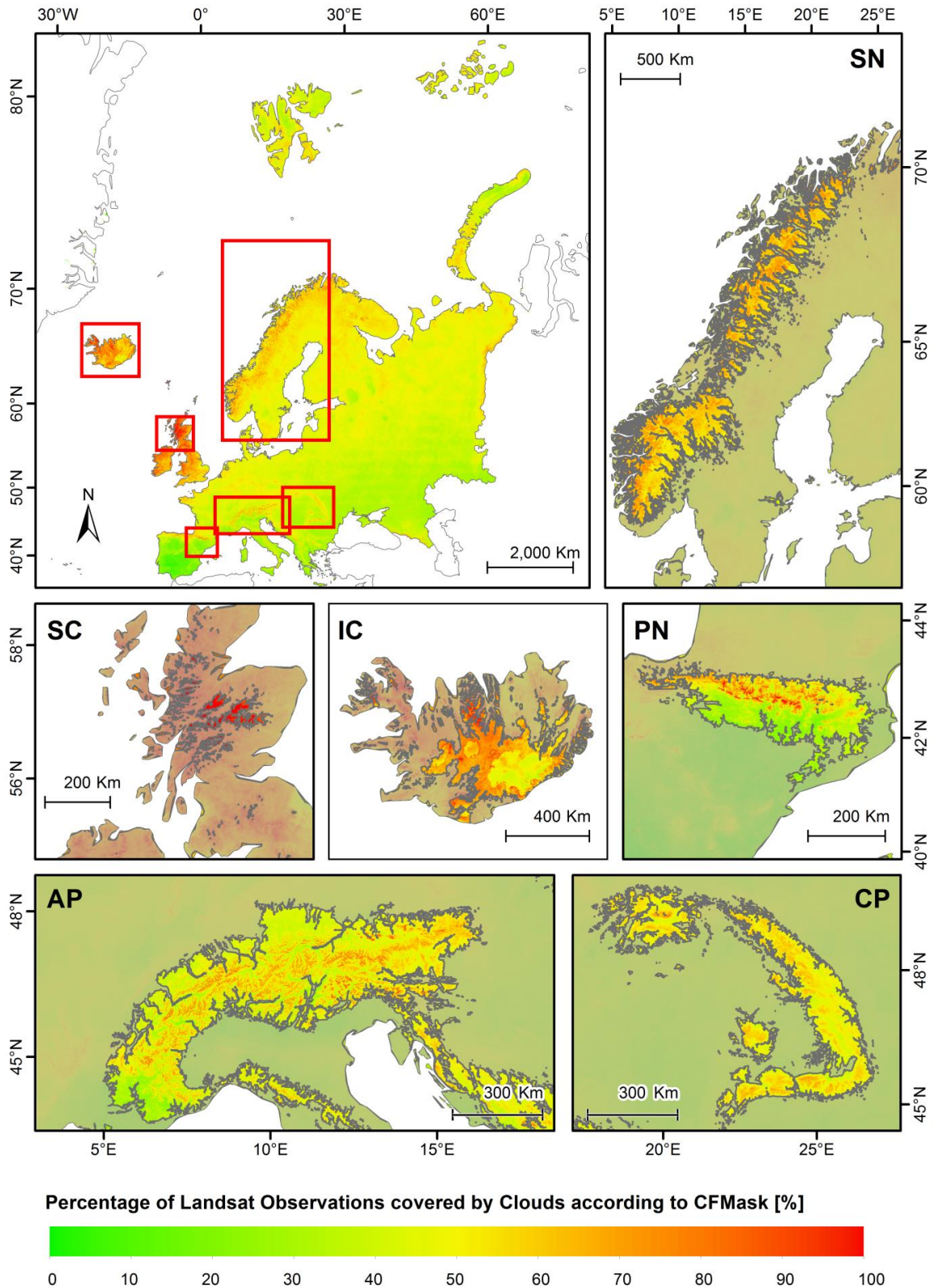
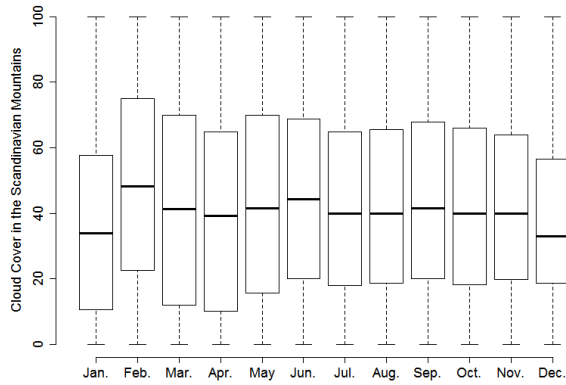
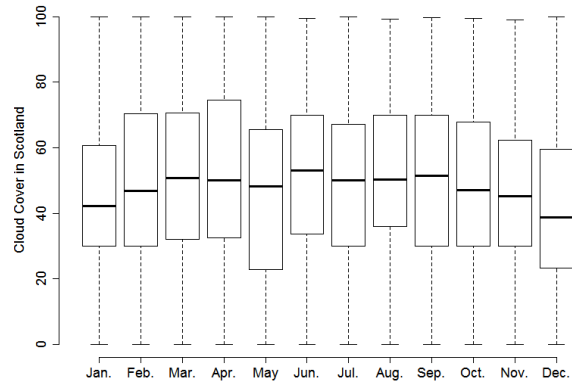


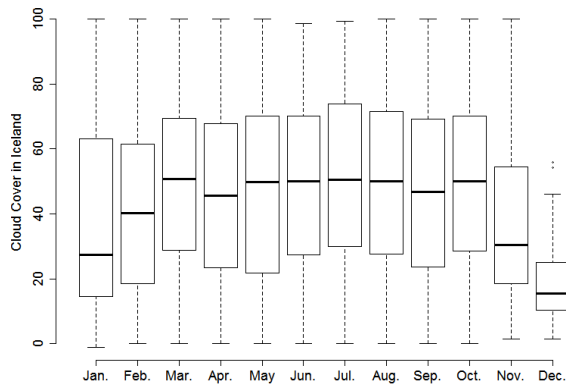
**Figure 6-4:** The frequency of cloud occurrence of Landsat 4–5 Thematic Mapper (TM), Landsat 7 Enhanced Thematic Mapper Plus (ETM+), and Landsat 8 Operational Land Imager/Thermal Infrared Sensor (OLI/TIRS) Level 1 Precision and Terrain (L1PT) scenes in Collection 1 archive based on Fmask.



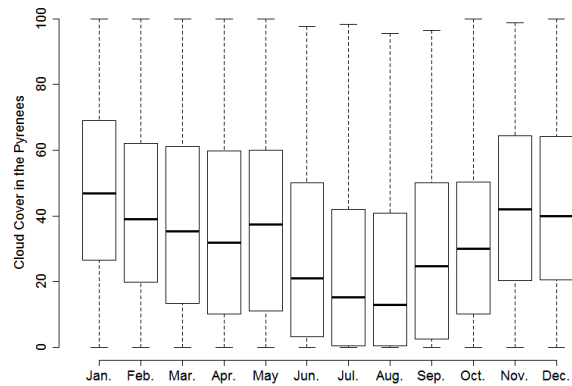
(a) Seasonal cloud cover in the Scandinavian Mountains



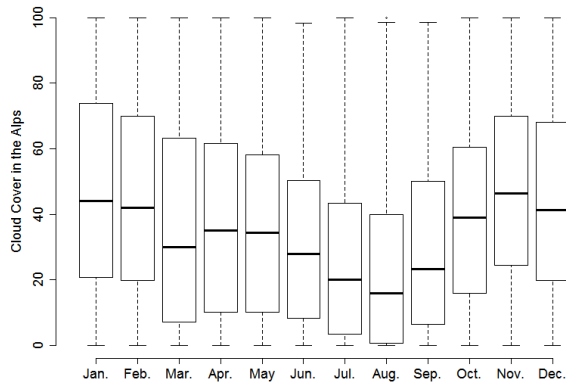
(b) Seasonal cloud cover in Scotland



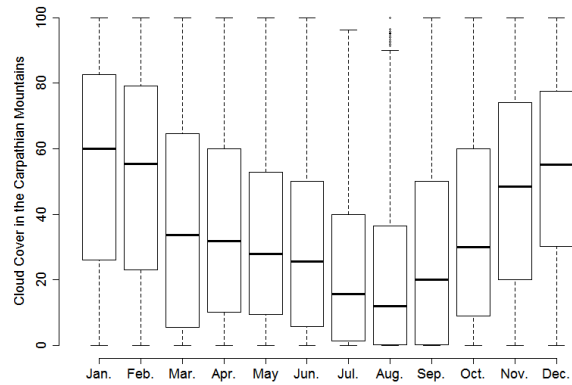
(c) Seasonal cloud cover in Iceland



(d) Seasonal cloud cover in the Pyrenees



(e) Seasonal cloud cover in the Alps



(f) Seasonal cloud cover in the Carpathian Mountains

**Figure 6-5:** Boxplots of seasonal cloud cover per scene in the main European mountain areas: (a) Scandinavian Mountains, (b) Scotland, (c) Iceland, (d) Pyrenees, (e) Alps, and (f) Carpathian Mountains. Modified according to Hu et al. (2019a).

## 6.2 Snow Cover Maps and Regional Snowline Elevation (RSE)

In this section, the results of snow classifications, EO-derived RSEs, RFR-densified RSEs are presented. This section starts with demonstrating the snow classifications in comparison to the MODIS-based snow classification results. It shows the necessity of employing higher-resolution satellite images for snow cover assessment in mountain areas than the prevalently used MODIS snow cover products. Also, the accuracy assessment of the obtained snow classification results is provided. In terms of the RSE results, firstly, the RSEs derived from the Landsat, ASTER, and Sentinel-2 images are demonstrated together with the corresponding accuracy assessment based on the five indices (section 5.3). Afterwards, the modelled daily RSE time series are displayed, as well as the corresponding validation results.

### 6.2.1 Snow Classifications and Accuracy Assessment

An example of the snow classification results based on the Landsat OLI/TIRS image near the catchment Drac is displayed in Figure 6-6.a and Figure 6-6.d. For a comparison purpose, the MODIS-based snow classification on the same date is shown aside (Figure 6-6.b and Figure 6-6.e). In the background the originally Landsat image is displayed in a false-colour composition (RGB: SWIR-NIR-Red). Therein, snow is of a typical bluish colour, while clouds are shown as bright white objects. The zoom-in images (Figure 6-6.d and Figure 6-6.e) illustrate a great underestimation in snow-covered areas. Moreover, within the snow-land boundary areas, 500m MODIS snow cover products show an obvious over-/underestimation of snow cover. In this regard, the medium-resolution based snow cover products are not well-suited for snowline estimation, while the Landsat Archive shows its strength in precisely extracting the high-resolution boundary between snow and snow-free areas.

To quantitatively assess the accuracy of the snow classification maps, a confusion matrix is generated (Table 6-1), based on 7720 ECA&D and NOAA-GHCN snow depth observations. Based on the confusion matrix, OA and  $\kappa$  are calculated as 96.71% and 0.72, respectively. In addition, based on the confusion matrix (Table 6-1), UA and PA in relation to snow are calculated. The obtained UA<sub>snow</sub> is 83.25%, which means that 83.25% of the classified snow pixels are truly snow-covered according to the ground truth data. The obtained PA<sub>snow</sub> is 65.41%, which means that 65.41% of the snow-covered pixels have been detected.



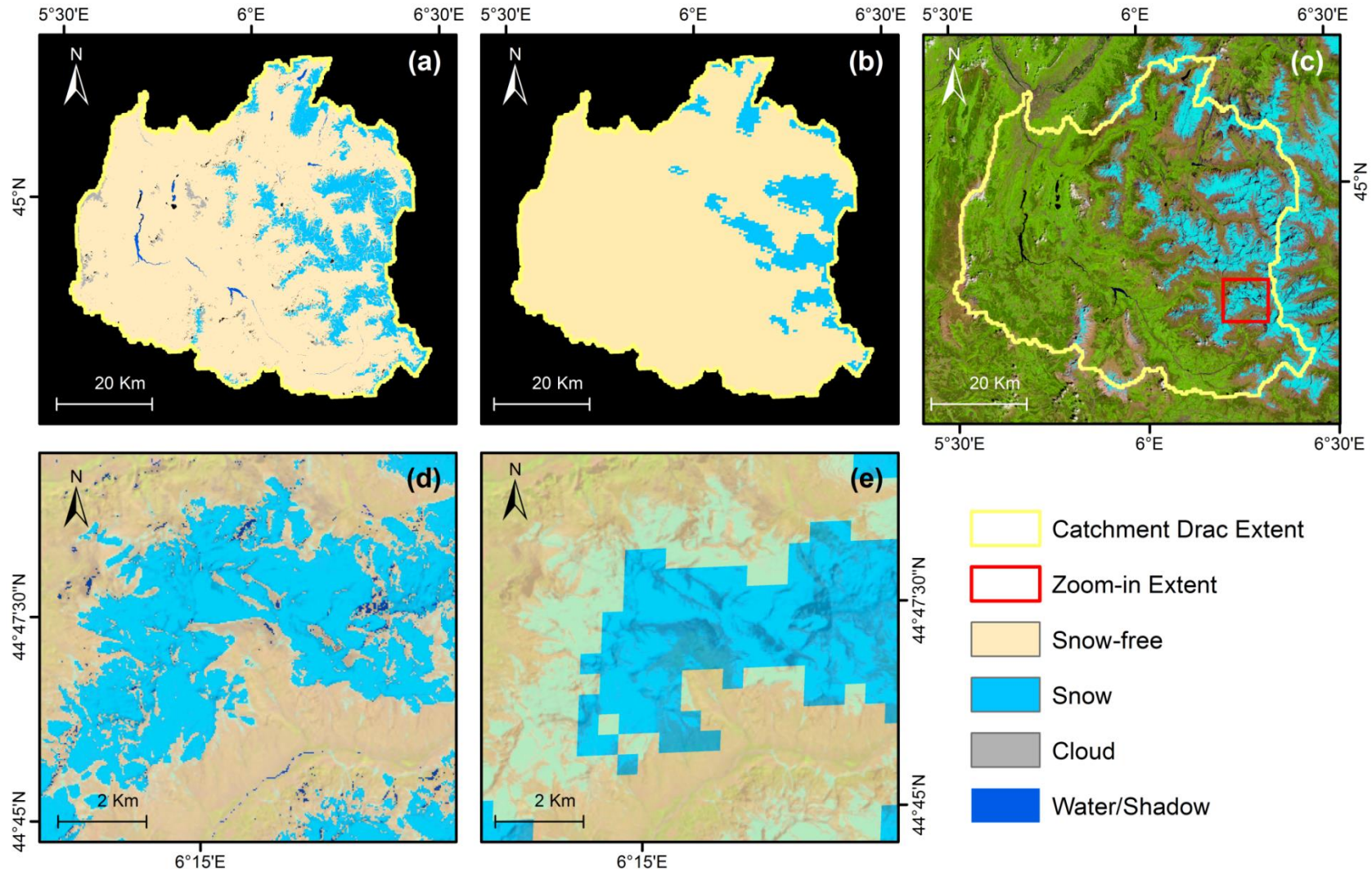


**Figure 6-6:** Snow Classification based on (a) Landsat 8 Operational Land Imager/Thermal Infrared Sensor (OLI/TIRS) and (b) Moderate Resolution Imaging Spectroradiometer (MODIS) imagery in the Catchment Drac on 07 June 2017, and the atmospherically and topographically corrected image in false colour composite (RGB: SWIR-NIR-RED) (c), as well as two zoom-ins (d–e).

**Table 6-1:** Confusion matrix relating satellite-derived snow classifications and ground snow-depth observations. Modified according to Hu et al. (2019b).

		Snow Depth Observations		
		Snow	Snow-free	UA
Classification	Snow	348	70	83.25%
	Snow-free	184	7118	97.48%
	PA	65.41%	99.02%	OA = 96.71%

### 6.2.2 Regional Snowline Elevations (RSEs) and Accuracy Assessment

To demonstrate the RSEs results, RSEs derived from the Landsat OLI/TIRS and ETM+ observations during the ablation season 2018 are displayed in Figure 6-7, it is representative for the general situation when dual Landsat sensors are in orbit (Figure 6-2) before the launch of Sentinel-2A in June 2015. As the acquisition dates of the original Landsat images differ spatially, for a better visualization, an ablation season is categorized into nine time slots in a near 10-day time interval (i.e. early/middle/end of April/May/June). "Spatially, in the northern Pyrenees (i.e. Ariege) RSEs are lower than in the southern part (i.e. Serge). Besides, the regional snowline in the northern part of Pyrenees is preserved longer compared to the southern part. In the two Carpathian catchments, particularly in Uzh, the RSEs last much shorter than in other investigated catchments during the ablation season 2018. In contrast, the regional snowlines are still preserved at the end of the ablation season 2018 in most of the Alpine catchments." (Hu et al., 2019b) One of the possible explanations is the higher elevation of the European Alps than the other investigated study areas, indicated by the elevation information provided by the DEM.

In terms of the temporal pattern, assuming snow is continuously melting, the snowline will be accordingly retreating towards a high elevation. In this regard, the occurrence of the reddish colour, indicating the snowline at the end of the ablation season (i.e. end of June), "should be located around the highest elevation. Otherwise, once the regional snowlines in reddish colour are located in lower elevation zones compared with previous ones, it indicates the occurrence of an intermediate snowfall event. Therefore, these results could help identify anomalies, such as intermediate snowfall events observed in Figure 6-7, where reddish/yellowish regional snowlines are of lower elevation than bluish/greenish ones. For example, the yellow-coloured (end of May) regional snowline appears in Adda and Tagliamento, and the coral-coloured (end of June) regional snowline is observed within Uzh." (Hu et al., 2019b) Moreover, within the Carpathian catchments, regional snowlines are rarely observed at the end of the ablation season, unless an intermediate snowfall event is occurs (e.g., Figure 6-7.h).

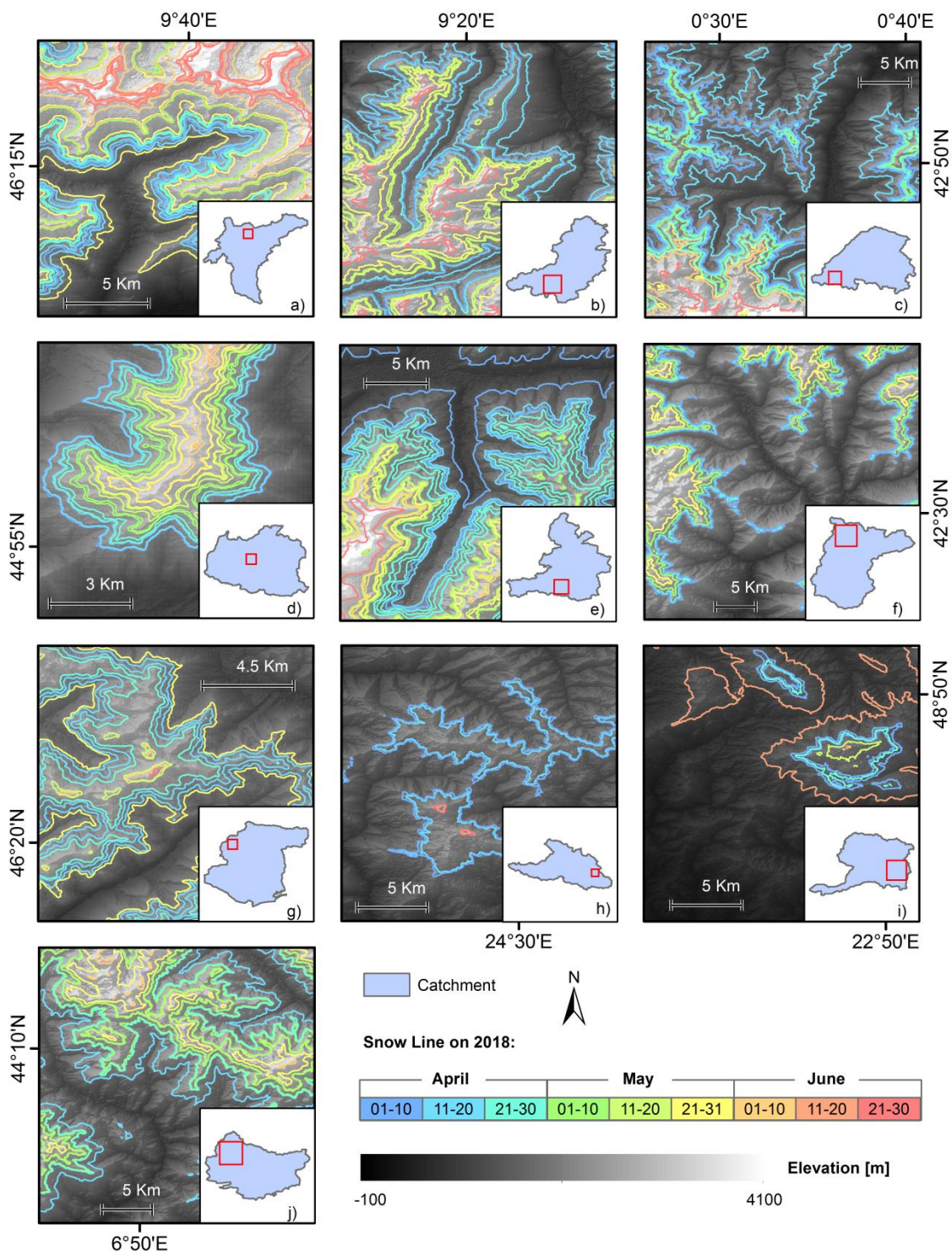


**Figure 6-7:** Snowlines based on Regional Snowline Elevations (RSEs) during the ablation season (from April to June) 2018 within the investigated catchments: a) Adda, b) Alpenrhein, c) Ariege, d) Drac, e) Salzach, f) Serge, g) Tagliamento, h) Tysa, i) Uzh, and j) Var. Modified according to Hu et al. (2019b).

Meanwhile, five quality indices (introduced in Section 5.3) are calculated (Figure 6-8). The first index, RI (Figure 6-8.a), illustrates the percentage of valid pixels (i.e. labelled as snow or land) from the satellite image within the catchment extent. The medians of RI in each catchment are more than 60%, and the upper and lower quantiles thereof are near

90% and 35%, respectively. It indicates an overall sufficient amount of valid pixels for RSE retrieval. The second index EI (Figure 6-8.b), measuring the percentage of erroneous pixels, indicates an overall low (median < 5%) erroneous pixels percentage. The medians of recall scores (Figure 6-8.c) are around 30%, which shows the median probability of detecting a classified snow pixel above the derived RSEs is around 30%. The medians of precision scores (Figure 6-8.d) are around 50% for the Alpine catchments (except Tagliamento), indicating 50% of the pixels above the derived RSEs are indeed snow. The last calculated index is F-score. The medians of the F-scores (Figure 6-8.e) are mostly near 30% for the Alpine catchments (except Tagliamento), while for the Pyrenean and Carpathian catchments the F-scores are comparably low.

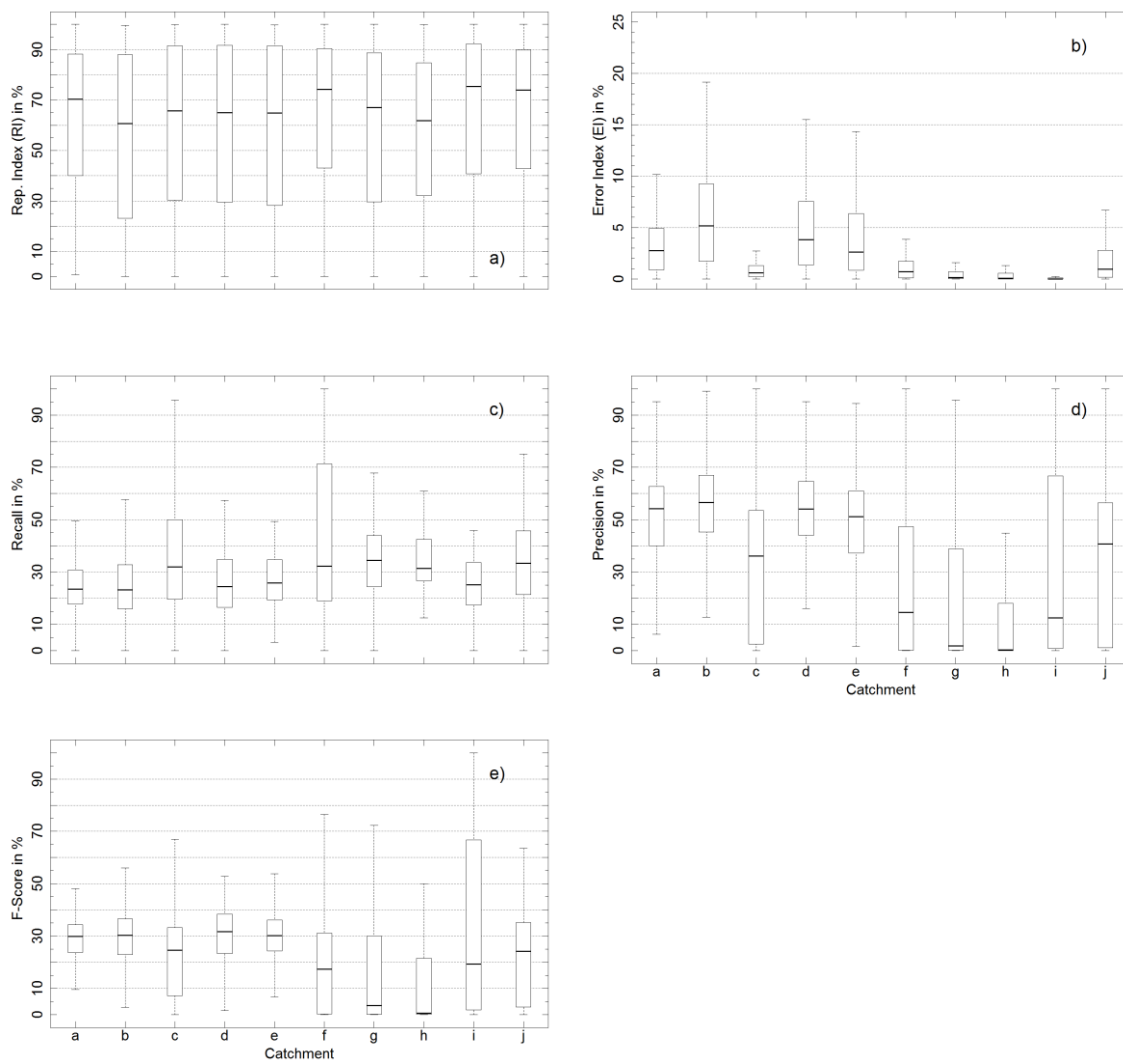


**Figure 6-8:** Accuracy assessment of the retrieved Regional Snowline Elevation (RSE) of each catchment, based on the Representativeness Index (RI), Error Index (EI), Precision, Recall, and F-score in each investigated catchment: a) Adda, b) Alpenrhein, c) Ariege, d) Drac, e) Salzach, f) Serge, g) Tagliamento, h) Tysa, i) Uzh, and j) Var.

### 6.2.3 Modelled Regional Snowline Elevations (RSEs) and Accuracy Assessment

Together with the daily snow coverage derived from the GSP, the densified time series of RSEs results are shown in Figure 6-9 for each investigated catchment. The increase of snow coverage during an ablation season could indicate the occurrence of snowfall events. It confirms the modelled RSE is able to represent the intermediate snowfall events, which is challenging in RSE retrieval using high resolution satellite data with long revisit time (Hall, 1985; Hu et al., 2019a, 2019 b). The snow coverage shows a high negative correlation to the RSE (mean correlation coefficient  $\bar{R} = -0.81$ , for the Alpine catchments  $\bar{R} = -0.87$ ).

The overall performance of RFR models is shown in Table 6-2, based on the Out-Of-Bag (OOB) results, including the percentages of explained variance and Root Mean Square Errors (RMSEs). In general all models show a good performance predicting the RSE, which achieved an overall average  $R^2$  around 0.66. It should be noted that performance of RFR models over-perform in Alpine catchment, whose mean  $R^2$  reaches 0.72, indicating the RFR models can explain 6% more variance there. The highest coefficient of determination ( $R^2$ ) is achieved in the catchment Drac ( $R^2 = 0.89$ ), and the least  $R^2$  is obtained in the catchment Uzh ( $R^2 = 0.48$ ). It is seemingly that the  $R^2$  may be in relation to the geographic settings of the catchment. Besides, the average RMSE is reported as 229.44 m.

**Table 6-2:** Percentage of the variance ( $R^2$ ) explained by the Random Forest Regression (RFR), and root mean squared error (RMSE).

Catchment	Percentage of explained Variance [%]	RMSE [m]
Adda	83.53	164.39
Alpenrhein	68.17	294.92
Ariege	64.17	298.45
Drac	89.27	144.44
Salzach	60.85	290.23
Serge	66.42	236.77
Tagliamento	48.08	339.90
Tysa	56.41	251.33
Uzh	42.99	108.62
Var	84.38	165.31

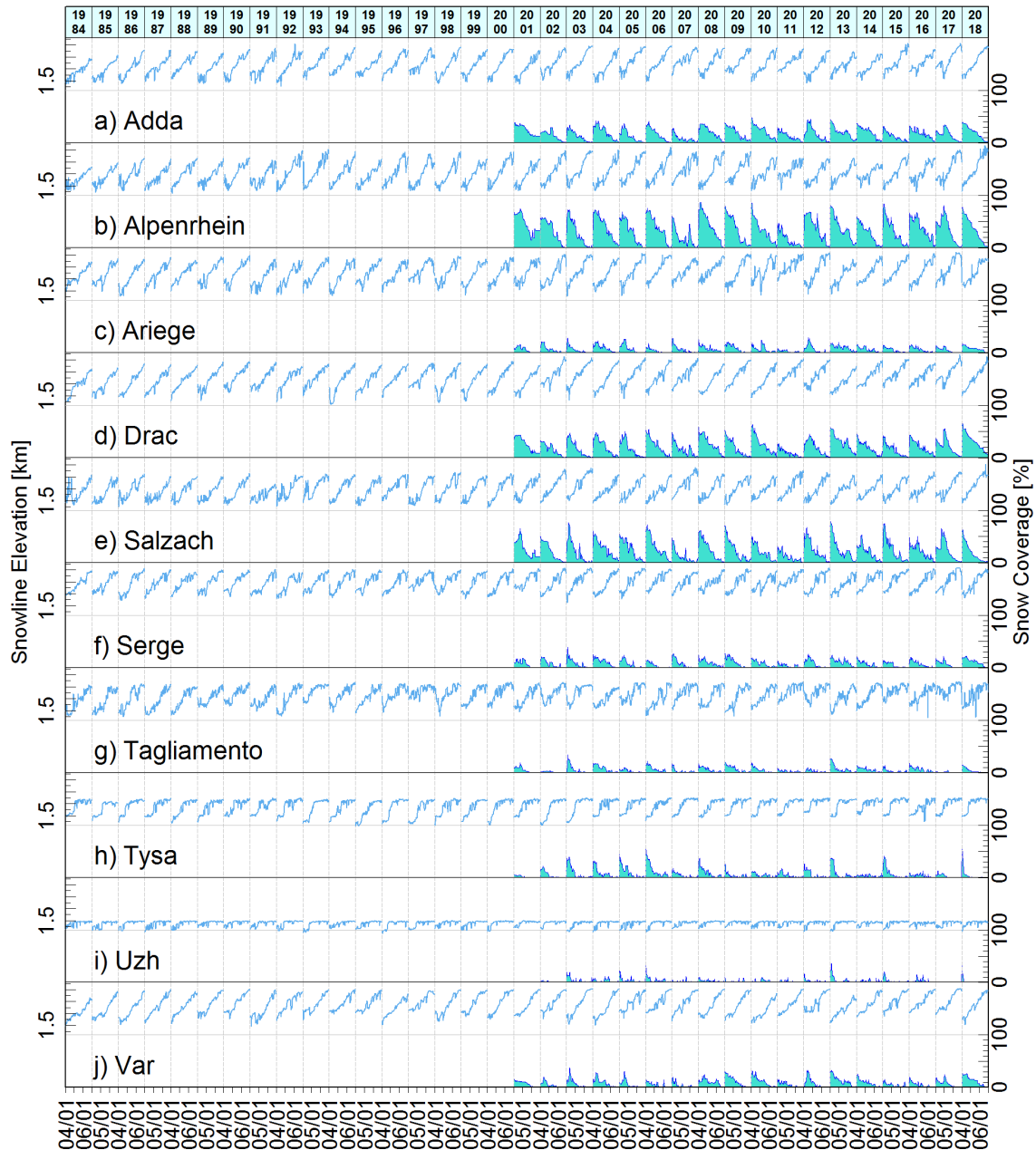


**Figure 6-9:** Time series of the modelled Regional Snowline Elevations (RSEs) displayed in solid blue line, and snow coverage derived from the Global Snow Pack (GSP) during the ablation seasons 1984–2018.

Regarding the importance of climate variables to RSE variability, the permutation importance of the RFR models is reported in Table 6-3. Cumulated sum of 2 m air temperature and mean snow depth are the most important variables, which are of MAE improvements range from 5.03% to 19.99%. Also, the cumulated skin temperatures are overall influential. In catchment Drac, the influence of runoff is more pronounced than the other investigated catchments. However, total precipitation is reported as the least important climate variable in predicting RSEs.

**Table 6-3:** Permutation importance of each input variable in the investigated catchments.

	<b>Parameters</b>	<b>Adda</b>	<b>Alpenrhein</b>	<b>Ariege</b>	<b>Drac</b>	<b>Salzach</b>
<b>2 m air Temperature</b>	Min	4.26	3.65	6.98	5.07	4.79
	25% Percentile	6.43	4.59	3.74	4.35	4.06
	Median	8.76	4.26	4.35	5.38	4.41
	25% Percentile	8.35	0.15	2.89	5.40	1.71
	Max	6.42	<b>-1.33</b>	4.87	5.86	1.05
	Mean	6.21	4.23	3.77	4.60	4.10
	Cumulated Sum	<b>14.22</b>	<b>10.54</b>	<b>19.46</b>	<b>14.14</b>	8.44
<b>Total Precipitation</b>	Min	2.81	0.67	1.47	1.99	<b>-3.22</b>
	25% Percentile	2.95	0.07	0.79	3.10	<b>-1.87</b>
	Median	4.00	0.17	2.61	4.20	0.45
	25% Percentile	4.30	2.04	3.65	5.48	0.47
	Max	3.93	1.41	2.72	6.97	<b>-0.72</b>
	Mean	3.96	<b>-0.55</b>	1.36	3.38	<b>-1.04</b>
	Cumulated Sum	8.58	2.24	7.42	3.69	3.78
<b>Runoff</b>	Min	6.45	3.36	4.68	<b>10.41</b>	6.09
	25% Percentile	<b>11.81</b>	6.12	3.09	<b>11.66</b>	2.75
	Median	8.14	7.08	4.69	<b>11.70</b>	4.01
	25% Percentile	8.73	3.90	3.75	<b>13.65</b>	0.36
	Max	6.81	<b>-0.44</b>	5.19	<b>10.83</b>	3.07
	Mean	6.66	4.66	1.00	<b>13.83</b>	3.54
	Cumulated Sum	8.35	2.99	6.92	8.67	3.80
<b>Snow Depth</b>	Min	0.00	<b>-2.36</b>	0.00	7.06	<b>-4.06</b>
	25% Percentile	3.83	6.56	0.00	8.75	<b>-1.24</b>
	Median	<b>12.06</b>	5.56	2.43	<b>12.03</b>	3.81
	25% Percentile	<b>11.21</b>	7.24	6.29	<b>11.06</b>	6.16
	Max	<b>10.27</b>	6.64	5.58	9.99	7.39
	Mean	<b>14.79</b>	9.32	<b>18.26</b>	<b>15.00</b>	9.20
	Cumulated Sum	7.09	1.53	2.83	9.79	2.10
<b>Skin Temperature</b>	Min	7.59	4.75	9.39	8.48	<b>-0.60</b>
	25% Percentile	9.02	8.61	7.70	8.03	6.10
	Median	<b>13.27</b>	7.56	6.98	7.68	6.20
	25% Percentile	<b>13.63</b>	3.81	5.45	6.64	3.92
	Max	8.28	<b>-2.36</b>	5.32	8.33	2.14
	Mean	6.66	6.65	5.11	7.47	4.13
	Cumulated Sum	<b>14.74</b>	<b>12.35</b>	<b>16.70</b>	<b>15.95</b>	9.80

Table 6-3 (Continued)

	Parameters	Serge	Tagliamento	Tysa	Uzh	Var
<b>2 m air Temperature</b>	Min	9.33	8.79	4.96	8.23	3.61
	25% Percentile	7.14	7.06	4.93	8.67	4.19
	Median	3.82	5.53	3.22	3.73	4.78
	25% Percentile	6.26	3.95	3.74	3.82	2.26
	Max	7.14	2.49	4.31	2.89	3.66
	Mean	4.27	6.39	4.01	6.24	3.03
	Cumulated Sum	<b>12.33</b>	8.03	<b>14.98</b>	<b>12.26</b>	<b>15.03</b>
<b>Total Precipitation</b>	Min	0.03	<b>-0.26</b>	0.10	<b>-2.22</b>	0.69
	25% Percentile	2.13	1.09	<b>-0.36</b>	<b>-1.50</b>	<b>-2.42</b>
	Median	0.05	5.21	2.25	2.66	<b>-0.84</b>
	25% Percentile	2.39	6.51	1.32	3.75	1.61
	Max	1.40	4.84	0.94	3.38	0.34
	Mean	0.91	3.99	<b>-2.11</b>	3.60	<b>-0.77</b>
	Cumulated Sum	3.65	6.16	5.48	5.75	1.37
<b>Runoff</b>	Min	<b>-1.51</b>	7.45	4.13	1.40	<b>10.85</b>
	25% Percentile	<b>-1.69</b>	5.04	4.77	2.30	9.40
	Median	3.44	4.95	4.35	3.36	6.98
	25% Percentile	3.23	5.93	4.45	2.46	4.37
	Max	1.63	4.34	4.49	3.75	2.67
	Mean	2.89	6.98	3.77	4.90	4.90
	Cumulated Sum	8.57	8.12	2.30	5.02	4.56
<b>Snow Depth</b>	Min	0.00	0.00	0.00	0.00	0.00
	25% Percentile	0.00	<b>-1.67</b>	<b>-1.00</b>	1.12	2.35
	Median	5.53	8.51	3.49	1.95	<b>12.44</b>
	25% Percentile	8.32	5.04	6.72	1.79	<b>10.73</b>
	Max	6.16	5.26	5.43	1.27	<b>11.98</b>
	Mean	<b>10.04</b>	<b>19.99</b>	8.46	5.03	<b>11.72</b>
	Cumulated Sum	<b>-0.27</b>	<b>-0.27</b>	6.71	<b>12.30</b>	9.33
<b>Skin Temperature</b>	Min	<b>10.03</b>	5.77	<b>10.56</b>	8.40	6.22
	25% Percentile	8.70	8.55	6.67	<b>14.23</b>	8.28
	Median	8.62	6.98	6.80	6.69	7.54
	25% Percentile	4.94	4.56	4.62	2.81	5.43
	Max	3.78	4.74	5.58	2.88	6.44
	Mean	6.22	7.43	6.62	6.34	6.12
	Cumulated Sum	<b>13.04</b>	9.22	<b>13.87</b>	<b>10.29</b>	15.62



## 6.3 Long-term Snowline Dynamics in European Mountains

The present study aims to characterize regional snowline dynamics during the ablation seasons. Within this context, two aspects of the regional snowline dynamics are presented in the following sections, i.e. intra-annual and inter-annual variations of regional snowlines. To assess the intra-annual variation, locations of RSEs at 1-day interval during an ablation season are analysed. Afterwards, three measures are presented with regards to the intra-annual variation, including RSRC steepness,  $AT_{MA}$ , as well as the 35-year trends of the median RSEs and the RSEs at the beginning of the ablation season. Lastly, a comprehensive accuracy assessment is provided in the last section.

### 6.3.1 Intra-annual Variations of Regional Snowlines during the Ablation Seasons 1984–2018

In terms of the intra-annual variations of the RSE, Figure 6-10 illustrates the frequency of an elevation covered by snow on a certain day of the ablation seasons 1984–2018. It shows that the RSEs are, in general, lower in the Northern Alps than the Southern Alps. The intra-annual variation of the RSEs is larger in the Southern Alps. In the southern Pyrenean catchment Serge, the RSEs at the beginning of the ablation seasons are lower than the northern Pyrenean catchment Ariege. Also, the variation of the RSEs in Ariege is larger than Serge during the ablation season 1984–2018. In the two investigated Carpathian catchments, the RSEs reach the maximum elevation in May, especially in the catchment Uzh. In general, the occurrences of the anomalously low RSEs also indicate the probable intermediate snowfall events therein. The width of the curves suggests the timing of the most significant RSEs variability. Among the all investigated catchments, the Apline catchment Tagliamento shows the uniquely high variation in the beginning of the ablation seasons, mainly towards a high elevation.

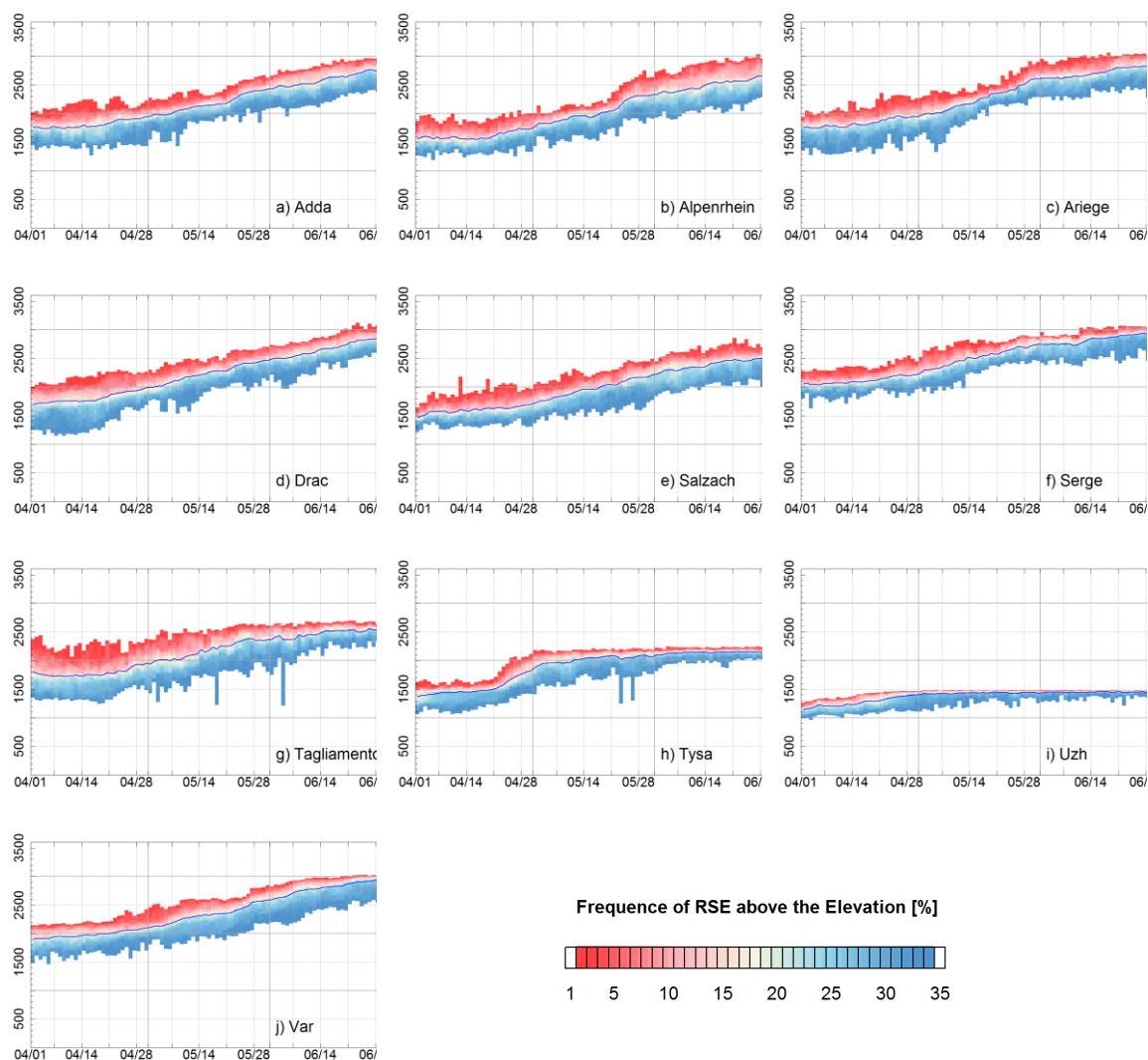


**Figure 6-10:** Frequency of the Regional Snowline Elevations (RSE) above a certain elevation during the ablation seasons between 1984 and 2018 within the investigated catchments: a) Adda, b) Alpenrhein, c) Ariege, d) Drac, e) Salzach, f) Serge, g) Tagliamento, h) Tysa, i) Uzh, and j) Var. The blue solid line indicates the 35-year median RSE at each day-of-year during an ablation season.

### 6.3.2 Inter-Annual Variability of Regional Snowlines during the Ablation Seasons 1984–2018

To demonstrate the inter-annual regional snowline variations, the time series of the steepness and  $AT_{MA}$  from RSRCs are shown in Figure 6-11 and Figure 6-13 for each study area. The steepness of the RSRC represents the velocity of regional snowline retreat, since the  $AT$  is related to the day-of-year in the ablation season. Among the investigated catchments, significantly positive trends have been detected, except for the Alpine catchment Alpenrhein, the Pyrenean catchment Ariege, and the Alpine catchment Var. This indicates the lift of the RSEs at the beginning of the ablation seasons. The 35-year  $AT$  time

series (see Figure 6-12) indicates a tendency of increasing AT during the ablation seasons. Such tendency intensifies the retreat of RSEs during the ablation season.

Also, it is necessary to investigate the timing of the snow-clearance process.  $AT_{MA}$  illustrates how much AT is required for a regional snowline to reach the middle of the RLE. Significantly negative trends of  $AT_{MA}$  are detected in some catchments, including Tagliamento and Tysa. It indicates that 11.8 and 3.97 less Celsius per year are needed for the regional snowlines to reach the middle of the RSRC in the Tagliamento and Tysa, respectively. In these two catchments, significantly positive trends of RSRCs' steepness are observed. It also suggests higher RSEs in early April, and that the disappearance of snowline retreat occurs earlier.

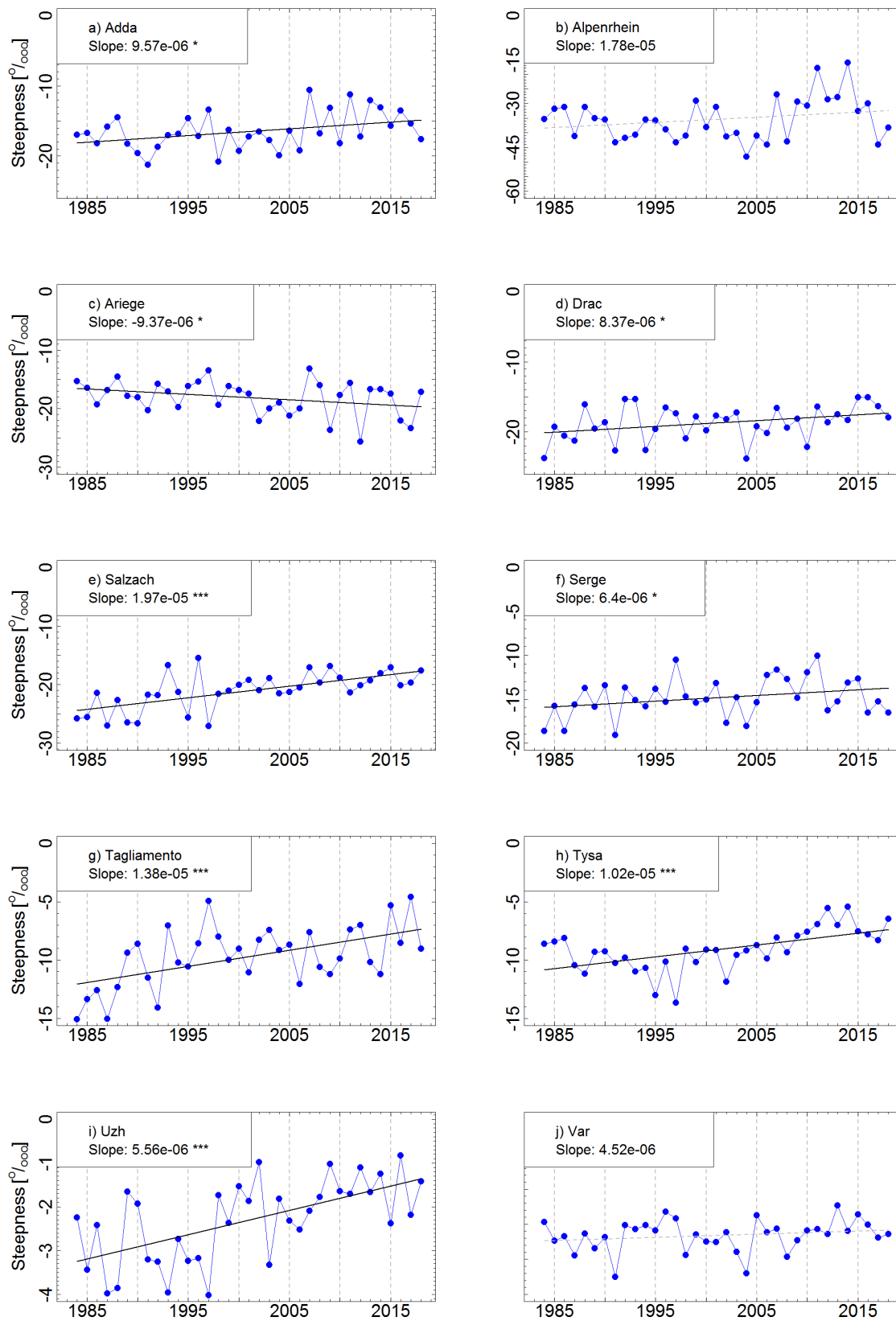


**Figure 6-11:** Steepness of the Regional Snowline Retreat Curves (RSRCs) of the investigated catchments between 1984 and 2018. Modified according to Hu et al. (2019b).

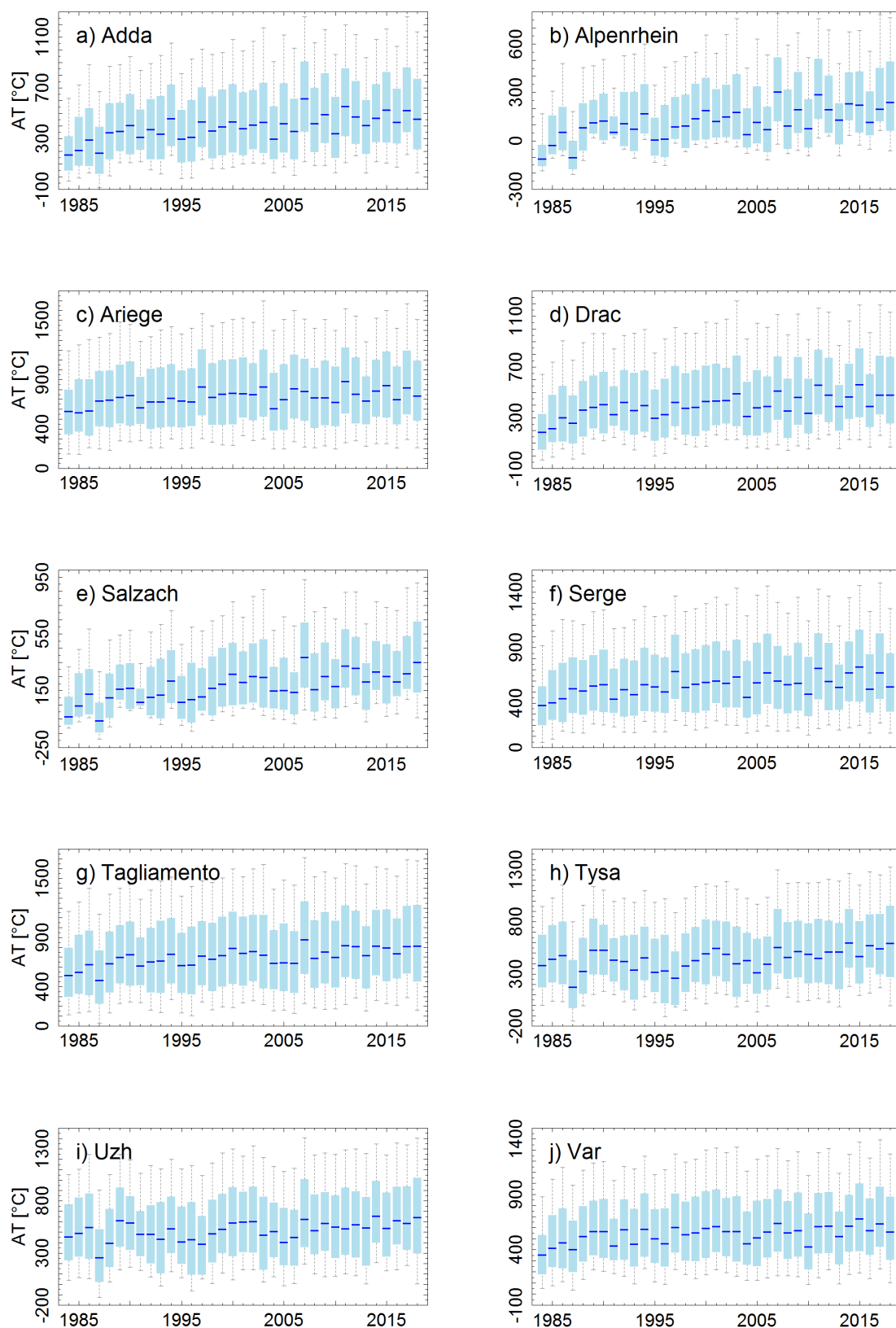


**Figure 6-12:** Box-whisker plots presenting max, min, median as well as 25<sup>th</sup> and 75<sup>th</sup> percentiles of the Accumulated Temperatures (ATs) between April and June of the investigated catchments (1984–2018). Modified according to Hu et al. (2019b).

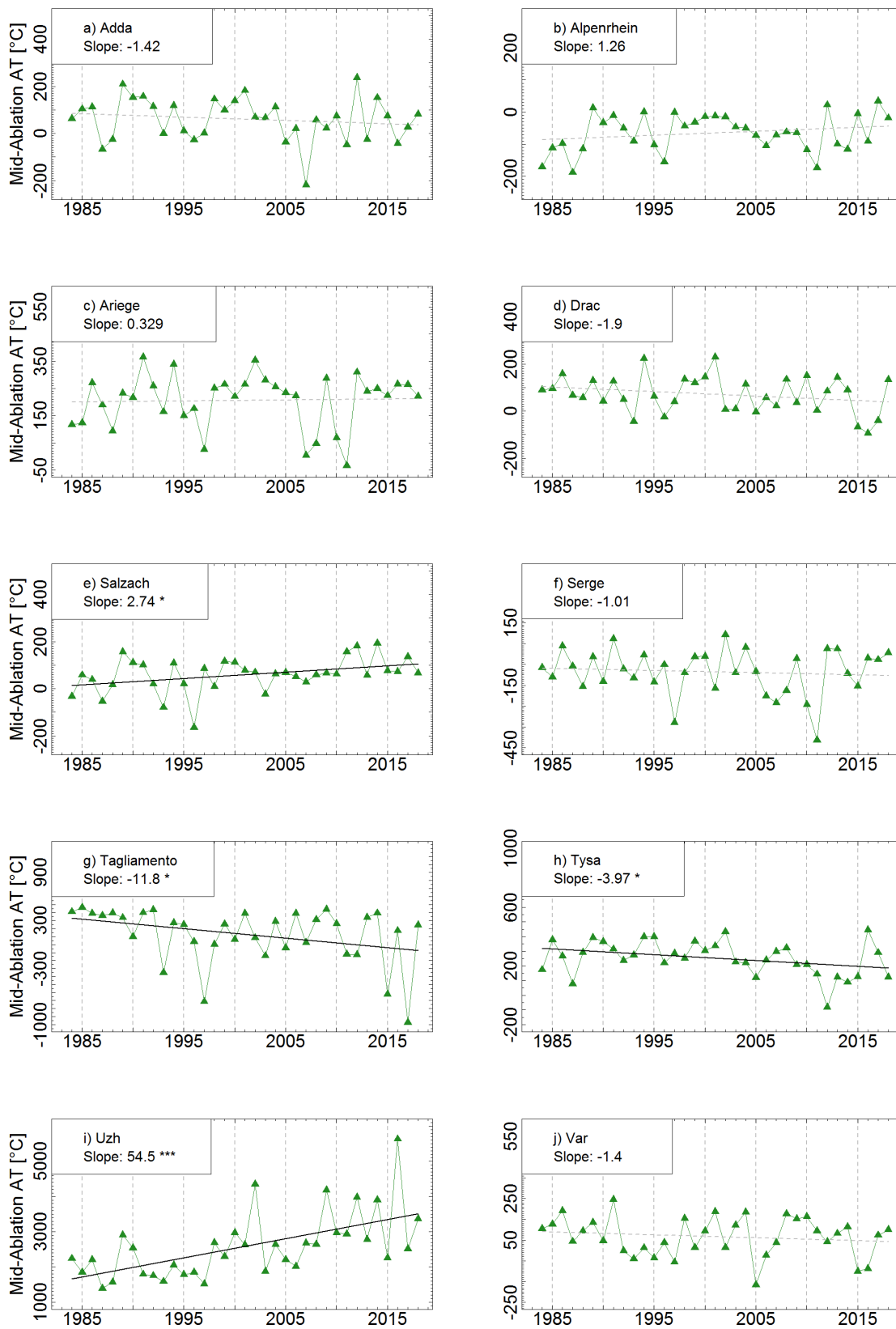


**Figure 6-13:** Accumulated Temperature of the Mid-Ablation season ( $AT_{MA}$ ) of the Regional Snowline Retreat Curves (RSRCs) of the investigated catchments between 1984 and 2018. Modified according to Hu et al. (2019b).

Results of the trend analysis with regards to median RSEs and the RSEs at the beginning of the ablation seasons between 1984 and 2018 have been summarized in Table 6-4. The results show an overall significant trend of higher median RSE (except for Serge and Uzh), and higher RSE at the beginning of the ablation season (except for Serge). The median RSE becomes higher in all the selected catchments, with an average speed of around  $4.66 \text{ m} \cdot \text{a}^{-1}$  (median) and  $5.87 \text{ m} \cdot \text{a}^{-1}$  (at the beginning of the ablation season). The fastest significant retreat is observed in the catchment Drac ( $10.66 \text{ m} \cdot \text{a}^{-1}$ , at the beginning of the ablation season), and the slowest significant retreat is observed in the catchment Uzh ( $1.74 \text{ m} \cdot \text{a}^{-1}$ , at the beginning of the ablation season). The RSE at the beginning of the ablation season suggests a faster retreat than the median, whose average difference is approximately  $1.21 \text{ m} \cdot \text{a}^{-1}$ , particularly in the catchment Drac ( $3.72 \text{ m} \cdot \text{a}^{-1}$ ).

**Table 6-4:** Summary of the Trend analysis with regards to median RSEs and the RSEs at the beginning of the ablation seasons between 1984 and 2018.

Catchment	5 %		Median	
	Slope [ $\text{m} \cdot \text{a}^{-1}$ ]	p-value	Slope [ $\text{m} \cdot \text{a}^{-1}$ ]	p-value
Adda	8.560	0.00020	5.243	0.00895
Alpenrhein	5.766	0.00001	5.642	0.00273
Ariège	7.771	0.00185	4.453	0.01470
Drac	10.656	0.00050	6.933	0.00108
Salzach	3.488	0.00505	4.660	0.03820
Serge	2.577	0.15100	1.568	0.30500
Tagliamento	8.821	0.00222	8.777	0.00255
Tysa	4.885	0.02990	3.6727	0.00016
Uzh	1.7376	0.02930	-0.1708	0.37500
Var	4.468	0.08430	5.778	0.04060

### 6.3.3 Accuracy Assessment of Regional Snowline Retreat Curves (RSRCs)

To assess the performance of the robust M-estimation of the derived RSRCs, the corrected  $R^2$  (Figure 6-14) for robust estimation, MAE (Figure 6-15), and RMSE (Figure 6-16) are calculated for each fitted RSRC. The three metrics summarize the fit of the RSLC to the RSE inputs. Within the Alpine catchments (excluding Tagliamento and the Carpathian catchments), the median corrected  $R^2$  is around 0.90. Therein, more than 90% of the variances in the RSEs can be explained by the variation of AT. According to the

median, the RSRCs explain on average approximately 10% less variation in the RSEs in the Pyrenean catchments than the aforementioned Alpine catchments. In the Tysa and Tagliamento, most of the RSRCs are only able to predict 65% of the RSE variability according to their comparably small median corrected  $R^2$  (near 65%). The models show weak performance in the Carpathian catchment Uzh, where the models explain only approximately 40% of the RSE variability therein. Besides, the upper quantile, median, and lower quantile of MAEs are generally around 25 m, 20 m, and 15 m, respectively. Most of the RMSEs are lower than 200 m.

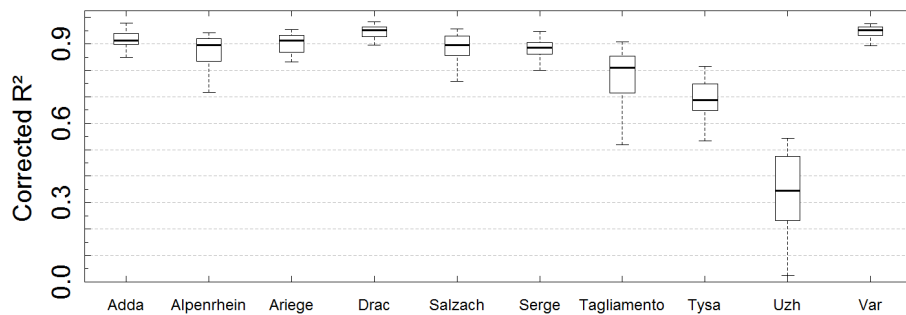


**Figure 6-14:** Box-whisker plots presenting max, min, median as well as 25<sup>th</sup> and 75<sup>th</sup> percentiles of the Corrected  $R^2$  of the Regional Snowline Retreat Curves (RSRCs).

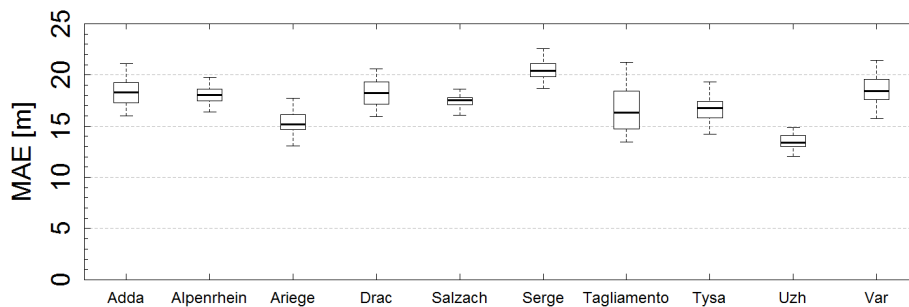


**Figure 6-15:** Box-whisker plots presenting max, min, median as well as 25<sup>th</sup> and 75<sup>th</sup> percentiles of the Mean Absolute Error (MAE) of the Regional Snowline Retreat Curves (RSRCs).

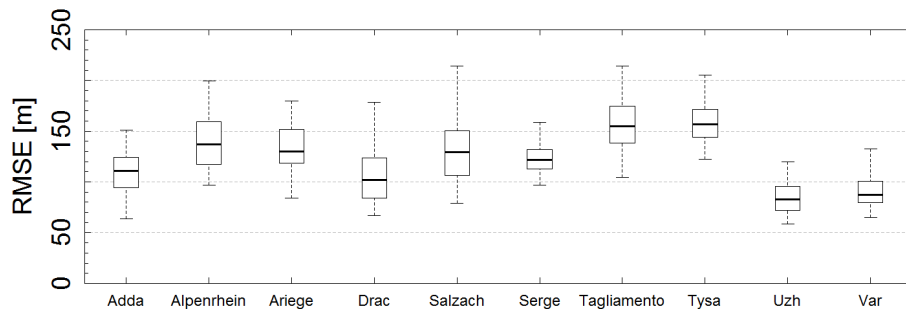


**Figure 6-16:** Box-whisker plots presenting max, min, median as well as 25<sup>th</sup> and 75<sup>th</sup> percentiles of the Root Mean Squared Error (RMSE) of the Regional Snowline Retreat Curves (RSRCs).



## 6.4 Potential Climate Drivers and Consequences of the Detected Long-Term Snowline Dynamics in the European Mountains

Based on the derived RSE dynamics in the previous sections, two case studies are carried out, linking RSEs to air temperature anomalies and river discharge dynamics, respectively. The first case study investigates the potential responses of the RSEs to the air temperature dynamics, which are assumed as the main climate driver of the observed snowline retreat. The second case study looks into the patterns between RSEs and river discharges, since the observed trends of river flood timing in Europe is shifting to the early ablation season.

### 6.4.1 Snowline Dynamics and Air Temperature Anomalies

The time series of RSE for each study area are displayed in Figure 6-17, together with the monthly air temperature difference to the 35-year mean. When heat wave events (e.g., 2003 and 2007) occurred in Europe, the mean monthly RSEs were much lower than the other years. When anomalously high air temperature occurs in the early ablation season, for example, in April 2007 within Adda, it does not only result in anomalously high RSE in the early ablation season, but also accelerate the recession of the regional snowline to its maximum elevation.

**Table 6-5:** Summary of the correlation analysis between Regional Snowline Elevations (RSEs) and monthly air temperature anomalies in each month during the ablation seasons 1984–2018.

Catchment	April	May	June
Adda	<b>0.80</b>	<b>0.77</b>	<b>0.84</b>
Alpenrhein	<b>0.78</b>	<b>0.87</b>	<b>0.85</b>
Ariege	<b>0.75</b>	<b>0.79</b>	<b>0.85</b>
Drac	0.64	<b>0.72</b>	<b>0.80</b>
Salzach	0.43	<b>0.83</b>	<b>0.79</b>
Serge	0.66	<b>0.84</b>	<b>0.92</b>
Tagliamento	0.31	<b>0.78</b>	<b>0.76</b>
Tysa	0.66	0.64	<b>0.76</b>
Uzh	<b>0.82</b>	0.17	-0.26
Var	0.38	<b>0.77</b>	0.64

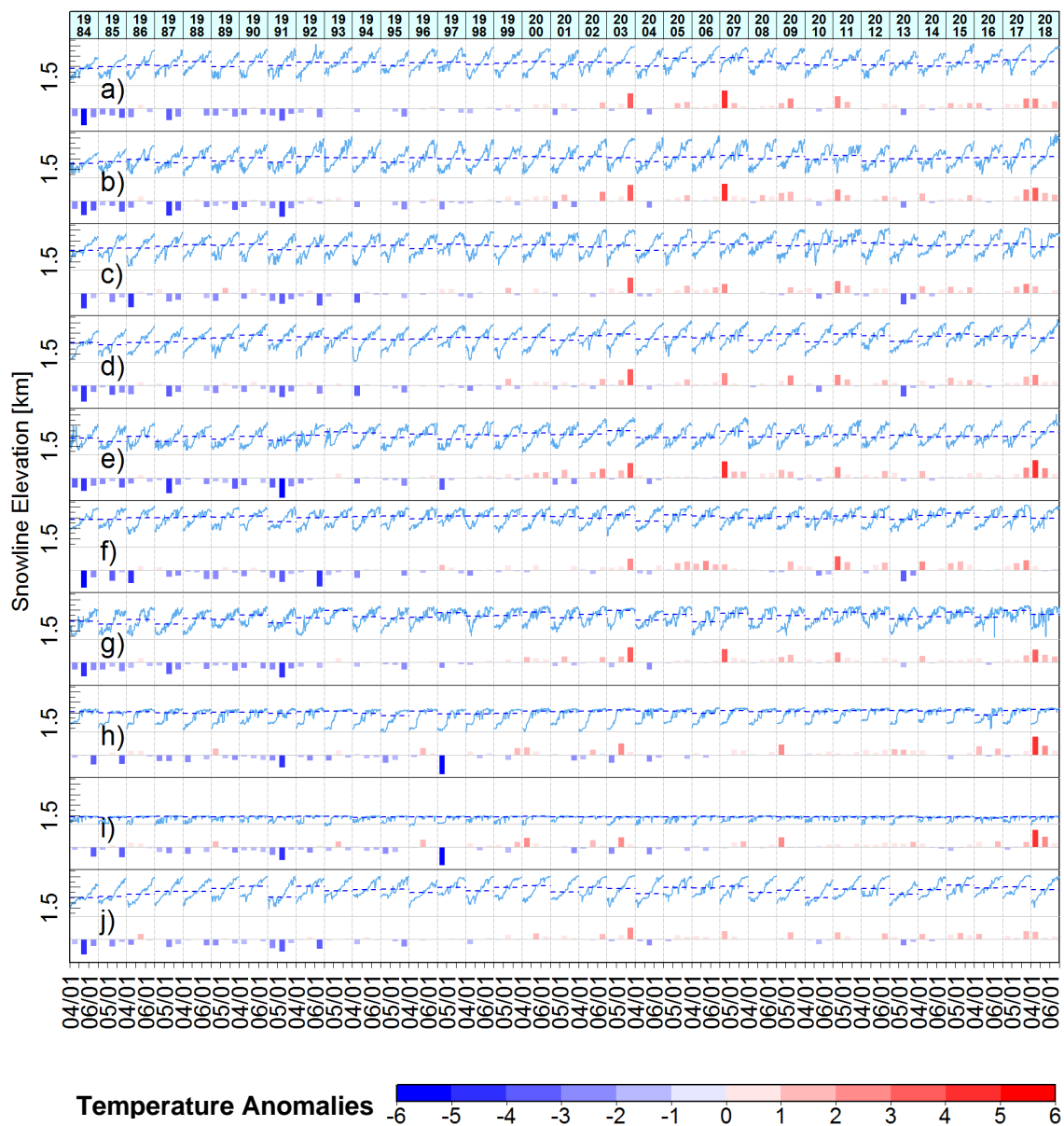


**Figure 6-17:** Temporal variation of the Regional Snowline Elevations (RSEs) during the ablation seasons 1984–2018 in each investigated catchment. The blue dash lines represent smoothed RSEs using Savitzky–Golay filter with 2<sup>nd</sup> order polynomial in 3-day window.

The retrieved monthly mean RSE (blue dash line) shows a good correlation ( $\bar{R} = 0.7$ , Table 6-5) with the monthly air temperature anomaly, which is well-pronounced in months with extremely low/high air temperature. The correlation coefficients increase along with the time during an ablation season. Generally, the correlation coefficients are higher in June than in April.

### 6.4.2 Snowline and Discharge Dynamics during the Ablation Seasons 2000–2016

The discharge time series from GRDC dataset is displayed in Figure 6-18 and Figure 6-19 for the ablation seasons 2000–2016, together with the RSE and snow coverage information. The peak discharge events are well-indicated in the time series of both RSEs and snow coverage, i.e. the turning points therein. Correlation analyses are performed to preliminarily investigate the relationship between river discharge and RSE, as well as between river discharge and snow coverage. The correlation coefficient ( $R$ ) between river discharge and RSE is 0.52 in the catchment Alpenrhein, and is 0.21 in the catchment Salzach. In term of the relationship assessment between river discharge and snow coverage, the correlation coefficient ( $R$ ) is  $-0.49$  in the catchment Alpenrhein, and is  $-0.21$  in the catchment Salzach. The absolute values of the correlation coefficients are quite similar in both between river discharge and RSE, and between river discharge and snow coverage. For the catchment Alpenrhein, the absolute value of correlation coefficient ( $R$ ) between river discharge and RSE is 0.03 higher than that between river discharge and snow coverage. It indicates that approximately 3% more variation in river discharge can be explained by RSE than that by snow coverage.

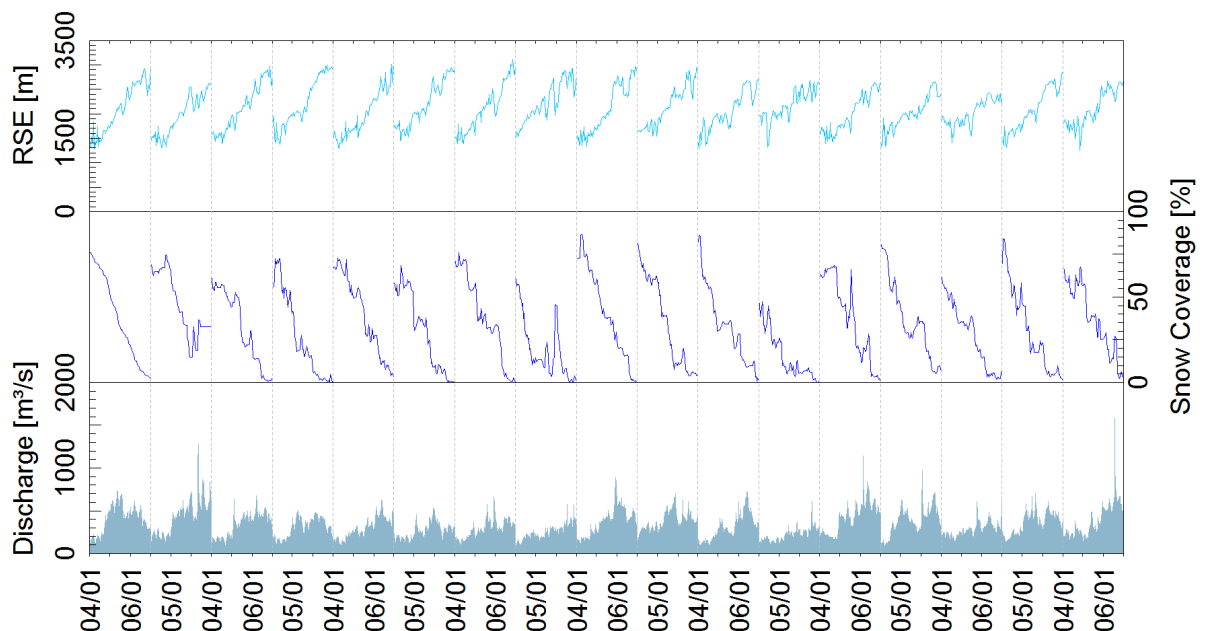


**Figure 6-18:** Landsat-based Regional Snowline Elevations (RSEs), MODIS-based snow coverage, and river discharges measured at ground station during the ablation season 2000–2016 in the Alpine catchment Alpenrhein.

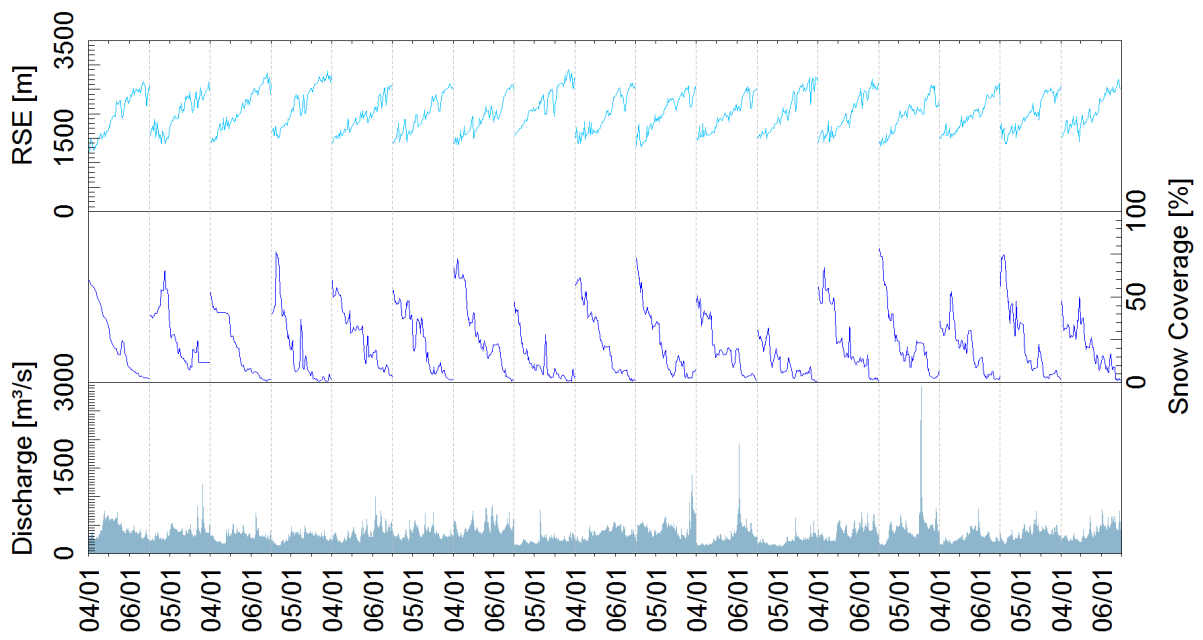


**Figure 6-19:** Landsat-based Regional Snowline Elevations (RSEs), MODIS-based snow coverage, and river discharges measured at ground station during the ablation season 2000–2016 in the Alpine catchment Salzach.

## CHAPTER 7

### 7 Discussion

This chapter discusses the presented results from the previous sections. This includes the following perspectives: (1) gaps in the long-term Landsat Collection 1 archive, (2) challenges regarding the snowline elevation derivation and validation, (3) different aspects of the retrieved snowline elevation dynamics, and (4) the potential triggers and consequences in relation to the detected snowline dynamics. The first part investigated the data gaps in the Landsat Archive due to missing observations and cloud contamination. Afterwards, challenging aspects about snowline dynamics retrieval and validation are discussed. Next, the estimated snowline dynamics are evaluated with respect to their peripheral geographical settings as well as in the context of existing studies. In the last part, potential applications of the derived RSE dynamics are discussed. Additionally, results from two case studies investigating associations between potential climate drivers and consequences of detected snowline elevation dynamics are examined.

#### 7.1 Gaps in the Long-Term Landsat Collection 1 Archive

In this section, the availability of the Landsat Collection-1 archive over Europe is analysed, to evaluate its suitability for time series analysis of snow cover dynamics in Europe. For this purpose, the data volume of the entire Landsat Collection-1 archive (TM/ETM+/OLI/TIRS) is presented with respect to ascending/descending orbit, data quality, and processing levels. Then the spatial distribution of the Landsat Collection-1 data over Europe is depicted together with the monthly data volume. Accordingly, spatial extent and periods of existing data gaps in Europe between 1982 and 2017 are identified. Furthermore, cloud coverage is a significant limiting factor with respect to the usage of optical satellite images. In this thesis, the CFMask algorithm was employed to generate cloud masks. The resulting cloud masks were analysed to delineate cloud-contaminated pixels as well as the severity of cloud cover in the Landsat Collection 1 time series.

##### 7.1.1 Significant TM Data Gaps in the 1990s and Southwestern Europe

In Section 6.1.2, data gaps and uneven spatiotemporal distribution of the Landsat Collection 1 data were discovered for Europe (see Figure 6-2). These data gaps and their

heterogeneous distribution were mainly caused by four reasons: (1) satellite sensor failures, (2) commercialization attempt, (3) data sharing and shortage, as well as (4) acquisition priority plan. Both instruments, Landsat 4–5 TM, had no onboard recording capacities. Therefore, data downlinking is crucial. The Landsat-4 satellite was launched in July 1982. In 1983 two solar panels and both direct downlink transmitters failed (Chander et al., 2007). Due to this failure, transmission of Landsat-4 TM data was not possible. Only after the Tracking and Data Relay Satellite System (TDRSS) became operable, Landsat-4 TM observations could be transmitted and relayed to the ground stations via TDRSS. Moreover, the primary Landsat-5 Ku-band TDRSS transmitters, as well as the secondary, failed in July 1987 and 1992, respectively. Since then Landsat-5 data transmission was limited to direct, real-time X-band transmission. Landsat-5 TM data sensed within the US and ICs international ground stations and their reception circle-vicinity were successfully transmitted (Chander and Micijevic, 2006). Otherwise, the observations that cannot be transmitted via direct and real-time X-band transmission, are permanently lost due to the Landsat-5 Ku-band TDRSS transmitter failure.

Another issue was the Landsat commercialization experiment (also known as “The era of privatization”, see Goward et al., 2006), when the Earth Observation Satellite Company (EOSAT) took over the Landsat operations between 1985 and 2001. Many Landsat observations were dismissed and the spatial coverage was shrunk, as the Landsat acquisition priorities were given to the requests of established customers. Meanwhile, researchers used free-of-charge meteorological satellite images or alternative EO imagery. Contemporarily, the French satellite SPOT constellation was orbiting the Earth providing a potential source to fill the gaps in the Landsat data archive.

Goward et al. (2006) reported that the total number of the Landsat data within the IC archives exceeds by far the sum of what the USGS archive was holding. Among the ICs, ESA holds most of the historical and current Landsat MSS/TM/ETM+/OLI/TIRS images (>1.5 million) (Goward et al., 2006; Saunier et al., 2017). Large quantities of these data are unique and not duplicated in the USGS Landsat Archive (Wulder et al., 2016). Since the implementation of Landsat Global Archive Consolidation (LGAC), historical Landsat data held by the ICs are being brought back to the Earth Resources Observation and Science (EROS) center. Several factors such as: IC business model, data sharing policy, antiquated/degrading media, and unfamiliar data formats still hamper the ingesting process. In Europe, approximately 500,000 Landsat5 TM images were archived at ESA’s KIS station and could not be geometrically and radiometrically corrected due to the missing Payload Correction Data (PCD) files (Micijevic et al., 2017; Wulder et al., 2016). Once these scenes are processed, the Landsat availability in Europe might be improved considerably.

Apart from the aforementioned factors, the seasonality pattern (Figure 6-2) is also a reflection of the preferential acquisition plan, i.e. the Long Term Acquisition Plan (LTAP) for Landsat 7 and Landsat 8 missions. The objective of the LTAP is to update the global

Landsat Archive with sunlit, substantially cloud-free land scenes for land surface dynamics monitoring (details see Arvidson et al., 2006, 2001), using a scheduler based on predicted scene quality, cloud cover statistics of the historical acquisitions, urgency and efficiency of acquisitions. Under the sunlit (sun elevation  $> 15^\circ$  in the Northern Hemisphere) and cloud-avoidance criteria, it would cause potential data availability decrement in high altitude and (especially) high latitude regions excluding the identified niche locations. For snow-related studies, it promotes the chance of late summer snow-line detection. On the other hand, the missing winter observations would result in formidable challenges in deriving vital temporal snow cover indices, such as the SCS and SCM.

### 7.1.2 Influence of Cloud Cover and Haze on Data Availability

Clouds frequently cover a large proportion of Europe, especially in high altitudes and/or high latitude regions as presented in Section 6.1.3. Cloud contamination is one of the most limiting factors with regards to optical EO data availability. An image-to-image registration tolerance of less than 12 m RMSE is an indispensable criterion for Landsat Collection 1 Tier 1 ("stackable" scenes) categorization. The trade-off between RMSE values and time series density is significantly pronounced in cloud persistent areas. Following the USGS criterion relaxation suggestion (i.e., from Tier 1 to L1TP), 176 (2%), 4518 (2.6%), 4520 (2.3%), and 5949 (6.6%) additional Landsat acquisitions for Landsat 4 TM, Landsat 5 TM, Landsat 7 ETM+, and Landsat 8 OLI/TIRS are added, respectively. It would potentially populate the snow cover time series in cloud-prone areas. Island areas such as Scotland and Iceland have already a limited number of Landsat acquisitions. However, the deficiency is further aggravated by the high cloud cover frequency, which leads to only approximately 100 clear-sky observations during the past three decades even taking the footprint overlapping effect into consideration. However, in Iceland, the effects of LTAP are well-pronounced, because Iceland has been considered as a niche location for Landsat acquisitions.

Since the derived cloud cover information is based on the CFMask-based cloud flag, the accuracy of the cloud detection algorithm (i.e., CFMask) should also be considered. Although the overall accuracy of CFMask algorithm was reported as 96.4% by Zhu and Woodcock (2012), commission errors of the CFMask over bright targets such as ice/snow, sand dunes, rocks and building roofs have been well-recognized by the remote sensing community (e.g. reported in Selkowitz and Forster, 2015). Moreover, the majority of the current USGS Collection 1 Level-2 Pixel Quality Assurance Bit Bands are generated using the default 22.5% cloud probability and three-pixel buffer. Therein, a three-pixel buffer amplifies the commission errors of the CFMask. In this context, revising and refining the cloud mask in mapping snow/ice covered areas would be strongly recommended. Apart from the cloud mask, the implemented snow classification method is actually insensitive to haze (see Figure 7-1). The method has successfully detected a large quantity of snow/ice

under haze. Therefore, further studies are needed to be related to (1) determining the thickness of haze on the premise of precisely detecting snow; (2) quantifying the accuracy of "snow beneath haze" class; (3) separating haze from the overall cloud mask.

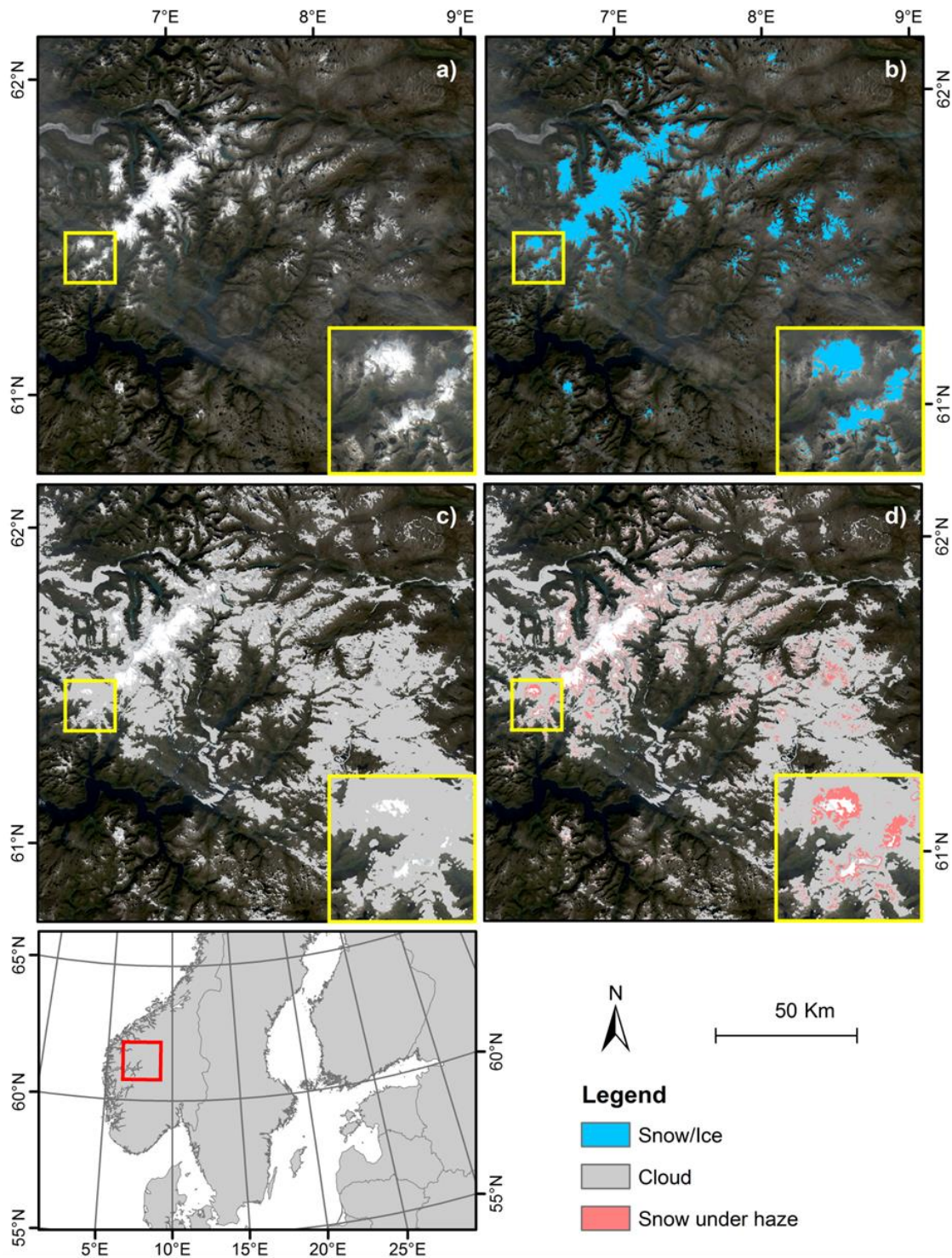


**Figure 7-1:** The influence of cloud/haze on snow cover classification. (a) Landsat surface reflectance true colour combination; (b) Snow cover classification; (c) CFmask cloud cover classification; (d) Snow beneath haze according to snow and cloud classification.



### 7.1.3 Influence of Cloud Cover on Snowline Elevation Statistics

As the clouds obstruct land cover information beneath them, missing snow pixels and their elevation information could bias the elevation distribution of snow covered pixels. It can thus result in over- and underestimation of the snowline elevation. Given the significant influence of cloud obstructions, thresholds between 70% and 90% of cloud coverage in optical images have been suggested by Gafurov and Bárdossy (2009), Krajčí et al. (2014), and Parajka et al. (2010a), to name a few. Hu et al. (2019a) assessed the influences of the cloud coverage on the snowline elevation statistics. The authors exemplified the spatial uncertainties of the median snowline elevations during the end of the ablation seasons. The results in the Pyrenees, the Alps, and the Carpathian Mountains are demonstrated in Figure 7-2. In general, overestimations (i.e. snow-free areas above median SLE) are most frequently observed in the southern slopes of the investigated mountains, while underestimations (i.e. snow-covered areas below the median SLE) are mostly observed on the northern slopes thereof. These spatial patterns of the error-prone areas coincide with areas more prone to precipitation (as snow in particular), given their location on windward slopes. Among the three regions, snowline elevations in the Carpathian Mountains are much more likely to be largely impacted by cloud obstruction than those in the other two mountain areas.

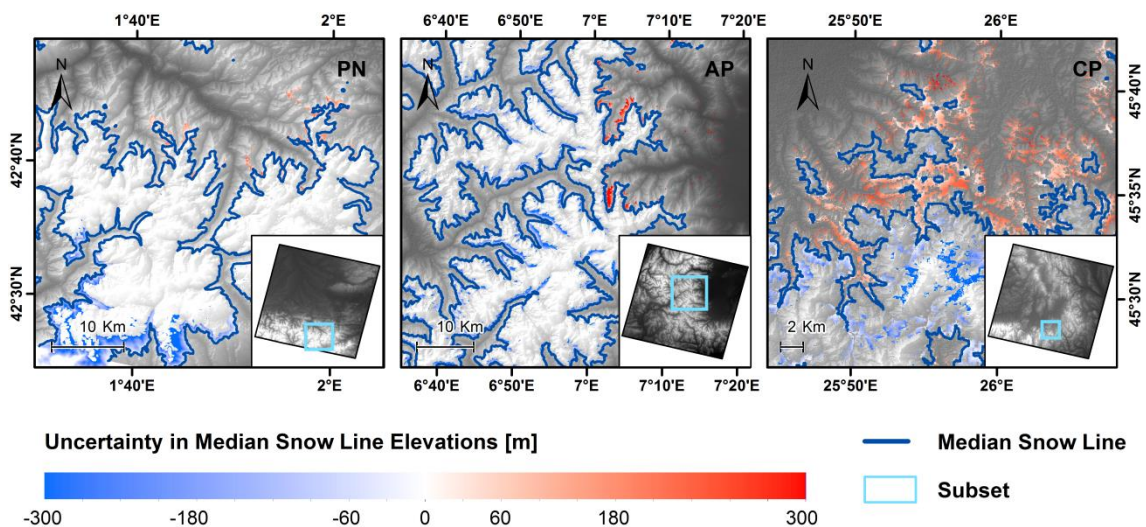


**Figure 7-2:** Details of the spatial uncertainty assessment of the Median Snowline Elevations (MSEs) during the end of the ablation seasons between 1984 and 2017 for the selected mountain areas: a) the Pyrenees (PN, Path/Row: 198/030) during June, b) the Alps (AP, Path/Row: 195/029) during May and c) the Carpathian Mountains (CP, Path/Row: 183/028) during April. Red colour indicates overestimated areas (snow-free areas above median SLE) and blue colour indicates underestimated areas (snow-covered areas below the median SLE). The base-map is a hill-shade derived from the Digital Elevation Model (DEM). Modified according to Hu et al. (2019a).

## 7.2 Challenges Regarding Accurate Snow Cover Mapping and Regional Snowline Elevation (RSE) Retrieval

This section presents the challenges with regards to (1) accurate snow cover mapping, (2) accurate RSE retrieval, (3) accurate RSE modelling, and (4) validation data as well as validation scheme for local snow-related EO products. At first, challenges regarding accurate snow cover mapping are discussed, including signal saturation, absence of thermal information, cloud contamination, and snow-in-forest. Afterwards, apart from the errors in the input snow classifications, further uncertainties within the retrieved RSEs from EO satellite images are evaluated, i.e. missing observations, and errors from the employed DEM data. Based on the retrieved RSEs from EO satellite images and climate reanalysis, the RSEs at the time without available EO satellite images are modelled. For accurate RSE modelling, there are several challenges discussed in this thesis, including errors propagated from the input data and input variable selection, as well as the interpretability of the applied RFR model. Lastly, the challenges regarding the validation schemes are discussed in the context of accuracy assessment for both snow cover maps and RSE results.

### 7.2.1 Challenges for Accurate Snow Cover Mapping

The precision of the classified snow cover maps is impacted by four major factors, including (1) signal saturation in the employed bands, (2) missing thermal information, (3) cloud contamination, and (4) snow in forest. Signal saturation is related to the radiometric resolution of the employed EO sensor. In this thesis, Landsat 4/5 TM, Landsat 7 ETM+ and ASTER are of 8-bit radiometric resolution. Therefore, the signals of snow-covered areas are often saturated in the images acquired by these sensors (Dozier, 1989, 1984). Given that the visible bands are often used to separate snow/cloud from other bright surfaces (Zhu and Woodcock, 2014b), signal saturation of the visible bands can lead to a poor accuracy in snow classification results. In contrast, the radiometric resolution of the current optical EO sensors (i.e. Landsat 8 OLI and Sentinel-2 MSI) has been improved to 12-bit with higher Signal-to-Noise Ratio (SNR) (Drusch et al., 2012; Roy et al., 2014). The signal saturation in snow-covered areas has been addressed (Wang et al., 2016). Hu et al. (2019a) have also discovered such improvement while classifying snow in European mountains. Besides, the absence of thermal bands in Sentinel-2 data should also be noted, since it could potentially identify some warm bright targets erroneously as snow. Another potential reason inducing commission error in the snow cover result is cloud contamination, when separating snow and clouds. Commission errors over bright targets (e.g., ice/snow, sand dunes, rocks and building roofs) during the application of cloud masks (e.g., MFmask, ACCA) have been well-recognized by the community (Hagolle et al., 2010; Irish, 2000; Selkowitz and Forster, 2015). This problem is significantly pronounced in separating snow and clouds (particularly

icy clouds). Last but not the least, as suggested in the previous section, the low accuracy regarding snow classification covered by forest canopy is noteworthy. Forest canopy does not only cover up the snow below it, but also casts shadow on its adjacent areas (Klein et al., 1998; Maurer et al., 2003). Although the prevalently used NDSI-NDVI algorithm has been employed in this thesis to improve the accuracy, further improvements are still needed for precisely mapping snow in the forested areas. At a regional scale, future studies focusing on adjusting the constraint values for each are desirable.

## **7.2.2 Challenges for Accurate Regional Snowline Elevation (RSE)**

### **Retrieval**

Apart from the errors mentioned in the previous section, the uncertainties within the retrieved RSEs are also in relation to missing observations, and errors from the employed DEM data. These factors can distort the histograms of the snow/land pixels, which is the core for the RSE estimation. Missing observations occur at both pixel and footprint levels. At a pixel level, the major issues causing the missing observations are cloud obstructions and sensor anomalies. Cloud obstruction is the greatest inherent issue impacting the usability of optical satellite imagery, particular in mountain areas during the winter time, since clouds usually persist a long period there. To date, the solutions for cloud obstruction is limited, mainly via image combination from different sensors/similar acquisition time and/or modelling. In terms of the sensor anomalies, Landsat 7 ETM+ SLC-off is the most well-known issue. Since 2003, SLC-off issue has resulted in approximately 20% less data availability in a single Landsat 7 ETM+ scene (Pringle et al., 2009). At a footprint level, missing scenes are mainly caused by the acquisition plan and sensor failure. Acquisition plan influence the spatiotemporal pattern of the data volume, for instance, the Landsat "Commercialization Era" (Goward et al., 2006) introduced in Section 7.1.1. Also, regarding the ASTER Archive, ASTER scheduler determines the spatiotemporal pattern of the ASTER data availability. The other issue, the sensor anomaly, influences the data usability. For example, the ASTER SWIR band failure makes the ASTER data acquired after April 2008 not suitable for precise snow cover detection. On the other hand, catchments are of better data availability, if the footprints overlap there. The increase of the data availability can be doubled and more, since the scenes acquired from two horizontally adjacent footprints are of one-week time difference.

DEM is indispensable for RSE retrieval. Nevertheless, obtaining an accurate DEM in complex terrains and high mountains is challenging for either interferometric or photogrammetric methods based on spaceborne satellite data. It has been recognized that the prevalent photogrammetric method (i.e. the correlation algorithm) for photogrammetric DEM generation often generation fails over snow covered areas (Kääb, 2002; Svoboda and Paul, 2009). Also, an interferometric DEM suffers from the problem of the voids in the original SAR data in mountain areas (Frey and Paul, 2012). In the Swiss Alps, the accuracy

comparison between the ASTER GDEM (a photogrammetric DEM) and the SRTM (an interferometric DEM) suggested that both DEMs are suitable for topographical parameters calculation in snow/ice-covered areas (Frey and Paul, 2012). In this thesis, the main objective is change detection of RSEs during a long period. Therefore, the errors induced by the employed DEM are systematic, and can be largely counteracted. However, given the high accuracy of DEMs generated from the airborne LiDAR, it is desirable to investigate the accuracy improvement using airborne LiDAR DEMs as valuable alternatives to interferometric or photogrammetric DEMs. Whereas, it should be still noted that the airborne LiDAR DEMs often only cover a small area (e.g., at a regional scale), and they are not freely-accessible.

### **7.2.3 Challenges for Accurate Regional Snowline Elevation (RSE) Modelling**

The greatest drawback of the Landsat time series in the context of snow dynamics observation is its near two-week revisit time. To conquer this problem, RFR is implemented in this thesis to fill the observation gaps in between, together with the relevant climate reanalysis data. On the one hand, the RFR shows its strength in relation to (1) capacity of coping with the small training dataset, (2) robustness to outliers and non-linear data, (3) ability of handling multicollinearity in explanatory variables, (4) low risk of overfitting, (5) calculation of explanatory variable importance, etc. The aforementioned advantages make RFR more preferable than other machine learning techniques or conventional multi-linear regression model for snowline modelling. On the other hand, RFR also has its limitation with regards to the model uncertainties and small model interpretability. Model uncertainties are largely resulted from the input data, i.e. RSE results derived from satellite images and the climate reanalysis data. Uncertainties in relation to RSE results derived from satellite images have been discussed above in Section 7.2.2. In terms of climate reanalysis data, the uncertainties are mainly raised from three perspectives, (1) the selection of the climate reanalysis dataset and the input climate variables, (2) accuracy of the input climate variables, and (3) the resolution of the input climate reanalysis data. To date, ERA5 from ECMWF provides climate reanalysis data of the complete globe from 1979 to within 3 months of real time. It provides large quantities of climate variables of 30 km spatial resolution and 1 hour temporal resolution. Most importantly, it is free-of-charge. In these regards, ERA5 is suitable for snowline modelling at a catchment level from 1984 to 2018. Whereas, processing such data is time consuming. Hence, only five parameters are selected based on the knowledge. Shown in Section 6.2.3, the accuracy and the importance results differ from one catchment to another. It indicates that the geographical settings in different catchments influence the snowline dynamics. Therefore, it would be also beneficial to include more variables and test the importance of those variables for snowline modelling. It would not only help the improvement of the model accuracy, but also enhance the comprehension of the contribution from different climate variables in the

context of snow dynamics. When it comes to the accuracy of the climate variables from the ERA5 dataset, information about uncertainties regarding the selected climate variables is included in ERA5 archive at reduced spatial and temporal resolutions. Importantly, the uncertainty of the selected variables is induced from the spatial statistics calculation. In complex terrains, the coarse resolution of ERA5 data results in omission of variation of the involved climate variables, especially for the catchments with a large proportion of flat areas. To tackle such problem, it is desired to use high resolution climate reanalysis data. However, such datasets are computational demanding, and often not freely accessible. Once such data can be acquired, it is worthy trying to investigate the influence of spatial resolution of the climate reanalysis with regards to snowline modelling.

#### **7.2.4 Challenges for Validating Snow Cover Maps and Regional Snowline Elevation (RSE) Results**

Validation is indispensable, in the context of the snow cover maps and RSEs derivation. Yet to validate snow cover maps and RSEs derived from the high-resolution optical satellite imagery is particularly challenging, due to the insufficient validation data and inefficient validation techniques. At present, field measurements and very-high-resolution resolution images are the mainstream validation sources for snow-related products. For example, Krajčí et al. (2014) utilized the Automatic Weather Station (AWS) records (e.g., SD and SWE) together with snow field measurements to validate the RLE results obtained from MODIS observations. The spacing among the involved AWSs and field measurement points is 100 m in the altitudinal direction. Such validation scheme is capable of assessing RSE results at a local scale. However, for large scale studies based on high resolution satellite imagery, conventional field measurements and AWS data are not well-suited for a statistical trustable accuracy assessment. The main obstacle is the requirement of large quantities of input measurements from densely distributed ground observation points. For this purpose, not only a considerably intensive labour and materials are required, but also low accessibility in mountain areas makes it unpractical. Besides, the time span of historical field measurements and/or AWS data hardly reaches back to 1980s, which poses another challenging for validation the resolution throughout the full time series.

Very high resolution satellite images hold a potential to validate snow cover maps and RSE results. Oftentimes, very high resolution satellite images are optical images, such as WorldView-3 (1.24 and 3.7 m), SPOT 5 (2.5 and 5 m), PlanetScope (3 m), Pléiades (0.5 and 2 m), RapidEye (5 m). The largest disadvantages of these satellites are the limited data access (especially not free-of-charge) and cloud obstruction. Since these very high resolution images are optical imagery, they still suffer from cloud obstructions on the same date when the snow is observed by Landsat/ASTER/Sentinel-2. Consequently, the land surface information below the clouds remains missing. Apart from these two drawbacks,

the suitability of the very high resolution satellite images in relation to snow cover maps and RSE validation is also deteriorated by other factors, including (1) absence of SWIR and thermal bands, (2) small footprints, (3) irregular and long revisit time, and (4) missing observations before year 2000. To detect the land surface information beneath the clouds, SAR images can be utilized, since SAR penetrates the clouds. Nowadays, the spatial resolution of the spaceborne SAR sensors is significantly improved under a certain acquisition mode, e.g., Radarsat-1/2, COSMO-SkyMed, TerraSAR-X, PAZ SAR satellite. Together with the SAR-based snow cover detection methods (Muhuri et al., 2017; Nijhawan et al., 2019; Wang et al., 2015), snow cover area (both dry and wet snow) can be mapped using SAR observations with an accuracy up to 98.1%. On the other hand, similar as the very high resolution optical data, such high resolution SAR images for long-term and large scale is hampered by the limited data access policy and observation scarcities before 2000 in particular.

Besides, WebCam data is also a potential dataset to validate the snow cover maps and RSE results, given their advantages of: (1) low cost, (2) very high temporal resolution, (3) long-term observation records, and (4) cloud independence. Still, the main challenge influencing the utility of long-term and large scale WebCam data is their pre-processing which is time-consuming. Meanwhile, collaboration (e.g., sharing policy making) and metadata standardization are required, to fuse WebCam images acquired at different places from different organizations, institutes, and countries. To date, Unmanned Aerial Vehicle (UAV) imagery data have drawn a great attention from the community, given that UAVs are easy and flexible to deploy with regards to the mounted sensors (e.g., multispectral, hyperspectral, thermal, microwave, LiDAR), and operation date as well as periods. The acquired UAV images are usually of higher spatiotemporal resolution than by those acquire by satellites. Hence, UAVs provide detailed spatiotemporal information regarding the snow cover, even during the cloudy days.

Regarding the validation schemes, it remains also challenging. Originally, Krajčí et al. (2014) validated the RSE results based on ground snow depth measurements from AWSs and field campaigns. The accuracy of the derived RSE results is presented using an accuracy index, indicating the agreement between the RSE results and the ground measurements. The index is a ratio between the sum of correctly classified station-days and the total number of station-days. Hu et al. (2019a) assessed the uncertainties below the cloud cover in Landsat-based snowline elevation results against those not covered by clouds derived from the Sentinel-2 images close to the Landsat acquisition date. The readers should notice that the presented validation method in this thesis is still imperfect, but what can be realized by the free-accessible data to a large extent. In this regard, further researches developing and/or improving validation methods is urgently required.

## 7.3 Characterizing Regional Snowline Elevation (RSE) Dynamics

This section discusses the uncertainties, the potential explanations, and the potential applications of the obtained intra- and inter-annual RSE dynamics. Firstly, the error sources of the observed RSE dynamics are discussed in relation to: (1) errors propagated from the erroneous input RSE data, (2) representativeness of the sigmoid transformation, (3) efficiency of the regression model, and (4) coarse resolution of the climate reanalysis data. Afterwards, the potential explanations of these detected RSE dynamics are discussed, together with the previous snow studies in Europe.

### 7.3.1 Challenges of Accurately Deriving Regional Snowline Retreat Curves (RSRCs)

RSRC is the main tool employed for characterizing the long-term RSE dynamics in this thesis. The accuracies of the RSRCs are mainly influenced by: (1) errors propagated from the erroneous input RSE data, (2) representativeness of the sigmoid transformation, (3) efficiency of the regression model, and (4) coarse resolution of the climate reanalysis data. The errors regarding the RSE input have been discussed previously in Section 7.2. When it comes to the representativeness of the sigmoid transformation, it is an issue linked to the geographical settings of the investigated area. In Section 3.5, based on the snow phenology characteristics and data exploration, a sigmoid shape RSRCs was developed by Hu et al. (2019b). As a non-linear transformation, several parameters have to be pre-defined (details see section 5.5). Amongst these parameters, the highest RSE ( $RSE_{max}$ ) is strongly depended on the glacier extent, if the study area is glaciated. Given that observations (e.g. summarized by Hu et al. (2017)) have suggested significant glacier retreat in alpine glaciers in Europe,  $RSE_{max}$  is rather a variable than a constant. However, the challenge is to obtain such glacier extent product even at an annual basis. Local studies investigating the influence of such effect in the future are required. Besides, also shown in the results (section 6.3.3), the corrected  $R^2$  of the M-estimation regression models are much lower in Carpathian catchments than those in the other investigated catchments. The main reason is the low efficiency of the applied M-estimation regression models, due to frequent intermediate snowfall events and significantly different geographical settings. Intermediate snowfall events lead to create anomalously low RLEs that are often treated as the 'outliers' in the RSLRCs by the M-estimator. Given the nature of the M-estimator, relatively high breakpoint, this effects are normally largely reduced in most catchments. However, in the investigated Carpathian catchments, the shape of RSRCs is often non-sigmoid shape. Apart from the distortions caused by the intermediate snowfall events, the elevation ranges also results in an ambiguous shape of the RSRC during an ablation

season. The generally low elevation of the Carpathian Mountain results in the limited ability holding snow for a long period, and hence the melting period is much faster than the high mountains. Together with the frequently intermediate snowfall events, the dynamics of the snowlines fluctuates greatly. Even by adjusting the pre-defined ablation period, the region is either full covered by snow, or shifting between snow-cover and snow-cleared rapidly. To capture snowline dynamics for such regions, RSRCs based on sigmoid transformation is not well-suited. Last but not least, the coarse spatial resolution ( $\sim 31$  km) of the employed ERA5 should also be considered. It directly leads to a potential problem regarding the representativeness. It is particularly true for catchments with a large proportion of low-elevation areas, since the calculated AT is rather representative for the snow-free areas thereof. Consequently, the information of high-elevation areas is omitted, in which the snowline is actually located. As an alternative, climate reanalysis products with higher spatial resolution, e.g., COSMO-REA6 (6 km) and COSMO-REA2 (2 km). Meanwhile, it should also be noted that such datasets are usually only limited to a certain time span and spatial coverage.

### **7.3.2 Observed Regional Snowline Dynamics in European Mountains**

The intra-annual variations of regional snowlines during the ablation seasons 1984–2018 show the patterns among the investigated catchments. The anomalously low RSEs within an ablation season are mainly caused by intermediate snowfall events. The frequency and the persistence of the intermediate snowfall events influence absolute value of the anomalously low RSEs. It is also linked to the local geographical settings. For instance, the Pyrenean catchment Ariege as well as the Alpine catchments Drac, Tagliamento, and Var has the largest intra-annual RSE variations, especially low RSE anomalies. These four catchments have a large part of windward slopes facing the nearby ocean. Such geolocation leads to more frequent intermediate snowfall events. Noticeably, unlike high RSE anomalies, low RSE anomalies are much often observed in the Carpathian catchments. It is because of their comparably low elevation and the frequent intermediate snowfall events therein, particularly demonstrated in the Carpathian catchment Uzh. As a consequence, snowline reaches its maximum elevation in the early ablation season, while anomalously low RSEs are caused by intermediate snowfall events during the middle-to-late ablation season. Another potential factor is the cold extremes and their persistence, which slow down the snowmelt process, and hence slow down the retreat of the regional snowline as well. Besides, the anomalously high RSEs indicate the potential consequence from the warming climate. To further investigate such effect, analysis regarding inter-annual RSE variation is required, together with the air temperature variations.

There are three aspects of the inter-annual RSE variation derived in this thesis, i.e. steepness and  $AT_{MA}$  from RSRCs, as well as the median RSEs and the RSEs at the



beginning of the ablation season between 1984 and 2018. The overall significantly-positive trends have been detected, indicating an increasing high RSE at the beginning of the ablation season. This result is in line with the independent trend analysis of the RSEs at the beginning of the ablation season between 1984 and 2018. Moreover, the results from trend analysis of  $AT_{MA}$  in these catchments are either insignificant or statistically negative (Tagliamento and Tysa). It indicates that either same or less AT is needed for the regional snowlines to reach its middle point of the RSRC. With the background of global warming, such effect would be aggravated. Consequently, an overall increasing high snowline elevation is expected, which is in accordance with the trend analysis of the median RSEs between 1984 and 2018. These results agree with the previous studies, Bulygina et al., 2009; Takala et al., 2009; Tedesco et al., 2009; Wu et al., 2018, to name a few. Meanwhile, there are the Pyrenean catchment Ariege (significantly negative trend of steepness), the Alpine catchment Salzach (significantly positive trend of  $AT_{MA}$ ) and the Carpathian catchment Uzh (significantly positive trend of  $AT_{MA}$ ). The significantly negative trend of steepness illustrates an accelerated snowline retreat velocity. Given the insignificant  $AT_{MA}$  in the corresponding RSRC, it indicates the snowline retreats to its highest elevation faster, and the ablation season is shortened. Because of the warming climate, the RSE at the beginning of the ablation season is retreating to a high elevation, which is confirmed by the trend analysis of the RSEs thereof at the beginning of the ablation season between 1984 and 2018. Thus, the characteristics of the snowline retreat in the Pyrenean catchment Ariege is increasingly high RSEs at the beginning of the ablation season, fastened snowline retreat velocity, and shortened ablation season. The significantly positive trend of  $AT_{MA}$  in the Alpine catchment Salzach, indicates more AT is needed for its RSRC to reach the middle point. Given the significantly positive trend of the RSRC steepness, it indicates the snowline variation in the Alpine catchment Salzach is less pronounced. The results are also confirmed by the independent trend analysis of the median RSEs and the RSEs at the beginning of the ablation season between 1984 and 2018, whose slopes of the resultant linear trend are comparable smaller than those of the other catchments. Lastly, the potential explanation for significantly positive trend of  $AT_{MA}$  the Carpathian catchment Uzh is mainly due to the low accuracy of both its RFR model for RSE densification, and M-estimation regression model for RSRC calculation. The low accuracy of these two models has been explained in the previous section 7.2.3 and section 7.3.1, respectively.

## 7.4 Potential Applications of Regional Snowline Dynamics

In this section, the potential application fields of the RSE dynamics are discussed. Firstly, the suitability of RSE in the context of local snowline elevation assessment is discussed. Afterwards, potential applications of RSE results are summarized, which includes snow phenology, climate change, winter tourism/sport management, flora and fauna studies, hydropower and freshwater management, and snow-related hazard management.

Lastly, to demonstrate the applications of RSE, the results from two case studies in this thesis are discussed.

RSE as an index developed for optical EO data, whose representativeness for the snowline conditions could be queried. Firstly, it is ideal for optical remote sensing, given the influences from clouds therein. It is particularly true in mountain areas, where cloud can be long-persisted and cover a large number of pixels. This fact significantly decreases the usability of the optical EO images for snow-related researches. RSE is a solution optimizing the representativeness for the local snowline conditions, meanwhile, controlling the effects from clouds by thresholding cloud coverage in the employed optical images. Hu et al. (2019a) have further evaluated the representativeness of a single statistical measure, and confirmed the representativeness of a single statistical index for local snowline elevation assessment (also see section 7.1.3). Besides, the suitability of RSE as an index for assessing local snowline elevation has been investigated by Krajčí et al. (2014). Krajčí et al. (2014) reported a mean accuracy around 86%, which is 14% greater than snowline estimate method previously proposed by Parajka et al. (2010a) or Da Ronco and De Michele (2014). Krajčí et al. (2014) also pointed out RSE also reduces the scatter adjacent to the snowline. Besides, the mean elevation of snow and land pixels could not provide a uniquely estimated elevation separating snow and land pixels. In these regards, RSE is a suitable index for the assessment of local snowline dynamics.

In terms of the potential applications of RSE results presented in this thesis, it can be further used in applications regarding snow phenology, climate change, winter tourism/sport management, flora and fauna studies, hydropower and freshwater management, and snow-related hazard management. "Snow cover phenology is a vital perspective of snow cover dynamics, which includes Snow Accumulation Onset (SAO), SCS, Snowmelt End (SME), SCD, just to name a few. However, given the revisit time and intermediate snowfall event occurrence, (semi-) high resolution optical EO sensor like Landsat is rather for monitoring snow dynamics in late ablation season. Since RSEs illustrate the spatial snow cover at an altitudinal direction, it could better illustrate the dynamics of snow clearance rather than the whole snowmelt process. This is because of the lower snowfall frequency and cloud coverage in the late ablation season. Climate change has a great impact on snow dynamics. Revealing the response of snow (an ECV) to the ongoing climate change is important. As RSE represents the regional (catchment-wise) dynamics of snow, spatial analysis based on long-term RSEs would provide a chance to carry out evidence-based statistical trend analysis. Furthermore, quantitative analyses linking RSE dynamics with other ECVs is beneficial to enhance the comprehension of regional response climate change. Thereby, better adaptation strategies could be made. Snowmelt runoff is fundamentally vital regarding water management and disaster warning in snowmelt-dominant catchments. Runoff can be predicted by calibrating hydrological models using spatial snow coverage derived from the RSLRCs. It would be intriguing to compare the performance using (semi-) high resolution based snow information and

medium resolution based information (e.g., Déry and Brown, 2007) in mountain areas. Winter tourism/sport management requires detailed spatial snow cover data for hiking routes planning, artificial snow planning, as well as the operation period length. Flora and fauna in high mid-latitude mountain regions are influenced by the snowline dynamics. The spatiotemporal snow dynamics affect the plant phenology (Asam et al., 2018; Böttcher et al., 2014; Thum et al., 2009), and animal activity (Mills et al., 2018; Pöyry et al., 2018; Zimova et al., 2018).” (Hu et al., 2019b) Given the high correlation between the snowline dynamics and river discharge, the observed RSEs results can also be applied in the hydrological researches. Since there are many snow-fed basins in European mountains, and river is dominant freshwater abstraction (65%) in many European countries (EEA 2018), RSE results provide valuable information for hydropower and freshwater management in Europe. Such evidence-based information also contributes to the snow-related hazard management. For example, spring floods have been observed shifting towards early ablation season in Europe (Blöschl et al., 2017). The shortened ablation season, fastened snowline retreat, and shift of the end of snowline retreat provide potential explanations. Joint researches taking RSE dynamics together with other geographical factors could potential promote the comprehension of the spring flood behaviour in the context of climate change.

To demonstrate the application of RSE results, two case studies are carried out. The first study investigates the relationship between snowline dynamics and air temperature anomalies. The results show a high correlation between monthly mean RSE and monthly air temperature anomaly during an ablation season. In the context of warming climate, high air temperature extreme events firstly accelerated the snowline retreat. Meanwhile, the consecutive high air temperature further exacerbates the regional snowline recession. Consequently, the risk of early ablation season flooding could increase, in accordance to the findings from Blöschl et al. (2017). Whereas, quantitative analyses projections of flood frequency and magnitude remain uncertain, this hence calls for further joint researches with, for example, physical model under different scenarios. The second case study investigates the relationship between snowline and discharge dynamics during the ablation seasons 2000–2016 in two Alpine catchments. RSE time series provides a new dimension, as a potential flood variation, a proxy for snowmelt during an ablation season. The correlation coefficients between RSEs and river discharge are comparable or even larger than those between snow coverage and discharge. Given that snow coverage has been applied in run off modelling, potential RSEs could also be applied for such purpose. Besides, RSE derived RSE time series can even reach back to 1970s, as long as the input climate variables are available at that time. On the other hand, the retreat of the snowline may be lagged compared to the absolute of the SCA. As suggested by Hall (2012), it is because that the snowmelt starts at all elevation zones (particularly within the high elevation zones) peripheral to sharp and steep rocks. In this regard, further studies are highly desirable, further investigating the potential of runoff modelling and/or prediction taking RSE as an input data.



## CHAPTER 8

### 8 Conclusion and Outlook

This chapter summarizes the conclusive findings in relation to the objectives and research questions raised in the introduction (section 1.2) of this thesis. Furthermore, an outlook of future opportunities of Earth Observation (EO) for long-term and large-scale snow dynamics observation is discussed, as well as the potential statistical techniques for further geoscientific analyses. Additionally, the findings on snowline dynamics in the mid-latitude European mountains are translated into recommendations for stakeholders and decision-makers.

#### 8.1 Summary and Conclusive Findings

During the winter, snow is the most extensive part of the cryosphere which is highly sensitive to climate change. Snow has great impacts on the Earth's energy budget, biodiversity and natural hazards, as well as hydropower management, freshwater management, and winter tourism/sports. Mid-latitude mountains in particular are experiencing significant alternations of snow and glaciers in response to climate change. In Europe, mountains cover approximately 2 million km<sup>2</sup> and are inhabited by more than 94 million people (Schuler et al., 2004), who benefit from the various ecosystem services and the socioeconomic wellbeing of the terrain. Since an increasing number of severe consequences have been observed as a result of climate change in mountain areas (Blöschl et al., 2017; EEA, 2017b; IPCC, 2014), long-term and evidence-based regional studies are urgently needed for promoting the comprehension of regional responses to climate change, and hence for developing effective regional and local adaptation-strategies. In this context, this dissertation improves the current knowledge of regional responses to climate change by providing quantitative information about long-term EO-derived snowline dynamics during the ablation seasons of 1984–2018. The primary goal of this dissertation is to retrieve and assess long-term snowline dynamics in European mountains, using combined free-accessible optical EO datasets. The answers to the four research questions and objectives defined in this thesis are summarized as follows:

### 8.1.1 The State-of-the-Art of Earth Observation in Cold Region Monitoring

**Objective 1** is to carry out a comprehensive literature review on cold region land surface dynamics in Europe using EO. The review aims to clarify the state-of-the-art of determining the cold region dynamics in Europe, especially for snow and glacier dynamics as they are particularly important and strongly interconnected in European mountains. Furthermore, leading methods for deriving data on snow and glacier dynamics are highlighted and compared. Ultimately, the current existing research gaps are identified.

**Research Question 1.1:** *How can Earth Observation support the delineation of a cold region boundary in Europe?*

Cold region boundaries can be delineated quantitatively, using the annual Snow Cover Duration (SCD) derived from EO images as an indicator. The result shows that the geographical extent of the cold region in Europe mainly includes: the Carpathian Mountains, the European Alps, Finland, Sweden, Iceland, and Norway (including the Svalbard Archipelago). A significant linear relationship ( $p$ -value  $< 0.001$ ) has been found between SCD and cold region stability, with a coefficient of determination ( $R^2=0.73$ ). Accordingly, the extent of the stable cold region can be identified as an area with  $>180$ -day mean SCD. The spatial resolution of the stable cold region is mapped at 500 m spatial resolution, using Moderate Resolution Imaging Spectroradiometer (MODIS)-based SCD information. Therefore, the EO-based cold region boundary is well-suited for regional cold region studies, especially in identifying the areas that are undergoing significant changes.

**Research Question 1.2:** *What are the most frequently applied EO satellites/sensors for the analysis of cold region dynamics in Europe?*

In total, over 250 research articles on cold region dynamics from Science Citation Index (SCI) journals from the past 30 years have been reviewed. So far, optical EO data are the most prevalently employed satellite datasets for investigating cold region dynamics. Optical data have been utilized in over 70% of all reviewed literature on snow and glacier dynamics in the cold regions of Europe. Within this literature, 100 studies have utilized Landsat data to study cold region dynamics. By contrast, only 25% of the reviewed snow-related studies used Synthetic Aperture Radar (SAR) and Passive Microwave (PM) data. PM data are used by  $\sim 20\%$  of the studies to derive Snow Water Equivalent (SWE) and Snow Depth (SD) with empirical equations. On the other hand, SAR data are more often used to study glacier motion and elevational change, which take up 34% of the studies on glacier dynamics. To investigate the glacier elevational change, Light Detection and Ranging (LiDAR) data are also applied, while only 3% of the reviewed literatures have employed LiDAR data.

**Research Question 1.3:** *What are the advantages and disadvantages of the existing different sensor types and methods?*

Optical satellite images are the backbone of cold-region-dynamic studies, due to their long-term records of the Earth's land surface, different spatiotemporal resolutions, good global spatiotemporal coverage, and good data accessibility. On the other hand, optical satellite images are not usable under cloud cover and in polar darkness. In this regard, SAR data have the advantage of both all-weather and day-night operation as well as the ability to penetrate dry snow and ice. Often, however, SAR data is handled in a complex data file format and large data size. Moreover, dense SAR time series do predate Sentinel-1, and not all SAR data can be accessed free-of-charge. PM data are less influenced by the atmosphere (excluding precipitation clouds). In addition, PM data usually have very high temporal resolution at global coverage. However, detecting wet snow from PM data can be difficult, as well as doing so for thin snow cover (<5 cm snow) in heavily forested areas. Mapping snow/ice in mountainous areas using PM data in coarse spatial resolution has also proven challenging. To date, there are only two space-borne LiDAR sensors, ICESat-1 GLAS (Ice, Cloud, and land Elevation Satellite-1 Geoscience Laser Altimeter System) and ICESat-2 ATLAS (Advanced Topographic Laser Altimeter System), which provide data from 2003–2009 (ICESat-1) and from 2018 to present (ICESat-2). Yet, they have relatively large footprints and ground track spacing, which hinders their application to small glacier monitoring. Despite this shortcoming, the value of ICESat-1 and ICESat-2 observations as a calibration and validation dataset should be emphasized, particularly for large ice caps.

**Research Question 1.4:** *What studies dealing with cold region dynamics in Europe have been undertaken so far?*

The literature review shows that cold regions in Europe are undergoing significant changes. To sum up, there are six key findings on snow and glacier dynamics in Europe:

- Mean SCD is shortening at a mean speed of around 6 days · a<sup>-1</sup> (between 1972 and 2000);
- Snowmelt onset is shifting towards the early ablation season at a rate of approximately 4 days · a<sup>-1</sup>;
- The amount of impurities above the snow pack is increasing, especially in spring;
- Glacier extents are shrinking (at a mean speed of approximately –0.3% per year), and a few have been totally vanished since the “Little Ice Age”;
- Glacier surging is especially accentuated within the Svalbard Archipelago, and for land-terminating glaciers - the highest motion velocity (500 m·a<sup>-1</sup>) was observed in the Mont Blanc region in 2003;
- Glacier elevation is lowering, particularly in the Alps, leading to increased mass loss.

**Research Question 1.5:** *What are the research and knowledge gaps with respect to cold region dynamics?*

To date, there remain a large number of research and knowledge gaps in cold region dynamics, specifically with respect to spatiotemporal scales, data availability and suitability, as well as method transferability and applicability. The major gaps are:

- Accurate methods for mapping snow-in-forest based on optical data;
- A long-term consistent dataset for validating EO-based snow cover and glacier extent;
- Satellite-image-derived high-spatial-resolution Snow Water Equivalent and Snow Depth products;
- Correcting snow/ice penetration of SAR data for snow/glacier observation;
- A framework that can handle multi-sensor EO data for cold region studies;
- The knowledge about the local and regional snow response to climate;
- Long-term glacier dynamics at a meso-/continental scale.

### **8.1.2 Availability and Suitability of the Long-Term Landsat Archive for Snow Monitoring in European Mountains**

**Objective 2** is to provide a comprehensive overview of data availability and suitability for a remote-sensing-based assessment of snow dynamics in European mountains. To that end, the potentials and opportunities of the long-term Landsat Archive for applications in snowline dynamic retrieval should be elucidated.

**Research Question 2.1:** *What is the spatiotemporal availability of the Landsat Collection 1 archive during the period of 1984-2018?*

As of January 16, 2018, a total of 477,224 Landsat scenes for Europe between 1982 and 2017 have been acquired and archived in Collection 1. Within that dataset, 315,000 scenes have been processed at L1TP level (i.e. Level 1 Precision and Terrain). In mountainous areas, approximately 500 acquisitions per footprint across the Alps are archived in Collection 1. A similar number of images have also been acquired over the Carpathian Mountains and the Pyrenees. The Landsat L1TP data is scarcer (up to 50% less) in high-latitude mountain areas than in low-latitude mountain areas. In Europe, Iceland and Scotland contain mountainous regions with the scarcest Landsat Collection 1 L1TP data. Although the footprint overlaps more significantly within these areas, for the majority of Iceland and Scotland, no more than 280 scenes per footprint have been acquired for any one location. The available Landsat 4-5 TM, Landsat 7 ETM+, and Landsat 8 OLI/TIRS data in Europe mainly span from 1984 to present. The most severe Landsat data-gaps in Europe occur during 1982-1984 and 1991-1999. Therefore, to carry out long term snow dynamics studies in European mountains, the data gaps should be noted and filled.



**Research Question 2.2:** *What are the most suitable processing levels and tiers of Landsat Collection 1 data for snowline dynamics retrieval?*

The implementation of Collections has resulted in a significant variation in the management of the Landsat Archive. At present, the selection of the Landsat data for data processing can be based on either processing levels or Tiers. In this thesis, the results show that Landsat data processed at L1TP level (i.e. Level 1 Precision and Terrain in both Tier 1 and Tier 2) are the most suitable for snowline dynamic retrieval. This is because Landsat L1TP achieves a good balance between data availability and precise geolocation for snow monitoring. The amount of Landsat L1TP data is approximately 14,000 scenes more than Landsat Tier 1 (i.e. "stackable" data for time-series analysis) data over the whole of Europe from between 1984 and 2017. In terms of the value of ascending scenes (i.e. "night-time" acquisitions), given that more than 93% of the ascending scenes contain sun elevation below 15°, they are not appropriate for accurate atmospheric correction and snow classification. In these regards, to determine snowline dynamics in European mountains, the most suitable Landsat products to ensure both data availability and geolocation precision are the Landsat L1TP data.

**Research Question 2.3:** *What are the advantages and disadvantages influencing the retrieval of snowline dynamics using Landsat imagery?*

Apart from the missing observations, the usability of Landsat images for snow dynamic retrieval is also influenced by cloud obstruction, cloud contamination, and the difficulty in detecting snow in forested and glaciated areas. Geographically, the occurrence of clouds tends to be more frequent in mountainous areas (> 70%) and high latitude regions (> 50%), and less frequent in low latitude plains (< 50%) and the Mediterranean (< 30%). This is highly consistent with the local geographical settings (e.g., topography and climatology). Scotland has the densest cloud cover, with > 80% near Ben Nevis. Severe cloud cover (> 60%) is also observed in the ice-cap peripheral areas in Iceland, the northwest face of the Scandinavian Mountains and the north face of the Pyrenees. Cloud obstruction is more severe (approximately 70%) during accumulation and ablation seasons, which influences the observation of snow onset and snowmelt. However, most of the Landsat summer acquisitions have no more than 50% cloud coverage. Other than cloud cover, detecting snow under cloud contamination and forest canopy based on optical imagery is not dependable. Glacier extent also greatly impacts the spatial variation and retreat velocity of snowline dynamics. It is hence necessary to correct for the influence of clouds, forests, and glaciers when determining snowline retrieval.

### 8.1.3 Spatiotemporally Transferable Framework for Snowline Derivation in Mountainous Areas

**Objective 3** is to develop a spatiotemporally transferable framework for snowline derivation in mountain areas using long-term free-of-charge optical datasets. Additionally, metrics based on the retrieved long-term snowline time-series need to be developed to characterize the snowline retreat during the ablation seasons.

**Research Question 3.1:** *How can snowlines in mountainous areas be retrieved using the long-term Landsat Archive and Sentinel-2 dataset?*

To achieve this goal, a three-step framework has been developed. Firstly, the optical EO images are atmospherically and topographically corrected to obtain physically comparable surface reflectance. Secondly, the Snow Cover Area (SCA) is mapped based on a multi-threshold decision tree. The misclassified pixels are then corrected with the corresponding masks (i.e. cloud, shadow, water, and thermal masks). The Overall Accuracy (OA) and Kappa coefficient ( $\kappa$ ) of the SCA maps achieved high accuracies of 96.71% and 0.72, respectively. Lastly, the Regional Snowline Elevation (RSE) has been determined using cumulative histogram optimization together with the elevation information derived from Digital Elevation Models (DEMs). The accuracy assessment according to the derived RSEs indicates a low proportion of erroneous pixels overall (median < 5%). The developed framework has been successfully applied to approximately 8000 Landsat, ASTER, and Sentinel-2 images acquired between 1984 and 2018 in ten catchments distributed in the Alps, Carpathian Mountains, and Pyrenees. Thus, the developed framework is spatiotemporally transferable. It is also applicable to different optical satellite images to accurately derive long-term snowlines in mountainous areas.

**Research Question 3.2:** *How can the gaps in snowline time series be filled when there are no satellite observations available?*

To tackle the inherent problem of exploiting the Landsat time series for the monitoring of snowline dynamics, this thesis implements random forest regression to fill the data gaps. The mean coefficient of determination ( $\overline{R^2}$ ) is 0.66, with the highest  $R^2$  achieved in the Alpine catchment Drac ( $R^2 = 0.89$ ). It indicates that the random forest regression models can explain 66% of the variations in snowline elevation dynamics on average. The mean RMSE is reported as 229.44 m. According to the permutation importance of the random forest regression models, cumulated sum of 2 m air temperature and mean snow depth are the most important variables, whose increases in Mean Absolute Error (MAE) range from 5.03% to 19.99%. Given the good performance of random forest regression, it is a suitable technique to fill the gaps in satellite-image-based snowline time series.

**Research Question 3.3:** *How can snow cover dynamics during ablation seasons in mountainous areas be characterized?*

To characterize the regional snowline dynamics during an ablation season, Regional Snowline Retreat Curves (RSRCs) have been generated using the robust M-estimator. From RSRC, Accumulated Temperature in the Mid Ablation season ( $AT_{MA}$ ) and steepness can be calculated to describe the velocity of regional snowline retreat, and the timing of the snow-clearance, respectively. The median corrected  $R^2 = \sim 0.90$  in the investigated Alpine and Pyrenean catchments, and  $R^2 = \sim 0.65$  in the Carpathian catchment Tysa. The upper-quantile, median, and lower-quantile of MAEs are generally around 25 m, 20 m, and 15 m, respectively. The trend analysis for median RSEs and the RSEs at the beginning of the ablation seasons between 1984 and 2018 is implemented to characterize inter-annual snowline dynamics. To investigate the intra-annual snowline dynamics, the frequency snow cover at a specific elevation on a certain day of the ablation season has been calculated. This calculation indicates not only magnitude, but also the timing of the anomalous snowline elevations during an ablation season.

#### **8.1.4 Characteristics, Potential Climate Drivers, and Consequences of the Detected Long-Term Snowline Dynamics in European Mountains**

**Objective 4** is to investigate long-term snowline dynamics in mid-latitude European mountains, their potential climate drivers, and their consequences. Constraints for these geographical uncertainties can contribute to strategizing responses to ongoing climate change.

**Research Question 4.1:** *What are the patterns of intra- and inter-annual snowline variations in mid-latitude European mountains?*

In terms of the intra-annual variations of the RSE, the Alpine catchment Tagliamento shows a uniquely high variation in the beginning of the ablation season, mainly towards a high elevation. As for the inter-annual variations of the RSE, the median RSE is increasingly higher in all the selected catchments, with an average speed of around  $4.66 \text{ m} \cdot \text{a}^{-1}$  (median) and  $5.87 \text{ m} \cdot \text{a}^{-1}$  (at the beginning of the ablation season). The fastest significant retreat is observed in the catchment Drac ( $10.66 \text{ m} \cdot \text{a}^{-1}$ , at the beginning of the ablation season), and the slowest significant retreat is observed in the catchment Uzh ( $1.74 \text{ m} \cdot \text{a}^{-1}$ , at the beginning of the ablation season). The RSE at the beginning of the ablation season suggests a faster retreat than the median, whose average difference is near  $1.21 \text{ m} \cdot \text{a}^{-1}$ , particularly in the catchment Drac ( $3.72 \text{ m} \cdot \text{a}^{-1}$ ).

**Research Question 4.2:** *What are the potential climate drivers of the detected long-term snowline dynamics in European mountains?*

In this thesis, the variation of air temperatures is regarded as an example of a potential climate driver. To investigate the responses of RSE to climate change, the RSEs are analysed with the corresponding air temperature records. The retrieved monthly mean RSEs are highly correlated (mean correlation coefficient  $\bar{R} = 0.7$ ) with the monthly air temperature anomalies, which is more significant in months with extremely low/high air temperature. The correlation coefficients increase over time during an ablation season. In general, the correlation coefficients are higher in the late ablation season (June) than in the early ablation season (April). In this regard, the variations in air temperature can explain a large proportion (nearly 50%) of snowline variations in ablation season, especially in the late ablation season (June). It is speculated that the velocity and elevation of snowlines in the European Mountains will be continuously increasing, in the context of global warming.

**Research Question 4.3:** *What are the potential consequences of the detected long-term snowline dynamics in European mountains?*

To demonstrate the potential consequences of the snowline dynamics, RSE results are analysed with river discharge data in two Alpine catchments (Alpenrhein and Salzach). The correlation analysis shows a good correlation between river discharges and RSEs (correlation coefficient,  $R=0.52$ ). The correlation coefficient is 0.03 higher than that between river discharges and snow coverages. It indicates that approximately 3% more variability in river discharge can be explained by the RSE than by snow coverage. It is speculated that the increases in RSEs will result in shorter ablation seasons. It could hence increase runoffs and shift the timing of spring floods and thus the risk of spring floods in snow-fed basins. These predictions not only call for regional and local adaptation-strategies for water management, but also for the development of better runoff monitoring and predictions in snow-fed basins.

## 8.2 Outlook and Future Opportunities

Long-term regional snowline assessments based on high resolution EO data can promote the comprehension of regional responses to climate change. In this thesis, the presented framework should be considered a first step toward increasing knowledge about snow dynamics in mountainous areas, and about potential triggers and consequences for the phenomena observed. Future researchers and further studies should focus on the following aspects:

- **Acquiring validation data to assess long-term snow-related observations based on high-resolution EO data.** The lack of appropriate validation datasets poses a great challenge to the accuracy assessment of long-term snow products that are derived from high-resolution EO data, especially in mountainous areas. The geographical setting significantly influences the spatiotemporal pattern of snow cover. The heterogeneous snow distribution in mountain areas requires either densely distributed conventional field measurements (e.g., meteorological station data, snow course measurements), or very high resolution cloud-free reference imagery acquired at simultaneously. WebCams and Unmanned Aerial Vehicle (UAVs) are the most suitable candidates for this task. Therefore, the assessment of regional snow products using high-resolution EO data reference images from WebCams and UAVs is highly desirable.
- **Conducting further studies to reveal the interaction between snow and its ambient environment.** To better characterize local and regional snow packs, platforms integrating snow-related observations from different data sources are indispensable, e.g., National Snow & Ice Data Center (NSIDC), Globsnow. Yet, a comprehensive platform integrating other related environment variables (e.g., river discharge, air temperature) is absent. Given the strong interaction between snow and its ambient environment, developing a consistent platform which integrates multiple snow and climate variables can not only improve the understanding of regional responses to climate change, but also support decision-making and adaptation-strategy-making in climate sensitive regions. Furthermore, efficient techniques for handling information from different data sources are needed to analyse the snow dynamics together with their surroundings.
- **Implementing regional and local adaptation strategies.** European mountains are highly sensitive to the influences of climate change. Snow in mountainous areas represents a significant ecosystem function and service, as well as an important factor for economic prosperity. The population in these mountains are particularly exposed to snow-related natural hazards such as spring floods, avalanches, and snow storms. These hazards not only threaten the habitants in mountain areas, but also their ambient areas (e.g., downstream regions). Global warming intensifies such phenomena. Thus, challenges for the design of adaptation-strategies need to be addressed urgently, especially at a regional scale. In winter sports, for example, as the snowline retreats with increasing speed, ski resorts are forced to use artificial snow to extend the ski seasons. Not only does this pattern take a financial toll on these businesses, but also there may be consequential environmental impacts on ski resorts that should be assessed. As a basis, these strategies call for the cooperation of environment scientists, hydrologists, meteorologists, etc. to better observe and analyse the historic and ongoing changes, and reduce the uncertainties in prediction.

EO is a highly effective, objective, and reliable technique for investigating long-term regional snow dynamics. The development of a spatiotemporal transferable framework has received interest as a potentially important tool in the work performed by many scientists, policy-makers, and business stakeholders. The framework developed in thesis is a step forward in better serving such work. The thesis also demonstrates the potentials of quantifying these changes, and analysing the interactions between snow and its ambient environment. Despite the advances made by the framework presented in this thesis, the above-mentioned knowledge and research gaps demand further consideration.

## References

- Adam, N., Jonsson, S., 1997. Comparison of two differential interferometry techniques for the monitoring of geodynamic events. *Earth Surf. Remote Sens.* 3222, 319–328.
- Albrecht, F., Wahl, T., Jensen, J., Weisse, R., 2011. Determining sea level change in the German Bight. *Ocean Dyn.* 61, 2037–2050.
- Allen, M.R., Dube, O.P., Solecki, W., Aragón-Durand, F., Cramer, W., Humphreys, S., Kainuma, M., Kala, J., Mahowald, N., Mulugetta, Y., Perez, R., Wairiu, M., Zickfeld, K., 2018: Framing and Context. In: *Global Warming of 1.5°C. An IPCC Special Report on the impacts of global warming of 1.5°C above pre-industrial levels and related global greenhouse gas emission pathways, in the context of strengthening the global response to the threat of climate change, sustainable development, and efforts to eradicate poverty* [Masson-Delmotte, V., Zhai, P., Pörtner, H.O., Roberts, D., Skea, J., Shukla, P.R., Pirani, A., Moufouma-Okia, W., Péan, C., Pidcock, R., Connors, S., Matthews, J.B.R., Chen, Y., Zhou, X., Gomis, M.I., Lonnoy, E., Maycock, T., Tignor, M., Waterfield, T. (eds.)]. In Press. Available Online: <https://www.ipcc.ch/sr15/chapter/chapter-1-pdf/> (accessed on 25 July, 2019).
- Altena, B., Kääh, A., 2017. Elevation change and improved velocity retrieval using orthorectified optical satellite data from different orbits. *Remote Sens.* 9, 300.
- Andersen, T., 1982. Operational snow mapping by satellites, in: *Proceedings of the Exeter Symposium: Hydrological Aspects of Alpine and High Mountain Areas*, Exeter, UK, 19–30 July, 1982; pp. 149–154.
- Andersland, O.B., Ladanyi, B., 2013. *An introduction to frozen ground engineering*. Springer Science & Business Media: Boston, MA, USA.
- Anisimov, O., 2007. Potential feedback of thawing permafrost to the global climate system through methane emission. *Environ. Res. Lett.* 2, 045016.
- Arendt, A., Bliss, A., Bolch, T., Cogley, J.G., Gardner, A.S., Hagen, J.O., Hock, R., Huss, M., Kaser, G., Kienholz, C., Pfeffer, W.T., 2015. *Randolph Glacier Inventory—A dataset of global glacier outlines: Version 5.0*. GLIMS Tech. Rep.; GLIMS: Boulder, CO, USA.
- Arino, O., Ramos Perez, J.J., Kalogirou, V., Bontemps, S., Defourny, P., Van Bogaert, E., 2012. *Global land cover map for 2009 (GlobCover 2009)*. European Space Agency (ESA) & Université catholique de Louvain (UCL), PANGAEA. Available Online: <https://doi.org/10.1594/PANGAEA.787668> (accessed on 25 July, 2019).

- Armstrong, R.L., Brodzik, M.J., 2001. Recent Northern Hemisphere snow extent: A comparison of data derived from visible and microwave satellite sensors. *Geophys. Res. Lett.* 28, 3673–3676.
- Arvidson, T., Gasch, J., Goward, S.N., 2001. Landsat 7's long-term acquisition plan—An innovative approach to building a global imagery archive. *Remote Sens. Environ.* 78, 13–26.
- Arvidson, T., Goward, S., Gasch, J., Williams, D., 2006. Landsat-7 long-term acquisition plan. *Photogramm. Eng. Remote Sens.* 72, 1137–1146.
- Asam, S., Callegari, M., Matiu, M., Fiore, G., De Gregorio, L., Jacob, A., Menzel, A., Zebisch, M., Notarnicola, C., 2018. Relationship between Spatiotemporal Variations of Climate, Snow Cover and Plant Phenology over the Alps—An Earth Observation-Based Analysis. *Remote Sens.* 10, 1757.
- Aschbacher, J., 1989. Land surface studies and atmospheric effects by satellite microwave radiometry. Ph.D. Thesis, University of Innsbruck, Innsbruck, Austria.
- Asrar, G., Asra, G., 1989. Theory and applications of optical remote sensing. Wiley Series in Remote Sensing (New York: John Wiley & Sons): New York, NY, USA.
- Atwood, D., Meyer, F., Arendt, A., 2010. Using L-band SAR coherence to delineate glacier extent. *Can. J. Remote Sens.* 36, S186–S195.
- Bachmann, M., Tungalagsaikhan, P., Ruppert, T., Dech, S., 2015. Calibration and Pre-processing of a Multi-decadal AVHRR Time Series, in: *Remote Sensing Time Series*. Springer, pp. 43–74.
- Barnett, T.P., Adam, J.C., Lettenmaier, D.P., 2005. Potential impacts of a warming climate on water availability in snow-dominated regions. *Nature* 438, 303–309.
- Bartsch, A., Grosse, G., Käab, A., Westermann, S., Strozzi, T., Wiesmann, A., Duguay, C., Seifert, F.M., Obu, J., Goler, R., 2016. GlobPermafrost- How Space-Based Earth Observation Supports Understanding of Permafrost, in: *Living Planet Symposium*. p. 332.
- Bates, R.E., Bilello, M.A., 1966. Defining the cold regions of the Northern Hemisphere. Technical Report No. 178; Cold Regions Research and Engineering Laboratory: Hanover, NH, USA.
- Baumann, S., Winkler, S., Andreassen, L., 2009. Mapping glaciers in Jotunheimen, South-Norway, during the " Little Ice Age" maximum. *The Cryosphere* 3, 231.
- Bayr, K.J., Hall, D., Kovalick, W., 1994. Observations on glaciers in the eastern Austrian Alps using satellite data. *Int. J. Remote Sens.* 15, 1733–1742.
- Beniston, M., Diaz, H.F., Bradley, R.S., 1997. Climatic change at high elevation sites: an overview. *Clim. Change* 36, 233–251.



- Berrisford, P., Dee, D., Poli, P., Brugge, R., Fielding, K., Fuentes, M., Kallberg, P., Kobayashi, S., Uppala, S., Simmons, A., 2011. The ERA-Interim archive Version 2.0, ERA Report Series 1, ECMWF, Shinfield Park. Read. UK 13177.
- Berthier, E., Arnaud, Y., Baratoux, D., Vincent, C., Rémy, F., 2004. Recent rapid thinning of the "Mer de Glace" glacier derived from satellite optical images. *Geophys. Res. Lett.* 31.
- Berthier, E., Vadon, H., Baratoux, D., Arnaud, Y., Vincent, C., Feigl, K., Rémy, F., Legresy, B., 2005. Surface motion of mountain glaciers derived from satellite optical imagery. *Remote Sens. Environ.* 95, 14–28.
- Błaszczak, M., Jania, J.A., Hagen, J.O., 2009. Tidewater glaciers of Svalbard: Recent changes and estimates of calving fluxes. *Pol. Polar Res.* 30, 85–142.
- Blöschl, G., Hall, J., Parajka, J., Perdigão, R.A., Merz, B., Arheimer, B., Aronica, G.T., Bilibashi, A., Bonacci, O., Borga, M., others, 2017. Changing climate shifts timing of European floods. *Science* 357, 588–590.
- Bogdanski, B.E.C., 2008. Canada's boreal forest economy: economic and socioeconomic issues and research opportunities. Natural Resources Canada, Canadian Forest Service, Pacific Forestry Centre: Victoria, BC, Canada, 2008; Volume 414.
- Bonan, G.B., Pollard, D., Thompson, S.L., 1992. Effects of boreal forest vegetation on global climate. *Nature* 359, 716–718.
- Böttcher, K., Aurela, M., Kervinen, M., Markkanen, T., Mattila, O.P., Kolari, P., Metsämäki, S., Aalto, T., Arslan, A.N., Pulliainen, J., 2014. MODIS time-series-derived indicators for the beginning of the growing season in boreal coniferous forest - A comparison with CO<sub>2</sub> flux measurements and phenological observations in Finland. *Remote Sens. Environ.* 140, 625–638.
- Braithwaite, R.J., 1984. Short Notes: Can the Mass Balance of a Glacier be Estimated from its Equilibrium-Line Altitude? *J. Glaciol.* 30, 364–368.
- Breiman, L., 2001. Random forests. *Mach. Learn.* 45, 5–32.
- Bulygina, O., Razuvaev, V., Korshunova, N., 2009. Changes in snow cover over Northern Eurasia in the last few decades. *Environ. Res. Lett.* 4, 045026.
- C3S, 2017. ERA5: Fifth generation of ECMWF atmospheric reanalyses of the global climate. Copernicus Climate Change Service Climate Data Store (CDS). Available Online: <https://cds.climate.copernicus.eu/cdsapp#!/home> (accessed on 26 July, 2019).
- Calluy, G., Björnsson, H., Greuell, J., Oerlemans, J., 2005. Estimating the mass balance of Vatnajökull, Iceland, from NOAA AVHRR imagery. *Ann. Glaciol.* 42, 118–124.

- Carturan, L., Filippi, R., Seppi, R., Gabrielli, P., Notarnicola, C., Bertoldi, L., Paul, F., Rastner, P., Cazorzi, F., Dinale, R., others, 2013. Area and volume loss of the glaciers in the Ortles-Cevedale group (Eastern Italian Alps): controls and imbalance of the remaining glaciers. *The Cryosphere* 7, 1339.
- Chander, G., Helder, D.L., Malla, R., Micijevic, E., Mettler, C.J., 2007. Consistency of L4 TM absolute calibration with respect to the L5 TM sensor based on near-simultaneous image acquisition, in: *Earth Observing Systems XII. International Society for Optics and Photonics*, p. 66770F.
- Chander, G., Markham, B.L., Helder, D.L., 2009. Summary of current radiometric calibration coefficients for Landsat MSS, TM, ETM+, and EO-1 ALI sensors. *Remote Sens. Environ.* 113, 893–903.
- Chander, G., Micijevic, E., 2006. Absolute calibration accuracy of L4 TM and L5 TM sensor image pairs, in: *Earth Observing Systems XI. International Society for Optics and Photonics*, p. 62960D.
- Chang, A., Foster, J., Hall, D.K., 1987. Nimbus-7 SMMR derived global snow cover parameters. *Ann. Glaciol.* 9, 39–44.
- Chen, X., Liang, S., Cao, Y., He, T., Wang, D., 2015. Observed contrast changes in snow cover phenology in northern middle and high latitudes from 2001–2014. *Sci. Rep.* 5.
- Chi, M., Plaza, A., Benediktsson, J.A., Sun, Z., Shen, J., Zhu, Y., 2016. Big Data for Remote Sensing: Challenges and Opportunities. *Proc. IEEE* 104, 2207–2219.
- Christensen, J.H., Christensen, O.B., 2003. Climate modelling: severe summertime flooding in Europe. *Nature* 421, 805–806.
- Christensen, J.H., Hewitson, B., Busuioc, A., Chen, A., Gao, X., Held, R., Jones, R., Kolli, R.K., Kwon, W., Laprise, R., others, 2007. Regional climate projections, in: *Climate Change, 2007: The Physical Science Basis. Contribution of Working Group I to the Fourth Assessment Report of the Intergovernmental Panel on Climate Change*, University Press: Cambridge, UK; Chapter 11; pp. 847–940.
- Ciscar, J.C., Iglesias, A., Feyen, L., Szabó, L., Van Regemorter, D., Amelung, B., Nicholls, R., Watkiss, P., Christensen, O.B., Dankers, R., others, 2011. Physical and economic consequences of climate change in Europe. *Proc. Natl. Acad. Sci.* 108, 2678–2683.
- Cleland, E.E., Chuine, I., Menzel, A., Mooney, H.A., Schwartz, M.D., 2007. Shifting plant phenology in response to global change. *Trends Ecol. Evol.* 22, 357–365.
- Cogley, J., Hock, R., Rasmussen, L., Arendt, A., Bauder, A., Braithwaite, R., Jansson, P., Kaser, G., Möller, M., Nicholson, L., others, 2011. Glossary of glacier mass balance and related terms, IHP-VII technical documents in hydrology No. 86, IACS Contribution No. 2. UNESCO-IHP: Paris, France.

- Cogley, J.G., 2009. Geodetic and direct mass-balance measurements: comparison and joint analysis. *Ann. Glaciol.* 50, 96–100.
- Da Ronco, P., De Michele, C., 2014. Cloud obstruction and snow cover in Alpine areas from MODIS products. *Hydrol. Earth Syst. Sci.* 18, 4579.
- Defourny, P., Kirches, G., Brockmann, M., C. an. Boettcher, Peters, M., Bontemps, S., Lamarche, C., Schlerf, M., Santoro, M., 2016. Land Cover CCI: Product User Guide Version 2. Available Online: [https://maps.elie.ucl.ac.be/CCI/viewer/download/ESACCI-LC-Ph2-PUGv2\\_2.0.pdf](https://maps.elie.ucl.ac.be/CCI/viewer/download/ESACCI-LC-Ph2-PUGv2_2.0.pdf) (accessed on 25 July, 2019).
- Déry, S.J., Brown, R.D., 2007. Recent Northern Hemisphere snow cover extent trends and implications for the snow-albedo feedback. *Geophys. Res. Lett.* 34.
- Di Mauro, B., Fava, F., Ferrero, L., Garzonio, R., Baccolo, G., Delmonte, B., Colombo, R., 2015. Mineral dust impact on snow radiative properties in the European Alps combining ground, UAV, and satellite observations. *J. Geophys. Res. Atmospheres* 120, 6080–6097.
- Diaz, H.F., Grosjean, M., Graumlich, L., 2003. Climate variability and change in high elevation regions: past, present and future. *Clim. Change* 59, 1–4.
- Dietz, A., Kuenzer, C., Dech, S., 2015. Global SnowPack: a new set of snow cover parameters for studying status and dynamics of the planetary snow cover extent. *Remote Sens. Lett.* 6, 844–853.
- Dietz, A., Wohner, C., Kuenzer, C., 2012. European snow cover characteristics between 2000 and 2011 derived from improved MODIS daily snow cover products. *Remote Sens.* 4, 2432–2454.
- Dong, J., Peters-Lidard, C., 2010. On the relationship between temperature and MODIS snow cover retrieval errors in the Western US. *IEEE J. Sel. Top. Appl. Earth Obs. Remote Sens.* 3, 132–140.
- Donlon, C., Berruti, B., Buongiorno, A., Ferreira, M.H., Féménias, P., Frerick, J., Goryl, P., Klein, U., Laur, H., Mavrocordatos, C., others, 2012. The global monitoring for environment and security (GMES) sentinel-3 mission. *Remote Sens. Environ.* 120, 37–57.
- Dozier, J., 1989. Spectral signature of alpine snow cover from the landsat thematic mapper. *Remote Sens. Environ.* 28, 9–22.
- Dozier, J., 1984. Snow reflectance from Landsat-4 thematic mapper. *IEEE Trans. Geosci. Remote Sens.* 323–328.
- Drusch, M., Del Bello, U., Carlier, S., Colin, O., Fernandez, V., Gascon, F., Hoersch, B., Isola, C., Laberinti, P., Martimort, P., Meygret, A., Spoto, F., Sy, O., Marchese, F., Bargellini, P., 2012. Sentinel-2: ESA's Optical High-Resolution Mission for GMES Operational Services. *Remote Sens. Environ.* 120, 25–36.

## References

---

- Dumont, M., Gardelle, J., Sirguey, P., Guillot, A., Six, D., Rabatel, A., Arnaud, Y., 2012. Linking glacier annual mass balance and glacier albedo retrieved from MODIS data. *The Cryosphere* 6, 1527–1539.
- EC, 2009. White paper-Adapting to climate change: Towards a European framework for action. Eur. Comm. Available Online: [https://ec.europa.eu/health/ph\\_threats/climate/docs/com\\_2009\\_147\\_en.pdf](https://ec.europa.eu/health/ph_threats/climate/docs/com_2009_147_en.pdf) (accessed on 25 July, 2019).
- EEA, 2018. Use of freshwater resources. Available Online: <https://www.eea.europa.eu/data-and-maps/indicators/use-of-freshwater-resources-2/assessment-3> (accessed on 25 July, 2019).
- EEA, 2017a. Climate change, impacts and vulnerability in Europe 2016 - An indicator-based report. Available Online: [https://www.eea.europa.eu/publications/climate-change-impacts-and-vulnerability-2016/at\\_download/file](https://www.eea.europa.eu/publications/climate-change-impacts-and-vulnerability-2016/at_download/file) (accessed on 25 July, 2019).
- EEA, 2017b. Overview of Global DEM Assessment of the current global DEMs and requirements for an updated global DEM. Available Online: [https://insitu.copernicus.eu/library/reports/OverviewofGlobalDEM\\_i0r7.pdf](https://insitu.copernicus.eu/library/reports/OverviewofGlobalDEM_i0r7.pdf) (accessed on 25 July, 2019).
- EEA, 2009. Regional Climate Change and Adaptation-The Alps Facing the Challenge of Changing Water Resources. Eur. Environ. Agency Copenhagen Den. Available Online: [https://www.eea.europa.eu/publications/alps-climate-change-and-adaptation-2009/at\\_download/file](https://www.eea.europa.eu/publications/alps-climate-change-and-adaptation-2009/at_download/file) (accessed on 25 July, 2019).
- Fily, M., Bourdelles, B., Dedieu, J., Sergent, C., 1997. Comparison of in situ and Landsat Thematic Mapper derived snow grain characteristics in the Alps. *Remote Sens. Environ.* 59, 452–460.
- Finsterwalder, R., 1954. Photogrammetry and glacier research with special reference to glacier retreat in the eastern Alps. *J. Glaciol.* 2, 306–315.
- Foga, S., Scaramuzza, P.L., Guo, S., Zhu, Z., Dilley, R.D., Beckmann, T., Schmidt, G.L., Dwyer, J.L., Hughes, M.J., Laue, B., 2017. Cloud detection algorithm comparison and validation for operational Landsat data products. *Remote Sens. Environ.* 194, 379–390.
- Follestad, B.A., Fredin, O., 2007. Late Weichselian ice flow evolution in south-central Norway? *Nor. Geol. Tidsskr.* 87, 281.
- Foppa, N., Hauser, A., Oesch, D., Wunderle, S., Meister, R., 2007. Validation of operational AVHRR subpixel snow retrievals over the European Alps based on ASTER data. *Int. J. Remote Sens.* 28, 4841–4865.
- Foppa, N., Wunderle, S., Hauser, A., Oesch, D., Kuchen, F., 2004. Operational sub-pixel snow mapping over the Alps with NOAA AVHRR data. *Ann. Glaciol.* 38, 245–252.

- Foster, J., Hall, D., Eylander, J., 2009. A new blended snow product using visible, microwave and scatterometer satellite data, in: Proceedings of the 2009 IEEE International Geoscience and Remote Sensing Symposium, Cape Town, South Africa, 12–17 July, 2009; Volume 2.
- Foster, J., Hall, D., Eylander, J., Kim, E., Riggs, G., Tedesco, M., Nghiem, S., Kelly, R., Choudhury, B., Reichle, R., others, 2007. Blended visible, passive microwave and scatterometer global snow products, in: Proceedings of the 64th Eastern Snow Conference, St. John's, NL, Canada, 29 May–1 June, 2007; Volume 28.
- Foster, J.L., Hall, D.K., Eylander, J.B., Riggs, G.A., Nghiem, S.V., Tedesco, M., Kim, E., Montesano, P.M., Kelly, R.E., Casey, K.A., others, 2011. A blended global snow product using visible, passive microwave and scatterometer satellite data. *Int. J. Remote Sens.* 32, 1371–1395.
- Frantz, D., Haß, E., Uhl, A., Stoffels, J., Hill, J., 2018. Improvement of the Fmask algorithm for Sentinel-2 images: Separating clouds from bright surfaces based on parallax effects. *Remote Sens. Environ.* 215, 471–481.
- Frey, H., Paul, F., 2012. On the suitability of the SRTM DEM and ASTER GDEM for the compilation of topographic parameters in glacier inventories. *Int. J. Appl. Earth Obs. Geoinformation* 18, 480–490.
- Füssel, H.M., Jol, A., others, 2012. Climate change, impacts and vulnerability in Europe 2012 an indicator-based report. EEA Report No. 12/2012; European Environment Agency: Copenhagen, Denmark.
- Gafurov, A., Bárdossy, A., 2009. Cloud removal methodology from MODIS snow cover product. *Hydrol. Earth Syst. Sci.* 13, 1361.
- Gao, B.C., 1996. NDWI—A normalized difference water index for remote sensing of vegetation liquid water from space. *Remote Sens. Environ.* 58, 257–266.
- Gardelle, J., Berthier, E., Arnaud, Y., 2012. Impact of resolution and radar penetration on glacier elevation changes computed from DEM differencing. *J. Glaciol.* 58, 419–422.
- Gardent, M., Rabatel, A., Dedieu, J.-P., Deline, P., 2014. Multitemporal glacier inventory of the French Alps from the late 1960s to the late 2000s. *Glob. Planet. Change* 120, 24–37.
- GEOSTAT, 2011. ReadMe file for the GEOSTAT 2011 data. Available Online: <https://ec.europa.eu/eurostat/web/gisco/geodata/reference-data/population-distribution-demography/geostat> (accessed on 26 July, 2019).
- Giuntoli, I., Renard, B., Lang, M., 2012. Floods in France. CRC Press, Wallingford, UK.
- Gorelick, N., Hancher, M., Dixon, M., Ilyushchenko, S., Thau, D., Moore, R., 2016. Google Earth Engine: Planetary-scale geospatial analysis for everyone. *Remote Sens. Environ.* 202, 18–27.

- Goward, S., Arvidson, T., Williams, D., Faundeen, J., Irons, J., Franks, S., 2006. Historical record of Landsat global coverage. *Photogramm. Eng. Remote Sens.* 72, 1155–1169.
- Greuell, W., Kohler, J., Obleitner, F., Glowacki, P., Melvold, K., Bernsen, E., Oerlemans, J., 2007. Assessment of interannual variations in the surface mass balance of 18 Svalbard glaciers from the Moderate Resolution Imaging Spectroradiometer/Terra albedo product. *J. Geophys. Res. Atmospheres* 112.
- Grody, N.C., 1991. Classification of snow cover and precipitation using the Special Sensor Microwave Imager. *J. Geophys. Res. Atmospheres* 96, 7423–7435.
- Grody, N.C., Basist, A.N., 1996. Global identification of snowcover using SSM/I measurements. *IEEE Trans. Geosci. Remote Sens.* 34, 237–249.
- Hagolle, O., Huc, M., Pascual, D.V., Dedieu, G., 2010. A multi-temporal method for cloud detection, applied to FORMOSAT-2, VEN $\mu$ S, LANDSAT and SENTINEL-2 images. *Remote Sens. Environ.* 114, 1747–1755.
- Haigh, I., Nicholls, R., Wells, N., 2010. Assessing changes in extreme sea levels: application to the English Channel, 1900–2006. *Cont. Shelf Res.* 30, 1042–1055.
- Hall, D., 2012. *Remote sensing of ice and snow*. Springer Science & Business Media: London, UK.
- Hall, D., Ormsby, J., Bindschadler, R., Siddalingaiah, H., 1987. Characterization of snow and ice reflectance zones on glaciers using Landsat Thematic Mapper data. *Ann. Glaciol.* 9, 104–108.
- Hall, D.K., Riggs, G.A., Salomonson, V.V., 1995. Development of methods for mapping global snow cover using moderate resolution imaging spectroradiometer data. *Remote Sens. Environ.* 54, 127–140.
- Hall, D.K., Riggs, G.A., Salomonson, V.V., DiGirolamo, N.E., Bayr, K.J., 2002. MODIS snow-cover products. *Remote Sens. Environ.* 83, 181–194.
- Hallikainen, M., 1984. Retrieval of snow water equivalent from Nimbus-7 SMMR data: Effect of land-cover categories and weather conditions. *IEEE J. Ocean. Eng.* 9, 372–376.
- Hallikainen, M.T., Halme, P., Takala, M., Pulliainen, J., 2003. Combined Active and Passive Microwave Remote Sensing of Snow in Finland. *IGARSS 2003 Learn. Earths Shapes Sizes 2003 IEEE Int. Geosci. Remote Sens. Symp. Proc. Cent. Congrès Pierre Baudis Toulouse Fr. 21-25 July 2003* 00, 830–832.
- Hallikainen, M.T., Jolma, P.A., 1992. Comparison of algorithms for retrieval of snow water equivalent from Nimbus-7 SMMR data in Finland. *IEEE Trans. Geosci. Remote Sens.* 30, 124–131.

- Hallikainen, M.T., Jolma, P.A., 1986. Retrieval of the water equivalent of snow cover in Finland by satellite microwave radiometry. *IEEE Trans. Geosci. Remote Sens.* 855–862.
- Hampel, F.R., Ronchetti, E.M., Rousseeuw, P.J., Stahel, W.A., 2011. *Robust statistics: the approach based on influence functions*. John Wiley & Sons: New York, NY, USA.
- Hannesdóttir, H., Björnsson, H., Pálsson, F., Aðalgeirsdóttir, G., Guðmundsson, S., 2015. Changes in the southeast Vatnajökull ice cap, Iceland, between~ 1890 and 2010. *The Cryosphere* 9, 565–585.
- Heal, O.W., 1998. Global change in Europe's cold regions: report on the Arteri workshops held at the Danish Polar Centre, Copenhagen, from 8 to 10 November (Part 1) and 4 to 7 November (Part 2) 1996. European Commission Ecosystems Research Report 27; Office for Official Publications of the European Communities: Luxembourg.
- Heid, T., Kääb, A., 2012a. Repeat optical satellite images reveal widespread and long term decrease in land-terminating glacier speeds. *The Cryosphere* 6, 467–478.
- Heid, T., Kääb, A., 2012b. Evaluation of existing image matching methods for deriving glacier surface displacements globally from optical satellite imagery. *Remote Sens. Environ.* 118, 339–355.
- Helfrich, S.R., McNamara, D., Ramsay, B.H., Baldwin, T., Kasheta, T., 2007. Enhancements to, and forthcoming developments in the Interactive Multisensor Snow and Ice Mapping System (IMS). *Hydrol. Process.* 21, 1576–1586.
- Henderson, G.R., Leathers, D.J., 2010. European snow cover extent variability and associations with atmospheric forcings. *Int. J. Climatol.* 30, 1440–1451.
- Holobacă, I.H., 2016. Recent retreat of the Elbrus glacier system. *J. Glaciol.* 62, 94–102.
- Hostert, P., Griffiths, P., van der Linden, S., Pflugmacher, D., 2015. Time series analyses in a new era of optical satellite data, in: *Remote Sensing Time Series*. Springer, pp. 25–41.
- Hu, Z., Dietz, A., Kuenzer, C., 2019a. The potential of retrieving snow line dynamics from Landsat during the end of the ablation seasons between 1982 and 2017 in European mountains. *Int. J. Appl. Earth Obs. Geoinformation* 78, 138–148.
- Hu, Z., Dietz, A.J., Kuenzer, C., 2019b. Deriving Regional Snow Line Dynamics during the Ablation Seasons 1984–2018 in European Mountains. *Remote Sens.* 11, 933.
- Hu, Z., Kuenzer, C., Dietz, A.J., Dech, S., 2017. The Potential of Earth Observation for the Analysis of Cold Region Land Surface Dynamics in Europe—A Review. *Remote Sens.* 9, 1067.
- Huss, M., 2013. Density assumptions for converting geodetic glacier volume change to mass change. *The Cryosphere* 7, 877–887.

- Ingmann, P., Veihelmann, B., Langen, J., Lamarre, D., Stark, H., Courrèges-Lacoste, G.B., 2012. Requirements for the GMES Atmosphere Service and ESA's implementation concept: Sentinels-4/-5 and-5p. *Remote Sens. Environ.* 120, 58–69.
- IPCC, 2014. *Climate change 2014: impacts, adaptation, and vulnerability-Part B: regional aspects-Contribution of Working Group II to the Fifth Assessment Report of the Intergovernmental Panel on Climate Change*. Cambridge University Press: Cambridge, UK.
- IPCC, 2013. *Climate change 2013: the physical science basis: Working Group I contribution to the Fifth assessment report of the Intergovernmental Panel on Climate Change*. Cambridge University Press: Cambridge, UK.
- Irish, R.R., 2000. Landsat 7 automatic cloud cover assessment, in: *Algorithms for Multispectral, Hyperspectral, and Ultraspectral Imagery VI*. International Society for Optics and Photonics, pp. 348–356.
- Irish, R.R., Barker, J.L., Goward, S.N., Arvidson, T., 2006. Characterization of the Landsat-7 ETM+ automated cloud-cover assessment (ACCA) algorithm. *Photogramm. Eng. Remote Sens.* 72, 1179–1188.
- Joughin, I.R., Kwok, R., Fahnestock, M.A., 1998. Interferometric estimation of three-dimensional ice-flow using ascending and descending passes. *IEEE Trans. Geosci. Remote Sens.* 36, 25–37.
- Kääb, A., 2008. Glacier volume changes using ASTER satellite stereo and ICESat GLAS laser altimetry. A test study on Edgeøya, Eastern Svalbard. *IEEE Trans. Geosci. Remote Sens.* 46, 2823–2830.
- Kääb, A., 2002. Monitoring high-mountain terrain deformation from repeated air- and spaceborne optical data: Examples using digital aerial imagery and ASTER data. *ISPRS J. Photogramm. Remote Sens.* 57, 39–52.
- Kääb, A., Berthier, E., Nuth, C., Gardelle, J., Arnaud, Y., 2012. Contrasting patterns of early twenty-first-century glacier mass change in the Himalayas. *Nature* 488, 495–498.
- Kääb, A., Lefauconnier, B., Melvold, K., 2005. Flow field of Kronebreen, Svalbard, using repeated Landsat 7 and ASTER data. *Ann. Glaciol.* 42, 7–13.
- Kääb, A., Paul, F., Maisch, M., Hoelzle, M., Haeberli, W., 2002. The new remote-sensing-derived Swiss glacier inventory: II. First results. *Ann. Glaciol.* 34, 362–366.
- Kääb, A., Winsvold, S.H., Altena, B., Nuth, C., Nagler, T., Wuite, J., 2016. Glacier Remote Sensing Using Sentinel-2. Part I: Radiometric and Geometric Performance, and Application to Ice Velocity. *Remote Sens.* 8, 598.
- Kaser, G., Großhauser, M., Marzeion, B., 2010. Contribution potential of glaciers to water availability in different climate regimes. *Proc. Natl. Acad. Sci.* 107, 20223–20227.



- Kim, Y., Kimball, J.S., Zhang, K., McDonald, K.C., 2012. Satellite detection of increasing Northern Hemisphere non-frozen seasons from 1979 to 2008: Implications for regional vegetation growth. *Remote Sens. Environ.* 121, 472–487.
- Klein, A.G., Hall, D.K., Riggs, G.A., others, 1998. Improving snow cover mapping in forests through the use of a canopy reflectance model. *Hydrol. Process.* 12, 1723–1744.
- Kongoli, C., Dean, C.A., Helfrich, S.R., Ferraro, R.R., 2007. Evaluating the potential of a blended passive microwave-interactive multi-sensor product for improved mapping of snow cover and estimations of snow water equivalent. *Hydrol. Process.* 21, 1597–1607.
- Köppen, W., 1884. Die Wärmezonen der Erde, nach der Dauer der heissen, gemässigten und kalten Zeit und nach der Wirkung der Wärme auf die organische Welt betrachtet. *Meteorol. Z.* 1, 5–226.
- Koskinen, J.T., Pulliainen, J.T., Hallikainen, M.T., 1997. The use of ERS-1 SAR data in snow melt monitoring. *IEEE Trans. Geosci. Remote Sens.* 35, 601–610.
- Kottek, M., Grieser, J., Beck, C., Rudolf, B., Rubel, F., 2006. World map of the Köppen-Geiger climate classification updated. *Meteorol. Z.* 15, 259–263.
- Krajčí, P., Holko, L., Perdigão, R.A.P., Parajka, J., 2014. Estimation of regional snowline elevation (RSLE) from MODIS images for seasonally snow covered mountain basins. *J. Hydrol.* 519, 1769–1778.
- Kuenzer, C., Dech, S., Wagner, W., 2015. Remote sensing time series revealing land surface dynamics: Status quo and the pathway ahead, in: *Remote Sensing Time Series*. Springer, pp. 1–24.
- Kuenzer, C., Ottinger, M., Wegmann, M., Guo, H., Wang, C., Zhang, J., Dech, S., Wikelski, M., 2014. Earth observation satellite sensors for biodiversity monitoring: potentials and bottlenecks. *Int. J. Remote Sens.* 35, 6599–6647.
- Kulkarni, A.V., 1992. Mass balance of Himalayan glaciers using AAR and ELA methods. *J. Glaciol.* 38, 101–104.
- Kurvonen, L., Hallikainen, M., 1997. Influence of land-cover category on brightness temperature of snow. *IEEE Trans. Geosci. Remote Sens.* 35, 367–377.
- Lambin, E.F., Strahlers, A.H., 1994. Change-vector analysis in multitemporal space: a tool to detect and categorize land-cover change processes using high temporal-resolution satellite data. *Remote Sens. Environ.* 48, 231–244.
- Lehner, B., Verdin, K., Jarvis, A., 2008. New global hydrography derived from spaceborne elevation data. *Eos, Transactions American Geophysical Union* 89, pp. 93–94.

## References

---

- Lemke, P., Ren, J., Alley, R., Allison, I., Carrasco, J., Flato, G., Fujii, Y., Kaser, G., Mote, P., Thomas, R., others, 2007. Observations: changes in snow, ice and frozen ground, climate change 2007: The physical science basis. Contribution of working group I to the fourth assessment report of the intergovernmental panel on climate change. Cambridge University Press: Cambridge, UK; New York, NY, USA.
- Lemmetyinen, J., Pulliainen, J., Karna, J., Tauriainen, S., Pihlflyckt, J., Hallikainen, M., 2006. Spatial Microwave Brightness Temperature Variations of Boreal Forests under Dry Snow Cover Conditions, in: IEEE MicroRad, 2006. IEEE, pp. 142–147.
- Li, J., Liu, Y., 2011. Study on Design Strategies for Improving Outdoor Thermal Comfort in the Cold Regions of China, in: Advanced Materials Research. Trans Tech Publ, pp. 3798–3801.
- Liaw, A., Wiener, M., others, 2002. Classification and regression by randomForest. R News 2, 18–22.
- Lougeay, R., 1974. Detection of buried glacial and ground ice with thermal infrared remote sensing. In Advanced Concepts and Techniques in the Study of Snow and Ice Resources; National Academy of Sciences: Washington, DC, USA.
- Luterbacher, J., Dietrich, D., Xoplaki, E., Grosjean, M., Wanner, H., 2004. European seasonal and annual temperature variability, trends, and extremes since 1500. Science 303, 1499–1503.
- Magnússon, E., Björnsson, H., Rott, H., Roberts, M.J., Pálsson, F., Gudmundsson, S., Bennett, R.A., Geirsson, H., Sturkell, E., 2011. Localized uplift of Vatnajökull, Iceland: subglacial water accumulation deduced from InSAR and GPS observations. J. Glaciol. 57, 475–484.
- Markham, B.L., Storey, J.C., Williams, D.L., Irons, J.R., 2004. Landsat sensor performance: history and current status. IEEE Trans. Geosci. Remote Sens. 42, 2691–2694.
- Martinec, J., 1975. Snowmelt-runoff model for stream flow forecasts. Hydrol. Res. 6, 145–154.
- Martinec, J., Rango, A., Roberts, R., Baumgartner, M.F., 1998. Snowmelt runoff model (SRM) user's manual. University of Berne, Department of Geography. Available Online: [https://aces.nmsu.edu/pubs/research/weather\\_climate/SRMSpecRep100.pdf](https://aces.nmsu.edu/pubs/research/weather_climate/SRMSpecRep100.pdf) (accessed on 25 July, 2019).
- Martinuzzi, S., Gould, W.A., González, O.M.R., 2007. Creating cloud-free Landsat ETM+ data sets in tropical landscapes: cloud and cloud-shadow removal. US Department of Agriculture, Forest Service, International Institute of Tropical Forestry. Gen. Tech. Rep. IITF-32., 32.

- Mason, P., Manton, M., Harrison, D., Belward, A., Thomas, A., Dawson, D., 2003. The second report on the adequacy of the global observing systems for climate in support of the UNFCCC. GCOS Rep 82. Available Online: [http://www.ocean-partners.org/sites/ocean-partners.org/files/public/attachments/243\\_GCOS-2-Adequacy-E S.pdf](http://www.ocean-partners.org/sites/ocean-partners.org/files/public/attachments/243_GCOS-2-Adequacy-E S.pdf) (accessed on 25 July, 2019).
- Matson, M., Wiesnet, D.R., 1981. New data base for climate studies. *Nature* 289, 451–456.
- Maurer, E.P., Rhoads, J.D., Dubayah, R.O., Lettenmaier, D.P., 2003. Evaluation of the snow-covered area data product from MODIS. *Hydrol. Process.* 17, 59–71.
- Menéndez, M., Woodworth, P.L., 2010. Changes in extreme high water levels based on a quasi-global tide-gauge data set. *J. Geophys. Res. Oceans* 115.
- Menne, M.J., I. Durre, B. Korzeniewski, S. McNeal, K. Thomas, X. Yin, S. Anthony, R. Ray, R.S. Vose, B.E. Gleason, and T.G. Houston, 2012: Global Historical Climatology Network - Daily (GHCN-Daily), Version 3. NOAA National Climatic Data Center. Available Online: <http://doi.org/10.7289/V5D21VHZ> (accessed on 26 July, 2019).
- Menzel, A., Sparks, T.H., Estrella, N., Koch, E., Aasa, A., Ahas, R., ALM-KÜBLER, K., Bissolli, P., Braslavská, O., Briede, A., others, 2006. European phenological response to climate change matches the warming pattern. *Glob. Change Biol.* 12, 1969–1976.
- Metsämäki, S., Huttunen, M., Anttila, S., 2004. The operative remote sensing of snow covered area in a service of hydrological modeling in Finland. *Remote Sens. Transit.* Available Online: [https://is.muni.cz/el/1431/podzim2013/Z0059/um/43842215/45505521/article\\_7.txt](https://is.muni.cz/el/1431/podzim2013/Z0059/um/43842215/45505521/article_7.txt) (accessed on 26 July, 2019).
- Metsämäki, S., Mattila, O.P., Pulliainen, J., Niemi, K., Luojus, K., Böttcher, K., 2012. An optical reflectance model-based method for fractional snow cover mapping applicable to continental scale. *Remote Sens. Environ.* 123, 508–521.
- Metsämäki, S., Pulliainen, J., Salminen, M., Luojus, K., Wiesmann, A., Solberg, R., Böttcher, K., Hiltunen, M., Ripper, E., 2015. Introduction to GlobSnow Snow Extent products with considerations for accuracy assessment. *Remote Sens. Environ.* 156, 96–108.
- Metsämäki, S., Vepsäläinen, J., Pulliainen, J., Sucksdorff, Y., 2002. Improved linear interpolation method for the estimation of snow-covered area from optical data. *Remote Sens. Environ.* 82, 64–78.
- Metsämäki, S.J., Anttila, S.T., Markus, H.J., Vepsäläinen, J.M., 2005. A feasible method for fractional snow cover mapping in boreal zone based on a reflectance model. *Remote Sens. Environ.* 95, 77–95.
- Micijevic, E., Haque, M.O., Mishra, N., 2017. Radiometric characterization of Landsat Collection 1 products, in: *Earth Observing Systems XXII. International Society for Optics and Photonics*, p. 104021D.

- Mihalcea, C., Brock, B., Diolaiuti, G., D'Agata, C., Citterio, M., Kirkbride, M., Cutler, M., Smiraglia, C., 2008. Using ASTER satellite and ground-based surface temperature measurements to derive supraglacial debris cover and thickness patterns on Miage Glacier (Mont Blanc Massif, Italy). *Cold Reg. Sci. Technol.* 52, 341–354.
- Mills, L.S., Bragina, E.V., Kumar, A.V., Zimova, M., Lafferty, D.J., Feltner, J., Davis, B.M., Hackländer, K., Alves, P.C., Good, J.M., others, 2018. Winter color polymorphisms identify global hot spots for evolutionary rescue from climate change. *Science* 359, 1033–1036.
- Moholdt, G., Nuth, C., Hagen, J.O., Kohler, J., 2010. Recent elevation changes of Svalbard glaciers derived from ICESat laser altimetry. *Remote Sens. Environ.* 114, 2756–2767.
- Muhuri, A., Manickam, S., Bhattacharya, A., 2017. Scattering mechanism based snow cover mapping using RADARSAT-2 C-Band polarimetric SAR data. *IEEE J. Sel. Top. Appl. Earth Obs. Remote Sens.* 10, 3213–3224.
- Nagler, T., Rott, H., 2000. Retrieval of wet snow by means of multitemporal SAR data. *IEEE Trans. Geosci. Remote Sens.* 38, 754–765.
- Nagler, T., Rott, H., Malcher, P., Müller, F., 2008. Assimilation of meteorological and remote sensing data for snowmelt runoff forecasting. *Remote Sens. Environ.* 112, 1408–1420.
- Nasholm, T., Ekblad, A., Nordin, A., Giesler, R., others, 1998. Boreal forest plants take up organic nitrogen. *Nature* 392, 914.
- Nijhawan, R., Das, J., Raman, B., 2019. A hybrid of deep learning and hand-crafted features based approach for snow cover mapping. *Int. J. Remote Sens.* 40, 759–773.
- Nolin, A.W., Dozier, J., Mertes, L.A., 1993. Mapping alpine snow using a spectral mixture modeling technique. *Ann. Glaciol.* 17, 121–124.
- Notarnicola, C., Duguay, M., Moelg, N., Schellenberger, T., Tetzlaff, A., Monsorno, R., Costa, A., Steurer, C., Zebisch, M., 2013. Snow cover maps from MODIS images at 250 m resolution, Part 1: Algorithm description. *Remote Sens.* 5, 110–126.
- Nuth, C., Kääb, A., 2011. Co-registration and bias corrections of satellite elevation data sets for quantifying glacier thickness change. *The Cryosphere* 5, 271.
- Nuth, C., Kohler, J., König, M., Deschwanden, A. von, Hagen, J.O.M., Kääb, A., Moholdt, G., Pettersson, R., 2013. Decadal changes from a multi-temporal glacier inventory of Svalbard. *The Cryosphere* 7, 1603–1621.
- Nuth, C., Moholdt, G., Kohler, J., Hagen, J.O., Kääb, A., 2010. Svalbard glacier elevation changes and contribution to sea level rise. *J. Geophys. Res. Earth Surf.* 115.

- Nuth, C., Schuler, T.V., Kohler, J., Altena, B., Hagen, J.O., 2012. Estimating the long-term calving flux of Kronebreen, Svalbard, from geodetic elevation changes and mass-balance modelling. *J. Glaciol.* 58, 119–133.
- Obrist, D., Agnan, Y., Jiskra, M., Olson, C.L., Colegrove, D.P., Hueber, J., Moore, C.W., Sonke, J.E., Helmig, D., 2017. Tundra uptake of atmospheric elemental mercury drives Arctic mercury pollution. *Nature* 547, 201–204.
- Oerlemans, J., 2001. *Glaciers and climate change*. CRC Press: Lisse, The Netherlands.
- Östlund, L., Zackrisson, O., Axelsson, A.L., 1997. The history and transformation of a Scandinavian boreal forest landscape since the 19th century. *Can. J. For. Res.* 27, 1198–1206.
- Painter, T.H., Dozier, J., Roberts, D.A., Davis, R.E., Green, R.O., 2003. Retrieval of subpixel snow-covered area and grain size from imaging spectrometer data. *Remote Sens. Environ.* 85, 64–77.
- Painter, T.H., Rittger, K., McKenzie, C., Slaughter, P., Davis, R.E., Dozier, J., 2009. Retrieval of subpixel snow covered area, grain size, and albedo from MODIS. *Remote Sens. Environ.* 113, 868–879.
- Painter, T.H., Roberts, D.A., Green, R.O., Dozier, J., 1998. The effect of grain size on spectral mixture analysis of snow-covered area from AVIRIS data. *Remote Sens. Environ.* 65, 320–332.
- Parajka, J., Kohnová, S., Bálint, G., Barbuc, M., Borga, M., Claps, P., Cheval, S., Dumitrescu, A., Gaume, E., Hlavčová, K., others, 2010a. Seasonal characteristics of flood regimes across the Alpine–Carpathian range. *J. Hydrol.* 394, 78–89.
- Parajka, J., Pepe, M., Rampini, A., Rossi, S., Blöschl, G., 2010b. A regional snow-line method for estimating snow cover from MODIS during cloud cover. *J. Hydrol.* 381, 203–212.
- Parry, M., Canziani, O.F., Palutikof, J.P., van der Linden, P.J., Hanson, C.E., others, 2007. *Climate change 2007: impacts, adaptation and vulnerability*. Cambridge University Press: Cambridge, UK.
- Paterson, W.S.B., 2016. *The physics of glaciers*. Pergamon: New York, NY, USA.
- Paul, F., 2002. Changes in glacier area in Tyrol, Austria, between 1969 and 1992 derived from Landsat 5 Thematic Mapper and Austrian Glacier Inventory data. *Int. J. Remote Sens.* 23, 787–799.
- Paul, F., 2000. Evaluation of different methods for glacier mapping using Landsat TM, in: *Proceedings, EARSeL-SIG Workshop, Dresden, Germany, 16–17 June 2000*.

- Paul, F., Andreassen, L.M., 2009. A new glacier inventory for the Svartisen region, Norway, from Landsat ETM+ data: challenges and change assessment. *J. Glaciol.* 55, 607–618.
- Paul, F., Andreassen, L.M., Winsvold, S.H., 2011a. A new glacier inventory for the Jostedalsgreen region, Norway, from Landsat TM scenes of 2006 and changes since 1966. *Ann. Glaciol.* 52, 153–162.
- Paul, F., Barrand, N.E., Baumann, S., Berthier, E., Bolch, T., Casey, K., Frey, H., Joshi, S., Kononov, V., Bris, R.L., others, 2013. On the accuracy of glacier outlines derived from remote-sensing data. *Ann. Glaciol.* 54, 171–182.
- Paul, F., Barry, R., Cogley, J., Frey, H., Haeberli, W., Ohmura, A., Ommanney, C., Raup, B., Rivera, A., Zemp, M., 2009. Recommendations for the compilation of glacier inventory data from digital sources. *Ann. Glaciol.* 50, 119–126.
- Paul, F., Bolch, T., Kääb, A., Nagler, T., Nuth, C., Scharrer, K., Shepherd, A., Strozzi, T., Ticconi, F., Bhambri, R., others, 2015. The glaciers climate change initiative: Methods for creating glacier area, elevation change and velocity products. *Remote Sens. Environ.* 162, 408–426.
- Paul, F., Frey, H., Le Bris, R., 2011b. A new glacier inventory for the European Alps from Landsat TM scenes of 2003: challenges and results. *Ann. Glaciol.* 52, 144–152.
- Paul, F., Huggel, C., Kääb, A., 2004a. Combining satellite multispectral image data and a digital elevation model for mapping debris-covered glaciers. *Remote Sens. Environ.* 89, 510–518.
- Paul, F., Kääb, A., 2005. Perspectives on the production of a glacier inventory from multispectral satellite data in Arctic Canada: Cumberland Peninsula, Baffin Island. *Ann. Glaciol.* 42, 59–66.
- Paul, F., Kääb, A., Haeberli, W., 2007. Recent glacier changes in the Alps observed by satellite: Consequences for future monitoring strategies. *Glob. Planet. Change* 56, 111–122.
- Paul, F., Kääb, A., Maisch, M., Kellenberger, T., Haeberli, W., 2004b. Rapid disintegration of Alpine glaciers observed with satellite data. *Geophys. Res. Lett.* 31.
- Paul, F., Kääb, A., Maisch, M., Kellenberger, T., Haeberli, W., 2002. The new remote-sensing-derived Swiss glacier inventory: I. Methods. *Ann. Glaciol.* 34, 355–361.
- Paul, F., Winsvold, S.H., Kääb, A., Nagler, T., Schwaizer, G., 2016. Glacier Remote Sensing Using Sentinel-2. Part II: Mapping Glacier Extents and Surface Facies, and Comparison to Landsat 8. *Remote Sens.* 8, 575.

- Penuelas, J., Sardans, J., Estiarte, M., Ogaya, R., Carnicer, J., Coll, M., Barbeta, A., Rivas-Ubach, A., Llusia, J., Garbulsky, M., others, 2013. Evidence of current impact of climate change on life: a walk from genes to the biosphere. *Glob. Change Biol.* 19, 2303–2338.
- Pepe, M., Boschetti, L., Brivio, P.A., Rampini, A., 2010. Comparing the performance of fuzzy and crisp classifiers on remotely sensed images: a case of snow classification. *Int. J. Remote Sens.* 31, 6189–6203.
- Petrow, T., Merz, B., 2009. Trends in flood magnitude, frequency and seasonality in Germany in the period 1951–2002. *J. Hydrol.* 371, 129–141.
- Pfeffer, W.T., Arendt, A.A., Bliss, A., Bolch, T., Cogley, J.G., Gardner, A.S., Hagen, J.-O., Hock, R., Kaser, G., Kienholz, C., others, 2014a. The Randolph Glacier Inventory: a globally complete inventory of glaciers. *J. Glaciol.* 60, 537–552.
- Pfeffer, W.T., Arendt, A.A., Bliss, A., Bolch, T., Cogley, J.G., Gardner, A.S., Hagen, J.-O., Hock, R., Kaser, G., Kienholz, C., others, 2014b. The Randolph Glacier Inventory: a globally complete inventory of glaciers. *J. Glaciol.* 60, 537–552.
- Pisarenko, A.I., Strakhov, V.V., 1996. Socio-economic assessment of the Russian boreal forests. IIASA Working Paper, 1996. Available Online: <http://pure.iiasa.ac.at/id/eprint/4968/1/WP-96-058.pdf> (accessed on 25 July, 2019).
- Poon, S.K., Valeo, C., 2006. Investigation of the MODIS snow mapping algorithm during snowmelt in the northern boreal forest of Canada. *Can. J. Remote Sens.* 32, 254–267.
- Pöyry, J., Böttcher, K., Fronzek, S., Gobron, N., Leinonen, R., Metsämäki, S., Virkkala, R., 2018. Predictive power of remote sensing versus temperature-derived variables in modelling phenology of herbivorous insects. *Remote Sens. Ecol. Conserv.* 4, 113–126.
- Pringle, M., Schmidt, M., Muir, J., 2009. Geostatistical interpolation of SLC-off Landsat ETM+ images. *ISPRS J. Photogramm. Remote Sens.* 64, 654–664.
- Pritchard, H.D., Arthern, R.J., Vaughan, D.G., Edwards, L.A., 2009. Extensive dynamic thinning on the margins of the Greenland and Antarctic ice sheets. *Nature* 461, 971–975.
- Pulliainen, J., Koskinen, J., Hallikainen, M., 2001. Compensation of forest canopy effects in the estimation of snow covered area from SAR data, in: *Proceedings of the 2001 IEEE International Geoscience and Remote Sensing Symposium, Sydney, Australia, 9–13 July, 2001; Volume 2, pp. 813–815.*
- Pulliainen, J.T., Grandell, J., Hallikainen, M.T., 1999. HUT snow emission model and its applicability to snow water equivalent retrieval. *IEEE Trans. Geosci. Remote Sens.* 37, 1378–1390.

- Qiu, Y., Savela, H., Key, J.R., Menenti, M., Vitale, V., Cheng, X., Friddell, J.E., Larsen, J.R., Enomoto, H., Guo, X., others, 2016. Statement on the GEO Cold Region Initiative (GEOCRI). Available Online: [https://earthobservations.org/documents/meetings/201603\\_arctic\\_summit/201603\\_arctic\\_summit\\_geocri\\_statement.pdf](https://earthobservations.org/documents/meetings/201603_arctic_summit/201603_arctic_summit_geocri_statement.pdf) (accessed on 25 July, 2019).
- Qiu, Y., Massimo, M., Li, X., Birendra, B., Joni, K., Narantuya, D., Liu, S., Gao, Y., Cheng, B., Wu, T., others, 2017. Observing and Understanding High Mountain and Cold Regions Using Big Earth Data. *Bull. Chin. Acad. Sci.* 32, 82–94.
- Rabatel, A., Dedieu, J.P., Vincent, C., 2016. Spatio-temporal changes in glacier-wide mass balance quantified by optical remote sensing on 30 glaciers in the French Alps for the period 1983–2014. *J. Glaciol.* 62, 1153–1166.
- Rabatel, A., Dedieu, J.-P., Vincent, C., 2005. Using remote-sensing data to determine equilibrium-line altitude and mass-balance time series: validation on three French glaciers, 1994–2002. *J. Glaciol.* 51, 539–546.
- Racoviteanu, A.E., Paul, F., Raup, B., Khalsa, S.J.S., Armstrong, R., 2009. Challenges and recommendations in mapping of glacier parameters from space: results of the 2008 Global Land Ice Measurements from Space (GLIMS) workshop, Boulder, Colorado, USA. *Ann. Glaciol.* 50, 53–69.
- Radić, V., Bliss, A., Beedlow, A.C., Hock, R., Miles, E., Cogley, J.G., 2014. Regional and global projections of twenty-first century glacier mass changes in response to climate scenarios from global climate models. *Clim. Dyn.* 42, 37–58.
- Ramsay, B.H., 1998. The interactive multisensor snow and ice mapping system. *Hydrol. Process.* 12, 1537–1546.
- Ranzi, R., Grossi, G., Iacovelli, L., Taschner, S., 2004. Use of multispectral ASTER images for mapping debris-covered glaciers within the GLIMS project, in: *Geoscience and Remote Sensing Symposium, 2004. IGARSS'04. Proceedings. 2004 IEEE International. IEEE*, pp. 1144–1147.
- Raup, B., Kääb, A., Kargel, J.S., Bishop, M.P., Hamilton, G., Lee, E., Paul, F., Rau, F., Soltesz, D., Khalsa, S.J.S., others, 2007a. Remote sensing and GIS technology in the Global Land Ice Measurements from Space (GLIMS) project. *Comput. Geosci.* 33, 104–125.
- Raup, B., Khalsa, S.J.S., 2010. GLIMS analysis tutorial. National Snow: Boulder, CO, USA.
- Raup, B., Racoviteanu, A., Khalsa, S.J.S., Helm, C., Armstrong, R., Arnaud, Y., 2007b. The GLIMS geospatial glacier database: a new tool for studying glacier change. *Glob. Planet. Change* 56, 101–110.
- Rawlins, M.A., McDonald, K.C., Frolking, S., Lammers, R.B., Fahnestock, M., Kimball, J.S., Vörösmarty, C.J., 2005. Remote sensing of snow thaw at the pan-Arctic scale using the SeaWinds scatterometer. *J. Hydrol.* 312, 294–311.



- Richter, R., Schläpfer, D., 2011. Atmospheric/topographic correction for satellite imagery: ATCOR-2/3 User Guide. DLR IB 501–565.
- Riggs, G.A., Hall, D.K., Salomonson, V.V., 1994. A snow index for the Landsat thematic mapper and moderate resolution imaging spectroradiometer, in: *Geoscience and Remote Sensing Symposium, 1994. IGARSS'94. Surface and Atmospheric Remote Sensing: Technologies, Data Analysis and Interpretation.*, International. IEEE, pp. 1942–1944.
- Ripper, E., Bippus, G., Nagler, T., Metsämäki, S., Fernandes, R., Crawford, C.J., Painter, T., Rittger, K., 2015. Guidelines for the Generation of Snow Extent Products from High Resolution Optical Sensors – FINAL. Available Online: [http://snowpex.enveo.at/Documents/D08\\_Guidelines\\_for\\_the\\_generation\\_of\\_snow\\_extent\\_products\\_from\\_HR\\_optical\\_sensors\\_FINAL\\_v2.1.pdf](http://snowpex.enveo.at/Documents/D08_Guidelines_for_the_generation_of_snow_extent_products_from_HR_optical_sensors_FINAL_v2.1.pdf) (accessed on 25 July, 2019).
- Rittger, K., Painter, T.H., Dozier, J., 2013. Assessment of methods for mapping snow cover from MODIS. *Adv. Water Resour.* 51, 367–380.
- Robinson, D.A., Dewey, K.F., Heim Jr, R.R., 1993. Global snow cover monitoring: An update. *Bull. Am. Meteorol. Soc.* 74, 1689–1696.
- Robson, B.A., Hölbling, D., Nuth, C., Strozzi, T., Dahl, S.O., 2016. Decadal Scale Changes in Glacier Area in the Hohe Tauern National Park (Austria) Determined by Object-Based Image Analysis. *Remote Sens.* 8, 67.
- Romanov, P., Gutman, G., Csiszar, I., 2000. Automated monitoring of snow cover over North America with multispectral satellite data. *J. Appl. Meteorol.* 39, 1866–1880.
- Rosenqvist, A., Shimada, M., Chapman, B., McDonald, K., De Grandi, G., Jonsson, H., Williams, C., Rauste, Y., Nilsson, M., Sango, D., others, 2004. An overview of the JERS-1 SAR global boreal forest mapping (GBFM) project, in: *Proceedings of the 2004 IEEE International Geoscience and Remote Sensing Symposium, Anchorage, AK, USA, 20–24 September 2004; Volume 2*, pp. 1033–1036.
- Rosenthal, W., Dozier, J., 1996. Automated Mapping of Montane Snow Cover at Subpixel Resolution from the Landsat Thematic Mapper. *Water Resour. Res.* 32, 115–130.
- Rotschky, G., Schuler, T.V., Kohler, J., Isaksson, E., others, 2011. Spatio-temporal variability of snowmelt across Svalbard during the period 2000-08 derived from QuikSCAT/SeaWinds scatterometry. *Polar Res.* 30.
- Roy, D.P., Wulder, M., Loveland, T.R., Woodcock, C., Allen, R., Anderson, M., Helder, D., Irons, J., Johnson, D., Kennedy, R., others, 2014. Landsat-8: Science and product vision for terrestrial global change research. *Remote Sens. Environ.* 145, 154–172.
- Rubel, F., Brugger, K., Haslinger, K., Auer, I., 2017. The climate of the European Alps: Shift of very high resolution Köppen-Geiger climate zones 1800–2100. *Meteorol. Z.* 26, 115–125.

- Rubel, F., Kottek, M., 2010. Observed and projected climate shifts 1901–2100 depicted by world maps of the Köppen-Geiger climate classification. *Meteorol. Z.* 19, 135–141.
- Sala, O.E., Chapin, F.S., Armesto, J.J., Berlow, E., Bloomfield, J., Dirzo, R., Huber-Sanwald, E., Huenneke, L.F., Jackson, R.B., Kinzig, A., others, 2000. Global biodiversity scenarios for the year 2100. *science* 287, 1770–1774.
- Salminen, M., Pulliainen, J., Metsämäki, S., Kontu, A., Suokanerva, H., 2009. The behaviour of snow and snow-free surface reflectance in boreal forests: Implications to the performance of snow covered area monitoring. *Remote Sens. Environ.* 113, 907–918.
- Salomonson, V., Appel, I., 2004. Estimating fractional snow cover from MODIS using the normalized difference snow index. *Remote Sens. Environ.* 89, 351–360.
- Salomonson, V.V., Appel, I., 2006. Development of the Aqua MODIS NDSI fractional snow cover algorithm and validation results. *IEEE Trans. Geosci. Remote Sens.* 44, 1747–1756.
- Santi, E., Pettinato, S., Paloscia, S., Pampaloni, P., Fontanelli, G., Crepaz, A., Valt, M., 2014. Monitoring of Alpine snow using satellite radiometers and artificial neural networks. *Remote Sens. Environ.* 144, 179–186.
- Santi, E., Pettinato, S., Paloscia, S., Pampaloni, P., Macelloni, G., Brogioni, M., 2012. An algorithm for generating soil moisture and snow depth maps from microwave spaceborne radiometers: HydroAlgo. *Hydrol. Earth Syst. Sci.* 16, 3659–3676.
- Sapiano, J.J., Harrison, W. t, Echelmeyer, K., 1998. Elevation, volume and terminus changes of nine glaciers in North America. *J. Glaciol.* 44, 119–135.
- Saunier, S., Northrop, A., Lavender, S., Galli, L., Ferrara, R., Mica, S., Biasutti, R., Goryl, P., Gascon, F., Meloni, M., others, 2017. European Space agency (ESA) Landsat MSS/TM/ETM+/OLI archive: 42 years of our history, in: *Analysis of Multitemporal Remote Sensing Images (MultiTemp)*, 2017 9th International Workshop on The. IEEE, pp. 1–9.
- Schellenberger, T., Dunse, T., Käab, A., Schuler, T.V., Hagen, J.O., Reijmer, C.H., 2017. Multi-year surface velocities and sea-level rise contribution of the Basin-3 and Basin-2 surges, Austfonna, Svalbard. *Cryosphere Discuss.* 1–27.
- Schellenberger, T., Van Wychen, W., Copland, L., Käab, A., Gray, L., 2016. An Inter-Comparison of Techniques for Determining Velocities of Maritime Arctic Glaciers, Svalbard, Using Radarsat-2 Wide Fine Mode Data. *Remote Sens.* 8, 785.
- Schowengerdt, R.A., 2006. *Remote sensing: models and methods for image processing.* San Diego, CA: Academic.

- Schubert, A., Faes, A., Kääh, A., Meier, E., 2013. Glacier surface velocity estimation using repeat TerraSAR-X images: Wavelet-vs. correlation-based image matching. *ISPRS J. Photogramm. Remote Sens.* 82, 49–62.
- Schuler, M., Stucki, E., Roque, O., Perlik, M., 2004. Mountain Areas in Europe: Analysis of mountain areas in EU member states, acceding and other European countries.
- Schuur, E.A., Vogel, J.G., Crummer, K.G., Lee, H., Sickman, J.O., Osterkamp, T., 2009. The effect of permafrost thaw on old carbon release and net carbon exchange from tundra. *Nature* 459, 556–559.
- Selkowitz, D.J., Forster, R.R., 2015. An automated approach for mapping persistent ice and snow cover over high latitude regions. *Remote Sens.* 8, 16.
- Seneviratne, S.I., Nicholls, N., Easterling, D., Goodess, C.M., Kanae, S., Kossin, J., Luo, Y., Marengo, J., McInnes, K., Rahimi, M., others, 2012. Changes in climate extremes and their impacts on the natural physical environment. In *Managing the Risks of Extreme Events and Disasters to Advance Climate Change Adaptation*; Cambridge University Press: Cambridge, UK; New York, NY, USA.
- Serandrei-Barbero, R., Rabagliati, R., Binaghi, E., Rampini, A., 1999. Glacial retreat in the 1980s in the Breonie, Aurine and Pusteresi groups (eastern Alps, Italy) in Landsat TM images. *Hydrol. Sci. J.* 44, 279–296.
- Severskiy, I., Zichu, X., 2000. Snow cover and avalanches in the Tien Shan mountains. Minist. Almaty, VAC Publishing House, 179 pp.
- Shotyk, W., 2017. Biogeochemistry: Arctic plants take up mercury vapour. *Nature* 547, 167–168.
- Slater, P.N., 1980. Remote sensing: optics and optical systems. Read. Mass Addison-Wesley Publ. CoRemote Sens. No 1 1980 593 P 1.
- Solberg, R., Wangenstein, B., Metsämäki, S., Nagler, T., Sandner, R., Rott, H., Wiesmann, A., Luoju, K., Kangwa, M., Pulliainen, J., 2010. GlobSnow snow extent product guide product version 1.0. Available Online: [http://www.globsnow.info/se/nrt/GlobSnow\\_SE\\_product\\_readme\\_v1.0.pdf](http://www.globsnow.info/se/nrt/GlobSnow_SE_product_readme_v1.0.pdf) (accessed on 26 July, 2019).
- Stocker, T.F., Qin, D., Plattner, G., Alexander, L., Allen, S., Bindoff, N., Breon, F., Church, J., Cubasch, U., Emori, S., others, 2013. Technical Summary- Climate Change 2013: The Physical Science Basis. Contrib. Work. Group Fifth Assess. Rep. Intergov. Panel Clim. Change 33–115.
- Strozzi, T., Luckman, A., Murray, T., Wegmuller, U., Werner, C.L., 2002. Glacier motion estimation using SAR offset-tracking procedures. *IEEE Trans. Geosci. Remote Sens.* 40, 2384–2391.

## References

---

- Strozzi, T., Wiesmann, A., Sharov, A., Kouraev, A., Wegmüller, U., Werner, C., 2006. Capabilities of L-band SAR data for arctic glacier motion estimation. In Proceedings of the IGARSS, Denver, CO, USA, 31 July–4 August, 2006.
- Svoboda, F., Paul, F., 2009. A new glacier inventory on southern Baffin Island, Canada, from ASTER data: I. Applied methods, challenges and solutions. *Ann. Glaciol.* 50, 11–21.
- Swamy, A., Brivio, P., 1996. Hydrological modelling of snowmelt in the Italian Alps using visible and infrared remote sensing. *Remote Sens.* 17, 3169–3188.
- Tachikawa, T., Hato, M., Kaku, M., Iwasaki, A., 2011. Characteristics of ASTER GDEM version 2, in: Proceedings of the 2011 IEEE International Geoscience and Remote Sensing Symposium, Vancouver, BC, Canada, 24–29 July, 2011.
- Takala, M., Pulliainen, J., Metsamäki, S.J., Koskinen, J.T., 2009. Detection of snowmelt using spaceborne microwave radiometer data in Eurasia from 1979 to 2007. *IEEE Trans. Geosci. Remote Sens.* 47, 2996–3007.
- Tedesco, M., Brodzik, M., Armstrong, R., Savoie, M., Ramage, J., 2009. Pan arctic terrestrial snowmelt trends (1979–2008) from spaceborne passive microwave data and correlation with the Arctic Oscillation. *Geophys. Res. Lett.* 36.
- Tedesco, M., Pulliainen, J., Takala, M., Hallikainen, M., Pampaloni, P., 2004. Artificial neural network-based techniques for the retrieval of SWE and snow depth from SSM/I data. *Remote Sens. Environ.* 90, 76–85.
- Thum, T., Aalto, T., Laurila, T., Aurela, M., Hatakka, J., Lindroth, A., Vesala, T., 2009. Spring initiation and autumn cessation of boreal coniferous forest CO<sub>2</sub> exchange assessed by meteorological and biological variables. *Tellus B Chem. Phys. Meteorol.* 61, 701–717.
- Torres, R., Snoeij, P., Geudtner, D., Bibby, D., Davidson, M., Attema, E., Potin, P., Rommen, B., Floury, N., Brown, M., others, 2012. GMES Sentinel-1 mission. *Remote Sens. Environ.* 120, 9–24.
- Turpin, O., Ferguson, R., Johansson, B., 1999. Use of remote sensing to test and update simulated snow cover in hydrological models. *Hydrol. Process.* 13, 2067–2077.
- USGS, 2015. Comparison of Landsat 7 and 8 bands with Sentinel-2. Available Online: [https://prd-wret.s3-us-west-2.amazonaws.com/assets/palladium/production/s3fs-public/styles/full\\_width/public/thumbnails/image/dmidS2LS7Comparison.png](https://prd-wret.s3-us-west-2.amazonaws.com/assets/palladium/production/s3fs-public/styles/full_width/public/thumbnails/image/dmidS2LS7Comparison.png) (accessed on 25 July, 2019).
- USGS/EROS, 2017. Landsat Collection 1 Level 1 Product Definition - Version 1. Sioux Falls, SD, USA. Available Online: [https://prd-wret.s3-us-west-2.amazonaws.com/assets/palladium/production/atoms/files/LSDS-1656\\_%20Landsat\\_Collection1\\_L1\\_Product\\_Definition-v2.0.pdf](https://prd-wret.s3-us-west-2.amazonaws.com/assets/palladium/production/atoms/files/LSDS-1656_%20Landsat_Collection1_L1_Product_Definition-v2.0.pdf) (accessed on 25 July, 2019).

- Van Vliet, M., Zwolsman, J., 2008. Impact of summer droughts on the water quality of the Meuse river. *J. Hydrol.* 353, 1–17.
- Vaughan, D.G., Comiso, J.C., Allison, I., Carrasco, J., Kaser, G., Kwok, R., Mote, P., Murray, T., Paul, F., Ren, J., others, 2013. Observations: cryosphere. *Clim. Change* 2103, 317–382.
- Veganzones, M.A., Dalla Mura, M., Dumont, M., Zin, I., Chanussot, J., 2014. Improved subpixel monitoring of seasonal snow cover: a case study in the Alps, in: *Proceedings of the 2014 IEEE International Geoscience and Remote Sensing Symposium (IGARSS)*, Quebec City, QC, Canada, 13–18 July, 2014; pp. 3976–3979.
- Vepsalainen, J., Metsamaki, S., Koskinen, J., Huttunen, M., Pulliainen, J., 2001. Estimation of snow covered area by applying apparent regional transmissivity, in: *Proceedings of the 2001 IEEE International Geoscience and Remote Sensing Symposium*, Sydney, Australia, 9–13 July, 2001; Volume 7, pp. 3237–3239.
- Vikhamar, D., Solberg, R., 2003a. Subpixel mapping of snow cover in forests by optical remote sensing. *Remote Sens. Environ.* 84, 69–82.
- Vikhamar, D., Solberg, R., 2003b. Snow-cover mapping in forests by constrained linear spectral unmixing of MODIS data. *Remote Sens. Environ.* 88, 309–323.
- Wang, L., Wolken, G., Sharp, M., Howell, S., Derksen, C., Brown, R., Markus, T., Cole, J., 2011. Integrated pan-Arctic melt onset detection from satellite active and passive microwave measurements, 2000–2009. *J. Geophys. Res. Atmospheres* 116.
- Wang, X., Xie, H., 2009. New methods for studying the spatiotemporal variation of snow cover based on combination products of MODIS Terra and Aqua. *J. Hydrol.* 371, 192–200.
- Wang, Y., Wang, L., Li, H., Yang, Y., Yang, T., 2015. Assessment of snow status changes using L-HH temporal-coherence components at Mt. Dagu, China. *Remote Sens.* 7, 11602–11620.
- Wang, Z., Erb, A.M., Schaaf, C.B., Sun, Q., Liu, Y., Yang, Y., Shuai, Y., Casey, K.A., Román, M.O., 2016. Early spring post-fire snow albedo dynamics in high latitude boreal forests using Landsat-8 OLI data. *Remote Sens. Environ.* 185, 71–83.
- Warren, S.G., 1982. Optical properties of snow. *Rev. Geophys.* 20, 67–89.
- Warren, S.G., Wiscombe, W.J., 1980. A model for the spectral albedo of snow. II: Snow containing atmospheric aerosols. *J. Atmospheric Sci.* 37, 2734–2745.
- Willett, J.B., Singer, J.D., 1988. Another cautionary note about R 2: Its use in weighted least-squares regression analysis. *Am. Stat.* 42, 236–238.
- Winsvold, S.H., Andreassen, L.M., Kienholz, C., 2014. Glacier area and length changes in Norway from repeat inventories. *The Cryosphere* 8, 1885–1903.

## References

---

- Winther, J.G., Hall, D.K., 1999. Satellite-derived snow coverage related to hydropower production in Norway: Present and future. *Int. J. Remote Sens.* 20, 2991–3008.
- Woodcock, C.E., Allen, R., Anderson, M., Belward, A., Bindschadler, R., Cohen, W., Gao, F., Goward, S.N., Helder, D., Helmer, E., Nemani, R., Oreopoulos, L., Schott, J., Thenkabail, P.S., Vermote, E.F., Vogelmann, J., Wulder, M.A., Wynne, R., 2008. Free Access to Landsat Imagery. *Science* 320, 1011–1011.
- Wu, X., Che, T., Li, X., Wang, N., Yang, X., 2018. Slower snowmelt in spring along with climate warming across the Northern Hemisphere. *Geophys. Res. Lett.* 45, 12–331.
- Wulder, M.A., Masek, J.G., Cohen, W.B., Loveland, T.R., Woodcock, C.E., 2012. Opening the archive: How free data has enabled the science and monitoring promise of Landsat. *Remote Sens. Environ.* 122, 2–10.
- Wulder, M.A., White, J.C., Loveland, T.R., Woodcock, C.E., Belward, A.S., Cohen, W.B., Fosnight, E.A., Shaw, J., Masek, J.G., Roy, D.P., 2016. The global Landsat archive: Status, consolidation, and direction. *Remote Sens. Environ.* 185, 271–283.
- Xiao, X., Zhang, Q., Boles, S., Rawlins, M., Moore III, B., 2004. Mapping snow cover in the pan-Arctic zone, using multi-year (1998-2001) images from optical VEGETATION sensor. *Int. J. Remote Sens.* 25, 5731–5744.
- Yang, Z., Liu, X., Zeng, Q., Chen, Z., 2000. Hydrology in cold regions of China (in Chinese). Science Press: Beijing, China; pp. 90–124.
- Zhu, Z., Wang, S., Woodcock, C.E., 2015. Improvement and expansion of the Fmask algorithm: cloud, cloud shadow, and snow detection for Landsats 4–7, 8, and Sentinel 2 images. *Remote Sens. Environ.* 159, 269–277.
- Zhu, Z., Woodcock, C.E., 2014a. Automated cloud, cloud shadow, and snow detection in multitemporal Landsat data: An algorithm designed specifically for monitoring land cover change. *Remote Sens. Environ.* 152, 217–234.
- Zhu, Z., Woodcock, C.E., 2014b. Continuous change detection and classification of land cover using all available Landsat data. *Remote Sens. Environ.* 144, 152–171.
- Zhu, Z., Woodcock, C.E., 2012. Object-based cloud and cloud shadow detection in Landsat imagery. *Remote Sens. Environ.* 118, 83–94.
- Zimova, M., Hackländer, K., Good, J.M., Melo-Ferreira, J., Alves, P.C., Mills, L.S., 2018. Function and underlying mechanisms of seasonal colour moulting in mammals and birds: what keeps them changing in a warming world? *Biol. Rev.* 93, 1478–1498.
- Zwally, H., Schutz, B., Abdalati, W., Abshire, J., Bentley, C., Brenner, A., Bufton, J., Dezio, J., Hancock, D., Harding, D., others, 2002. ICESat's laser measurements of polar ice, atmosphere, ocean, and land. *J. Geodyn.* 34, 405–445.

## Eidesstattliche Erklärung

Hiermit erkläre ich, dass ich die von mir eingereichte Dissertation mit dem Titel „Earth Observation for the Assessment of Long-Term Snow Dynamics in European Mountains - Analysing 35-Year Snowline Dynamics in Europe Based on High Resolution Earth Observation Data between 1984 and 2018“ selbständig und ausschließlich unter Verwendung der angegebenen Literatur und sonstigen Quellen verfasst habe. Alle den angeführten Quellen wörtlich oder sinngemäß entnommenen Stellen habe ich als solche kenntlich gemacht.

---

Oberpfaffenhofen, den 27.07.2019

---

Zhongyang Hu





# Zhongyang Hu

## *Curriculum Vitae*

Münchener Straße 20  
82234, Weßling  
Germany  
+49 8153 28 2851  
Zhongyang.hu@dlr.de

### Research Experience

#### Since 2016 **Ph.D. Student**

Department: Land Surface Dynamics, German Remote Sensing Data Center, German Aerospace Center, in collaboration with Institute of Geography and Geology, University of Wuerzburg

Topic: Analysing 35-Year Snowline Dynamics in Europe Based on High Resolution Earth Observation Data between 1984 and 2018

#### 2015–2016 **Master Thesis**

Department of Environmental Remote Sensing and Geoinformatics, University of Trier

Topic: Using UAV-Derived Airphotos for Assessing the Accuracy of Spectral Unmixing Applied to EO Data of Dryland Ecosystems

#### 2015–2016 **Research Assistant**

Department of Environmental Remote Sensing and Geoinformatics, University of Trier

Major Tasks: Landsat and UAV Airphotos Processing

#### 2012–2013 **Bachelor Thesis**

Department of Geography and Environment, Jiangxi Normal University

Topic: Study on Spectrum Response of Carex Cinerascens Kukenth to Zinc

### Education

since 2016 **Ph.D. Student**, University of Wuerzburg, Wuerzburg, Germany  
Remote Sensing

2013–2016 **Master**, University of Trier, Trier, Germany.  
Environmental Science (specialization: Environmental Remote Sensing)

2009–2013 **Bachelor**, Jiangxi Normal University, Nanchang, China  
Geographical Science

## Languages

English      **Highly proficient in spoken and written English**

German      **Good working knowledge**

Chinese      **Native speaker**

## Computer Skills

GIS Software      **ESRI ArcGIS and Quantum GIS**

RS Software      **Google Earth Engine (JavaScript API), Erdas Imagine, ENVI/IDL, ATCOR, and GDAL/OGR**

Programming      **R, Python, and IDL**

Office      **Microsoft Word, Excel, Powerpoint, Outlook, and Lync**